Nordström, Karl Anders Mattias (2017) Phenomenology for the large hadron collider. PhD thesis.

Phenomenology for the Large Hadron Collider

Karl Anders Mattias Nordström

Supervised by Dr. Christoph Englert and Dr. David Miller

Submitted in fulfillment of the requirements for the degree of
Doctor of Philosophy

August 2017

The University of Glasgow
College of Science and Engineering

Phenomenology for the Large Hadron Collider

Abstract:

The search for physics Beyond the Standard Model is the underlying motivation for the physics programme of the Large Hadron Collider at CERN. In this thesis we will present studies into the Large Hadron Collider phenomenology of dark matter inspired extensions to the Standard Model, di-Higgs + 2 jet ($hhjj$) production, $\mathcal{CP}$ violating effects in the Higgs sector, and the use of shape information from top polarisation measurements in searches for new physics.

Full scans of the parameter space of Simplified Dark Matter models are demonstrated to be viable and allow for intriguing comparisons to relic density constraints. Strongly self-interacting dark sectors are shown to leave a potentially measurable imprint on the energy scaling of mediator production. The weak boson fusion induced production of $hhjj$ turns out to be sensitive to a number of new physics effects, including $\mathcal{CP}$ violation in the Higgs sector. The use of top polarisation measurements to discover new physics which predicts polarised resonances is shown to be an effective way to ameliorate the loss of shape information for kinematically challenging regions of parameter space.

Keywords: particle physics phenomenology, collider phenomenology, Higgs physics, dark matter physics, top quark physics

Declaration of originality

This thesis is my own work, except where explicit attribution to others is made. In particular Chapters 4, 5, 6, 7 are based on the following publications:

- Chapter 4:

  Mapping monojet constraints onto Simplified Dark Matter Models [1], written in collaboration with Dr. Thomas Jacques.

- Chapter 5:

  Towards resolving strongly-interacting dark sectors at colliders [2], written in collaboration with Dr. Christoph Englert and Dr. Michael Spannowsky.

- Chapter 6:

  hhjj production at the LHC [3], written in collaboration with Dr. Matthew Dolan, Dr. Christoph Englert, Dr. Nicolas Greiner, and Dr. Michael Spannowsky, and

  Perturbative Higgs CP violation, unitarity and phenomenology [4], written in collaboration with Dr. Christoph Englert, Dr. Kazuki Sakurai, and Dr. Michael Spannowsky.

- Chapter 7:

  Constraining new resonant physics with top spin polarisation information [5], written in collaboration with Dr. Christoph Englert and Dr. James Ferrando.

All results and figures presented in these chapters are my own, except for the calculation in Section 5.6 which was done by Dr. Christoph Englert, the calculation in Section 6.8 which was done by Dr. Christoph Englert and Dr. Kazuki Sakurai, the Figures 5.3, 5.4 which were created by Dr. Christoph Englert, the Figures 6.1, 6.5 which were created by Dr. Nicolas Greiner, and the Figures 6.11, 6.12, 6.13 which were created by Dr. Christoph Englert and Dr. Kazuki Sakurai.

För Ethel och Åke

Acknowledgments

Contents

Introduction

The Large Hadron Collider is currently exploring the highest energies ever probed systematically by a man-made experiment. After its seminal discovery of the Higgs boson in 2012 [6,7] we are now at a crossroads: if further new physics exists within its energy range, it should show up at any moment as the 13 TeV run quickly approaches 100 fb^{-1} of integrated luminosity [8]. If such new physics is discovered it will finally herald the end of the era of the Standard Model, which has lasted for almost five decades and has established quantum field theory as arguably the most successful theoretical paradigm for describing the world ever conceived. Whatever shape the discovery would take, it would surely revolutionise our understanding of the fundamental physical laws of nature and open up completely new frontiers to explore.

If no new physics is discovered within the Large Hadron Collider energy range we are instead left in the confusing situation where we know the Standard Model is deeply flawed and new physics is required to explain both large and small-scale observations, but we are unable to find any direct evidence for the nature of this new physics. We would instead have to turn to precision measurements of Standard Model predictions in order to search for indirect hints of the underlying structure of the higher energy completion. The Higgs and top quarks sectors are excellent candidates for such measurements, as they are the heaviest particles in the Standard Model and the least explored experimentally.

Advances in precision cosmology and astronomy will also offer new experimental results which will have an increasing impact on particle physics. In this regard the search for dark matter is an early example of how such an interplay can manifest: the firm establishment of the ΛCDM 'Standard Model' of cosmology has led to a large number of effectively particle physics experiments which search for hints of the microscopic nature of dark matter. Colliders such as the Large Hadron Collider also provide considerable information about these expected extensions of the Standard Model, and connecting collider measurements to large scale observations such as the

relic density is an interesting problem in itself.

In this thesis we will discuss the phenomenology of new physics searches at the Large Hadron Collider, with a focus on the Higgs and top quark sectors of the Standard Model, and extensions which are motivated by dark matter. Chapter 2 introduces the Standard Model and the calculational tools which will be used throughout the rest of the thesis. Chapter 3 discusses the arguments for the existence of physics Beyond the Standard Model, focusing on the nature of electroweak symmetry breaking and dark matter.

The remainder of the thesis consists of novel studies into these topics. In Chapter 4 we perform a full parameter scan of a so-called Simplified Dark Matter model, and connect it to a calculation of the relic density. Chapter 5 considers the collider phenomenological consequences of adding a mostly secluded dark sector with strong self-interactions to the Standard Model, connected through a Higgs portal. In Chapter 6 we present a thorough study of $hhjj$ production at the LHC, both through gluon fusion using a full leading order matrix element calculation, and through weak boson fusion. We also investigate perturbative unitarity constraints on $\mathcal{CP}$ violating effects in the Higgs sector, using the $hhjj$ analysis to get a handle on a certain type of effect. In Chapter 7 we investigate the use of top polarisation measurements in top resonance searches, and demonstrate their utility by applying them to a benchmark Randall-Sundrum model.

In Chapter 8 we finally present some concluding remarks.

The Standard Model. . .

*"You come in to me now as an interviewer and you're asking me about the **latest** discoveries of the day. Nobody ever asks about a simple ordinary phenomenon in the street or 'what about those colors' or something like that, 'what about those colors on butterfly wings' – whole big deal – don't care about that. You want the big, final result, and see then it's going to be complicated because I am at the end of 400 years of a very effective method of finding out about the world."*

Richard Feynman in interview with the BBC, 1981

Contents

2.1   Representations of the Lorentz group

A particle is associated with a unique irreducible representation of the Poincaré group $ISO(1,3)$, as required by the transformation properties we expect from particles under Poincaré transformations. All of the unitary representations we use in quantum theories are infinite-dimensional and have been classified by Wigner using the method of induced representations. The classification is given by a non-negative mass m and a spin representation given by a non-negative half-integer [9]. In general it is impossible to build a consistent relativistic quantum theory without interpreting particles as excitations of quantised fields rather than as quantised particles [10]. We will therefore build our quantum theory lagrangians out of operator-valued fields, so we are interested in representations of the proper orthochronous real Lorentz group $SO^+(1,3;\mathbb{R})$. Representations of this group are most easily found by making the observation that we can define a complexified linear combination of the generators which creates a pair of two commuting $su(2)$ subalgebras, implying that:

$$\mathbb{C} \times so(1,3) \simeq su(2) \oplus su(2). \tag{2.1}$$

Thus we can find irreducible representations of the complexified Lorentz group by using the well-known irreducible representations of $su(2)$. We might worry that complexifying the algebra in order to make the connection to $SU(2)$ introduces complex representations that act strangely when embedded in real space. This is in fact what allows us to find spinor representations which are not real representations of $SO^+(1,3;\mathbb{R})$ since they don't map rotations by 2π to the identity element. It is as if these representations have some internal coordinates to perform a Möbius rotation in. This can be understood physically as we are ultimately interested in representations which on top of their normal properties additionally also allow group elements to change the phase of a state since we can't distinguish this in practice by quantum mechanics. These *projective* representations of $SO^+(1,3;\mathbb{R})$ correspond exactly to those of its spin group $SL(2,\mathbb{C})$, rendering spinors physical in a quantum theory [11].

When interpreting the excitations of a field as particle states these must fall into one of Wigner's classes. The spin of a particle is determined by its transformation properties under the Little Group, the subgroup of $ISO(1,3)$ under which its momentum is invariant. The Little Group is $SO(3)$ for massive particles and $ISO(2)$

Representation of $su(2) \oplus su(2)$	$(\mathbf{0}, \mathbf{0})$	$(\mathbf{1/2}, \mathbf{0})$	$(\mathbf{0}, \mathbf{1/2})$	$(\mathbf{1/2}, \mathbf{1/2})$
Representations of $so(3)$	$\mathbf{0}$	$\mathbf{1/2}$	$\mathbf{1/2}$	$\mathbf{1} \oplus \mathbf{0}$

Table 2.1: The Lorentz representations used in the Standard Model, and the possible spin representations of $so(3)$ which can be embedded in these. The half-integer representations of $so(3)$ are projective.

for massless particles[*], both of which are finite-dimensional, and in particular the projective representations of $SO(3)$ are given by the representations of $SU(2)$, allowing half-integer spins.[†] The irreducible Lorentz-representations of the fields do not in general decompose into irreducible representations of the Little Group, and in order to embed particles we need to make sure that only a single irreducible spin representation propagates by projecting it out with the equations of motion.

The $su(2) \oplus su(2)$ representations used in the Standard Model are detailed in Table 2.1, together with the projective $so(3)$ representations that can be embedded in these.

The first of these is the singlet representation $(0, 0)$ which acts on scalars. It carries no Lorentz indices and therefore transforms trivially under Lorentz transformations. In the Standard Model only the Higgs field transforms under this representation.

The two following representations are the left-handed and right-handed Weyl spinor representations $(1/2, 0)$ and $(0, 1/2)$. Since the two $su(2)$ representations in these cases are not equal we can imagine using fields which transform under these to construct theories which are not invariant under $(A, B) \to (B, A)$ transformations: such theories are called *chiral* and the Standard Model is an example of such a theory. Weyl spinors have two degrees of freedom, usually denoted by dotted and undotted indices for right- and left-handed Weyl spinors respectively:

$$\psi_L = \psi^\alpha, \qquad \psi_R = \tilde{\psi}_{\dot{\beta}}, \qquad \tilde{\psi}_{\dot{\beta}} = \begin{pmatrix} 0 & 1 \\ -1 & 0 \end{pmatrix}_{\dot{\beta}\alpha} (\psi^\alpha)^*, \tag{2.2}$$

They can be used to write down a Lorentz invariant theory of massless fermions, however if the fermion is charged a mass term ends up mixing left- and right-handed spinors which necessitates the use of Dirac spinors. These combine pairs of

---

[*]Giving all non-scalar massless particles two degrees of freedom corresponding to positive and negative helicity.

[†]There is (as always) a very lucid physical discussion of this in Feynman Vol. 3, Lecture 6 [12].

left- and right-handed spinors into a single object with four degrees of freedom for describing massive fermions, which transform in the reducible Dirac representation $(\frac{1}{2}, 0) \oplus (0, \frac{1}{2})$:

$$\psi_D = \begin{pmatrix} \psi^\alpha \\ \tilde{\psi}_{\dot\beta} \end{pmatrix}. \tag{2.3}$$

When working with the Dirac representation it is helpful to introduce Dirac or gamma matrices defined through the following anti-commutation relation:

$$\{\gamma_\mu, \gamma_\nu\} = 2g_{\mu\nu}. \tag{2.4}$$

This is the Clifford algebra of Minkowski space. In the Weyl basis these gamma matrices are given by:

$$\gamma^\mu = \begin{pmatrix} 0 & \sigma^\mu \\ \bar\sigma^\mu & 0 \end{pmatrix}, \qquad \begin{matrix} \sigma^\mu = (1, \vec\sigma) \\ \bar\sigma^\mu = (1, -\vec\sigma) \end{matrix}. \tag{2.5}$$

Here σ^i are the Pauli matrices. While we will only use the Weyl representations when writing down the Standard Model it turns out that the Dirac representation is very useful when describing physics after electroweak symmetry breaking, in particular Quantum Electrodynamics is not a chiral theory and calculations can therefore be simplified by considering Dirac spinors and gamma matrices rather than Weyl spinors and Pauli matrices. When working with Weyl spinors embedded into Dirac spinors it is very useful to be able to project out the Weyl spinors when needed. This can be achieved with the following chirality operators:

$$\mathbb{P}_{L,R} = \frac{1}{2}(\mathbb{I} \pm \gamma_5) = \frac{1}{2}(\mathbb{I} \pm i\gamma_0\gamma_1\gamma_2\gamma_3), \tag{2.6}$$

The final representation used is the Lorentz vector $(1/2, 1/2)$ which acts on real 4-vectors. As can be seen in Table 2.1 this representation can be used to describe both spin-0 and spin-1 representations of $so(3)$: when writing down the Standard Model we will only be interested in using it for spin-1 particles, which can be achieved by using the equations of motion to project out the spin-1 component only. This is in general achieved by using the Proca lagrangian[*]:

$$\mathcal{L} = -\frac{1}{4}F_{\mu\nu}^2 + \frac{1}{2}m_A^2 A_\mu^2. \tag{2.7}$$

---

[*]The terms used here will be defined later in Section 2.4.1.

We will in general introduce vector fields as connections which ensure local gauge invariance under the Standard Model gauge group. This will disallow the mass term and indeed all of the vector fields in the standard model are massless before symmetry breaking, however Equation 2.7 can arise in a gauge-invariant manner for a non-compact $U(1)$ gauge group through the Stückelberg mechanism [13].

For the purpose of constructing Lorentz-invariant operators it is also useful to note the (covariant) derivative ∂_μ (D_μ) is a Lorentz vector.

2.2   Path Integral Formulation of Quantum Field Theory

When working in Quantum Field Theory (QFT) it is often preferable to use path integral quantization over the canonical approach of promoting classical fields to continuous operator distributions acting on the Fock space. The central object in path integral quantisation is the generating functional:

$$Z(J) = \exp(iW(J)) = \int \mathcal{D}\phi\mathcal{D}\psi\mathcal{D}\bar{\psi}\mathcal{D}A \exp\left(i\mathcal{S} + iJ[\phi, \psi, \bar{\psi}, A]\right), \qquad (2.8)$$

where $\mathcal{S} = \int d^4x \mathcal{L}$ is the classical action, the path integral measure $\mathcal{D}\phi$ denotes integration over all configurations of ϕ, and $J[\phi, \psi, \bar{\psi}, A]$ can be used to generate a dynamic field at a point x by taking a functional derivative with respect to the appropriate classical source $J(x)$. When writing down a classical action of fermions in order to define the path integral we have to introduce Grassmann-valued fields to mimic the desired behaviour. The functional path integral is dominated by classical trajectories which minimise the action, but also receives quantum corrections from paths which are slightly deformed from these: in this sense the path integral formulation can be considered a quantum generalisation of the principle of least action. In this formulation the Lorentz and gauge symmetries are manifest, and it therefore often gives additional insight into QFTs. For example quantum anomalies show up when a classical symmetry deforms the path integral measure $\mathcal{D}\phi \to |\mathcal{J}|\mathcal{D}\phi$, and the Jacobian itself is a functional of the fields.

Starting with the generating functional the Feynman rules for propagators can be determined from the kinematic terms in the free action, and those for vertices are dictated by the interaction terms. We can calculate time-ordered n-point correlation functions by taking n functional derivatives with respect to the correct classical sources. This allows for a convenient way of performing the perturbative expansion
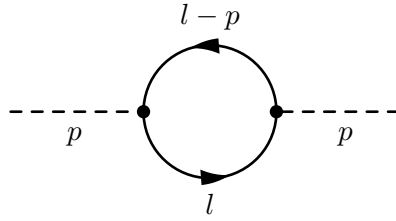
Figure 2.1: Simple one loop diagram.

in the interaction strength g to generate all Feynman diagrams up to a certain order, and in this way we can interpret $W(J)$ as the sum of all connected diagrams. As outlined by the Lehmann-Symanzik-Zimmermann reduction formula [14], the S-matrix which governs physical scattering amplitudes between asymptotic free on-shell states is given exactly by projecting out these states from the correlation functions.

2.3 Renormalisation and Scale Dependence

When performing calculations in QFT we will generically find ultraviolet (UV) divergences. These are encountered when integrating loop momenta and signal that we include effects from arbitrarily short length physics. For example the diagram in Figure 2.1 will, after performing the spinor algebra and dropping the mass terms in the denominator, give rise to the following divergent term (among others):

$$\int^{|l|_{\max}} \frac{d^4 l}{(2\pi)^4} \frac{1}{l^2(l-p)^2} \propto \log|l|_{\max} \,. \tag{2.9}$$

When we naively interpret a bare parameter in a lagrangian in terms of a measured physical value we make the claim that our theory is valid up to arbitrary scales and try to include contributions from all scales in the parameter value, which is made explicit when integrating over the loop momentum l and taking the limit $|l|_{\max} \to \infty$. Physically we could reason that quantum corrections have an ultimate cutoff scale given by the Planck scale $\Lambda_{\mathrm{Planck}}$. Following Wilson [15] we could therefore define our lagrangian at some scale $\Lambda < \Lambda_{\mathrm{Planck}}$ and not worry about $|l| > \Lambda$ which would give finite results. However we are interested in using measurements to make predictions at scales $p_0 \ll \Lambda$ and would prefer if the physics at the Planck scale didn't affect these too much, so we will take a different approach and instead redefine the terms in the lagrangian to reflect this hope:

$$A_0^\mu = \sqrt{Z_A(p_0)} A_R^\mu(p_0) = (1 + \delta_A(p_0)) A_R^\mu(p_0), \tag{2.10}$$

$$g_0 = Z_g(p_0) g_R(p_0) = (1 + \delta_g(p_0)) g_R(p_0), \ \ldots \tag{2.11}$$

We can then try to use the counterterm δs to subtract away terms associated with physics at much higher scales than the measurement scale, and equate the renormalised objects $A_R^\mu(p_0), g_R(p_0)$, and so on with the physical objects we are actually dealing with at this measurement scale. If all UV divergences in the theory can be removed by fixing the available counterterms the theory is called renormalisable, which signals that it does not have a cutoff scale. A non-renormalisable theory will in general have a cutoff scale above which it can not be used to calculate predictions reliably. We have already indicated that we expect the δs and renormalised parameters at p_0 to now depend on the scale p_0 since we will use the δs to subtract a term that will be $\propto \log \Lambda/p_0$, and the renormalised parameters must cancel this to remove any dependence from the bare parameters.

In order to perform the necessary regularisation we could for example introduce the new heavy mass scale Λ explicitly by hand to cancel contributions to loops for $|l| > \Lambda$. An example of this is Pauli-Villars regularization which introduces new unphysical particles at Λ which cancel the physical contributions to loop integrals from momentum modes with $|l| \gg \Lambda$ [16]. We can then renormalise the theory by using the counterterms to set the values of the renormalised parameters to those measured in experiment at some scale p_0, which allows us to regularise calculations in the theory at this scale even if the bare objects and counterterms diverge as we take $\Lambda \to \infty$. In practice we would have to define a specific renormalisation scheme which would tell us which of the finite terms from the loop calculation we keep in the renormalised parameter and which we subtract away with the divergence. The physics should of course not depend on this choice.

For most practical purposes Pauli-Villars regularisation is not very convenient since it breaks non-Abelian gauge invariance, and Dimensional Regularisation (DR) is used instead: loop integrals are calculated in $d = 4 - 2\varepsilon$ dimensions and the divergences show up as $\frac{1}{\varepsilon}$ poles when we take the physical limit $\varepsilon \to 0$. Taking the diagram in Figure 2.1 as an example, in the numerator we have:

$$\text{Tr}\left[(\slashed{l} - \slashed{p} + M)(\slashed{l} + M)\right] = 4(M^2 + l^2 - l.p).\tag{2.12}$$

We will focus on the M^2 term which can be pulled out of the integral and which we will ignore for now and drop the mass terms in the denominator, giving us the integral we mentioned above. We will also explicitly insert the coupling g which we keep dimensionless using an arbitrary parameter μ with mass dimension 1[*]:

---

[*]We will discuss the mass dimensions of fields later, but to be self-contained we here assume

$$
\begin{aligned}
\int \frac{d^d l}{(2\pi)^d} \frac{\mu^{4-d} g^2}{l^2 (l-p)^2} =& \frac{\mu^{4-d} g^2}{(2\pi)^d} \int_0^1 dx \int d^d l \frac{1}{((l-xp)^2 - x^2 p^2 + xp^2)^2} \\
=& i \frac{\mu^{2\varepsilon} g^2}{(4\pi)^2} (4\pi)^\varepsilon \Gamma(\varepsilon) \int_0^1 dx (x(x-1)p^2)^{-\varepsilon} \\
=& i \frac{g^2}{(4\pi)^2} (1 + \varepsilon \log(\mu^2))(1 + \varepsilon \log(4\pi))(\frac{1}{\varepsilon} - \gamma^E) \\
& \times (1 + 2\varepsilon - \varepsilon \log(-p^2)) \\
=& \frac{i g^2}{16\pi^2} \left[2 + \frac{1}{\varepsilon} + \log\left(\frac{-\mu^2}{p^2} \right) \right] .
\end{aligned}
\tag{2.13}
$$

Here we have only kept finite and divergent terms as $\varepsilon \to 0$ and already pulled factors of γ^E and $\log 4\pi$ into $\frac{1}{\varepsilon}$ on the last line. This can again be subtracted by a counterterm, and only subtracting the divergent part corresponds to the so-called $\overline{\text{MS}}$ renormalisation scheme.* In order to keep the the bare couplings dimensionless we again had to introduce a new mass scale μ, which plays the same role as the renormalisation scale p_0 in Pauli-Villars. This appearance of an unphysical mass scale is an unavoidable feature of any regularisation method. Using the Wilsonian language, it is equivalent to the scale at which we define our effective lagrangian: starting with the lagrangian at the actual cutoff we have integrated out momenta down to μ, and the generic logarithms with ratios of scales which appear as in Equation 2.13 have been resummed and incorporated into the definition of the parameters themselves as in Equations 2.10, 2.11. This result suggests we should try to use a lagrangian defined at $\mu^2 \approx p^2$ to avoid large logarithms when calculating predictions for a process with a typical scale p^2, and post hoc rationalises why the counterterm approach is the correct way to deal with UV divergences in a particle physics context where the actual cutoff of the theory could be very far away.

The invariance of the bare lagrangian to variations in the unphysical scale μ can be used to calculate how the renormalised parameters change with μ:

$$
\mu \frac{d}{d\mu} g_0 = 0 \to \mu \frac{d}{d\mu} (\mu^\varepsilon Z_g(\mu) g_R(\mu)) = 0 .
\tag{2.14}
$$

Extending the same logic of invariance under the unphysical renormalisation scale μ to bare n-point A^μ correlation functions G_0^n, where A_0^μ has been renormalised as in Equation 2.11, gives an example of a Callan-Symanzik equation [17]:

---

the particle in the loop is a fermion and the particle whose self-energy we are calculating is a scalar, which gives $[g] = d - \frac{d-2}{2} - 2\frac{d-1}{2} = \frac{4-d}{2}$.

*The MS stands for Minimal Subtraction, and the standard MS only differs in that it does not pull the γ^E and $\log 4\pi$ factors into $\frac{1}{\varepsilon}$.

$$\left(\mu\frac{\partial}{\partial\mu} + \frac{n}{2}\gamma_A + \beta(g_R)\frac{\partial}{\partial g_R}\right) G_R^n = 0 \,. \tag{2.15}$$

This allows us to define the so-called beta functions β and anomalous dimensions γ_A:

$$\beta(g_R) = \mu\frac{dg_R(\mu)}{d\mu}, \quad \gamma_A = \frac{\mu}{Z_A}\frac{dZ_A}{d\mu}\,. \tag{2.16}$$

The beta functions tell us exactly how dimensionless parameters change as we integrate down from the bare lagrangian, or in a particle physics context, how they change as we perform calculations at different scales. The anomalous dimensions tell us how the scaling behaviour of dimensionful objects differs from the classical scaling expected based on their mass dimension. The combination of all the beta functions for a theory is called the renormalisation group equations (RGEs) and therefore tells us how to convert a theory with parameters measured at one scale into the equivalent theory at some other scale. While the bare lagrangian must be invariant under the arbitrary scale μ and all orders calculations therefore can not have a dependence on μ, the fixed order perturbation theory calculations we typically use in practice do have a dependence on μ so in this sense the beta functions are approximations of physical corrections. The RGEs can therefore be used to gain qualitative insights into the behaviour of the theory at energy ranges outside of those experimentally probed, and as a shortcut to calculating the full quantum corrections to an observable when they are expected to be dominated by the resummed logarithms. A useful thing to notice is that the appearance of logarithms of the type $\log\left(\frac{p^2}{\mu^2}\right)$ which are resummed by the beta functions always is accompanied by the divergent $\frac{1}{\varepsilon}$ pieces: this allows us to calculate the beta functions efficiently by only focusing on the divergent parts of diagrams which contribute to them.

The condition that we can regularise all UV divergences in a theory with a finite number of counterterms is called renormalisability. A renormalisable theory can in theory be used to obtain predictions at any scale once we have performed the necessary measurements to find the values of all of the parameters at one scale, and renormalisability is therefore considered a desireable feature of a theory[*].

---

[*]Theories with massless particles will in general also have infrared divergences which ultimately cancel between loop and phase space integrals when dealing with inclusive observables, as shown by Kinoshita, Lee, and Naunberg [18, 19].

2.4   Introduction to the Standard Model

The Standard Model is the crowning achievement of hundreds of years of investigations into the fundamental nature of the physical world. It uses the language of Quantum Field Theory introduced in the previous section and successfully describes empirical results gathered from thousands of experiments covering many orders of magnitude in energy. In theory it could be argued that it is obtainable in a fairly elegant way by postulating a gauge group $\mathcal{G}_{SM} = SU(3)_C \otimes SU(2)_L \otimes U(1)_Y$ and writing down all of the invariant and renormalisable operators which can be formed making the modest assumptions that there is some fermion matter content and a complex scalar with a quartic potential. The lagrangian then takes the general form (assuming the only dimensionful parameter is the $\tilde{\mu}^2$ term in the scalar potential):

$$\mathcal{L}_{SM} = -\frac{1}{4}G^A_{\mu\nu}G^{A\mu\nu} - \frac{1}{4}W^I_{\mu\nu}W^{I\mu\nu} - \frac{1}{4}B_{\mu\nu}B^{\mu\nu} \qquad \text{(Gauge sector)} \qquad (2.17)$$

$$+ (D_\mu H)^\dagger(D^\mu H) - \tilde{\mu}^2 H^\dagger H - \lambda(H^\dagger H)^2 \qquad \text{(Higgs sector)} \qquad (2.18)$$

$$+ i\psi^\dagger_{L,a}\bar{\sigma}^\mu(D_\mu)^{ab}\psi_{L,b} + i\psi^\dagger_{R,c}\sigma^\mu(D_\mu)^{cd}\psi_{R,d} \quad \text{(Fermion sector)} \qquad (2.19)$$

$$- (\bar{\psi}_a Y^{ab}\psi_b H + \bar{\psi}_c Y^{cd}\psi_d H^\dagger + \text{h.c.}) \qquad \text{(Yukawa sector)} \qquad (2.20)$$

Eventually we add the assumptions that the complex scalar tranforms non-trivially under the $SU(2)_L \otimes U(1)_Y$ subgroup and breaks this down to $U(1)_{QED}$ thanks to a non-zero vacuum expectation value, achieved by assigning $\tilde{\mu}^2 < 0$.[*]

In practice this is a beautiful lie which looks good on t-shirts but ignores all of the undeniable *strangeness*[†] in the details that are required to fill in this outline. Taking a step back and looking at the space of possible QFTs[‡] we can draw a parallel to the Aarne-Thompson classification system for fairytales [20, 21]: let's assume the Standard Model belongs to an archetype refered to as the *Snow White* QFTs. This suggests we have a reasonable idea of the characteristics of the main character and her companions, who the antagonist is, and how the fairytale plays out. However while this is strictly speaking true, when reading the book of the Standard Model we are immediately introduced to five sets of triplet dwarves, two of which are left-handed and three of which are right-handed and all of which have customary evil twins. Within each dwarf triplet there is a size hierarchy that goes from miniscule

---

[*]Note that only a scalar can have a Lorentz-invariant non-zero vacuum expectation value.

[†]Used here strictly without its physics connotation although it of course is intimately connected.

[‡]Which is effectively infinite, but we could imagine requiring some reasonable measure of simplicity and elegance to end up with a practical list.

to huge (with one of the dwarfs in particular being a giant the size of a house). At the end of the story we are not filled with the satisfaction of having read a classic fairytale, rather we are left wondering what possibly could have compelled someone to come up with such a contrived scenario just to tell a simple story. Upon closer inspection we notice that there is structure and logic to the madness, but ultimately we are still left with more questions than answers. The Standard Model appears to be a fairytale à la Nostradamus, and the interesting details are often well-hidden in nooks and crannies that have to be meticulously explored. In this way, even though it appears far from a well-presented story at first, it has managed to remain the central object of attention in the particle physics community for decades.

This innate strangeness, present even before we consider any of the number of theoretical and experimental problems we know to be present in the Standard Model as presented here, is often internalised through daily exposure among practitioners in the field as we are wont to bleed the everyday of its peculiarities. It is however of scientific interest as 13 of the 19 free parameters of the model originate from this hierarchical 'three-generation' structure of the fermion sector*, see Table 2.2. We will later investigate techniques for discvering a model which explains the mass hierarchy of the fermion sector by introducing a warped extra dimension [22, 23] in Chapter 7.

Before having a look at each section of the lagrangian in more detail we can already determine the mass dimensions of all of the fields in the lagrangian: $\mathcal{S} = \int d^4x \mathcal{L}$ suggests $[\mathcal{L}] = -[d^4x]$ since we want the action to be dimensionless. We will in general operate with $[h] = [c] = 1$ which implies $[x] = [\partial_\mu^{-1}] = [E^{-1}] = [M^{-1}]$, which leads us to conclude the mass dimension of every term in the lagrangian must be 4, or $4 - 2\varepsilon$ when using dimensional regularisation.

From the Higgs kinetic term we can see that $[H] = 1$. The mass dimensions of the field strength tensors can also be determined to be 2, and we will later see that this expands into gauge fields A_μ with mass dimension 1. The mass dimension of the chiral fermions can be determined from their kinetic terms to be 3/2.

We can now see that all of the operators in the Standard Model carry four dimensions of mass in their field and derivative content alone, with a single exception: the $\tilde{\mu}^2 H^2$ term. This term therefore breaks the classical conformal invariance that

---

*Note that I don't include the masses and mixing angles of the neutrino sector which additionally complicate the simple picture presented here and would bring this number to at least 20 out of 26.

Parameter	Measured value
m_e	0.511 MeV*
m_μ	105 MeV*
m_τ	1.78 GeV*
m_u	$2.2^{+0.6}_{-0.4}$ MeV†
m_d	$4.7^{+0.5}_{-0.4}$ MeV†
m_s	96^{+8}_{-4} MeV†
m_c	1.28 ± 0.03 GeV††
m_b	$4.18^{+0.04}_{-0.03}$ GeV††
m_t	173.1 ± 0.6 GeV*
θ_{12}	$13.02° \pm 0.04°$ **
θ_{23}	$2.36° \pm 0.08°$ **
θ_{23}	$0.20° \pm 0.02°$ **
δ	$69° \pm 5°$ **
g_1	0.356 †††
g_2	0.649 †††
g_s	1.218 ± 0.006 †††
$\bar{\theta}$	≈ 0
m_H	125.09 ± 0.24 GeV*
v	246.2 GeV***

Table 2.2: Free parameters of the Standard Model and their current experimental measurements. Values are taken from the 2017 update of the PDG Review [24]. For details of the physical meaning of the parameters see Sections 2.4.1 to 2.4.4. Absence of error band indicates that experimental uncertainty is smaller than the presented precision.

*: Pole mass.

†: $m(\mu = 2 \text{ GeV})$ in $\overline{\text{MS}}$.

††: $m(\mu = m)$ in $\overline{\text{MS}}$.

**: Measurement scale not defined but CKM elements run very weakly [25] so the effect is negligible.

†††: $\mu = m_Z$ in $\overline{\text{MS}}$.

***: Defined as $v = 1/(\sqrt{2}G_F)$ with G_F measured at $\mu = m_\mu$.

is present in the rest of the theory by introducing a dimensionful coefficient $\tilde{\mu}$. We could equally imagine introducing operators which have a mass dimension > 4 in their field and derivative content, which therefore would have coefficients of negative mass dimension. In general, operators $\mathcal{O}$ and their coefficients C are classified according to the mass dimension of their field and derivative content as:

- Relevant: $[\mathcal{O}] = d < 4$, $[C] = 4 - d$

- Marginal: $[\mathcal{O}] = d = 4$, $[C] = 0$

- Irrelevant: $[\mathcal{O}] = d > 4$, $[C] = 4 - d$

The naming convention is connected to the scale dependence we had to introduce when renormalizing a theory discussed in Section 2.3. The name irrelevant originates from attempts to understand why physical solid state systems with widely different microscopic descriptions fall into a small number of simpler classes in the

infrared (IR) or low energy regime. The modern way to explain this is through the observation [15] that only relevant and marginal operators contribute to the macroscopic low-energy description of a system, and these can be systematically studied in the same way we've been able to write down all of the allowed operators under the Lorentz and gauge symmetries we impose. The microscopic differences enter through irrelevant operators which only contribute at higher scales (smaller lengths). In high-energy physics we are usually interested in the high-energy behaviour of our theory, so we might wonder why there are no higher mass dimension operators in the Standard Model. In general this is a consequence of requiring all of the operators to be renormalisable [26] which means it is, in theory, predictive up to an arbitrary energy scale[*]. A better way to motivate the absence of non-renormalizable operators is through the Wilsonian picture of renormalisation discussed in Section 2.3: assuming the cutoff scale of the more complete theory of which the Standard Model is a low-energy description is much higher than the weak scale, any irrelevant operators which do contribute to the theory at this higher scale will be completely negligible at the weak scale.

However there is no reason to believe the Standard Model is the final theory of nature up to a very high scale: as we will later discuss there are many unsolved problems both in small- and large-scale physics which strongly suggest it must be only an effective description of a more fundamental theory which is not necessarily widely separated in scale. We can then write down higher-dimensional irrelevant operators suppressed by powers of this scale, which make increasing contributions at smaller length scales. While such theories are non-renormalisable, and hence come up with a cutoff scale above which they can not be used to calculate predictions (given by $\sim \Lambda$), we can operate perfectly well within the range of validity and even calculate quantum corrections by limiting our expansion in Λ to a certain order. This is motivated by the fact that new effects will take the form $(|p|/\Lambda)^n$ where $|p|$ is the scale of the interaction we study. As long as $|p| \ll \Lambda$ we are able to quickly cut off the expansion in $|p|/\Lambda$ since higher order terms will be suppressed. Note that it is this suppression by $|p|/\Lambda$ which renders these operators irrelevant in the IR and increases their significance at higher scales. That the expansion starts breaking down just as the size of the effect loses its mass-scale suppression is a fundamental feature of these *Effective Field Theories* (EFT), and means they are best used to describe small deformations from the Standard Model expectation.[†] Calculating quantum

---

[*]The QED Landau pole notwithstanding.

[†]In other words, situations where Λ is well-separated from the weak scale but not large enough

corrections requires that we include all of the necessary operators in order to be able to cancel UV-divergences with new structures not present in the renormalisable theory which will generically appear. This is guaranteed to be the case if we use all of the Lorentz- and gauge-invariant operators that can be formed out of the fields of the theory up to the inverse power of Λ we calculate to. A set of effective operators up to a certain order in the expansion is called a *basis*; in general we can not construct a complete and unique basis of operators for a given order of Λ due to redundancies introduced by the classical equations of motion and integration-by-parts identities. A complete basis of dimension-6 ($\propto 1/\Lambda^2$) operators in the Standard Model is given in [27].

Having discussed and motivated the general form of the Standard Model lagrangian, we will have a more detailed look at the individual components:

2.4.1 Gauge sector

The gauge sector Equation 2.17 describes the dynamics associated with the local, internal symmetries of the Standard Model given by $\mathcal{G}_{SM}$. It is built exclusively out of field strength tensors, which for $SU(N)$ gauge theories* are given by:

$$F_{\mu\nu}^a = \partial_\mu A_\nu^a - \partial_\nu A_\mu^a + g f^{abc} A_\mu^b A_\nu^c \, . \tag{2.21}$$

Here A_μ^a is a gauge vector field in the direction of the generator t^a of the algebra $su(N)$. The generators satisfy:

$$\left[t^a, t^b \right] = i f^{abc} t^c \, . \tag{2.22}$$

To ensure the defining local invariance under gauge transformations, the derivative operator is elevated to a covariant derivative when operating on a field that transforms non-trivially under $\mathcal{G}_{SM}$:

$$(D_\mu)_{ij} = \partial_\mu - i g^{(\alpha)} A_\mu^{a,(\alpha)} t_{ij}^{a,(\alpha)} \, . \tag{2.23}$$

The expansion over (α) is done in accordance with the representations of $\mathcal{G}_{SM}$ the target field transforms in, for example for the left-handed quark doublet which is charged under all of the subgroups:

$$(D_\mu q_L)^{\alpha j} = (\partial_\mu - i g_s T_{\alpha\beta}^A G_\mu^A - i g_2 \tau_{jk}^I W_\mu^I - i g_1 Y_q B_\mu) q_L^{\beta k} \, . \tag{2.24}$$

---

for the effects to be completely unobservable.

*For $U(1)$ gauge theories the last piece disappears and we are left with a Maxwell tensor.

Here g_s, g_2, and g_1 are the gauge coupling constants of $SU(3)_C$, $SU(2)_L$, and $U(1)_Y$ respectively, which determine the strength of said gauge interactions. $T^A = \frac{1}{2}\lambda^A$ and $\tau^I = \frac{1}{2}\sigma^I$ are the generators of the fundamental representations of $su(3)$ and $su(2)$ respectively, and the greek and latin indices on q denote the colour and isospin degrees of freedom on which they act while the A and I denote the indices of the adjoint representations to which G and W belong. The generator of the $U(1)_Y$ algebra is just a single commuting real number Y. The covariant derivative of the field strength is given by:

$$(D_\rho F_{\mu\nu})^a = \partial_\rho F_{\mu\nu}^a - ig A_\mu^b (t_{adj}^b)^{ac} F_{\mu\nu}^c = \partial_\rho F_{\mu\nu}^a + g f^{abc} A_\mu^b F_{\mu\nu}^c, \qquad (2.25)$$

where we used $(t_{adj}^a)^{bc} = -if^{abc}$ and swapped indices on the structure constant. For an Abelian group the second term is of course absent, however for non-Abelian groups like $SU(2)_L$ and $SU(3)_C$ this term generates self-interactions among the gauge bosons themselves. As we will see later this simple result creates significant physical differences between Yang-Mills ($SU(N)$) and Abelian ($\sim$ Maxwell) gauge theories, and is responsible for the *confinement* of $SU(3)_C$ at low energies which swaps the degrees of freedom in the theory from coloured quarks to colour-neutral hadrons and mesons.

When quantizing a gauge theory we run into a problem: the determinant of the operator $k^2 g^{\mu\nu} - k^\mu k^\nu$ is 0, so we can't invert it in order to find the propagator using the standard Green's function approach [28]. This is not surprising since the freedom to perform gauge transformations means it is impossible to uniquely solve for A_μ, which equally makes it impossible to construct the free theory in order to use perturbation theory. In the path integral approach the situation is clarified: integrating over the lagrangian as defined in Equation 2.17 means we sum over *gauge-equivalent* field configurations, or gauge orbits, of the classical action, which gives divergent results. The obvious solution is to fix the gauge before quantizing the theory. This is elegantly done by using an auxiliary field ξ as a Lagrange multiplier to force the integration to only pick up a single unique gauge orbit, following Faddeev-Popov [29]:

$$\mathcal{L}_{g.f.} = -\frac{1}{2\xi}(\partial^\mu A_\mu^a)^2. \qquad (2.26)$$

When adding this term to the classical action we break the gauge invariance and end up cancelling the integration over equivalent gauge orbits when calculating Green's functions, leaving the physical result (ξ is guaranteed to cancel in the end). There is one additional subtlety to deal with: when using non-Abelian groups, the extra

factor we use to define the integration over equivalent gauge orbits is a functional of A_μ and not simply a number that automatically cancels. The customary way to deal with this is to rewrite this term using two Grassmann-valued fields c and $\bar{c}$ for each gauge field. The lagrangian for these is given by:

$$\mathcal{L}_{ghost} = \partial^\mu \bar{c}^a D_\mu^{ac} c^c = \partial^\mu \bar{c}^a (\delta^{ac} \partial_\mu + g f^{abc} A_\mu^b) c^c \,. \tag{2.27}$$

The new fields are called *ghosts* due to being anti-commuting complex scalars. The spin-statistics theorem means they can not be physical states, but they do appear in the path integral.[*] From a practical perspective the ghosts can be understood as a way to remove unphysical degrees of freedom from virtual gauge bosons: when we take gauge bosons off-shell we are naively not guaranteed that the number of degrees of freedom stays physical. In Abelian theories the Ward identity guarantees that longitudinal polarisations cancel in the final result, but due to the gauge boson self-interactions which are present in non-Abelian theories there is no simple similar identity for non-Abelian theories. Heuristically the fermionic -1 which will accompany ghost loops can then be considered to cancel the unphysical contribution from longitudinal gauge boson polarisations.

2.4.2   Higgs sector

The Higgs sector Equation 2.18 describes how the electroweak group $SU(2)_L \otimes U(1)_Y$ is broken down to $U(1)_{QED}$ [30,31] by a complex scalar H in the $(\mathbf{2}, \frac{1}{2})$ electroweak gauge representation. Until recently it was the only part of the Standard Model which had not been experimentally verified, but following the seminal discovery by ATLAS and CMS in 2012 [6,7] of a scalar consistent with the properties expected of a Standard Model Higgs boson we are currently quickly moving towards an era of precision Higgs physics.

The sign of the mass term of the H field in the Higgs potential Equation 2.18 is of fundamental importance. This is because it is exactly when the mass term has the opposite sign to the quartic interaction term ($\tilde{\mu}^2 < 0$) that the Higgs potential develops a non-zero vacuum expectation value, $\langle H_0 \rangle \neq 0$. Without loss of generality we can choose the resulting vacuum expectation value to be real and in the second component of the Higgs doublet:

---

[*]Another way to understand the absense of ghosts in Abelian gauge theories is through the formal definition of an Abelian group which is exactly that $f^{abc} = 0$, forcing the ghosts to completely decouple from the rest of the theory.

$$H = \exp\left(2i\frac{\pi^a \tau^a}{v}\right)\frac{1}{\sqrt{2}}\begin{pmatrix} 0 \\ v+h \end{pmatrix}, \qquad v = \sqrt{\frac{-\tilde{\mu}^2}{\lambda}}. \tag{2.28}$$

Here we have written H in terms of the Goldstone bosons π^a of the symmetry breaking in a sigma form. The Goldstone bosons are perturbations along directions on the vacuum manifold given by the broken generators, so $\tau^a = \frac{1}{2}\sigma^a$ here. This is a generic way to parameterize the Goldstones bosons which arise when the vacuum of a theory is only invariant under a subgroup $\mathcal{H}$ of the full lagrangian symmetry group $\mathcal{G}$ as in our situation. When working with spontaneously broken gauge theories the gauge-fixing term in Equation 2.26 needs to be modified to include the Goldstone bosons. A convenient choice is the R_ξ gauge [32] which modifies the gauge-fixing term thus:

$$\mathcal{L}_{g.f.} = -\frac{1}{2\xi}(\partial^\mu A_\mu^a - \xi m_A \pi^a)^2. \tag{2.29}$$

After performing the Faddeev-Popov procedure we pick up mass terms $\sqrt{\xi}m_A$ for the Goldstone bosons and the ghosts. Unitary gauge is then defined as taking $\xi \to \infty$, or equivalently $\pi^a = 0$. This is the gauge we will use to study the effects of breaking $SU(2)_L \otimes U(1)_Y$ with a non-zero v. When expanding out the covariant derivative we see that v generates mass terms for the W_μ^I and B_μ bosons:

$$|D_\mu H|^2 \supset g_2^2 \frac{v^2}{8}\left[(W_\mu^1)^2 + (W_\mu^2)^2 + \left(\frac{g_1}{g_2}B_\mu - W_\mu^3\right)^2\right]. \tag{2.30}$$

Diagonalising we find:

$$W_\mu^\pm = \frac{1}{2}(W_\mu^1 \mp W_\mu^2), \; m_W = \frac{v}{2}g_2 \tag{2.31}$$

$$Z_\mu = \frac{1}{\sqrt{g_1^2 + g_2^2}}(g_2 W_\mu^3 - g_1 B_\mu), \; m_Z = \frac{v}{2}\sqrt{g_1^2 + g_2^2} = \frac{m_W}{\cos\theta_W} \tag{2.32}$$

$$A_\mu = \gamma_\mu = \frac{1}{\sqrt{g_1^2 + g_2^2}}(g_2 W_\mu^3 + g_1 B_\mu), \; m_A = 0. \tag{2.33}$$

Here we have introduced the notation $\tan\theta_W = g_1/g_2$ for the angle we rotate B_μ and W_μ^3 by. It is typically referred to as the *weak* or *Weinberg* angle. The remaining massless A_μ boson is associated with the unbroken Abelian generator $Q = \tau^3 + 1/2\,Y = diag(1,0)$ and is identified as the photon γ_μ of $U(1)_{QED}$. After rotating all of the terms in the full lagrangian to these mass eigenstates we have found the

Production mode	Theory (8 TeV)	η, 8 TeV	Theory (13 TeV)	η, 13 TeV
ggF	$21.42^{+4.4\%}_{-6.9\%}$ pb	$1.03^{+0.16}_{-0.14}$	$48.58^{+4.6\%}_{-6.7\%}$ pb	$0.99^{+0.14}_{-0.13}$
VBF	$1601.3 \pm 2.2\%$ fb	$1.18^{+0.25}_{-0.23}$	$3782.0 \pm 2.1\%$ fb	$1.7^{+1.17}_{-0.90}$
$(W^+ \to l\nu)h$	$49.52 \pm 2.0\%$ fb	$0.89^{+0.40}_{-0.38}$	$94.26 \pm 1.8\%$ fb	$3.2^{+3.7}_{-3.2}$
$(W^- \to l\bar{\nu})h$	$28.62 \pm 2.1\%$ fb	$0.89^{+0.40}_{-0.38}$	$59.83 \pm 2.0\%$ fb	$3.2^{+3.7}_{-3.2}$
$(Z^0 \to ll)h$	$14.18 \pm 1.7\%$ fb	$0.79^{+0.38}_{-0.36}$	$29.82 \pm 1.6\%$ fb	NA
tth	$133.0 \pm 9.2\%$ fb	$2.3^{+0.7}_{-0.6}$	$507.1 \pm 9.2\%$ fb	NA

Table 2.3:   Theoretical predictions for cross sections of the most important Higgs production modes assuming $m_h = 125$ GeV, taken from the 4th Higgs Cross Section Working Group Report [33], and ATLAS and CMS measurements of the signal strength $\eta = \sigma_{\text{obs}}/\sigma_{\text{theory}}$ for the same production mode where available [34, 35]. The gluon fusion and vector boson fusion components are denoted ggF and VBF, respectively. The gluon fusion cross section prediction relies on the N^{3}LO calculation in [36]. The fermions are detailed in Table 2.5 below, and the masses are given in Table 2.2 above.

lagrangian after symmetry breaking. In non-unitary gauges the interactions of the Goldstone bosons π^a also have to be kept track of.

The $U(1)_{QED}$ interaction strength is set by $e = g_2 \sin \theta_W$. Due to the large masses of $W^\pm_\mu$ and Z_μ their effects are highly suppressed at the scales of everyday interactions. Looking at the remaining degrees of freedom of H we identify the would-be Goldstone bosons of the symmetry breaking* $\pi^a = \phi^0, \phi^\pm$ with the new longitudinal degrees of freedom of $W^\pm_\mu$ and Z_μ, however they do show up explicitly in calculations when not in unitary gauge. There is a remaining degree of freedom which describes fluctuations around v, and so is described by a real singlet scalar h.† Note that since it appears linearly with v, all of its couplings to other fields are scaled by their mass after symmetry breaking. This real scalar is often referred to as the *Higgs boson* and can be identified with the resonance found by ATLAS and CMS [6,7] with $m_h \approx 125$ GeV. The production cross sections of the most important production modes are given in Table 2.3 and the branching fractions of the most important decay modes are given in Table 2.4.

While h does not couple directly to the massless photon field γ it still has a

---

*Written here in terms of their $U(1)_{QED}$ charges.

†This field is responsible for the $\sqrt{2}$ in Equation 2.28 which corrects for the difference in canonical normalisation between a real and complex scalar.

Decay mode	Br, Theory	η, Experiment
$h \to b\bar{b}$	0.582	0.52 ± 0.40
$h \to \tau\bar{\tau}$	6.27×10^{-2}	$1.43^{+0.43}_{-0.37}$
$h \to W^+W^-$	2.14×10^{-1}	$1.16^{+0.24}_{-0.21}$ *
$h \to Z^0Z^0$	2.62×10^{-2}	$1.44^{+0.40}_{-0.33}$ **
$h \to \gamma\gamma$	2.27×10^{-3}	1.17 ± 0.27

*: Measured using only the $W^+W^- \to 2l2\nu$ channel with
a theoretical branching ratio of 2.34×10^{-2}.

**: Measured using only the $Z^0Z^0 \to 4l$ channel with
a theoretical branching ratio of 2.75×10^{-4}.

Table 2.4: Theoretical predictions for branching ratios of the most important Higgs decay modes assuming $m_h = 125$ GeV, taken from the 4th Higgs Cross Section Working Group Report [33], and ATLAS measurements of the signal strength $\eta = \sigma_{\text{obs}}/\sigma_{\text{theory}}$ for the same decay mode where available [37]. The fermions are detailed in Table 2.5 below, and the masses are given in Table 2.2 above.
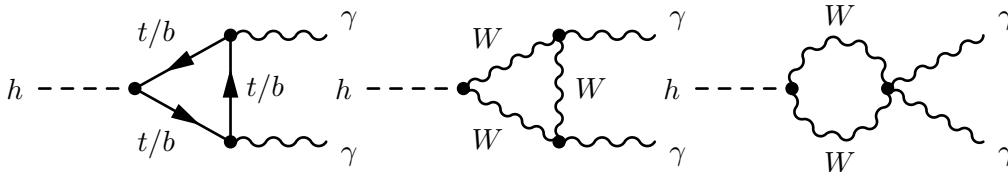
Figure 2.2: Example diagrams which contribute to $h \to \gamma\gamma$ at one loop. The fermionic and bosonic loop contributions enter with opposite sign and therefore interfere destructively.

non-zero branching rate to $\gamma\gamma$ due to quantum effects. The dominating contributions come from $W^\pm$ and top loops as shown in Figure 2.2. This was in fact the most important decay mode in the experimental discovery of the Higgs boson. The di-photon invariant mass distribution from the CMS discovery paper is shown in Figure 2.3.

2.4.2.1 Perturbative unitarity in longitudinal gauge boson scattering

In order to show the physical significance of the Higgs boson, we will consider scattering of longitudinally polarised weak gauge bosons. As explained above these polarisations correspond to three of the four degrees of freedom in H. Since they are the physical manifestation of electroweak symmetry breaking in the sense that
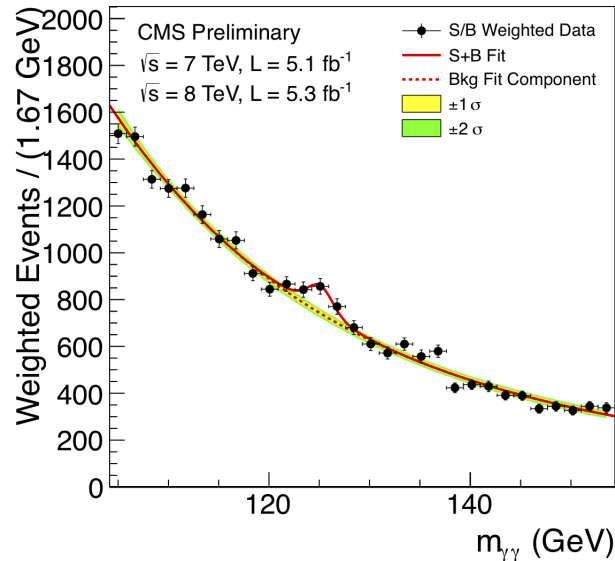
Figure 2.3: Di-photon mass distribution from the CMS Higgs discovery paper [7].

they allow the weak bosons to appear massive, they encode information about the broken symmetries. Gauge symmetries will in general ensure unitary behaviour of high energy vector boson scattering, so it is interesting to investigate what the high energy behaviour of these states is. In order to do so we will make use of partial wave analysis in order to determine whether these scattering processes are perturbatively unitary: such analysis is also later used in Chapter 6, so we will introduce the formalism here to remain self-contained, using Schwartz as our reference [28].

In general, the total cross section of scattering of two particles $AB \to AB$ at a center-of-mass energy $\sqrt{s}$ can be calculated as:

$$\sigma = \frac{1}{32\pi E_{CM}^2} \int d\cos\theta |\mathcal{M}(s,\theta)|^2 \,. \tag{2.34}$$

Here $\mathcal{M}(s,\theta)$ is the matrix element of the process. This can be decomposed into partial waves using Legendre polynomials P_j:

$$\mathcal{M}(s,\theta) = 16\pi \sum_{j=0}^{\infty} a_j(s)(2j+1)P_j(\cos\theta) \,. \tag{2.35}$$

We can also write the $a_j(s)$ in terms of $\mathcal{M}(s,\theta)^*$:

$$a_j(s) = \frac{1}{32\pi} \int d\cos\theta\, P_j(\cos\theta)\mathcal{M}(s,\theta)\,. \tag{2.37}$$

The decomposition allows us to perform the integral in order to get an expression for the total cross section as a function of the $a_j(s)$ coefficients:

$$\sigma = \frac{16\pi}{E_{CM}^2} \sum_{j=0}^{\infty} (2j+1)|a_j(s)|^2\,. \tag{2.38}$$

The optical theorem relates the imaginary part of the forward scattering amplitude to the total cross section:

$$\operatorname{Im}\mathcal{M}(AB \to AB, \theta = 0) = 2E_{CM}|\vec{p}| \sum_X \sigma(AB \to X)$$

$$\geq 2E_{CM}|\vec{p}|\sigma(AB \to AB)\,. \tag{2.39}$$

Hence[†]:

$$\sum_{j=0}^{\infty} (2j+1)\operatorname{Im} a_j(s) \geq \frac{2|\vec{p}|}{E_{\mathrm{CM}}} \sum_{j=0}^{\infty} (2j+1)|a_j(s)|^2\,. \tag{2.40}$$

This places strict bounds on the unitarily allowed values of a_j. In practice the contributions from $j > 1$ are often small, and the sum over j can be dropped by considering scattering of angular momentum eigenstates. Consider additionally elastic scattering where this is an equality and the high energy limit where $E_{CM} = 2|\vec{p}|$[‡]. We then simply have:

$$\operatorname{Im} a_j(s) = |a_j(s)|^2\,. \tag{2.41}$$

The solution to this is shown in Figure 2.4. We will calculate the $a_j(s)$ using perturbation theory, so $a_j(s) = a_j^0(s)g^2 + a_j^1(s)g^4 + \ldots$. Modulo small $\mathcal{CP}$ violating

---

[*]This uses the orthogonality of the Legendre polynomials:

$$\int P_i(x)P_j(x)dx = \frac{2}{2i+1}\delta_{ij}\,. \tag{2.36}$$

[†]Note that $P_j(1) = 1$.

[‡]A similar bound follows more generally by taking inelastic scattering into account, but assuming elastic scattering yields conservative bounds since taking inelastic scattering into account the unitary circle will become an ellipse which tends to larger imaginary values.

effects, the tree level contribution (assuming the leading contribution is tree level) $a_j^0(s)$ is real, and will hence in general not sit on the unitary circle: this is shown in Figure 2.4 as the red dot. This is not a problem since we can expect that going to all orders will restore unitarity by bringing the solution back to the circle, as shown by the green dot. Requiring our theory to be perturbative means we should not allow these higher order contributions to be of the same magnitude as the leading term, however. This means we need to define a convention for when we consider perturbative unitarity to be violated by the value of $a_j^0(s)$: we will take this to be $|\mathrm{Re}\, a_j^0(s)| > 1$ here and in Chapter 6. An alternative choice is $|\mathrm{Re}\, a_j^0(s)| > 1/2$ which is motivated by the fact this already would require a 41% correction in *exactly* the correct direction on the Argand diagram, and while higher order corrections of the size 100% are not uncommon in QCD, there is no reason expect these to go in exactly this direction.

Having thus introduced the machinery for performing partial wave analysis in order to determine whether or not a scattering process violates perturbative unitary, we return to the scattering of longitudinally polarised weak bosons. We will consider the process $W_L^+(p_1)Z_L(p_2) \rightarrow W_L^+(p_3)Z_L(p_4)$. In order to calculate we will need the Feynman rules for WWZ, $WWZZ$, and VVh vertices given below in Equations 2.69, 2.70, and 2.71. The contributing diagrams at tree level are given in Figure 2.5. To simplify the expressions we will use $g_1 = 0$ (so $m_Z = m_W$). The longitudinal polarisation vectors we use are given by[*]:

$$
\begin{aligned}
N \times \varepsilon_\mu^1 &= \frac{p_{1,\mu}}{m_W} + \frac{2m_W p_{3,\mu}}{t - 2m_W^2}, \quad N \times \varepsilon_\mu^2 = \frac{p_{2,\mu}}{m_W} + \frac{2m_W p_{4,\mu}}{t - 2m_W^2}, \\
N \times \varepsilon_\mu^3 &= \frac{p_{3,\mu}}{m_W} + \frac{2m_W p_{1,\mu}}{t - 2m_W^2}, \quad N \times \varepsilon_\mu^4 = \frac{p_{4,\mu}}{m_W} + \frac{2m_W p_{2,\mu}}{t - 2m_W^2}.
\end{aligned}
\tag{2.42}
$$

We take all momenta to be incoming. The amplitudes are then given by:

---

[*]The normalisation is $N = \left(\sqrt{3 + \frac{4m_W^4}{(t - 2m_W^2)^2}} \right)^{-1}$.
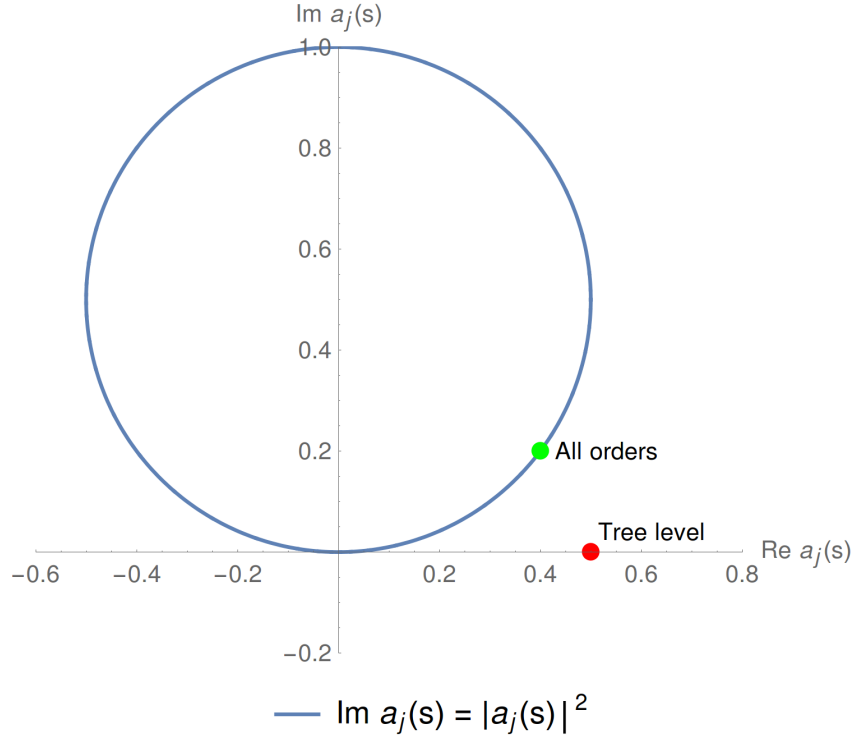
Figure 2.4: The Argand diagram for the solution of Equation 2.41. The red dot shows a tree level value of $a_j^0(s)$ which will in general be unitarity-violating. The green dot shows an all-order value of $a_j(s)$ which must be unitary. Corrections from inelastic scattering will elongate the unitary circle into an ellipse with Im $a_j(s) > |a_j(s)|^2$ and arguments based on the assumption of elastic scattering are therefore conservative.

$$
\begin{aligned}
i\mathcal{M}_s =&(ig_2)^2\ \varepsilon_\mu^1\varepsilon_\nu^2\varepsilon_\alpha^{*3}\varepsilon_\beta^{*4}\ \frac{-i}{s-m_W^2}\left(g_{\lambda\kappa}-\frac{k^\lambda k^\kappa}{m_W^2}\right)\\
&\times\left(g^{\mu\nu}(p_1-p_2)^\lambda+g^{\nu\lambda}(p_2+k)^\mu-g^{\lambda\mu}(k+p_1)^\nu\right)\\
&\times\left(g^{\alpha\beta}(p_4-p_3)^\kappa-g^{\beta\kappa}(p_4-k)^\alpha-g^{\kappa\alpha}(k-p_3)^\beta\right),\quad k=p_1+p_2
\end{aligned}\tag{2.43}
$$

$$
\begin{aligned}
i\mathcal{M}_u =&(ig_2)^2\ \varepsilon_\mu^1\varepsilon_\nu^2\varepsilon_\alpha^{*3}\varepsilon_\beta^{*4}\ \frac{-i}{u-m_W^2}\left(g_{\lambda\kappa}-\frac{k^\lambda k^\kappa}{m_W^2}\right)\\
&\times\left(g^{\mu\beta}(p_1-p_4)^\kappa+g^{\beta\kappa}(p_4-k)^\mu+g^{\kappa\mu}(k-p_1)^\beta\right)\\
&\times\left(g^{\alpha\nu}(p_3-p_2)^\lambda+g^{\nu\lambda}(p_2+k)^\alpha+g^{\lambda\alpha}(-k-p_3)^\nu\right),\quad k=p_2+p_3
\end{aligned}\tag{2.44}
$$

$$
i\mathcal{M}_4 =ig_2^2\ \varepsilon_\mu^1\varepsilon_\nu^2\varepsilon_\alpha^{*3}\varepsilon_\beta^{*4}\ \left(g^{\mu\nu}g^{\alpha\beta}+g^{\mu\beta}g^{\nu\alpha}-2g^{\mu\alpha}g^{\nu\beta}\right)\tag{2.45}
$$

$$
i\mathcal{M}_h =(ig_2)^2\ \varepsilon_\mu^1\varepsilon_\nu^2\varepsilon_\alpha^{*3}\varepsilon_\beta^{*4}\ g^{\mu\alpha}g^{\nu\beta}\ \frac{m_W^2}{t-m_h^2}\tag{2.46}
$$
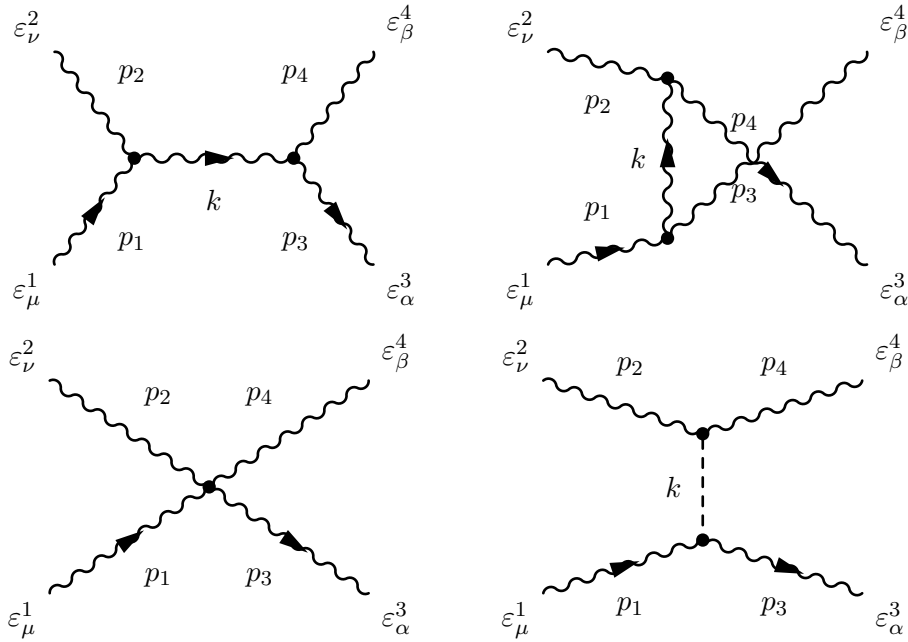
Figure 2.5: Tree-level contributions to $W_L^+(p_1)Z_L(p_2) \to W_L^+(p_3)Z_L(p_4)$ scattering. We denote these, from the top to bottom and left to right, $\mathcal{M}_s$, $\mathcal{M}_u$, $\mathcal{M}_4$, and $\mathcal{M}_h$.

After calculating the diagrams we find that using only the first three diagrams leaves a piece which grows with energy:

$$\mathcal{M}_s + \mathcal{M}_u + \mathcal{M}_4 \supset \frac{t}{v^2} \, . \tag{2.47}$$

Such a contribution, left as it is, will ensure that our theory can not be perturbatively unitary above some energy scale at which this term forces $|a_j| > 1$. The Higgs diagram adds a piece which has the following behaviour:

$$\mathcal{M}_h \supset \frac{-t^2}{v^2(t - m_h^2)} \, . \tag{2.48}$$

This piece will exactly cancel off the problematic term for $t \gg m_h$. When combined with requiring our model to be perturbatively unitarity, this allows us to calculate a maximum value for m_h which allows the cancellation to occur before the amplitude violates the $|a_j| > 1$ bound. The behaviour for three different cases in our toy model are presented in Figure 2.6: in the absence of a Higgs (or if it is very heavy) the amplitude violates perturbative unitarity at $\sqrt{s} \approx 2.5$ TeV. A light Higgs, such as the one found at the LHC, completely unitarises the behaviour. A
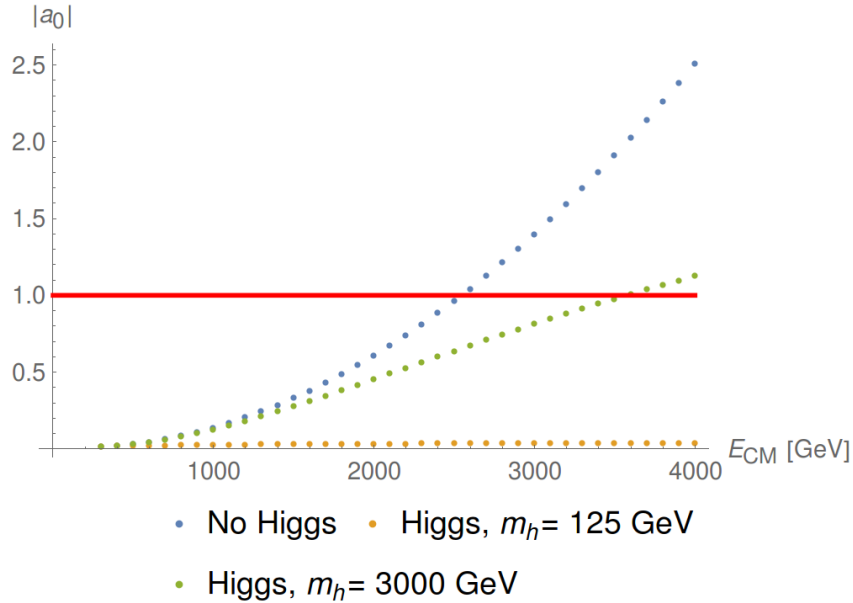
Figure 2.6: Values of $|a_0|$ as a function of center-of-mass energy for $W_L Z_L \to W_L Z_L$ scattering in our toy model with $g_1 = 0$. The red line shows where perturbative unitarity is considered violated. While a light Higgs at $m_h = 125$ GeV completely unitarises the amplitude, a heavy Higgs with $m_h = 3000$ GeV still causes the unitarity bound to be violated at $\sqrt{s} = 3.5$ TeV.

heavy Higgs which could still be kinematically accessible at the LHC with $m_h = 3$ TeV does not cancel the unitarity-violating behaviour fast enough, and perturbative unitarity is still violated at $\sqrt{s} \approx 3.5$ TeV.

We could in fact calculate the first three diagrams in an easier way by using a Callan-Coleman-Wess-Zumino (CCWZ) expansion [38] since they only involve interactions among the Goldstone bosons, which can be studied using only the pattern of symmetry breaking. Let us return to the Goldstone matrix in Equation 2.28:

$$U(x) = \exp\left(2i\frac{\pi^a \tau^a}{v}\right) = \exp\left[\frac{i}{v}\begin{pmatrix} w^0 & \sqrt{2}w^- \\ \sqrt{2}w^+ & -w^0 \end{pmatrix}\right],$$

$$w^0 = \pi^3, \ w^\pm = \frac{1}{\sqrt{2}}(\pi^1 \pm i\pi^2). \quad (2.49)$$

This field was introduced to describe the Goldstone dynamics when $\mathcal{G} = SU(2)_L \otimes U(1)_Y$ is broken to its subgroup $\mathcal{H} = U(1)_{QED}$ by the vacuum, as small perturbations along the broken generator directions which span the vacuum mani-

fold. The CCWZ expansion gives the nonlinear sigma model obtained when decoupling h by generating all of the terms allowed by $\mathcal{G}$ involving U. To leading order this is given by:

$$\frac{v^2}{4}\text{Tr}\left[(\partial_\mu U)(\partial^\mu U)^\dagger\right] \supset \frac{1}{2}\partial_\mu w^0\partial^\mu w^0 + \partial_\mu w^-\partial^\mu w^+$$
$$- \frac{1}{3v^2}\left[w^0(\partial_\mu w^-) - w^-(\partial_\mu w^0)\right]\left[w^0(\partial^\mu w^+) - w^+(\partial^\mu w^0)\right] . \quad (2.50)$$

Here I have only included the terms which are relevant for $W_L Z_L \to W_L Z_L$ scattering. Since the Goldstone bosons are massless this corresponds to the $\xi = 0$ gauge. In this gauge the $w^\pm, w^0$ fields are the longitudinal modes of $W^\pm$ and Z and we can re-calculate $\mathcal{M}_s + \mathcal{M}_u + \mathcal{M}_4$ in a single diagram:
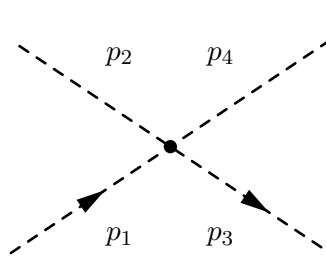
$$iM_{\xi=0} = \frac{-i}{3v^2}\Bigg[-p_1.p_3 + p_1.p_4 + p_2.p_3 - p_2.p_4$$
$$+(p_2 \leftrightarrow p_4)\Bigg]$$
$$= \frac{-i}{3v^2}\left(-\frac{t}{2} + \frac{u}{2} + \frac{u}{2} - \frac{t}{2} - \frac{t}{2} + \frac{s}{2} + \frac{s}{2} - \frac{t}{2}\right)$$
$$\Rightarrow \mathcal{M}_{\xi=0} = \frac{t}{v^2}$$

$$(2.51)$$

This result follows from the Goldstone Equivalence Theorem [39] which states that the high energy behaviour $(s \gg M_W, M_Z)$ of longitudinal gauge boson scattering is the same as for Goldstone boson scattering. That we get a result which violates perturbative unitarity at high energies when using only the CCWZ expansion is not surprising: it is an effective theory which does not know about the mechanism of symmetry breaking and is not renormalisable. To mend these issues we need to use a linear sigma model instead, where it is explicit that the symmetry is spontaneously broken since we keep the field which describes radial excitations along the vacuum direction in the theory. This field is exactly h in our setup.

The physical significance of the Higgs boson is therefore that it unitarises interactions between the massive $SU(2)_L \otimes U(1)_Y$ gauge bosons at high energies where the longitudinal components (Goldstone modes) dominate. A detailed analysis following the perturbative unitarity argument presented above in the full Standard Model with all scatterings considered allows a theoretical upper bound to be set on

m_h [40]:

$$m_h \leq \sqrt{\frac{16\pi}{3}\frac{1}{v}} \approx 1 \text{ TeV}. \tag{2.52}$$

This was a major motivation for the construction of the Large Hadron Collider as it provided a no-lose theorem: either the Higgs would be discovered, or some other new physics would have to occur at the TeV-scale to unitarise longitudinal gauge boson scattering. In Chapter 6 we will make use of perturbative unitarity arguments to constrain the allowed size of $\mathcal{CP}$ violating effects in the Higgs sector.

2.4.2.2 Measuring the Higgs potential

While we have assumed a specific form for the Higgs potential here, the experimental discovery of the Higgs boson itself can not tell us if this is in fact the actual Higgs potential realised in nature. Looking at the potential in Equation 2.18 in more detail:

$$V(H^\dagger H) = \tilde{\mu}^2 H^\dagger H + \lambda (H^\dagger H)^2 \supset \frac{1}{2}m_h^2 h^2 + \sqrt{\frac{\lambda}{2}}m_h h^3 + \frac{\lambda}{4}h^4. \tag{2.53}$$

Now $m_h^2 = -2\tilde{\mu}^2$ can be interpreted as the coefficient of the first term in an expansion in powers of h. We can infer the value of the trilinear coupling $\lambda_{\text{SM}}^3 = \sqrt{\frac{\lambda}{2}}m_h$ in the Standard Model using the assumed relation given in Equation 2.28 but from a model-independent perspective we can not determine its value with our current experimental measurements. The measurement of $h \to hh$ is however very challenging as it suffers from very low signal rates, partly due to destructive interference between box and triangle diagrams in the leading gluon fusion production channel, see Figure 2.8. A measurement of the trilinear coefficient is hence one of the ultimate challenges and goals of the LHC physics program [41]. In Chapter 6 we will investigate the phenomenology of the di-Higgs + two jets ($hhjj$) production channel, and assess the potential contributions it can make to the wider study of the Higgs sector.

2.4.3 Fermion sector

The Fermion sector in Equation 2.19 describes the kinematic terms of the fermion fields which make up the matter content of the Standard Model. Since all of the fields are chiral and charged under at least one gauge group there can be no mass terms; these are introduced through couplings to H which are described later in
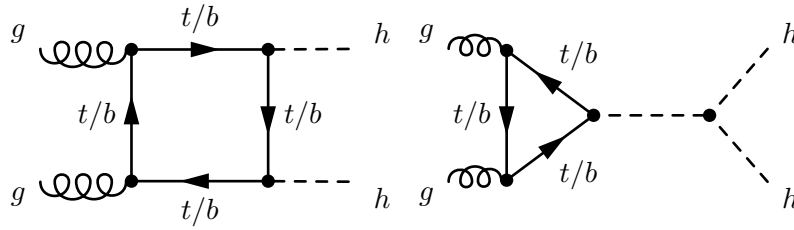
Figure 2.7: Example diagrams which contribute to $gg \to hh$ at one loop. The triangle and box contributions interfere destructively, as demonstrated in Figure 2.8 below.
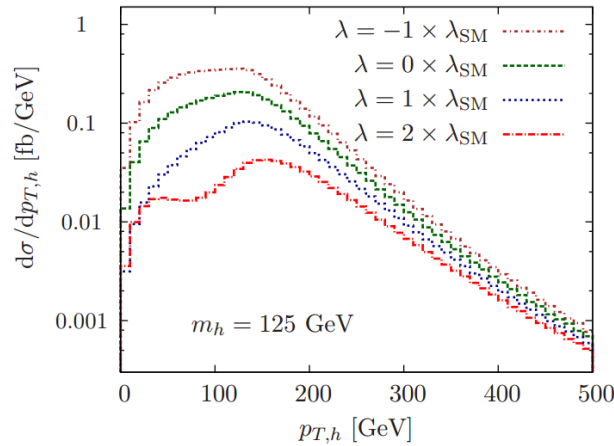
Figure 2.8: Interference between box and triangle diagrams in the leading Higgs p_T distribution in $gg \to hh$ di-Higgs production. Λ_{SM} here refers to the Standard Model coefficient of the trilinear term in the Higgs potential, so $\Lambda_{\mathrm{SM}} = \sqrt{\frac{\lambda}{2}} m_h$ in our notation. Taken from [41].

Section. 2.4.4. At this point we can summarise all of the fields of the Standard Model and their gauge and Lorentz representations, given in Table 2.5. Since the left- and right-handed fermions carry different charges the Standard Model is a chiral theory which violates parity.

2.4.4 Yukawa sector

Using the fields we have written down so far we can construct some additional renormalisable operators. While we introduced the field H in order to break electroweak symmetry, we can also form Lorentz- and gauge-invariant operators which couple this field to various combinations of the fermions. Expanding out after electroweak

$\mathcal{L}$-state	$\mathcal{G}_{SM}$	m-state	$U(1)_{QED}$	$SL(2,\mathbb{C})$	$[\boldsymbol{D}]$	B	L
G_μ^A	$(\boldsymbol{8},\boldsymbol{1},0)$	G_μ^A/g	0				
W_μ^I	$(\boldsymbol{1},\boldsymbol{3},0)$	$W_\mu^\pm$	± 1	$(\boldsymbol{1/2},\boldsymbol{1/2})$	1	0	0
B_μ	$(\boldsymbol{1},\boldsymbol{1},0)$	$Z_\mu^0, A_\mu/\gamma_\mu$	0				
H^j	$(\boldsymbol{1},\boldsymbol{2},\frac{1}{2})$	$\phi^\pm$	± 1	$(\boldsymbol{0},\boldsymbol{0})$	1	0	0
		h,ϕ^0	0				
q_{Lg}^j	$(\boldsymbol{3},\boldsymbol{2},\frac{1}{6})$	$(u_g,d_g)_L$	$(\frac{2}{3},-\frac{1}{3})$	$(\boldsymbol{1/2},\boldsymbol{0})$		$\frac{1}{3}$	0
l_{Lg}^j	$(\boldsymbol{1},\boldsymbol{2},-\frac{1}{2})$	$(\nu_g,e_g)_L$	$(0,-1)$		$\frac{3}{2}$	0	1
u_{Rg}	$(\boldsymbol{3},\boldsymbol{1},\frac{2}{3})$	u_{Rg}	$\frac{2}{3}$			$\frac{1}{3}$	0
d_{Rg}	$(\boldsymbol{3},\boldsymbol{1},-\frac{1}{3})$	d_{Rg}	$-\frac{1}{3}$	$(\boldsymbol{0},\boldsymbol{1/2})$			
e_{Rg}	$(\boldsymbol{1},\boldsymbol{1},-1)$	e_{Rg}	-1			0	1

Table 2.5: The fields of the Standard Model in the interaction eigenstates and the representations of the gauge group $\mathcal{G}_{SM} \equiv SU(3)_C \otimes SU(2)_L \otimes U(1)_Y$ they transform under. The mass eigenstates and $U(1)_{QED}$ charge after electroweak symmetry breaking are also presented. j denotes a $SU(2)_L$ index and g the generation index. $SL(2,\mathbb{C})$, $[\boldsymbol{D}]$, B, L denote spin group representation, mass dimension, baryon, and lepton numbers respectively.

symmetry breaking we get the following mass terms:

$$\mathcal{L}_{mass} = -\bar{q}_{L,p}Y_{pr}^d H d_{R,r} - \bar{q}_{L,p}Y_{pr}^u i\sigma_2 H^* u_{R,r} - \bar{e}_{L,p}Y_{pr}^e H e_{R,r} + \text{h.c.}$$
$$\rightarrow -\frac{v}{\sqrt{2}}\bar{d}_{L,p}Y_{pr}^d d_{R,r} - \frac{v}{\sqrt{2}}\bar{u}_{L,p}Y_{pr}^u u_{R,r} - \frac{v}{\sqrt{2}}\bar{e}_{L,p}Y_{pr}^e e_{R,r} + \text{h.c.}. \quad (2.54)$$

Here $Y_{pr}^{u/d/e}$ are complex 3×3 matrices with p,r denoting generation. Using singular value decomposition we can rewrite these as $Y^x = L^x M^x (R^x)^\dagger$ with L^x, R^x unitary 3×3 matrices and M^x a real non-negative diagonal 3×3 matrix. We can then rotate the basis of the left- and right-handed quarks as $u_L \rightarrow L^d d_L$, $u_L \rightarrow L^u u_L$, $e_L \rightarrow L^e e_L$, $u_R \rightarrow R^u u_R$, $d_R \rightarrow R^d d_R$, $e_R \rightarrow R^e e_R$ to end up in the diagonal mass basis:

$$\mathcal{L}_{mass} = -m_j^d \bar{d}_L^j d_R^j - m_j^u \bar{u}_L^j u_R^j - m_j^e \bar{e}_L^j e_R^j. \quad (2.55)$$

Here m_j^x are the diagonal elements of $\frac{v}{\sqrt{2}}M^x$. Since there is no right-handed neutrino field in the minimal Standard Model we consider here, we are free to cancel the effect of the e_L, e_R rotation using ν_L so there is no physical effect from diago-

nalising the lepton masses. However in the quark sector we can't do this since we've already defined rotations for all the fields in order to diagonalise both matrices, so interactions which mix up- and down-type quarks end up being sensitive to a residual unitary mixing matrix $V = (L^u)^\dagger L^d$, known as the *Cabbibo-Kobayashi-Maskawa* matrix [42, 43]. In the mass basis:

$$\mathcal{L}_{mass} \supset \frac{g_2}{\sqrt{2}} \left(W^+_\mu \bar{u}^i_L \gamma^\mu V_{ij} d^j_L + W^-_\mu \bar{d}^i_L \gamma^\mu V^\dagger_{ij} u^j_L \right), \quad V = \begin{pmatrix} V_{ud} & V_{us} & V_{ub} \\ V_{cd} & V_{cs} & V_{ct} \\ V_{td} & V_{ts} & V_{tb} \end{pmatrix}. \tag{2.56}$$

This is a unitary complex matrix so it has 9 degrees of freedom: 3 of these are rotation angles[*] and hence 6 are complex phases. 5 of these phases can be removed by using the remaining $U(1)^6$ symmetry of the lagrangian[†]:

$$d^j_{L/R} \to e^{i\alpha_j} d^j_{L/R}, \quad u^j_{L/R} \to e^{i\beta_j} u^j_{L/R}. \tag{2.57}$$

The most general parameterisation of V is then given by three real rotations in generation space $\theta_{12}, \theta_{13}, \theta_{23}$ and a complex phase δ, which introduces tree-level $\mathcal{CP}$ violation:

$$V = \begin{pmatrix} 1 & 0 & 0 \\ 0 & \cos\theta_{23} & \sin\theta_{23} \\ 0 & -\sin\theta_{23} & \cos\theta_{23} \end{pmatrix} \begin{pmatrix} \cos\theta_{13} & 0 & \sin\theta_{13}e^{i\delta} \\ 0 & 1 & 0 \\ -\sin\theta_{13}e^{i\delta} & 0 & \cos\theta_{13} \end{pmatrix} \begin{pmatrix} \cos\theta_{12} & \sin\theta_{12} & 0 \\ -\sin\theta_{12} & \cos\theta_{12} & 0 \\ 0 & 0 & 1 \end{pmatrix}. \tag{2.58}$$

2.4.5   Feynman Rules

Having discussed the field content of the Standard Model it is straightforward to extract the momentum-space propagators by inverting the kinetic terms. Using Feynman gauge ($\xi = 1$) for QCD and unitary gauge ($\xi \to \infty$) for the electroweak sector, respectively, with momentum flow from left to right:

---

[*]As can be seen from considering all components real.

[†]One phase remains since V is invariant under an overall $U(1)$ rotation given by $\alpha_j = \beta_j = \theta$.

$$g_\mu^a(k) \;\; \text{\small \texttt{QQQQQQQ}} \;\; g_\nu^b(k) \quad = \frac{-ig_{\mu\nu}\delta^{ab}}{k^2} \,, \tag{2.59}$$

$$u_g^a(k) \;\; \text{\small \texttt{ooooo▶oooo}} \;\; u_g^b(k) \quad = \frac{i\delta^{ab}}{k^2} \,, \tag{2.60}$$

$$V_\mu(k) \;\; \text{\small \texttt{\char126\char126\char126}} \;\; V_\nu(k) \quad = \frac{-i}{k^2 - m_V^2 + im_V\Gamma_V} \left(g_{\mu\nu} - \frac{k_\mu k_\nu}{m_V^2 - im_V\Gamma_V}\right) \,, \tag{2.61}$$

$$f_i(k) \;\; \text{\small \texttt{——▶——}} \;\; f_j(k) \quad = \frac{i\delta^{ij}k_\mu\gamma^\mu}{k^2} = \frac{i\delta^{ij}\slashed{k}}{k^2} \,, \tag{2.62}$$

$$h(k) \;\; \text{\small \texttt{---▶---}} \;\; h(k) \quad = \frac{i}{k^2 - m_h^2} \,. \tag{2.63}$$

The finite lifetime of the massive electroweak bosons has been taken into account through a Breit-Wigner propagator in Equation 2.61, and the indices on the δ in the fermion propagator should be read as running over all quantum numbers. The vertex rules can be derived from the interaction terms in the lagrangian and are for the QCD sector given by:
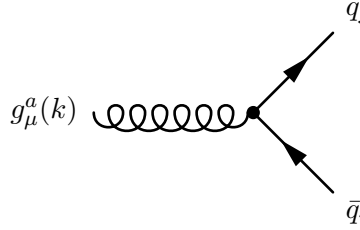
$$g_\mu^a(k) \quad\text{—}\quad \overset{q_j}{\diagup} \atop \underset{\bar{q}_i}{\diagdown} \qquad = ig_s t_{ij}^a \gamma_\mu \,, \tag{2.64}$$
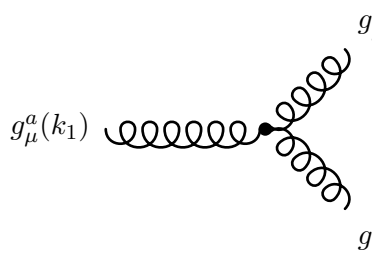
$$
\begin{aligned}
g_\mu^a(k_1) \quad &\overset{g_\rho^c(k_3)}{\text{—}} \underset{g_\nu^b(k_2)}{} \\
&= g_s f^{abc}\bigg[g_{\mu\nu}(k_1 - k_2)_\rho + g_{\nu\rho}(k_2 - k_3)_\mu \\
&\qquad\qquad\qquad + g_{\rho\mu}(k_3 - k_1)_\nu \bigg] \,,
\end{aligned}
\tag{2.65}
$$
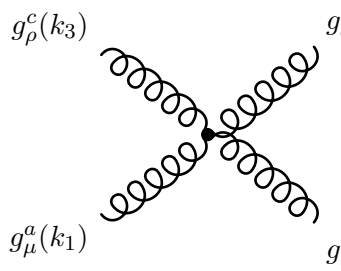
$$
\begin{aligned}
&= -ig_s^2\bigg[f^{abe}f^{cde}(g_{\mu\rho}g_{\nu\sigma} - g_{\mu\rho}g_{\nu\sigma}) \\
&\qquad + (b \leftrightarrow c)(\nu \leftrightarrow \rho) - (b \leftrightarrow d)(\rho \leftrightarrow \sigma)\bigg] \,,
\end{aligned}
\tag{2.66}
$$
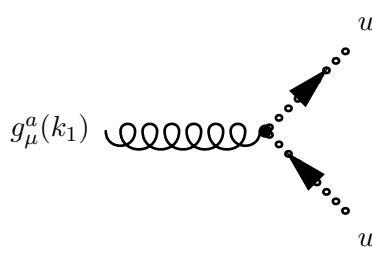
$$g_\mu^a(k_1) \quad\text{—}\quad \overset{u_g^c(k_3)}{} \underset{u_g^b(k_2)}{} \qquad = -g_s f^{abc} k_3^\mu \,. \tag{2.67}$$

In Equations 2.65 - 2.67 all momenta are taken as incoming. The electroweak sector has a much richer structure even in unitary gauge so only a subset of vertices are presented:
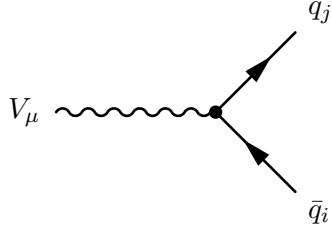
$$= ie\gamma_\mu(C_L\mathbb{P}_L + C_R\mathbb{P}_R)\,, \qquad (2.68)$$
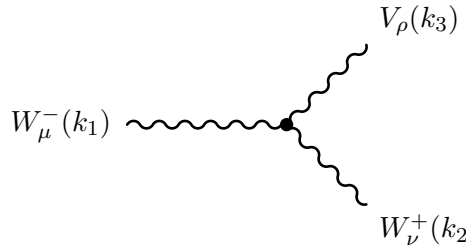
$$= ieC_{\gamma/Z}\left[g_{\mu\nu}(k_1 - k_2)_\rho + g_{\nu\rho}(k_2 - k_3)_\mu \right.$$
$$\left. + g_{\rho\mu}(k_3 - k_1)_\nu\right]\,, \qquad (2.69)$$
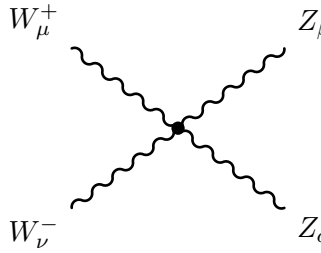
$$= ie^2\cot^2\theta_W\left[g_{\alpha\mu}g_{\beta\nu} + g_{\alpha\nu}g_{\beta\mu} - 2g_{\alpha\beta}g_{\mu\nu}\right]\,, \qquad (2.70)$$
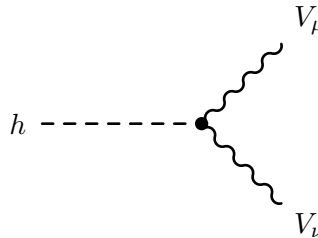
$$= i\frac{e}{\sin\theta_W}\frac{m_V^2}{m_W}g_{\mu\nu}\,. \qquad (2.71)$$

In Equation 2.69 $C_\gamma = 1$, $C_Z = -\cot\theta_W$, and the values for C_L and C_R in Equation 2.68 are given in Table 2.6 where we have introduced the following short-hands:

$$g_f^+ = -\tan\theta_W Q_f, \qquad g_f^- = \frac{T_f^3 - \sin^2\theta_W Q_f}{\sin\theta_W\cos\theta_W}\,. \qquad (2.72)$$

2.4.5.1 Higgs coupling to gluons

While the Higgs boson h does not couple to massless particles such as gluons directly, loops with massive particles induce effective couplings to these particles. Since the

	$\gamma\,\bar{f}_i f_j$	$Z\,\bar{f}_i f_j$	$W^+ \bar{u}_i d_j$	$W^- \bar{d}_i u_j$	$W^+ \bar{\nu}_i \ell_j$	$W^- \bar{\ell}_i \nu_j$
C_L	$-Q_f \delta_{ij}$	$g_f^- \delta_{ij}$	$\frac{1}{\sqrt{2}s_w} V_{ij}$	$\frac{1}{\sqrt{2}s_w}(V_{ij})^\dagger$	$\frac{1}{\sqrt{2}s_w}\delta_{ij}$	$\frac{1}{\sqrt{2}s_w}\delta_{ij}$
C_R	$-Q_f \delta_{ij}$	$g_f^+ \delta_{ij}$	0	0	0	0

Table 2.6: Values of C_L and C_R in Equation 2.68. Q_f denotes the electric charge of fermion f and, i and j represent flavour indices, and $g_f^\pm$ are explained in the text.
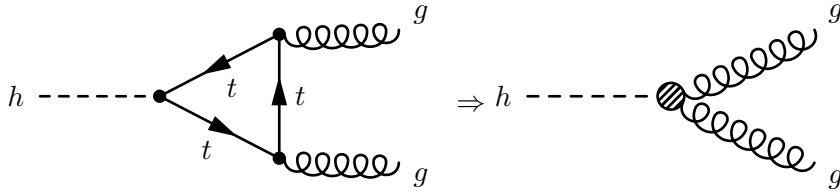

Figure 2.9: Contraction of top loop which leads to an effective tree-level coupling of the Higgs boson to gluons.

dominant production mode of the Higgs boson is through a top-quark loop in so-called gluon fusion, it is useful to introduce an effective theory which incorporates this effect in the $m_t \to \infty$ limit. Such approximations are called low-energy theorems [44–46] since they are only valid for momentum transfers inside the loop which are smaller than m_t. In the limit where the Higgs has zero momentum and is much lighter than some other particles i in the theory (in the Standard Model this only applies to the top quark, but in general it is possible to calculate for example corrections to the $h \to \gamma\gamma$ branching fraction from new heavy fermions charged under $SU(2)_L \times U(1)_Y$ using this framework), the physical effect of including it is captured by the replacement

$$m_i \to m_i \left(1 + \frac{h}{v}\right) \tag{2.73}$$

This is thanks to h appearing linearly with v, which generates all of the tree level mass terms in the Standard Model. Another way of writing this, which extends to higher order in perturbation theory, is

$$\lim_{p_h \to 0} \mathcal{M}(A \to B + h) = \sum_i \frac{m_i^0}{v^0} \frac{\partial \mathcal{M}(A \to B)}{\partial m_i^0} \tag{2.74}$$

where $\mathcal{M}(A \to B)$ is the matrix element for $A \to B$ and the ^{0} superscript denotes bare quantities. The effective coupling of two gluons to the Higgs due to infinitely heavy fermions is therefore encoded in the gluon vacuum polarisation, $g \to g$, which at loop level receives corrections which depend on bare mass terms. At one loop level, the gluon vacuum polarisation gets contributions from the diagrams in Figure 2.10. We are interested in fermions which are heavier than h, so will only focus on the top quark contribution to $\mathcal{M}_F^{\mu\nu}$ which will have a dependence on m_t, as required by Equation 2.74. Since we assume the top is infinitely heavy we can drop any pieces which disappear as $p^\mu \to 0$. We will use a (b) as the adjoint index of the incoming (outgoing) gluon, and i, j as the color indices of the quarks in the loop. We then have[*]:

$$
\begin{aligned}
i\mathcal{M}_t^{\mu\nu} &= -(ig_s)^2 \, t_{ij}^a t_{ji}^b \int \frac{d^4l}{(2\pi)^4} \frac{i^2 \, \mathrm{Tr}[\gamma^\mu(\slashed{l} - \slashed{p} + m_t)\gamma^\nu(\slashed{l} + m_t)]}{[(l-p)^2 - m_t^2][l^2 - m_t^2]} \\
&= -g_s^2 \, \mathrm{tr}[t^a t^b] \int \frac{d^4l}{(2\pi)^4} \frac{8l^\mu l^\nu - 4l^\mu p^\nu - 4l^\nu p^\mu + 4g^{\mu\nu}(m_t^2 + l.p - l^2)}{[(l-p)^2 - m_t^2][l^2 - m_t^2]} \\
&=_{p^\mu \to 0} ig_s^2 \left(\frac{T(F)\delta^{ab}}{16\pi^2}\right)(g^{\mu\nu}p^2 - p^\mu p^\nu)\left[\frac{4}{3}\log\frac{\mu^2}{m_t^2}\right],
\end{aligned} \tag{2.75}
$$

where we have only kept the factors of p^μ and p^2 which are required for the propagator structure, and μ is the renormalisation scale. We have separated the traces over spinor indices from traces over generators by using Tr and tr respectively. We have also introduced a new notation for the index of the fundamental representation $T(F)\delta^{ab} \equiv \mathrm{tr}[t^a t^b]$. This generalises to other representations, so $T(A)\delta^{ab} \equiv \mathrm{tr}[t_{adj}^a t_{adj}^b]$ and so on. Setting $a = b$ we can see that $\mathrm{tr}[t_R^a t_R^a] = d(G)T(R)$ where $d(G)$ is the number of generators or dimension of the group. In the following diagrams we will also use the quadratic Casimirs of representations, which are defined as $C(R)\mathbb{I}_{d(R)} \equiv t_R^a t_R^a$ (a is summed over and $d(R)$ is the dimension of the representation). This suggests $\mathrm{tr}[t_R^a t_R^a] = d(R)C(R)$, so we have the relation $d(G)T(R) = d(R)C(R)$. In QCD we are only interested in the fundamental and adjoint representations, which in our conventions have $T(F) = \frac{1}{2}$, $C(F) = \frac{N^2-1}{2N}$, $T(A) = N$, $C(A) = N$. We have kept the dependence on N for a general $SU(N)$ gauge group explicit here since we will consider such gauge groups later in Chapter 5 and these are useful for reference.

Returning to the calculation at hand, we can now write down the term in the one loop correction to the gluon propagator which has a dependence on m_t in the

---

[*]I will use PackageX [47] to perform all of the integrals in this section.

$m_t \to \infty$ limit:

$$\mathcal{L}_{gg} = -\frac{1}{4} G^{A\mu\nu} G^A_{\mu\nu} \left[1 + \Pi_t(0) \right], \; \Pi_t(0) = \frac{g_s^2 T(F)}{16\pi^2} \frac{4}{3} \log \frac{\mu^2}{m_t^2} . \qquad (2.76)$$

Differentiating with respect to m_t and using $T(F) = \frac{1}{2}$, $\alpha_s = g_s^2/4\pi$, we get:

$$\mathcal{L}_{ggh} = -\frac{1}{4} G^{A\mu\nu} G^A_{\mu\nu} \left(\frac{\alpha_s}{6\pi} \frac{m_t \partial}{\partial m_t} \log \frac{\mu^2}{m_t^2} \right) \frac{h}{v} . = \frac{\alpha_s}{12\pi} G^{A\mu\nu} G^A_{\mu\nu} \frac{h}{v} \qquad (2.77)$$

We can further derive the low energy theorems for any number of Higgs bosons coupling to two gluons by making the replacement $1/v \to g_t/m_t$, where g_t is the (scaled) Yukawa coupling. Then,

$$\mathcal{L}_{ggh^n} = \frac{\alpha_s}{12\pi} \frac{h^n}{n!} G^{A\mu\nu} G^A_{\mu\nu} g_t^n \frac{\partial^{n-1}}{\partial m_t^{n-1}} \frac{1}{m_t} = -\frac{\alpha_s}{12\pi} \frac{1}{n} \left(\frac{-h}{v} \right)^n G^{A\mu\nu} G^A_{\mu\nu}$$

$$\Rightarrow \mathcal{L}_{gg(h)} = \frac{\alpha_s}{12\pi} G^{A\mu\nu} G^A_{\mu\nu} \log \left(1 + \frac{h}{v} \right) \quad (2.78)$$

where we have resummed the logarithm to provide an expression for all n on the last line. We will use this low energy theorem in Chapter 6 to generate multi-Higgs gluon fusion events. Note our approximation that the momentum going through the top loop should be smaller than m_t is questionable already for the second term in the series since $2m_h > m_t$, and for cases where a single Higgs is produced in association with for example jets since the new scales which can enter the loop quickly begin to resolve the top threshold. Also note the destructive interference discussed in Section 2.4.2.2 is reflected in the signs of the ggh and $gghh$ terms.

2.4.6   Renormalisation Group Equations

With the Feynman rules determined, we will return to the discussion of scale dependence in Section 2.3 and calculate the one loop beta function for g_s. To begin we focus on the gluon field counterterm δ_3 since it will be necessary regardless of if we try to calculate $\beta(g_s)$ using the three-gluon vertex or gluon-fermion-fermion vertex. The relevant diagrams are given in Figure 2.10.

Taking them in order, we begin with the fermion bubble $\mathcal{M}_F^{\mu\nu}$ we calculated above. As pointed out in Section 2.3, the logarithms we are looking to resum correspond to UV divergences, so for the purpose of calculating RGEs we can set all masses inside loops to 0. This makes the calculation slightly different to Equation 2.75 and gives:
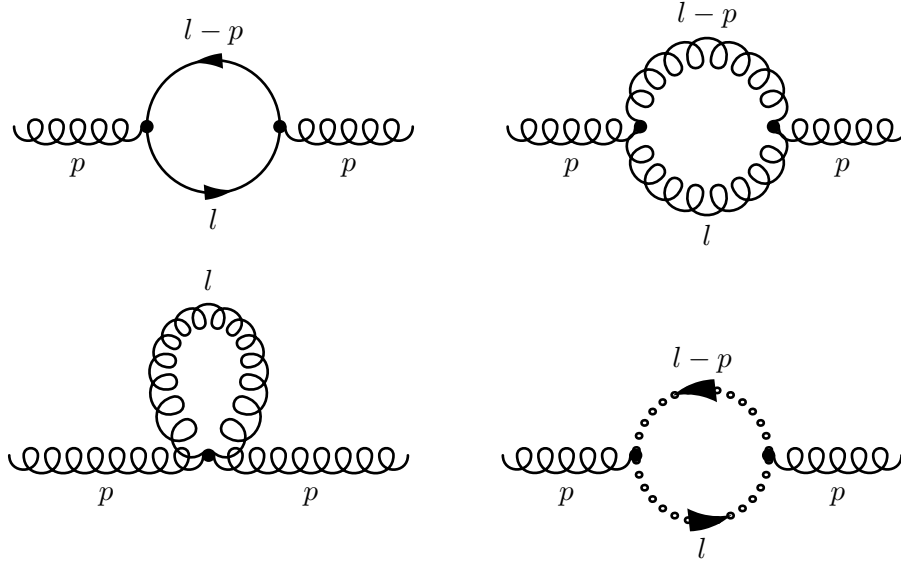
Figure 2.10: One-loop contributions to the QCD vacuum polarisation. We denote these, from left to right, $\mathcal{M}_F^{\mu\nu}$, $\mathcal{M}_3^{\mu\nu}$, $\mathcal{M}_4^{\mu\nu}$, and $\mathcal{M}_{gh}^{\mu\nu}$.

$$
\begin{aligned}
i\mathcal{M}_F^{\mu\nu} = & -(ig_s)^2 \, t_{ij}^a t_{ji}^b \, \int \frac{d^4l}{(2\pi)^4} \frac{i^2 \, \text{Tr}[\gamma^\mu(\slashed{l}-\slashed{p})\gamma^\nu(\slashed{l})]}{(l-p)^2 l^2} \\
= & -g_s^2 \, \text{tr}[t^a t^b] \, \int \frac{d^4l}{(2\pi)^4} \frac{8l^\mu l^\nu - 4l^\mu p^\nu - 4l^\nu p^\mu + 4g^{\mu\nu}(l.p - l^2)}{(l-p)^2 l^2} \\
= & -ig_s^2 \left(\frac{T(F)\delta^{ab}}{16\pi^2} \right) (g^{\mu\nu}p^2 - p^\mu p^\nu) \left[\frac{20}{9} + \frac{4}{3} \left(\frac{1}{\varepsilon} + \log \frac{-\mu^2}{p^2} \right) \right] . \quad (2.79)
\end{aligned}
$$

Moving on to the first gluon loop, we have[*]:

$$
\begin{aligned}
i\mathcal{M}_3^{\mu\nu} = & \frac{g_s^2}{2} \int \frac{d^4l}{(2\pi)^4} \frac{(-i)^2 \, f^{acd} f^{bdc} \, N^{\mu\nu}}{(l-p)^2 l^2} \\
= & -ig_s^2 \left(\frac{C(A)\delta^{ab}}{16\pi^2} \right) \left[p^\mu p^\nu \left(\frac{67}{18} + \frac{11}{6} \left(\frac{1}{\varepsilon} + \log \frac{-\mu^2}{p^2} \right) \right) \right. \\
& \left. - p^2 g^{\mu\nu} \left(\frac{58}{18} + \frac{19}{12} \left(\frac{1}{\varepsilon} + \log \frac{-\mu^2}{p^2} \right) \right) \right] . \quad (2.81)
\end{aligned}
$$

Note that $\mathcal{M}_3^{\mu\nu} \not\propto (g^{\mu\nu}p^2 - p^\mu p^\nu)$ so this diagram is not gauge invariant. The

---

[*]Here $N^{\mu\nu}$ can be read off from Equation 2.65 as:

$$
N^{\mu\nu} = g_{\alpha\beta} \, g_{\rho\sigma} \left[g^{\mu\alpha}(p+l)^\rho + g^{\alpha\rho}(p-2l)^\mu + g^{\rho\mu}(l-2p)^\alpha \right] \left[g^{\nu\beta}(p+l)^\sigma - g^{\beta\sigma}(2l-p)^\nu - g^{\sigma\nu}(2p-l)^\beta \right] .
$$
$$
(2.80)
$$

next diagram $\mathcal{M}_4^{\mu\nu}$ features a scaleless loop integral so will vanish in dimensional regularisation and we do not have to calculate it.

The final diagram is the ghost loop, and we have:

$$
\begin{aligned}
i\mathcal{M}_{gh}^{\mu\nu} = &- (-g_s)^2 \int \frac{d^4 l}{(2\pi)^4} \frac{(i)^2 \, f^{acd} f^{bdc} \, (l-p)^\mu l^\nu}{(l-p)^2 l^2} \\
= &- ig_s^2 \left(\frac{C(A)\delta^{ab}}{16\pi^2} \right) \left[p^\mu p^\nu \left(-\frac{5}{18} - \frac{1}{6} \left(\frac{1}{\varepsilon} + \log \frac{-\mu^2}{p^2} \right) \right) \right. \\
&\left. - p^2 g^{\mu\nu} \left(\frac{2}{9} + \frac{1}{12} \left(\frac{1}{\varepsilon} + \log \frac{-\mu^2}{p^2} \right) \right) \right] .
\end{aligned}
\tag{2.82}
$$

Adding everything up and assuming there are n_f fermions running in the loop in 2.79, we get that:

$$
\begin{aligned}
\mathcal{M}_{\text{one loop}}^{\mu\nu} = \delta^{ab} \left(\frac{g_s^2}{16\pi^2} \right) (g^{\mu\nu} p^2 - p^\mu p^\nu) &\left[\left(C(A) \frac{5}{3} - n_f T(F) \frac{4}{3} \right) \left(\frac{1}{\varepsilon} + \log \frac{-\mu^2}{p^2} \right) \right. \\
&\left. + \frac{31}{9} C(A) - \frac{20}{9} T(F) \right] .
\end{aligned}
\tag{2.83}
$$

As expected the final result is gauge invariant. We can read off the gluon field counterterm:

$$
\delta_3 = \frac{1}{\varepsilon} \left(\frac{g_s^2}{16\pi^2} \right) \left(\frac{5}{3} C(A) - n_f \frac{4}{3} T(F) \right) .
\tag{2.84}
$$

We will extract $\beta(g_s)$ from the gluon-fermion-fermion vertex, so we still need to calculate the quark field counterterm δ_2 and the gluon-fermion-fermion vertex counterterm δ_1. The relevant diagrams are given in Figure 2.11.

For the fermion self-energy we have, setting all masses to 0 again:

$$
\begin{aligned}
i\Sigma_F(\not{p}) = &(ig_s)^2 \int \frac{d^4 l}{(2\pi)^4} \frac{-i^2 \left(\sum_{a,b,k,l} t_{ki}^a t_{jl}^b \delta^{ab} \delta^{kl} \right) \gamma^\mu \not{l} \gamma_\mu}{l^2 (p-l)^2} \\
= &- ig_s^2 \frac{C(F)\delta^{ij}}{16\pi^2} \not{p} \left(-1 - \frac{1}{\varepsilon} - \log \frac{-\mu^2}{p^2} \right) .
\end{aligned}
\tag{2.85}
$$

This allows us to extract the quark field counterterm:

$$
\delta_2 = -\frac{1}{\varepsilon} \left(\frac{g_s^2}{16\pi^2} \right) C(F) .
\tag{2.86}
$$
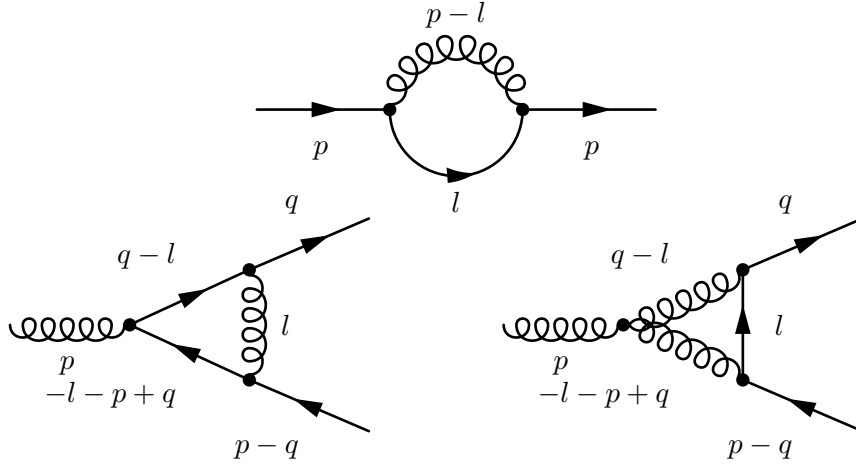
Figure 2.11: One-loop contributions to the fermion self-energy and the gluon-fermion-fermion vertex. We denote these, from top to bottom and left to right, Σ_F, $\Gamma_{1G}^{a,\mu}$, and $\Gamma_{2G}^{a,\mu}$.

To simplify the vertex corrections we will set $q^\mu = 0$ (since we are only interested in the divergent pieces). The first diagram is then given by:

$$
\begin{aligned}
ig_s\Gamma_{1G,\text{div}}^{a,\mu}(p^2) =& (ig_s)^3(t^c t^a t^b)_{ij}\delta^{bc}\int\frac{d^4l}{(2\pi)^4}\frac{-i^3\gamma^\nu(-\slashed{l})\gamma^\mu(-\slashed{p}-\slashed{l})\gamma_\nu}{l^2l^2(l+p)^2}\\
=& ig_s\frac{g_s^2}{16\pi^2}\left(C(F)-\frac{C(A)}{2}\right)t_{ij}^a\left[\gamma^\mu\left(-1+\frac{1}{\varepsilon}+\log\frac{-\mu^2}{p^2}\right)+p^\mu\frac{2\slashed{p}}{p^2}\right].
\end{aligned}
$$
(2.87)

And the second diagram is:

$$
\begin{aligned}
ig_s\Gamma_{2G,\text{div}}^{a,\mu}(p^2) =& g_s(ig_s)^2 f^{abc}(t^c t^b)_{ij}\delta^{bc}\int\frac{d^4l}{(2\pi)^4}\frac{i^3\gamma_\rho(\slashed{l})\gamma_\nu}{l^2l^2(l+p)^2}\\
&\times(g^{\mu\nu}(2p+l)^\rho+g^{\nu\rho}(-p-2l)^\mu+g^{\rho\mu}(l-p)^\nu)\\
=& ig_s\frac{g_s^2}{16\pi^2}\frac{C(A)}{2}t_{ij}^a\gamma^\mu\left(4+\frac{3}{\varepsilon}+3\log\frac{-\mu^2}{p^2}\right).
\end{aligned}
$$
(2.88)

Adding both contributions up again:

$$
\begin{aligned}
\Gamma_{\text{one loop, div}}^{a,\mu}(p^2) =& \frac{g_s^2}{16\pi^2}t_{ij}^a\left[(C(F)+C(A))\gamma^\mu\left(\frac{1}{\varepsilon}+\log\frac{-\mu^2}{p^2}\right)\right.\\
&\left.+\gamma^\mu\left(-C(F)+\frac{5C(A)}{2}\right)+p^\mu\left(C(F)-\frac{C(A)}{2}\right)\frac{2\slashed{p}}{p^2}\right].
\end{aligned}
$$
(2.89)

This allows us to extract the vertex counterterm:

$$\delta_1 = -\frac{1}{\varepsilon}\left(\frac{g_s^2}{16\pi^2}\right)(C(F)+C(A))\,. \tag{2.90}$$

We now have all the required counterterms to extract $\beta(g_s)$ at one loop from the gluon-fermion-fermion interaction term in the lagrangian:

$$\mathcal{L} \supset \mu^{\frac{4-d}{2}} g_R \frac{Z_1}{Z_2\sqrt{Z_3}} G_\mu^{a(0)} \bar{\psi}_i^{(0)} \gamma^\mu t_{ij}^a \psi_j^{(0)}\,. \tag{2.91}$$

As explained in Section 2.3, we use the invariance of the bare parameter g_0 under changes in the renormalisation scale μ:

$$\begin{aligned}
\mu\frac{d}{d\mu}\left[g_R\frac{Z_1}{Z_2\sqrt{Z_3}}\mu^{\frac{4-d}{2}}\right] &= 0 \\
\Rightarrow \mu\frac{dg_R}{d\mu} &= -g_R\left[\varepsilon + \mu\frac{d}{d\mu}\left(\delta_1 - \delta_2 - \frac{\delta_3}{2}\right)\right] \\
\Rightarrow \mu\frac{dg_R}{d\mu} &= -\varepsilon g_R + \varepsilon g_R^2 \frac{\partial}{\partial g_R}\left(\delta_1 - \delta_2 - \frac{\delta_3}{2}\right) \\
&= -\varepsilon g_R + \varepsilon g_R^2\left(-\frac{1}{\varepsilon}\frac{g_R}{16\pi^2}\left(\frac{11}{3}C(A) - n_f\frac{4}{3}T(F)\right)\right)\,.
\end{aligned} \tag{2.92}$$

So in the end we have:

$$\beta(g_s) = -\frac{g_s^3}{16\pi^2}\left[\frac{11}{3}C(A) - n_f\frac{4}{3}T(F)\right]\,. \tag{2.93}$$

While we had to go through a fair amount of work to obtain this one loop beta function for QCD, the fact that beta functions only depend on the UV divergent parts of the relevant diagrams makes it possible to derive general forms for the RGEs for renormalisable, perturbative quantum field theories. In Chapter 5 we will calculate beta functions for extensions of the Standard Model, and make use of such general results which have been derived in [48–50] in order to avoid calculating them all by hand.

The explicit renormalisation group equations of the dominant parameters of the

Standard Model to one loop order are:

$$\mu\frac{\mathrm{d}g_1}{\mathrm{d}\mu} = \frac{41}{6}\frac{g_1^3}{16\pi^2} \tag{2.94a}$$

$$\mu\frac{\mathrm{d}g_2}{\mathrm{d}\mu} = -\frac{19}{6}\frac{g_2^3}{16\pi^2} \tag{2.94b}$$

$$\mu\frac{\mathrm{d}g_s}{\mathrm{d}\mu} = -7\frac{g_s^3}{16\pi^2} \tag{2.94c}$$

$$\mu\frac{\mathrm{d}y_t}{\mathrm{d}\mu} = \left(\frac{9y_t}{2} - \frac{17g_1^2}{12} - \frac{9g_2^2}{4} - 8g_s^2\right)\frac{y_t}{16\pi^2} \tag{2.94d}$$

$$\mu\frac{\mathrm{d}\lambda}{\mathrm{d}\mu} = \left(\frac{3g_1^4}{8} + \frac{3g_1^2g_2^2}{4} + \frac{9g_2^4}{8} - 6y_t^4 - (3g_1^2 + 9g_2^2 - 12y_t^2)\lambda + 24\lambda^2\right)/(16\pi^2) \tag{2.94e}$$

Here y_t is $M_{3,3}^u$ and hence has a value of ≈ 0.99 at the top pole, and $\lambda = \frac{m_h^2}{2v^2}$ and has a value of ≈ 0.13 at the Higgs pole. Note in particular that the β-function for g_s is negative: this means g_s will become infinitely large in the IR and we can expect a perturbative description of the physics at this scale to be impossible to find. We can solve for $\alpha_s(Q^2) = \frac{g_s^2(Q^2)}{4\pi}$ in terms of the value measured at some scale μ^2:

$$\alpha_s(Q^2) = \frac{4\pi\alpha_s(\mu^2)}{4\pi + 7\alpha_s(\mu^2)\log(\frac{Q^2}{\mu^2})}. \tag{2.95}$$

When the denominator becomes 0 this will dynamically define a new scale $Q_{\mathrm{crit}} = \Lambda_{QCD}$. Measurements of the effective coupling have been performed above the scale where the perturbative description breaks down and confirm this general picture, see Figure 2.12, and give $\Lambda_{QCD} \approx 1$ GeV. Looking at the form of Equation 2.93 we see that it is exactly the self-interactions among the gluons that give rise to this behaviour. Note that this feature of $SU(3)_C$ has allowed us to generate a new fundamental scale Λ_{QCD} in our theory through quantum corrections, without putting it in by hand. This is an example of dimensional transmutation [51] and can be used to construct extensions to the Standard Model which attempt to explain the appearance of other scales $\ll \Lambda_{\mathrm{Planck}}$, in particular why the weak scale is so small. In the UV the coupling instead tends to 0 indicating the theory becomes free at very high scales, a phenomenon referred to as *asymptotic freedom*. In Chapter 5 we will investigate the hadron collider phenomenology of secluded dark sectors with QCD-inspired self-interactions using similar RGE scaling behaviour to generate a scale that can explain the dark matter relic abundance.
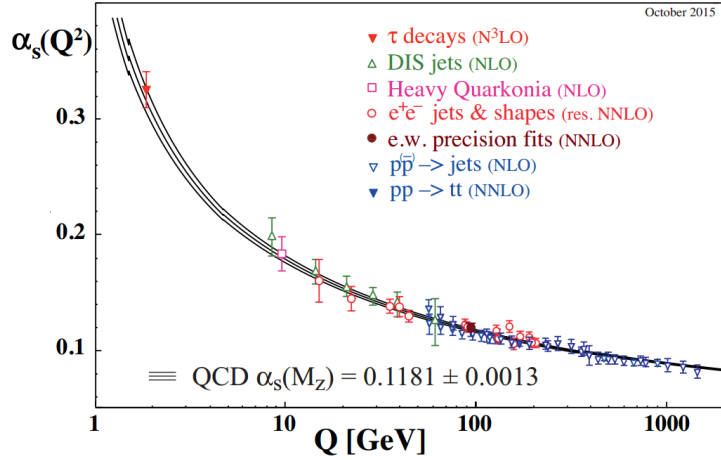
Figure 2.12: The effective value of $\alpha_s(\mu) = \frac{g_s^2(\mu)}{4\pi}$ as extracted at different values of $\mu = Q$ using various observables and methods. Taken from the PDG Review [24].

2.4.7 $\bar{\theta}$ and the Strong $\mathcal{CP}$ problem

We can add some additional $\mathcal{CP}$ violating Lorentz- and gauge-invariant renormalisable operators to the gauge sector:

$$\mathcal{L}_{CPV} = \frac{\theta}{32\pi^2} \varepsilon^{\mu\nu\alpha\beta} G^A_{\mu\nu} G^A_{\alpha\beta} + \frac{\theta_2}{32\pi^2} \varepsilon^{\mu\nu\alpha\beta} W^I_{\mu\nu} W^I_{\alpha\beta} + \frac{\theta_1}{32\pi^2} \varepsilon^{\mu\nu\alpha\beta} B_{\mu\nu} B_{\alpha\beta} \,. \quad (2.96)$$

These terms arise as a modification of the path integral measure when we perform a chiral transformation of a left-handed quark since the chiral symmetry is anomalous, and similarly for chiral rotations of the other fermion fields (however since they aren't charged under all of the $\mathcal{G}_{SM}$ subgroups not all three terms are generated). We can therefore attempt to remove these terms by performing chiral rotations which leave observables invariant. Since the right-handed fields are uncharged under $SU(2)_L$ we can rotate θ_2 into the Yukawa couplings using the left-handed fields and then remove it by rotating the right-handed fields. Similarly we can use right-handed neutrinos introduced with for example a seesaw mechanism to rotate θ_1 away from the neutrino Yukawas after putting it in there,[*] however since you can't lasso a basketball[†] this term would ultimately not have any physical effects anyway since all these terms can be rewritten as total derivatives:

---

[*]While this depends on the specific mechanism we use to introduce neutrino masses and mixing, it is a fairly generic statement that this is possible.

[†]Or, in a less colloquial manner, $\pi_k(U(1)) = 0$ for $k \geq 2$, where π_k is the k-th homotopy group.

$$
\begin{aligned}
\varepsilon^{\mu\nu\alpha\beta}G^a_{\mu\nu}G^a_{\alpha\beta} =& \varepsilon^{\mu\nu\alpha\beta}(\partial_\mu g^a_\nu - \partial_\nu g^a_\mu + g_s f^{abc} g^b_\mu g^c_\nu)(\partial_\alpha g^a_\beta - \partial_\beta g^a_\alpha + g_s f^{ade} g^d_\alpha g^e_\beta) \\
=& 2\varepsilon^{\mu\nu\alpha\beta}\left[2(\partial_\mu g^a_\nu)(\partial_\alpha g^a_\beta) + g_s(\partial_\mu g^a_\nu)f^{ade}g^d_\alpha g^e_\beta + g_s(\partial_\alpha g^a_\beta)f^{abc}g^b_\mu g^c_\nu\right] \\
=& 4\varepsilon^{\mu\nu\alpha\beta}\partial_\mu\left[g^a_\nu \partial_\alpha g^a_\beta + \frac{g_s}{3}f^{abc}g^a_\nu g^b_\alpha g^c_\beta\right] .
\end{aligned}
\tag{2.97}
$$

When there are no non-trivial mappings of spatial infinity S^3 unto the group elements such terms will disappear when converted into a surface integral.

Since q_L, u_R, d_R all transform under $SU(3)_C$ we can't use the Yukawas to rotate away θ and instead we pick up another contribution $\theta_F = -\arg\det(Y^u Y^d)$ (where these are defined as in Section 2.4.4), so we end up with a total coefficient $\bar\theta = \theta - \theta_F$. Since the QCD vacuum has a non-trivial structure thanks to $\pi_3(SU(N)) = \mathbb{Z}$ for $N \geq 2$ this term will have physical effects, although they are difficult to calculate directly in QCD. The so-called Strong $\mathcal{CP}$ problem is then why the Yukawa-induced term seems to almost exactly cancel the bare θ: $\bar\theta < 10^{-10}$. This limit can be set by calculating the contribution $\bar\theta$ would make to the electric dipole moment of the neutron using chiral perturbation theory [52], which effectively amounts to using a CCWZ expansion to describe the dynamics of the low-energy QCD bound states after chiral symmetry breaking.

2.5 Parton distribution functions

When calculating the cross section for a process in proton-proton collisions we have to take the composite nature of the protons into account. Since the composition of the proton is determined by non-perturbative physics it is difficult to calculate analytically, so we parameterise it in terms of so-called *parton distribution functions* (PDFs) $f_i(x)$ which represent the probability number densities to find a parton i carrying a momentum fraction x of the proton. These can be fit to experimental results for well-understood processes, and then used for making predictions for other processes. Alternatively PDFs can also be calculated using lattice QCD from first principles [53]. The use of fitted functions to capture low energy non-perturbative physics implicitly assumes that QCD factorises [54]: this is the statement that $\sigma = f_i \otimes H + \mathcal{O}(\Lambda_{QCD}/Q)$, where H is the process-dependent hard function and Q the hard energy scale $Q \gg \Lambda_{QCD}$. In order to remove infrared divergences from summing over collinear radiation from the initial state at fixed x we absorb these into the (now renormalised) PDFs. This introduces an unphysical factorisation scale

μ_F which defines the scale at which we probe the proton. Just as parameters in the lagrangian run with the renormalisation scale, the renormalised $f_i(x, \mu_F)$ run with μ_F. From a Wilsonian perspective the situation is however reversed: the cutoff scale of the theory here is $\sim \Lambda_{QCD} \ll Q$ and we define the bare, finite PDFs at this scale, and incorporate the effect of integrating *up* over collinear radiation into the definition of the renormalised PDFs. Factorisation can then be thought of as an inverse of the expectation that calculations at the weak scale should be insensitive to the UV completion of the Standard Model which lead us to only consider renormalisable operators in the lagrangian: here we instead expect calculations at scales much higher than Λ_{QCD} to be insensitive to the non-perturbative completion we know exists, but is difficult to explicitly calculate with. The evolution is given by the DGLAP equation [55–57]:

$$\mu_F \frac{d}{d\mu_F} \begin{pmatrix} f_{q_i}(x, \mu_F) \\ f_g(x, \mu_F) \end{pmatrix} = \frac{\alpha_s}{2\pi} \sum_j \int_x^1 \frac{d\xi}{\xi} \begin{pmatrix} P_{q_i q_j}(x/\xi) & P_{q_i g}(x/\xi) \\ P_{g q_j}(x/\xi) & P_{gg}(x/\xi) \end{pmatrix} \begin{pmatrix} f_{q_j}(\xi, \mu_F) \\ f_g(\xi, \mu_F) \end{pmatrix}.$$
$$(2.98)$$

The splitting functions $P_{ij}(y)$ encode the probability that a parton of type j emits a collinear parton of type i with a fraction y of the momentum of the parent, and can be calculated from considering $g \to gg$, $g \to q\bar{q}$, and $q \to qg$. Just as with the renormalisation scale μ, μ_F should be chosen to be close to the hard scale Q in order to avoid the reappearance of large logarithms of the type $\alpha_s^n \log^n(Q^2/\mu_F^2)$ which this procedure resums. Combining theoretical calculations and experimental observations in order to create the best PDF fit possible is a crucial ingredient for calculating any cross section at the LHC. An example PDF fit is shown in Figure 2.13. The unified PDF interface LHAPDF [58] will be used to access PDF values throughout this thesis.

2.6   Jets

The infrared divergences associated with collinear radiation discussed in Section 2.5 show up in any process with coloured particles in the final state. The splitting functions $P_{ij}(y)$ are universal and can be used to define a semi-classical approximation for resumming such collinear radiation down to Λ_{QCD} called the parton shower. Taking the radiation of a collinear gluon from a quark as an example, this will take the general form:
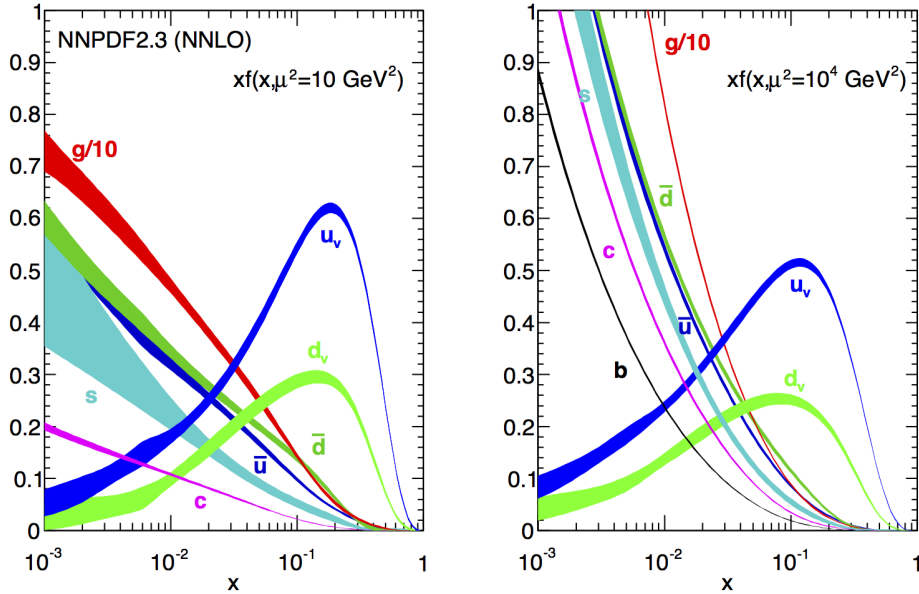
Figure 2.13: Example parton distributions for the proton at $\mu_F^2 = 10$ and 10^4 GeV^2, fitted by the NNPDF Collaboration. Taken from [59].

$$d\sigma(X \to Yq+g) = d\sigma(X \to Yq)dtdz\ \frac{1}{t}\left[\frac{\alpha_s}{2\pi}P_{qq}(z) + \mathcal{O}\left(\frac{t}{Q^2}\right)\right],$$

$$P_{qq}(z) = C(F)\frac{1+z^2}{1-z} \quad (2.99)$$

where z is the energy fraction of the original quark carried by the daughter quark, and t is a virtuality scale of the splitting such as the resulting mass m^2, momentum transverse to the direction of travel of the original quark k_T^2, or αQ^2 where α is the opening angle and Q^2 a hard scale of the process*. Since we cut off the radiation at a scale $t_c \sim \Lambda_{QCD}$ where confinement kicks in and we no longer can perform perturbative calculations with quarks and gluons this leads to an ultimate upper bound on z which will in general depend on the choice of t, so we do not have to worry about the $z \to 1$ pole in P_{qq} here. Using $t = k_T^2$, the minimum and maximum values of z are:

---

*Different parton shower implementations use different choices of t: the important thing is that $t \to 0$ in the collinear limit. Choices which respect angular ordering (k_T^2 and αQ^2) turn out to also model coherent radiation due to the non-zero colour charge of the gluon correctly so are favoured in practice.
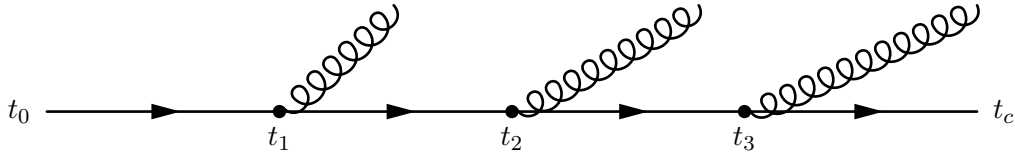
Figure 2.14: Diagrammatic representation of a parton shower. $Q^2 \sim t_0 > t_1 > t_2 > t_3 > t_c \sim \Lambda_{QCD}$ and the opening angle tends to become smaller for smaller t. The radiated gluons also radiate further, so the full parton shower runs Markov Chain Monte Carlo until all legs are evolved down to $\sim t_c$. Note that since $\Delta(t_i, t_j) \sim \exp(-\alpha_s)$, the resulting jet shape is sensitive to the running of α_s.

$$z_{\max} = 1 - \sqrt{\frac{t}{Q^2}}, \quad z_{\min} = \sqrt{\frac{t}{Q^2}}. \tag{2.100}$$

This allows us to perform the integral over z:

$$R(t) = \frac{C(F)}{t} \frac{\alpha_s}{2\pi} \int_{\sqrt{t/Q^2}}^{1-\sqrt{t/Q^2}} dz \, \frac{1+z^2}{1-z}$$

$$= \frac{C(F)}{t} \frac{\alpha_s}{2\pi} \left[\log \frac{Q^2}{t} - \frac{3}{2} + \mathcal{O}\left(\frac{t}{Q^2}\right) \right]. \tag{2.101}$$

$R(t)$ can be interpreted as the probability of finding a gluon at the scale t. We can then define the probability to *not* find any gluons between t and Q^2, $\Delta(Q^2, t)$:

$$\frac{d\Delta(Q^2, t)}{dt} = -R(t)\Delta(Q^2, t)$$

$$\Rightarrow \Delta(Q^2, t) = \exp\left(-\int_t^{Q^2} R(t')dt'\right)$$

$$\approx \exp\left[-\frac{\alpha_s}{4\pi} C(F) \left(\log^2 \frac{Q^2}{t} - 3 \log \frac{Q^2}{t}\right)\right]. \tag{2.102}$$

This is called a Sudakov factor and encodes the leading logarithmic resummation of a gluon radiating from a final state quark in QCD. For example, the rate for $e^+ e^- \to q\bar{q}$ with no additional resolvable radiation off the quarks is given by the fixed order cross section times the Sudakov factor for no additional radiation from Q^2 down to the resolvable resolution of the detector (to make this statement precise we require a mathematically consistent definition of a 'jet', which will be discussed below). A diagrammatic representation is shown in Figure 2.14. Recursively radiating partons using a Markov Chain Monte Carlo algorithm from all of the coloured

legs of a *parton level* event (generated by unweighting a fixed order calculation) until all resulting colored legs reach a scale $\sim t_c$ is referred to as *parton showering*, since the final multiplicity of colored particles will be very large. After modelling confinement (in practice done using phenomenological models tuned to data) this effect means that colored partons in the final state of a fixed order calculation will appear as collimated collections of colour-neutral hadrons in physical *hadron level* events, with roughly the same total momentum as the original parton. These objects are called *jets*. In order to define a jet we need to decide on a way to cluster these particles together. Since we have just determined that the theoretical description of jets relies on the resummation of collinear and soft radiation, we should use jet clustering algorithms which are collinear and infrared-safe in order to be able to connect experimental measurements of jets to theory calculations with final state coloured partons unambiguously [60]. This can be done by using sequential recombination algorithms, with the following central objects:

$$d_{ij} = \min(k_{t,i}^{2p}, k_{t,j}^{2p}) \frac{\Delta R_{ij}^2}{R^2}, \quad d_{iB} = k_{t,i}^{2p} \tag{2.103}$$

where $k_{t,i}$ is the transverse momentum of pseudo-particle[*] i, ΔR_{ij} is the distance between pseudo-particles i and j in the $y - \phi$ plane, and R is an input parameter called the *jet radius*. These algorithms proceed by recursively identifying the smallest d, and:

- if $\min d = d_{ij}$, combine i and j into a new object i'.

- if $\min d = d_{iB}$, remove i from the event and call it a jet.

Once there are no pseudo-particles left in the event it is completely clustered and a physics analysis can proceed. The parameter p determines the general behaviour of the algorithm and there are three common choices:

- $p = 1$ is the k_t algorithm [61], which corresponds to recursively 'un-doing' the parton shower algorithm we just described.

- $p = 0$ is the Cambridge-Aachen algorithm [62], which corresponds to recursively 'un-doing' an angular-ordered parton shower algorithm.

---

[*]By pseudo we here mean that these also can refer to already clustered collections of particles.

- $p = -1$ is the anti-k_t algorithm [63], and does not correspond to any theoretically motivated model for jet formation. However it is infrared and collinear-safe, and provides circular jets, which makes it very popular among the experimental collaborations.

...and Beyond!

"There are obviously many things which we do not understand, and may never be able to."

Leela, Ship Operations AI, UESC Marathon

Contents

3.1 Known unknowns at short length scales

The Standard Model as presented in the last chapter is well-established as the correct theory of nature at the short length scales we have managed to probe it at. However there are several experimental and theoretical observations which suggest it can't be the final theory before Quantum Gravity kicks in at the Planck scale. The most glaring one is the observation of neutrino oscillations [64] which suggests neutrinos must have mass. This can be achieved by adding a right-handed neutrino field to the theory, which allows a Dirac mass term to be generated through a Yukawa coupling as for the other fermion fields. Since the right-handed neutrino would not carry any

Standard Model charges there would be nothing to stop us from writing a Majorana mass term which would naively sit at the cutoff scale of the Standard Model:

$$\mathcal{L}_{\nu,\text{mass}} = -m\bar{\psi}_L\psi_R - \frac{M}{2}\bar{\psi}_R\psi_R\,. \tag{3.1}$$

Diagonalising the mass matrix we find the eigenvalues to be given by $\frac{M}{2} \pm \sqrt{m^2 + \frac{M^2}{4}} \approx -\frac{m^2}{M}, M$. If $m \sim v$ and $M \sim \Lambda_{\text{Planck}}$ we find that the lighter mass eigenstate has $m_{\text{light}} \approx 10^{-6}$ eV and is predominantly left-handed. This method of generating very small neutrino masses from a large hierarchy is called the see-saw mechanism [65]. In this sense the observation of very small neutrino masses can be easily accommodated in the Standard Model, but the mechanism we use to to do so intrinsically does not predict any further observables at low scales.

Another issue with the Standard Model is the strong $\mathcal{CP}$ problem which was already introduced in Section 2.4.7 as the absence of an allowed total derivative term which would generate physical effects through topologically non-trivial gauge configurations. It was shown that the coefficient of this term is given by $\bar{\theta} = \theta - \arg\det(Y^uY^d) < 10^{-10}$, and there must therefore be an almost perfect cancellation between the two contributing parameters. However θ is naively an $\mathcal{O}(1)$ parameter of QCD, and $\arg\det(Y^uY^d)$ is an $\mathcal{O}(1)$ parameter of the electroweak sector, so there is no reason to believe they should cancel in this way. This is an example of *fine-tuning*, where different parameters of a theory are forced to take very particular values for no discernable reason. The strong $\mathcal{CP}$ problem is therefore another major motivation for the existence of physics beyond the Standard Model (BSM). Solutions to this problem usually introduce new light scalars called axions.

3.1.1 The Nature of Electroweak Symmetry Breaking

A third issue is the so-called hierarchy problem, which is the question of why the weak scale is ~ 100 GeV when quantum corrections naively bring it to the cutoff scale Λ_{CO} of the theory[*]. Technically this shows up as large quantum corrections to the physical mass term of the Higgs boson m_P^h: when calculating generic mass corrections at the cutoff scale, these will naively add terms $\propto \Lambda_{CO}$ to the bare masses in the theory. This turns out not to be true for the mass terms m_B^i of the gauge bosons and fermions of the Standard Model since these are protected by the

---

[*]See for example [66] for a modern discussion on the merits of the hierarchy problem as presented here.

custodial symmetries[*] which the mass terms have broken. Since these symmetries are exact when $m_B^i \to 0$, quantum corrections must be $\propto m_B^i$, explaining why we don't necessarily expect $m_P^i \sim \Lambda_{CO}$.

The Higgs boson, as a fundamental scalar, is not protected by any custodial symmetry so we would therefore expect that the pole mass at the cutoff is given by $m_P^2 = m_B^2 + \Sigma(m_B^2) \approx m_B^2 + \Lambda_{CO}^2$ where $\Sigma(m_B^2)$ are real corrections to the self-energy. This can be shown explicitly by calculating the self-energy contribution from a heavy fermion with mass $M \approx \Lambda_{CO}$, the diagram on the left in Figure 3.1. This loop calculation is similar to that done in Section 2.3 but with an explicit mass term M for the particles in the loop, and we keep all the numerator terms to make sure we do not miss any cancellations[†]:

$$i\Sigma_h(p^2) \supset \mu^{4-d}y^2 \int \frac{d^d l}{(2\pi)^d} \frac{\text{Tr}\left[(\slashed{l} - \slashed{p} + M)(\slashed{l} + M)\right]}{((l-p)^2 - M^2)(l^2 - M^2)}$$

$$= \mu^{4-d}y^2 \int \frac{d^d l}{(2\pi)^d} \frac{4(M^2 + l^2 - l.p)}{((l-p)^2 - M^2)(l^2 - M^2)}$$

$$= \frac{iy^2}{16\pi^2}\left(20M^2 - 4p^2 + 2(6M^2 - p^2)(\frac{1}{\varepsilon} + \log\frac{\mu^2}{M^2}) + f(p^2, M^2)\right). \quad (3.2)$$

Here $f(p^2, M^2)$ is a function with a branch cut that starts at $p^2 = 4M^2$ and extends to $p^2 = \infty$. We will assume we are calculating at the cutoff of the theory and assume it is the Planck scale, so $p^2 = \mu^2 = M^2 = (10^{18} \text{ GeV})^2$, and similarly assume $y = 1$ as a reasonable value for the coupling. Since we are at the cutoff we ignore the ε term. This gives:

$$\Sigma_h(\Lambda_{\text{Planck}}^2) \approx \frac{5}{16\pi^2} \times 10^{36} \text{ GeV}^2. \quad (3.3)$$

To have a pole mass at $m_P = 125$ GeV if the cutoff is at the Planck scale would therefore require that $m_B^2 = (-\frac{5}{16\pi^2} + 10^{-32})\Lambda_{\text{Planck}}^2$ at one loop, if this diagram is the only contribution (diagrams with particles with masses $\sim v$ will of course also contribute but only with terms $\sim v^2$, and do not change the overall argument). This fine-tuning of the bare parameter value to an order of 10^{-32} is the hierarchy problem, and shows up whenever we take the cutoff of the Standard Model to be $\gg v$.

---

[*]In the case of the gauge bosons, gauge invariance, and in the case of the fermions, chiral symmetry.

[†]I will again use PackageX [47] to perform the integral.
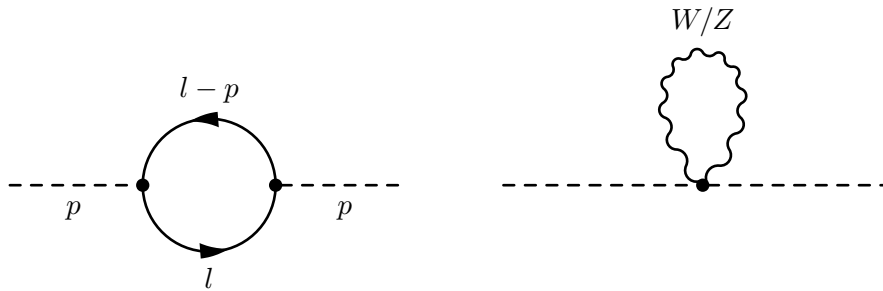
Figure 3.1: Representative diagrams contributing to the Higgs boson self-energy.

Solutions to the hierarchy problem typically modify the Higgs sector of the Standard Model in order to for example introduce additional symmetries which ensure cancellations in the self-energy calculation. In other words, the hierarchy problem is deeply related to the question of what the underlying nature of electroweak symmetry breaking is in the Standard Model. Most extensions to the Standard Model designed to solve the hierarchy problem predict that the higher order terms in the Higgs potential such as λ^3 discussed in Section 2.4.2.2 are modified from the Standard Model expectation, $\lambda^3 \neq \lambda^3_{\mathrm{SM}}$. This is for example a generic feature of Two Higgs Doublet Models [67] and hence models of supersymmetry, and models where the Higgs is a bound state of a new strongly interacting sector rather than an elementary particle [68]. Therefore measuring the coefficients of the higher order terms is not just a precision test of the Standard Model itself: it also provides considerable insight into the specific mechanism of electroweak symmetry breaking nature has employed and hence potentially allows physics beyond the Standard Model to be indirectly discovered, even if the LHC does not find any new resonant states within its energy range. The study of $hhjj$ production in Chapter 6 is in this sense a study of Beyond the Standard Model physics, even if the main topic is a measurement of the Higgs trilinear coupling.

Another avenue to study the hierarchy problem if no new resonant states are produced is to measure the Standard Model parameters that go into the Higgs self-energy calculation. In dimensional regularisation there is strictly speaking no hierarchy problem in the Standard Model itself: it only shows up when we explicitly introduce new, heavy states into our theory as above. In order to remain model-independent in our treatment it could therefore be argued we should first calculate and measure the dominant Standard Model contributions before worrying about hypothetical new physics: the leading one is given by the top Yukawa coupling

y_t through a similar diagram as that calculated above with $y = y_t \approx 0.93$ and $M = m_t \approx 163$ GeV in $\overline{\text{MS}}$, which gives a difference between the pole and $\overline{\text{MS}}$ masses $\frac{\sqrt{m_P^2 - m_{\overline{\text{MS}}}^2}}{m_P}$ of order $\leq 1\%$ if $m_P = 125$ GeV using the result in Equation 3.2. The absolute size of this correction is insensitive to the pole mass of the Higgs boson, however: if $m_P = 80$ GeV the correction would be of the order 15%, and for $m_P \leq 40$ GeV over 100%. The underlying cause is the large top mass and hence large size of the top Yukawa coupling, $y_t \approx 1$. This suggests the top quark could play a special role in electroweak symmetry breaking, and motivates the study of the top quark sector as a proxy for its dynamics. In Chapter 7 we will present a study of the use of top polarisation measurements for constraining a Randall-Sundrum model [22, 23] designed to solve the hierarchy problem and explain the Yukawa structure of the Standard Model, and show how such measurements allow the top sector to provide additional sensitivity to the underlying dynamics.

The first subleading contribution to the Higgs self-energy comes from quartic $hhV^\dagger V$ couplings in diagrams of the type on the right in Figure 3.1. Much like the Higgs trilinear and quartic self-couplings these are predicted by the Standard Model through our assumptions about the Electroweak Symmetry Breaking mechanism employed by nature, but can be generically modified in extensions which expand or change the Higgs sector. These quartic $hhV^\dagger V$ couplings are difficult to directly measure at the LHC. However they do contribute to the vector boson fusion component of $hhjj$ production: in Chapter 6 we will therefore also show how a measurement of $hhjj$ production can be used to constrain their values.

3.2 Known unknowns at long length scales

There is another group of known unknowns which tell us there must be some beyond the Standard Model physics. Unlike the ones discussed so far they are all related to astronomical and cosmological observations, and we connect them to short length scale particle physics by considering the evolution of the universe as it cools down after the big bang.

One such unexplained phenomenon is the baryon anti-baryon asymmetry of the universe. While the complex phase of the CKM matrix and the $\bar{\theta}$ angle are sources of $\mathcal{CP}$ violation, they are not sufficient to explain the observed baryon dominance as outlined by the Sakharov conditions [69]. These state that in order to generate a baryon anti-baryon asymmetry, the following must be true in the early universe:

- Baryon number is violated.

- $\mathcal{C}$ and $\mathcal{CP}$ is violated.

- There are interactions out of thermal equilibrium.

Baryon number is violated in the Standard Model by non-perturbative effects, but again not to a great enough extent to generate the observed asymmetry. Introducing sufficient sources for baryon number and $\mathcal{CP}$ violation, and a strong enough phase transition to keep the universe sufficiently out of equilibrium as it cools, are major motivations for introducing BSM physics. One avenue to introduce additional $\mathcal{CP}$ violation and a stronger phase transition into the Standard Model is modifications to the Higgs sector. $\mathcal{CP}$ violating effects in the Higgs sector, parameterised in terms of effective operators, will be studied in Chapter 6.

As alluded to above, the Standard Model does not include a quantum description of gravity. It is possible to construct a general effective quantum theory of a massless spin-2 boson which turns out to be equivalent to General Relativity at low energies [70] when the cutoff is given by the Planck scale. This suggests that whatever the quantum gravity UV completion is, it is expected to behave like General Relativity all the way up to the Planck scale. The experimental discovery of an accelerated rate of expansion of the universe [71] suggests a non-zero cosmological constant ρ. This constant ρ faces a similar hierarchy problems as the Higgs mass in that quantum corrections would be expected to bring it to the cutoff of the theory $\rho \sim (\Lambda_{CO})^4$ but it is measured to be $\rho \lesssim (\mathrm{mEV})^4$. Searches for some types of solutions to this cosmological constant problem can be performed at the LHC [72, 73].

A final known unknown is the apparent presence of large quantities of non-interacting matter throughout the universe that can be inferred from a range of astronomical and cosmological observations over a large range of length and energy scales. This matter is called *dark matter* and since searches for particle physics descriptions of it will be the topic of Chapters 4 and 5 we will discuss it in more detail in the next section.

3.2.1   Dark Matter

The existence of dark matter is heavily implied by a number of observations. In chronological order these include for example Zwicky's observations of the radial velocity dispersion of galaxies in the Coma cluster [74], Babcock's observation of
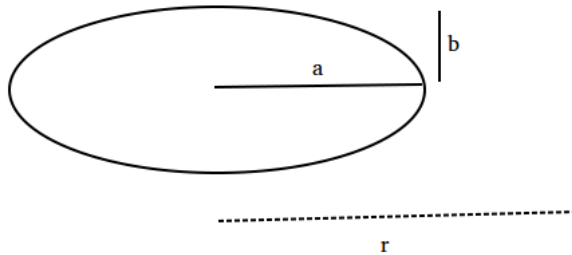
Figure 3.2: Diagram of the setup for the rotational velocity calculation.

the rotational velocity curve of the Andromeda galaxy [75], and Ostriker's and Peebles' numerical observation that the presence of a massive non-interacting spherical component (halo) is required to stabilise the kinematics of galaxy disks [76]. More recently the combination of X-ray spectroscopy of the visible matter and gravitional lensing analysis of the total matter content of the Bullet cluster, created from the collision of two other clusters, strongly indicates the presence of large amounts of invisible, non-interacting matter distributed in halos around the two original clusters. This has ruled out alternative explanations which modify gravitional interactions rather than the matter content [77]. The current cosmological 'Standard Model' ΛCDM also requires a large dark matter component to overcome the thermal and radiation pressure of baryonic matter in the early universe in order to allow galaxy and star formation which matches observations [78] and to explain observed anisotropies in the Cosmic Microwave Background [79].

Focusing on the rotational velocity of spiral galaxies we can calculate the expected result in Newtonian gravity with and without a dark matter halo. When there is no dark matter present the gravitional potential Φ is dominated by a disk-shaped core with a radius a and height b that we will assume has constant density. A sketch of the setup is given in Figure 3.2. In cylindrical coordinates the potential can then be approximated by a Miyamoto-Nagai form [80]:

$$\Phi_{\text{disk}}(r, z) = -\frac{G_N M_{\text{disk}}}{\left(r^2 + (a + \sqrt{b^2 + z^2})^2\right)^{1/2}} .$$

(3.4)

In a gravitional potential the rotational velocity of an orbiting object is found by balancing the transverse acceleration against the potential, so $v_{\text{rot}} = \sqrt{r\frac{d\Phi}{dr}}$ which gives:

$$v_{\text{rot, no DM}}(r) = \sqrt{\frac{G_N M_{\text{disk}} r^2}{\left(r^2 + (a + \sqrt{b^2 + z^2})^2\right)^{3/2}}} \, . \tag{3.5}$$

Adding a sphere of radius R with uniform density and a total mass M_{DM} which envelops the disk (a dark matter halo) modifies the potential as follows:

$$\Phi_{\text{disk+sphere}}(r, z) = -\frac{G_N M_{\text{disk}}}{\left(r^2 + (a + \sqrt{b^2 + z^2})^2\right)^{1/2}} - \frac{G_N M_{\text{DM}}(3R^2 - r^2)}{2R^3} \, . \tag{3.6}$$

This gives the following rotational velocity:

$$v_{\text{rot, sphere}}(r) = \sqrt{\frac{G_N M_{\text{disk}} r^2}{\left(r^2 + (a + \sqrt{b^2 + z^2})^2\right)^{3/2}} + \frac{G_N M_{\text{DM}} r^2}{R^3}} \, . \tag{3.7}$$

For more a more realistic description of the dark matter distribution we can use the Navarro-Frenk-White (NFW) [81] density:

$$\rho(r) = \frac{\rho_0}{\frac{r}{R_s}\left(1 + \frac{r}{R_s}\right)^2} \, . \tag{3.8}$$

Following through the same calculation gives the following rotational velocity:

$$v_{\text{rot, NFW}}(r) = \left[\frac{G_N M_{\text{disk}} r^2}{\left(r^2 + (a^2 + \sqrt{b^2 + z^2}^2)\right)^{3/2}}\right.$$
$$\left. + 4\pi G_N \rho_0 \left(\frac{R_s^3 \log(1 + r/R_s)}{r} - \frac{R_s^2}{1 + r/R_s}\right)\right]^{1/2} \, . \tag{3.9}$$

The results along the $z = 0$ axis, with typical and comparable values used for the free parameters[*], are shown in Figure 3.3. The rotation curve of the Milky Way is presented in Figure 3.4 for comparison, and shows clearly that the observed values are incompatible with only the visible disk contributing to the gravitational potential, whereas a dark matter halo with a NFW density profile fits the data well.

---

[*]In order to define the total mass in the NFW case we need to cut off the integral, which is done at $5R_s$ which corresponds to a typical value for a spiral galaxy.
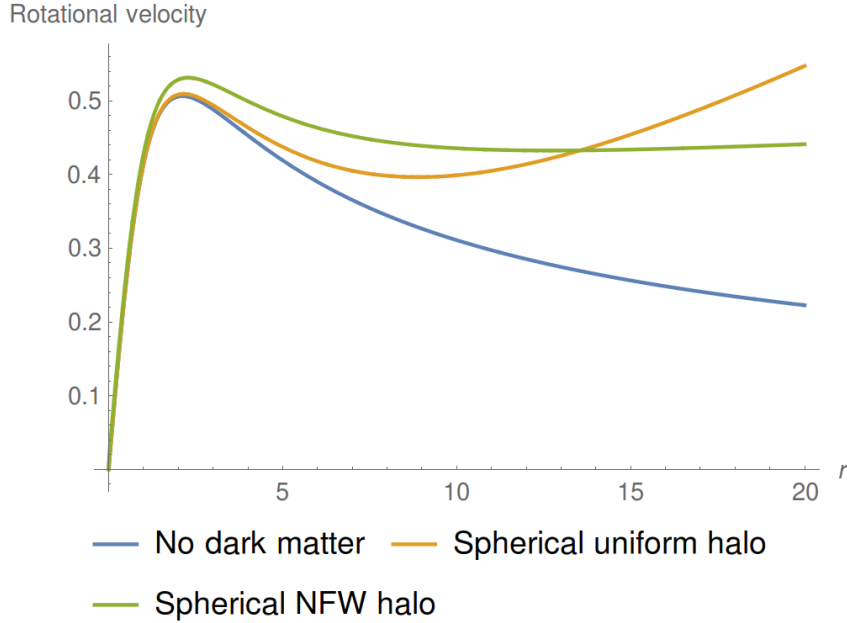
Figure 3.3: Galaxy rotation curves without a dark matter halo, with a uniform spherical dark matter halo, and with a NFW dark matter halo. $M_{\mathrm{DM}}/M_{\mathrm{disk}} = 5$, $a = 1$, $b = 1/2$, $R/a = R_s/a = 20$.

3.2.1.1 Calculating the Relic Density

Building a short length quantum field theory description of dark matter requires us to consider how such a model would generate the astronomical signals outlined at the start of the last section. The first thing to make sure is that it can explain the total dark matter abundance at the current time, $\Omega_d h^2 \approx 0.12$ [83]. Here $\Omega_d = \frac{\rho_d}{\rho_c}$ where ρ_c is the critical density which exactly defines a flat universe, and $h = \frac{H_0}{100 \, \mathrm{km \, s^{-1} \, Mpc^{-1}}} \approx 0.7$ is the dimensionless Hubble constant, where the Hubble constant itself is defined as $H_0 = \frac{\dot{r}}{r}$.

In the ΛCDM paradigm this is assumed to be a thermal relic of a stable particle χ which was frozen out as the universe cooled down: in the early universe the dark matter is in thermal equilibrium with the Standard Model particles f:

$$\chi\bar{\chi} \leftrightarrow f\bar{f}. \tag{3.10}$$

As the temperature falls below the mass of χ it stops being produced and its yield $Y = n_\chi/s$ (where n_χ is the number density of χ and s is the total entropy of
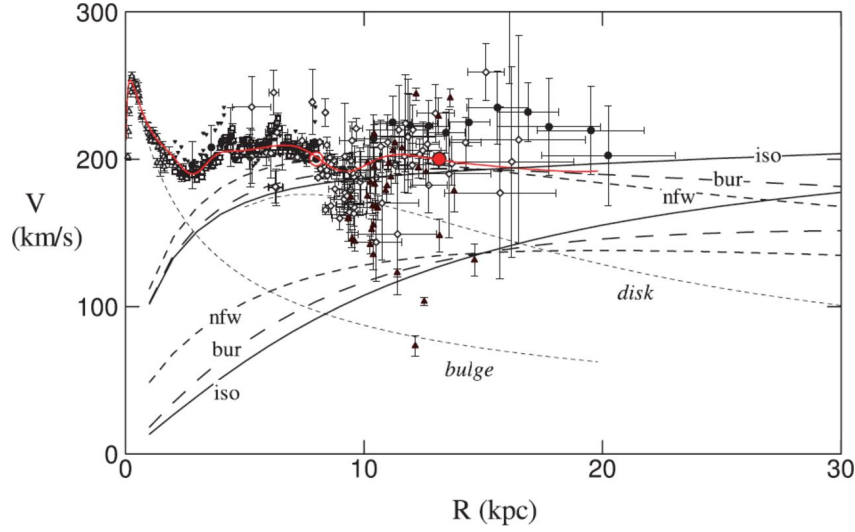
Figure 3.4: Rotation curve of the Milky Way. Taken from [82]. We have ignored the dense core or bulge in our calculations, but for $R > 3$ kpc it is clear that a dark matter halo is required to explain the observed values for the rotational velocity. Note that the iso model here does not correspond to our uniform model.

the universe[*]) starts falling exponentially as a result of one-sided $2 \to 2$ annihilation processes into Standard Model states:

$$\chi\bar{\chi} \to f\bar{f}. \tag{3.11}$$

However at some point n_χ becomes low enough that the annihilation effectively stops since the absolute density is too low for $2 \to 2$ annihilation processes to occur. After this *freeze-out Y* is almost constant and taking $t \to \infty$ corresponds to the relic density today. This kind of out-of-equilibrium behaviour is statistically described by a Boltzmann equation which in terms of our definition of the yield Y and $x = m_\chi/T$ is given by[†]:

$$\frac{dY}{dx} = -\frac{1}{x^2}\frac{s(m_\chi)}{H(m_\chi)}\langle\sigma v\rangle(Y^2 - Y_{eq}^2). \tag{3.12}$$

---

[*]Introduced as a shorthand to normalise for the expansion of the universe.

[†]We will follow Flip Tanedo's notes [84] in the treatment of the Boltzmann equation.

The relevant cosmological quantities are:

$$s(T) = \frac{2\pi^2}{45} g_{*s} T^3 \tag{3.13}$$

$$H(T)^2 = \frac{8\pi}{3} G_N \rho(T) \tag{3.14}$$

$$\rho_R(T) = \frac{\pi^2}{30} g_* T^4 \tag{3.15}$$

$$Y_{eq} = g \left(\frac{m_\chi T}{2\pi}\right)^{3/2} e^{-m_\chi/T} \times \left(\frac{2\pi^2}{45} g_{*s} T^3\right)^{-1} = 0.145 \frac{g}{g_{*s}} x^{3/2} e^{-x}. \tag{3.16}$$

Here we used the non-relativistic expression for the number density n_χ when calculating the equilibrium yield Y_{eq}. We will assume that for the purposes of the freeze-out calculation the universe is radiation-dominated so $\rho \approx \rho_R$. g is the internal number of degrees of freedom for the dark matter particle. g_{*s} and g_* are the effective relativistic degrees of freedom for the entropy and energy density respectively, and are defined as:

$$g = \sum_{\text{bosons}} g_i \left(\frac{T_i}{T}\right)^n + \frac{7}{8} \sum_{\text{fermions}} g_i \left(\frac{T_i}{T}\right)^n, \tag{3.17}$$

where $n = 3$ for g_{*s} and $n = 4$ for g_*. Here T is the temperature of the background plasma which is assumed to be in equilibrium. For $T > 1$ MeV* $g_{*s} = g_*$ holds to a good approximation [85] so they are interchangeable for the temperatures we consider, but we will keep them separate for clarity. They are approximately constant with $g_{*(s)} \approx 100$ above the electroweak scale, below which they start falling.

We can expand the thermally averaged cross section in powers of the velocity:

$$\langle \sigma v \rangle = \langle \sigma v \rangle_0 v^p + \mathcal{O}(v^{p+2}). \tag{3.18}$$

We will assume s-wave annihilation dominates, so $p = 0$. Equation 3.12 is difficult to solve numerically since there are many relevant scales that contribute in the freeze-out region: $Y^2 \approx Y_{eq}^2 \gg Y^2 - Y_{eq}^2 \gg \langle \sigma v \rangle_0$. We therefore multiply through both sides of Equation 3.12 by $\frac{s(m_\chi)}{H(m_\chi)} \langle \sigma v \rangle_0$ to get:

$$\frac{dy}{dx} = -\frac{1}{x^2} \left(y^2 - y_{eq}^2\right), \quad y_{eq} = 0.145 \frac{g}{g_{*s}} \frac{s(m_\chi)}{H(m_\chi)} \langle \sigma v \rangle_0 x^{3/2} e^{-x}. \tag{3.19}$$

This equation should be easier to numerically solve since the relevant scales are now reduced to $y^2 \approx y_{eq}^2 \gg y^2 - y_{eq}^2$. We will choose representative parameter values

---

*This is when neutrinos decouple and we no longer have $T_\nu = T$.
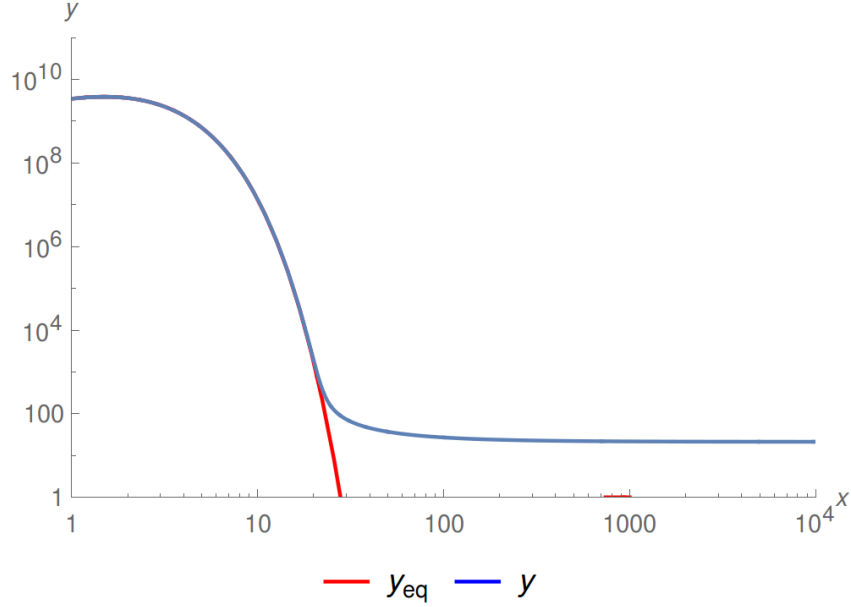
Figure 3.5: The equilibrium scaled yield y_{eq} and the actual scaled yield y as a function of $x = m_\chi/T$.

which ensure freeze-out occurs at $T \sim v$ and approximate $g_{*(s)} = 100$[*], and take $g = 2$ which corresponds to Majorana fermion dark matter. Expanding everything out and plugging in values:

$$y_{eq} = 0.192 \frac{g}{\sqrt{g_*}} \frac{m_\chi}{\sqrt{8\pi G_N}} \langle \sigma v \rangle_0 x^{3/2} e^{-x} = 0.0384 \frac{m_\chi}{\sqrt{8\pi G_N}} \langle \sigma v \rangle_0 x^{3/2} e^{-x} . \quad (3.20)$$

As a boundary condition we use that $y = y_{eq}$ at small x, for example at $x = 1$ (going to smaller x would not be justified since we used the non-relativistic expression for the number density of χ). The remaining free parameters are m_χ which is set to 1 TeV, and $\langle \sigma v \rangle_0$ which we set to 10^{-10} GeV^{-2} = 39 fb, corresponding to typical weak scale values. With these we can numerically solve the Boltzmann equation. The result is plotted in Figure 3.5.

To convert to the relic abundance we use:

$$\rho_d = m_\chi Y_\infty s_0 = m_\chi \frac{s_0}{s(m_\chi)} \frac{H(m_\chi)}{\langle \sigma v \rangle_0} y_\infty . \quad (3.21)$$

___

[*]The solution could be improved by correctly taking the T dependence of $g_{*(s)}$ into account, but this ultimately has a small effect on the final result so we neglect it here.

Here Y_∞ is the yield at large x (or equivalently as $t \to \infty$) and we have converted this to a form where we can use our numerical answer $y_\infty \approx 21.3$. This requires the entropy of the universe today, $s_0 = 2890$ cm^{-3}. Plugging in values again[*]:

$$\Omega_d = \frac{\rho_d}{\rho_c} = \frac{\sqrt{8\pi G_N}\, s_0\, y_\infty}{1.32\,\sqrt{g_*}\,\langle\sigma v\rangle_0} \times \frac{8\pi G_N}{3H_0^2} = \frac{1.84}{h^2}\,. \tag{3.25}$$

So our parameter choices overproduce dark matter by about an order of magnitude since we want $\Omega_d h^2 = 0.12$. In order to get the correct relic abundance we therefore have to increase the thermally averaged interaction cross section $\langle\sigma v\rangle_0$ and recalculate y_∞. In general y_∞ does not depend strongly on $\langle\sigma v\rangle_0$ so to a first order we can approximate the required $\langle\sigma v\rangle_0^*$ by:

$$\frac{\Omega_d}{\Omega_d^*} \propto \frac{\langle\sigma v\rangle_0^*}{\langle\sigma v\rangle_0}\,, \tag{3.26}$$

which means we could reproduce the correct relic abundance if our model predicted a ~ 15 times higher annihilation cross section. Calculations of this type will be used in Chapter 4 in order to estimate the sensitivity of the LHC to the full parameter space of a realistic dark matter model.

Note that a thermal freeze-out is only one of many possible mechanisms proposed for generating a dark matter relic density. It is the most popular one thanks to the feature we've just demonstrated: it gives the correct abundance for roughly weak-scale values for the mass of the dark matter particle m_χ and the annihilation cross section $\langle\sigma v\rangle_0$. This is referred to as the *Weakly Interacting Massive Particle (WIMP) miracle* and has motivated searches for heavy, stable, and neutral particles at both direct detection experiments [86] and colliders [87]. In Chapter 4 we will present a study of a Simplified Dark Matter model, which is a minimalistic extension of the Standard Model incorporating a WIMP dark matter candidate. Other mechanisms include the freeze-in of very weakly interacting massive particles [88], and independent freeze-out in an almost entirely secluded dark sector through $3 \to 2$ interactions, where very weak interactions with the Standard Model are used to transfer the extra heat from these annihilations into the Standard Model sector [89].

---

[*]In GeV these are given by:

$$G_N = 6.707 \times 10^{-39}\ \text{GeV}^{-2} \tag{3.22}$$

$$H_0 = 2.131 \times 10^{-42}\ \text{GeV}\ h \tag{3.23}$$

$$s_0 = 2890 \times (1.98 \times 10^{-14}\ \text{GeV})^3 \tag{3.24}$$

3.2.1.2   Other Large Scale Constraints

Another strong constraint on the nature of dark matter comes from observations of the the current cosmic structure. In particular it is well-known that a strictly top-down model of structure formation is disfavored by experiment, see Figure 3.6. This rules out hot dark matter models where the dark matter is relativistic and forms large structures first, before eventually forming smaller scale structure. Numerical simulations show that this top-down structure formation creates a cutoff in the density fluctuations at shorter correlation lengths which is not observed. Cold and warm dark matter models, where none or only a fraction of the dark matter is relativistic, instead produce bottom-up structure formation, where small scale structures are created first and later cluster into larger scale structures. This leads to a smoother curve of density fluctuations and no cutoff at smaller correlation lengths, in agreement with observations [90].

The relic abundance and bottom-up structure formation are only two of many large scale observations that a quantum field theory description of dark matter should address. However from a practical perspective they are often the most useful ones, since many of the other observations come with considerable caveats attached: ΛCDM is for example known to have many apparent issues when comparing state-of-the-art numerical simulations with modern experimental observations, including the core vs cusp [92], too-big-to-fail [93], missing satellite [94] and Tully-Fisher Galaxy Halo [95–97] problems. Whether these are caused by the limited resolution of current numerical simulations, a local statistical fluctuation in the region of the universe we are able to observe, or are genuine physical effects is difficult to ascertain. However as constraints on WIMPs of the type we discussed in the last section have become stronger, these failures of ΛCDM can be used to provide hints for new directions to explore. In particular all of the afore-mentioned issues could be ameliorated by self-interactions among the dark matter particles [98]. In self-interacting DM scenarios an energy transfer from the outer hotter region of the halo to the central colder region can produce a core structure in agreement with current observations. In addition, the number of Milky Way satellite galaxies is significantly reduced. A search strategy for specific signatures of such self-interacting dark matter at the LHC and future hadron colliders is investigated in Chapter 5.
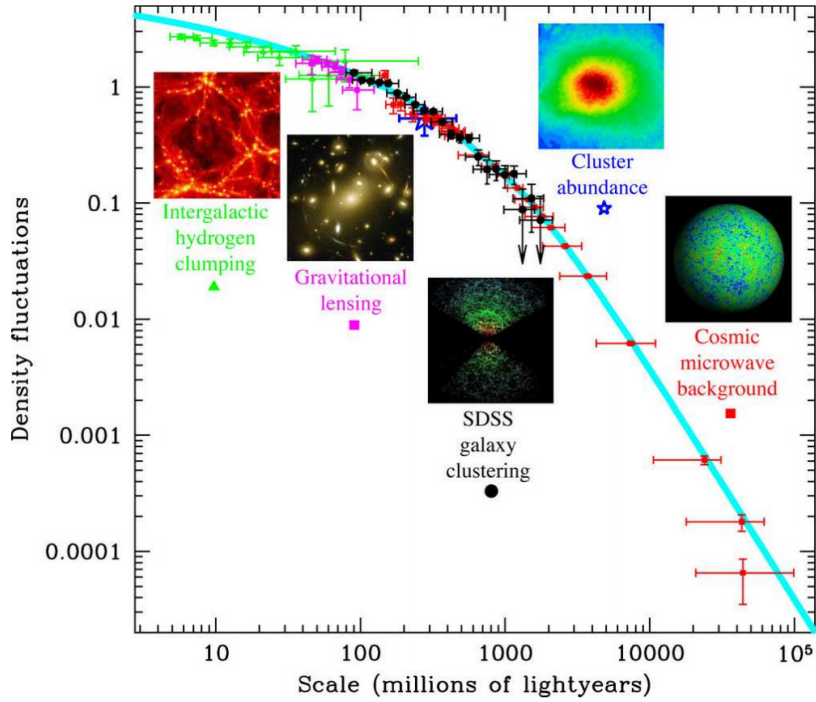
Figure 3.6: Density fluctuations of the universe as a function of correlation length as measured by different experiments [91]. The right side of the plot corresponds to long-length, pre-galaxy formation fluctuations, whereas left side corresponds to increasingly short-length fluctuations. The blue line is a ΛCDM fit which strongly favours cold or warm dark matter with bottom-up structure formation, as hot dark matter would result in a cutoff in the short-length correlations due to the top-down structure formation it predicts.

3.3 Statistics in searches for Beyond Standard Model physics

Since we will be interested in making statements about the (non-)existence of physics beyond the Standard Model, we have to define a way to quantify agreement or disagreement with a model hypothesis. We will in general employ the Modified Frequentist confidence level CL_s as outlined in [99], using a Poissonian likelihood ratio as our test statistic. Using binned events:

$$X = \prod_i^{\text{bins}} \frac{\text{Poisson}(d_i|s_i + b_i)}{\text{Poisson}(d_i|b_i)} = \prod_i^{\text{bins}} e^{-\mu s_i} \left(1 + \frac{\mu s_i}{b_i}\right)^{d_i} \qquad (3.27)$$

where s_i, b_i and d_i are the expected number of signal and background, and observed number of events for each bin respectively. Using the likelihood ratio we can compute the observed value of the test statistic X_{obs} by using the actual observed number of events for d_i (when calculating projections we can use $d_i = b_i$ instead), and then calculate the probabilities of observing a smaller test statistic X for the background and background+signal models by Monte Carlo sampling the predicted distributions of d_i:

$$CL_{s+b} = P_{s+b}\left(X < X_{\mathrm{obs}}\right) , \tag{3.28}$$

$$CL_b = P_b\left(X < X_{\mathrm{obs}}\right) , \tag{3.29}$$

$$CL_s = CL_{s+b}/CL_b . \tag{3.30}$$

A value of $CL_s < 0.05$ is interpreted as excluding the corresponding value of μ at 95% confidence level [100]. This setup is similar to those used by the LHC experiments: the biggest differences will be introduced when considering systematic uncertainties in distributions with more than one bin. Without detailed understanding of the experiments it is impossible to determine the correct correlation matrix.

For discussions later in Chapter 7 it is useful to clarify the relation between this simple statistical setup, the Fisher information of the full available phase space, and machine learning algorithms often in use by the experiments[*]. We will denote the true parameter values of our model g, and measurements of these parameters $\hat{g}$. Assuming our measurements are not perfect, $\hat{g}$ will follow a probability distribution $f(\hat{g}|g)$. If our measurements are unbiased, the expectation value of a parameter value $\bar{g}_i$ is equal to its true value:

$$\bar{g}_i \equiv E[\hat{g}_i|g] = g_i . \tag{3.31}$$

The precision with which we can relate our measurements to the true parameters is encoded in the covariance matrix:

$$C_{ij}(g) \equiv E[(\hat{g}_i - \bar{g}_i)(\hat{g}_j - \bar{g}_j)|g] . \tag{3.32}$$

In our case we will extract the $f(\hat{g}|g)$ relation between true parameter values and measured values using Monte Carlo simulations of both the theory model and the

---

[*]This section is partly based on [101] where we borrow our notation from.

detector response. If we can calculate it exactly, we can define the Fisher information matrix:

$$I_{ij}(g) \equiv -E\left[\frac{\partial^2 \log f(\hat{g}|g)}{\partial g_i \partial g_j}\bigg|g\right]. \tag{3.33}$$

The Cramér-Rao [102] bound states that the values of the covariance matrix in Equation 3.32 are bounded from below by the inverse Fisher information:

$$C_{ij} \geq (I^{-1})_{ij}. \tag{3.34}$$

That is, if we can calculate the Fisher information, we are guaranteed to be able to access all of the available information in the measurements made. The Fisher information is invariant under reparameterisations of $\hat{g}$ [101], so since the LHC experiments typically make measurements of physical observables x and bin these in phase space points x_i, we rewrite $f(\hat{g}|g)$:

$$f(\hat{g}|g) \rightarrow f(x|g) = \text{Poisson}(\hat{\sigma}|\sigma(g)) \prod_i f^{(1)}(x_i|g). \tag{3.35}$$

Here we have factorised out the total normalisation $\sigma(g)$ and the total observed event rate $\hat{\sigma}$ from the single event normalised phase space probability density $f^{(1)}(x_i|g)$. $\sigma(g)$ is of course given by the total event rate from a Monte Carlo simulation, and $f^{(1)}(x_i|g)$ contains all of the shape information from the same simulation. To a good approximation the Fisher information contained in a distribution can be approximated with Poissonian likelihoods like we do in this thesis: it is only terms in $f^{(1)}(x_i|g)$ which are nonlinear in g which break the equivalence. To be explicit, for a bin r with an expected number of events $\sigma_r(g)$ and an observed number $\hat{\sigma}_r$, the Poisson likelihood is:

$$L_r(g) = \text{Poisson}(\hat{\sigma}_r|\sigma_r(g)) = \sigma_r(g)^{\hat{\sigma}_r} e^{-\sigma_r(g)}. \tag{3.36}$$

The total likelihood for several bins is then given by:

$$L_{\text{tot}}(g) = \prod_r L_r = L_{\text{norm}}(g) L_{\text{shape}}(g),$$

$$L_{\text{norm}}(g) = \sigma(g)^{\hat{\sigma}} e^{-\sigma(g)}, \quad L_{\text{shape}}(g) = \prod_r \left(\frac{\sigma_r(g)}{\sigma(g)}\right)^{\hat{\sigma}_r} \tag{3.37}$$
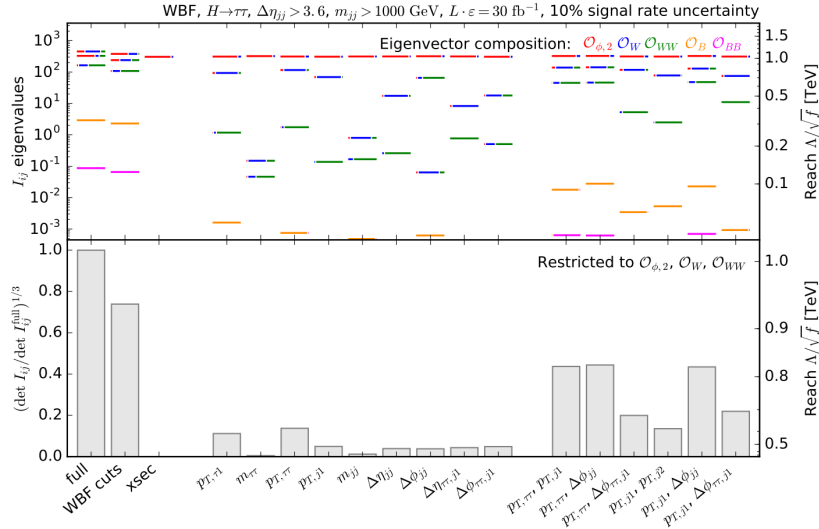
Figure 3.7: Fisher information in weak boson fusion Higgs production for a number of effective operator extensions to the Standard Model with various selections applied to the phase space and for various combinations of observables. Taken from [101].

where $\hat{\sigma}$ is the total number of observed events. This shows that a Poissonian likelihood factorises in the same way into a term which contains information about the total normalisation and is identical to the term which we derived from the general phase-space probability distribution, and another term which contains all shape-related information [103].

If we only measure the total cross section in our experiment, the shape information is trivial and the Fisher information is effectively given by differentiating the cross section with respect to the theory parameters. In general, the act of binning the continuous underlying distribution will always reduce or at best keep the Fisher information constant. Similarly, the act of selecting only specific phase space regions (applying *cuts*) will *always* reduce the amount of information in the distributions. This is demonstrated in Figure 3.7.

Having established the statistical framework in which we consider LHC analyses, we might wonder why the experiments (and phenomenologists, as will become clear in this thesis) apply selections on their data before performing limit setting, if they are guaranteed to lose information when doing so. Triggers are, of course, easy to understand: it is simply impossible to store all collision data, so the phase space needs to be cut down for practical purposes. However beyond this the situation is more subtle. One, it would still be computationally prohibitive to calculate $f(x|g)$

from first principles with only trigger-level data in most cases. Two, when using such an inclusive phase space we have to rely on theoretical extrapolations to describe for example the parts of phase space which are described by non-perturbative physics, and experimental extrapolations to describe the detector response for far corners of observables. It is arguably the second point which makes an inclusive approach impossible: limits calculated in such a way would not be reliable unless we could be certain the models used to generate the physics and detector response distributions were completely valid (or at least provided reliable errors) for the entire, incredibly high-dimensional phase space.

However the first point is also important. Techniques for extracting information from very high-dimensional distributions in a computationally efficient manner have been developed over the recent decades, with neural networks and boosted decision trees having seen widespread use also by particle physics experiments. Since these techniques operate on the continuous phase space they can in theory retain the full Fisher information of the considered observables. The well-known Universal Approximation Theorem for neural networks [104, 105] states that a single-hidden-layer network can represent a general degree d polynomial in a compact $\mathbb{R}^n$ space as long as it has $\mathcal{O}(n^d)$ hidden neurons. This means that an infinite-sized network with an infinite amount of training data (under otherwise reasonable assumptions about activation functions) will always be able to represent the optimal mapping of $f^{(1)}(x|g) \to f^{(1)}(o|g)$, where o is a (potentially one-dimensional) output which encodes all of the shape information in the full, high-dimensional x distribution*. There are of course many practical problems which make this very difficult to achieve in practice, such as local minima in the weight distribution which can 'trap' the training in a suboptimal position, overfitting on limited data sets, and questions of if (and if so, how) a network is ever guaranteed to be able to find this optimal configuration. It has recently been proven [106] that a one-hidden-layer network with complex weights using standard gradient descent training will always be able to find the optimal configuration, and that there are no robust local minima in this setup. Such results are mainly of theoretical interest and have little relevance to the practical application of neural networks and similar algorithms. However, even without a complete understanding of the underlying mechanics of neural networks their real-world performance has shown them to be very useful for the types of problems discussed in this section. In practice these methods are already used by

---

*In practice all distributions used in a particle physics context will be compact by design.

the experiments to access much more of the full shape information $f^{(1)}(x|g)$ than they could using simple cut-and-count experiments.

These techniques still run into the same issues as mentioned above if considering observables which we are not confident are well-described by our theoretical and experimental models, but do at least provide a computationally feasible way to make use of shape information from a reasonable number of well-modelled observables.

3.4   Beyond the Standard Model physics at the LHC

Having thus introduced the Standard Model and some of its problems, the remainder of this thesis will be devoted to specific studies into the phenomenology of extensions which could solve some of these shortcomings. The following two chapters will be concerned with searches for a microscopic model of dark matter at the LHC:

- In Chapter 4 we will study the phenomenology of a so-called Simplified Model of dark matter, which can be viewed as a minimalistic extension of the Standard Model introduced only to explain dark matter.

- In Chapter 5 we will calculate the RGEs for a mostly secluded dark sector extension, and investigate if quantum corrections can be used to study the internal structure of such a dark sector at a hadron collider.

Having considered ways to introduce dark matter extensions to the Standard Model, we will return to the hierarchy problem and the nature of electroweak symmetry breaking more generally in Chapters 6 and 7:

- In Chapter 6 we will study the phenomenology of di-Higgs + 2 jet production, and show that a future measurement can be used to constrain the trilinear Higgs self-coupling, quartic $V^\dagger V h h$ interactions, and $\mathcal{CP}$ violating effects in the Higgs sector.

- In Chapter 7 we will show how a measurement of the top polarisation in resonant top pair production can be used to improve sensitivity to generic new physics in the top sector, using a Randall-Sundrum model as a benchmark.

Simplified Dark Matter Model Phenomenology

4.1 Attribution Notice

This chapter is based on results first presented in [1] which I wrote together with Dr. Thomas Jacques. I performed all of the calculations except for the relic density scan and created all of the original figures.

Contents

4.2 Summary

Run II of the LHC has seen the experiments move towards the adoption of so-called Simplified Dark Matter models in order to set stronger and more robust

constraints on the dark sector [107, 108]. In these models we introduce both a stable dark matter particle χ and a mediating particle, which together can be used to generate the observed relic abundance in the thermal freeze-out paradigm. However the generality of these models necessarily introduces a large number of a priori free parameters that need to be considered and makes general scans difficult to perform. In this chapter we will make use of the monojet + missing energy channel to constrain a representative simplified model with the dark matter coupling to an axial-vector Z' over the full parameter space, and investigate the validity of a narrow width approximation to greatly reduce the computational demands of doing so. We validate our analysis and the approximation using an early ATLAS 8 TeV dataset, provide limits using the full ATLAS 8 TeV dataset, and provide predictions for limits that can be set with 20 fb^{-1} of 14 TeV data. Our technique provides a broad benchmark for comparing constraints on simplified models, which we demonstrate by comparing to actual limits on our model from the recently published ATLAS 13 TeV monojet search, which agree very well with our 14 TeV predictions and suggest a move towards constraining the full parameter space is computationally feasible using a narrow width approximation.

4.3   Motivating Simplified Dark Matter Models

Run I of the LHC saw EFTs become a popular framework with which to constrain the dark sector [109]. In the simplest cases, the dark couplings and mediator masses can be combined into a single effective energy scale, Λ, leaving this and the dark matter mass, m_χ, as the only free parameters for each effective operator. EFT constraints have the advantage of being relatively model-independent, allowing constraints to be placed across a broad range of models and parameters. In addition they facilitate an easy comparison with direct detection experiments via the shared energy scale Λ. However it is clear that EFTs must be used with extreme care at LHC energies, where the typical momentum transfer is large enough that the momentum expansion used in the construction of the EFT can not be assumed to be valid. At these energies and luminosities the energy carried by the mediator can be larger than the mediator mass, violating the expansion, except in the case of large mediator masses or for dark sector couplings approaching the perturbativity limit [110]. Depending on the mass and width of the mediator, this can lead to EFT constraints that are either stronger or weaker than the constraints would be on a more complete model, reducing their

utility and making their validity questionable.

One solution is to rescale EFT constraints by truncating the simulated signal such that only events for which the EFT approximation are valid are used to derive constraints [111–113]. This weakens constraints but at the same time makes them substantially more robust, which is critical when considering bounds on Beyond Standard Model parameters. Whilst this technique has the advantage of maintaining some of the elegance of EFTs, it also has the serious disadvantage that it does not make full use of all potential signal events available in a more complete model and so does not address the region of parameter space where EFT constraints are too weak. To constrain this region we need to consider models where the mediator can be resolved. On the other hand, the parameter space of full, well-motivated models such as supersymmetry [114] or extra dimensions [115] is broad, and by focusing solely on such models we run the risk of missing more generic signatures of the dark sector.

Hence, the usage of simplified models where the model is expanded to include an explicit mediator has become the accepted practice [107, 108, 116–119]. Simplified models have the advantage of a relatively small set of free parameters, and do not encounter the same validity problems as EFTs. However the parameter space is still larger than for EFTs, which often necessitates arbitrary choices for one or more parameters in order to constrain the remaining free parameters. Here we will instead leave the dark matter mass, mediator mass, and coupling strengths all as free parameters which we scan over and constrain in contours. We will use publicly available ATLAS constraints on the monojet + missing energy channel to constrain a simplified model with dark matter coupling to the standard model via exchange of an axial-vector Z' mediator, and show that the use of a narrow width approximation makes a scan of the full parameter space feasible.

In Section 4.4, we outline the choice of simplified model that we will be constraining, and discuss modelling issues surrounding the width of the vector mediator. In Section 4.5, we describe our technique for converting the model-independent constraints on the visible monojet cross section into constraints on this simplified model. In Section 4.7 we validate the constraints we get from our analysis against published ATLAS results for an EFT model and in Section 4.8 we validate the cross section reweighting with a narrow width approximation. In 4.9 and 4.10 we present our results. Our 14 TeV predictions are compared to recently published ATLAS 13 TeV results in Section 4.11. We conclude in Section 4.12.

4.4 Model

We consider a widely-used benchmark simplified model where Dirac DM interacts with the SM via a Z'-type mediator. This is described by the following Lagrangian interaction term:

$$\mathcal{L} = -\sum_f Z'_\mu [\bar{q}\gamma^\mu (g_q^V - g_q^A \gamma_5)q] - Z'_\mu \ [\bar{\chi}\gamma^\mu (g_\chi^V - g_\chi^A \gamma_5)\chi], \qquad (4.1)$$

where g_i^V, g_i^A are respectively the vector and axial-vector coupling strengths between the mediator and quarks $(i = q)$ and DM $(i = \chi)$. The LHC is relatively insensitive to the mixture of Vector/Axial-vector couplings [113], however this ratio has a large effect on the sensitivity of direct detection experiments to this model. A vector coupling induces a spin-independent (SI) WIMP-nucleon scattering rate, while an axial-vector coupling induces a spin-dependent (SD) rate [120]. Current bounds on SI interactions are much stronger than those on SD, to the point where direct detection constraints are generally stronger than LHC constraints on models with pure vector couplings, and vice-versa for pure axial-vector couplings, as seen in e.g. [121]. For this reason we consider a pure axial-vector coupling, setting $g_\chi^V = g_q^V = 0$, and defining $g_\chi \equiv g_\chi^A$, $g_q \equiv g_q^A$.* For simplicity, as is common, we assume that the quark-mediator coupling g_q is the same for each species of quark. In order to keep the model perturbative we restrict couplings such that $\Gamma_{\text{OS}}/M < 1$ where M is the Z' mass and Γ_{OS} is the on-shell width of the Z'.

---

*This choice of couplings to the quarks will in general not respect the gauge invariance of the Standard Model quark Yukawa couplings. This can be fixed by setting some vector couplings non-zero and will lead to larger cross sections, so our choice can be considered conservative. More crucially, gauge invariance of the lepton Yukawa coupling also requires that the Z' couples to leptons, which introduces strong constraints from di-lepton searches [122]. This can be fixed by enlarging the Standard Model Higgs sector with for a example a second Higgs doublet, as in Two Higgs Doublet Models [67]. Using purely vector couplings to quarks would avoid these issues entirely while keeping the LHC phenomenology similar. Perturbative unitarity of the process $\bar{\chi}\chi \to Z'_L Z'_L$ also requires the introduction of a new Higgs state which is not too much heavier than the Z' [122] which we assume we can ignore in our analysis. In this sense the model should not be viewed as UV-complete but rather as a well-defined limit of a number of possible UV-completions, as customary in the Simplified Model paradigm.

For the model we consider, Γ_{OS} is at tree level given by:

$$\Gamma(k^2) = \frac{g_\chi^2 M (1 - 4m_\chi^2/k^2)^{3/2}}{12\pi} \Theta(k^2 - 4m_\chi^2)$$
$$+ \sum_q \frac{g_q^2 M (1 - 4m_q^2/k^2)^{3/2}}{4\pi} \Theta(k^2 - 4m_q^2). \quad (4.2)$$

The on-shell width Γ_{OS} is then given by $\Gamma_{\text{OS}} = \Gamma(M^2)$. With the assumption that g_q is equal for each flavor of quark this width can become very large, for example rising above $\Gamma_{\text{OS}} \sim M$ at $g_q = g_\chi \approx 1.45$ when $g_q = g_\chi$. This width assumes no additional decay channels aside from quarks and DM, however it is conceivable that the mediator could decay to standard model leptons or additional dark sector particles. Given that the the structure of a possible dark sector is unknown and that couplings to leptons are more appropriately constrained by searches for dilepton resonances [123, 124], we confine ourselves to the more 'minimal' model where the mediator couples only to quarks and DM.

In the event generation we will use a Breit-Wigner form for the Z' propagator with constant on-shell widths as introduced in Equation 2.61:

$$\Delta_{Z'}(k^2, M, \Gamma_{\text{OS}}) \propto \frac{1}{k^2 - M^2 + iM\Gamma_{\text{OS}}} . \quad (4.3)$$

This approximation will begin to break down when we no longer can rely on $\Gamma_{\text{OS}} \ll M$ [125, 126]: it amounts to a replacement of $k^2\Gamma(k^2)/M \rightarrow \Gamma_{\text{OS}}M$ in the imaginary part of the resummed self-energy, which clearly can only be motivated for small widths for which the cross section is dominated by $k^2 \sim M^2$. Additionally we identify $\Gamma(k^2)$ as its on-shell value Γ_{OS}; this is again only justified when $\Gamma_{\text{OS}}/M \ll 1$. A consistent treatment of our model in the part of parameter space where we can't assume that $\Gamma_{\text{OS}}/M \ll 1$ hence requires a more careful consideration of the propagator than we employ in our simulation, and we therefore use cross section reweighting for the parts of parameter space where we are not conservative to correct for this. In Figure 4.1 we show a comparison of line shapes for various values of Γ_{OS}/M with fixed M, m_χ using the naive Breit-Wigner shape we employ and a fully kinetic propagator, which reflects that our simulation will become increasingly poor as Γ_{OS}/M increases.

We have estimated the ratio of final cross sections using a Breit-Wigner propagator and a kinetic one by convolving them with PDFs and requiring that we can produce a $\chi\bar{\chi}$ pair on-shell and found that within this approximation the choice of propagator makes for modest differences for most of our parameter space, with large
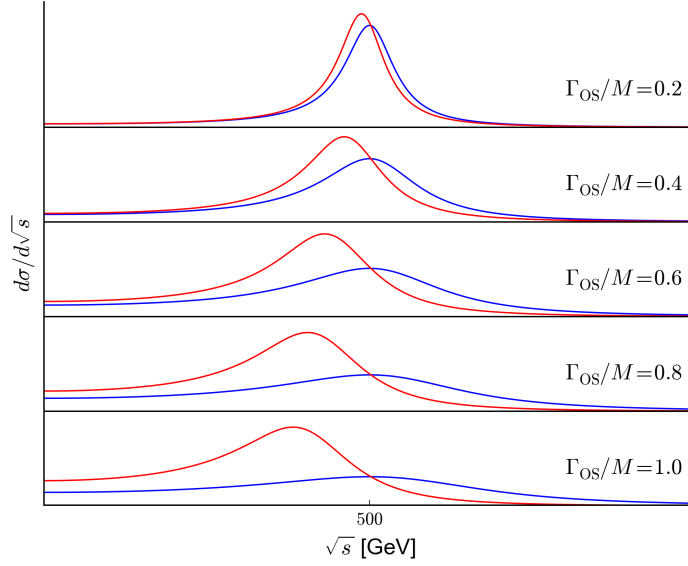
Figure 4.1: Line shapes for our Breit-Wigner propagator 4.3 (blue) and a kinetic propagator with the replacement $\Gamma_{\mathrm{OS}}M \to k^2\Gamma(k^2)/M$ in the imaginary part of the self-energy (red) for various values of Γ_{OS}/M. The normalisation is arbitrary and differs between the plots to allow for a straightforward shape comparison, and both axes are linear. $M = 500$ GeV and $m_\chi = 100$ GeV which corresponds to a typical parameter space point.

effects in specific regions: for $m_\chi \ll M$ and $\Gamma_{\mathrm{OS}}/M \gtrsim 0.5$ our propagator gives a cross section that can be as much as 50% too low compared to a kinetic propagator. In the other extreme end where $m_\chi \gtrsim M$ and $\Gamma_{\mathrm{OS}}/M \gtrsim 0.5$ we see an opposite effect where our cross section can be several times too large. Since our propagator in this region is not conservative we will reweight the visible cross section we get at the end of our simulation whenever $\sigma_{\mathrm{Breit-Wigner}} > \sigma_{\mathrm{kinetic}}$ using the ratio of the two (where these cross sections are estimated as described above) to allow our limits to remain robust. In general we do not set strong limits in this region in the first place, so the effect of this reweighting procedure is in the end limited.

4.5   Reinterpreting Monojet Constraints

Our signal prediction is obtained by implementing the model in the FEYNRULES [127] and MADGRAPH5_AMC@NLO 2.1.2 [128] framework to generate leading

order (LO) parton level events using the NNPDF2.3 LO PDFs [129]. These are matched to PYTHIA 8.185 [130] using the MLM algorithm with a matching scale of 80 GeV* for showering and hadronisation using tune 4C. We generate $\chi\bar{\chi} + 0$, 1, and 2 jets in the matrix element before matching to the parton shower. We use the default MADEVENT factorization and renormalisation scales ($\mu_{R,F}$) which in this case both are approximately the transverse mass of the $\chi\bar{\chi}$ system. Our approach only makes leading order + parton shower (LOPS) predictions compared to the next-to-leading order + parton shower (NLOPS) predictions used in a similar study of CMS results [131] in [108], which means we suffer from larger theoretical uncertainty due to scale dependencies which we can attempt to estimate by varying our choice of $\mu_{R,F}$ by a factor of two. This shows a weak dependence on the choice of scales of $^{+10\%}_{-5\%}$ for a few representative choices of M, m_χ which is clearly not a realistic estimate of the uncertainty: previous studies [132–134] with other choices of scales have found fixed-order NLO corrections ranging from $\sim 20 - 40\%$. We do however note that based on the results in [134], we expect NLO corrections to ultimately be modest after matching to a parton shower and applying the ATLAS monojet analysis cuts since the parton shower dilutes differences, helped by the loose cuts on additional jets. As such they should have a limited impact on our quantitative results and be negligible for qualitative results.

We analyze the generated events using the ATOM framework [135, 136] based on Rivet [137]. We first divide the final state into topological clusters and find jets with the anti-k_t algorithm [63] using $R = 0.4$ in FASTJET [138]. We then perform a smearing of the p_T of these jets based on typical values for the ATLAS detector, leaving the $E_\mathrm{T}^\mathrm{miss}$ unsmeared†. Our procedure has been validated by recreating the limits set on an EFT operator by ATLAS and the results of this validation is given in Section 4.7.

Some past constraints on simplified models have used a fixed benchmark width. In this case, the cross section is only sensitive to the *product* $g_\chi \cdot g_q$ and not to the couplings individually; Further, this easily factorises out,

$$d\sigma(g_\chi, g_q) = (g_\chi \cdot g_q)^2 d\sigma(g_\chi = g_q = 1), \qquad (4.4)$$

---

*Chosen to correspond to the matching scale used in the original ATLAS EFT interpretation which we use to validate our method.

†We are not aware of any ATLAS $E_\mathrm{T}^\mathrm{miss}$ smearing values which could be unambiguously applied to our case, based on the results in [139] we expect the plateau to have been reached for all our signal regions however.

which simplifies the analysis since the coupling affects only the magnitude of the signal, not the spectral shape. Including the physical width complicates things, since now both the magnitude and signal spectrum have a dependence on both $g_\chi \cdot g_q$ and g_q/g_χ. This results in necessary complications if one wants to present 2D contour limits on $g_\chi \cdot g_q$ when the width is known. However it is possible to make an approximation for the cross section in the resonant region using the narrow width approximation as $\sigma \propto g_q^2 g_\chi^2/\Gamma_{\text{OS}}$ (for fixed M, m_χ) and $\sigma \propto g_q^2 g_\chi^2$ for the off-shell region, which allows us to set limits on $g_\chi \cdot g_q$ while avoiding a scan in this dimension, leaving only $M - m_\chi$ as free parameters for any given choice of g_q/g_χ. The approximation follows from integrating over the Breit-Wigner propagator and making the substitution $\tan\theta = \frac{m_*^2 - M^2}{\Gamma_{\text{OS}}M}$, $\theta_{\max} \approx \pi/2$, $\theta_{\min} \approx -\pi/2$:

$$
\begin{aligned}
\int \frac{dm_*^2}{(m_*^2 - M^2)^2 + \Gamma_{\text{OS}}^2 M^2} =& \frac{1}{\Gamma_{\text{OS}}^2 M^2} \int \frac{dm_*^2}{\frac{(m_*^2-M^2)^2}{\Gamma_{\text{OS}}^2 M^2} + 1} \\
=& \frac{\Gamma_{\text{OS}} M}{\Gamma_{\text{OS}}^2 M^2} \int \frac{d\tan\theta}{\tan^2\theta + 1} \\
=& \frac{1}{\Gamma_{\text{OS}} M} \int \frac{d\theta \sec^2\theta}{\tan^2\theta + 1} = \frac{\pi}{\Gamma_{\text{OS}} M}
\end{aligned}
\tag{4.5}
$$

This approximation should work well for the part of parameter space where $\Gamma_{\text{OS}} \ll M$ [140, 141], and we present a full study of this approximation (including the effect of the mediator shape reweighting) in Section 4.8 which further motivates restricting the parameter space to $\Gamma_{\text{OS}}/M < 0.5$.

4.6   Including Relic Density Constraints

We also include relic density constraints by finding out which parts of our parameter space would result in a larger relic abundance than observed experimentally. Rather than using the approximations introduced in Section 3.2.1.1 we use the well-known formalism described in, for example, Refs. [142, 143] to constrain $\langle\sigma v\rangle_0$ by simultaneously solving an expression for the freeze-out temperature as a function of $\langle\sigma v\rangle_0$, and the relic abundance as a function of both $\langle\sigma v\rangle_0$ and the freeze-out temperature. This technique ceases to be valid when the Breit-Wigner expression for the width breaks down. We will allow for values up to $\Gamma_{\text{OS}}/M = 1$ when performing the relic density scan, so some care needs to be taken when interpreting relic density contours for large couplings. We use the annihilation rate to quarks for our model as calculated in [144].

Signal Region	SR1	SR2	SR3	SR4
p_T^{j1} & $E_T^{\text{miss}} >$ [GeV]	120	220	350	500
ATLAS $\sigma_{\text{vis}}^{95\% \text{ CL}}$ [fb]	2800	160	50	20

Table 4.1: Signal region definitions in the 10.5 fb^{-1} 8 TeV analysis and ATLAS 95 % CL exclusion limits on the visible cross section from BSM contributions.

When presenting later results in Figures 4.5 and 4.7 we use the relic density calculation to define a contour, within which the LHC constraint on the coupling is stronger than the coupling which would give thermal relic DM. For regions inside this line the coupling strength is constrained to be less than the coupling which gives the correct relic density. Hence, the annihilation rate is smaller than required, and the relic density will naively be too large. For DM to lie in this region, either the thermal relic scenario must break down, or the DM annihilates via additional channels not considered here.

4.7 Validation of Procedure using EFT Limits

We use the ATLAS monojet analysis for 10.5 fb^{-1} of 8 TeV data [145] to validate our procedure and approximations, so we apply the following cuts: We require at most two jets with $p_T > 30$ GeV and $|\eta| < 4.5$, with $|\eta^{j1}| < 2$ and $\Delta\phi(j2, E_T^{\text{miss}}) > 0.5$ where $j1$ and $j2$ are the leading and subleading jet respectively. We define four signal regions based on p_T^{j1} and E_T^{miss} as outlined in Table 4.1.

Our overall limit-setting procedure has been validated by recreating the ATLAS limits set on Λ for the D8 EFT operator which corresponds to our simplified model with the mediator integrated out. A comparison for SR3 is presented in Table 4.2. We consistently overestimate the limit by a few percent which reflects the less advanced nature of our detector simulation, however the agreement is good enough for our purposes as we have sub-2% differences for m_χ values which are relevant for us. Note that we only perform the comparison for SR3 as it usually is the most discerning signal region and the only one for which ATLAS results are reported, however we assume the results are similar for the other signal regions. Similarly we assume this agreement carries over to our analyses of the full 8 TeV dataset and our 14 TeV predictions.

m_χ [GeV]	ATLAS 95% CL on Λ [GeV]	Our 95% CL on Λ [GeV]	Difference [%]
≤ 80	687	700	$+1.9$
400	515	525	$+1.9$
1000	240	250	$+4.2$

Table 4.2: Comparison of limits set on the D8 EFT operator by ATLAS [145] and us using only SR3.

Signal Region	SR1	SR2	SR3	SR4	SR5	SR6	SR7	SR8	SR9
$E_{\mathrm{T}}^{\mathrm{miss}}$ & $2 \cdot p_T^{j1} >$ [GeV]	150	200	250	300	350	400	500	600	700
ATLAS $\sigma_{\mathrm{vis}}^{90\% \ \mathrm{CL}}$ [fb]	599	158	74	38	17	10	6.0	3.2	2.9

Table 4.3: Signal region definitions in the full dataset 8 TeV analysis and 90 % CL exclusion limits on the visible cross section from BSM contributions.

4.8 Validation of Cross Section Reweighting

Our limits set using results from [145] using interpolation in $M - m_\chi - g_\chi \cdot g_q$ are presented in Figure 4.2, limits set using the narrow width cross section approximation are presented in Figure 4.3, and the ratios of the limits set in the two cases are presented in Figure 4.4. To visualise the breakdown of our approximations we extend the limit of our parameter space to $\Gamma_{\mathrm{OS}}/M < 1$.

Values of $g_q/g_\chi > 1$ are hardly probed at all by monojet searches as evident from our results for $g_q/g_\chi = 2$: such models are much better constrained by dijet searches which motivates not including these in our main study.

4.9 20.3 fb^{-1} 8 TeV Limits

We make use of 90% C.L. limits set using the full ATLAS 8 TeV dataset [113] for our definite 8 TeV study as the ATLAS analysis uses selection criteria which are better suited towards events with several jets than the full 8 TeV dataset analysis by CMS [146]. The analysis defines signal regions based on $E_{\mathrm{T}}^{\mathrm{miss}}$ and initially only requires the leading jet $p_T^{j1} > 120$ GeV with the additional requirement that $2 \cdot p_T^{j1} > E_{\mathrm{T}}^{\mathrm{miss}}$ for the harder signal regions, and does not veto events due to additional jets as long as $\Delta\phi(\mathrm{jet}, E_{\mathrm{T}}^{\mathrm{miss}}) > 1.0$. The signal regions are given in Table 4.3.
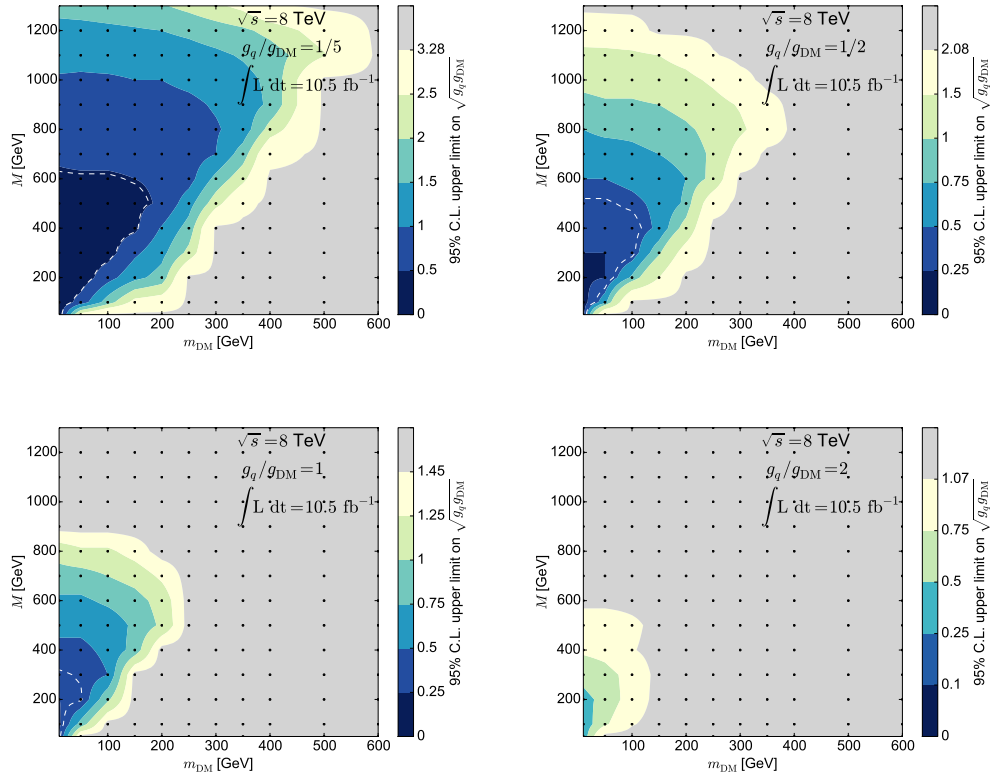
Figure 4.2: Our results using interpolation in $M - m_\chi - g_\chi \cdot g_q$ space. The dashed white line shows where $\Gamma_{\mathrm{OS}}/M = 0.05$. The black dots are interpolation knots in $M - m_\chi$ space. See the text for further details. Note $g_{\mathrm{DM}} = g_\chi$, $m_{\mathrm{DM}} = m_\chi$ in our notation.

4.9.1 Discussion of constraints

The results of our full 8 TeV scan are shown in Figure 4.5. We see that we can exclude mediator masses up to ~ 1.3 TeV for $g_q = g_\chi = 1$ and ~ 0.9 TeV for $g_q = g_\chi = 0.5$ at 90% C.L. Lower g_q/g_χ values are relatively well-constrained by monojet searches as expected due to resonant enhancement of the cross section. Additionally because g_q is small, dijet constraints are relatively weak for this part of parameter space as we will discuss below.

The area inside the black line in Figure 4.5 indicates the region where the constraint on $\sqrt{g_q g_\chi}$ is stronger than the coupling strength which gives the correct relic abundance. Naively, $M - m_\chi$ values inside the region outlined by the black line would therefore lead to a larger relic abundance than observed. However, if the DM is not produced thermally or if the DM has other annihilation channels not consid-
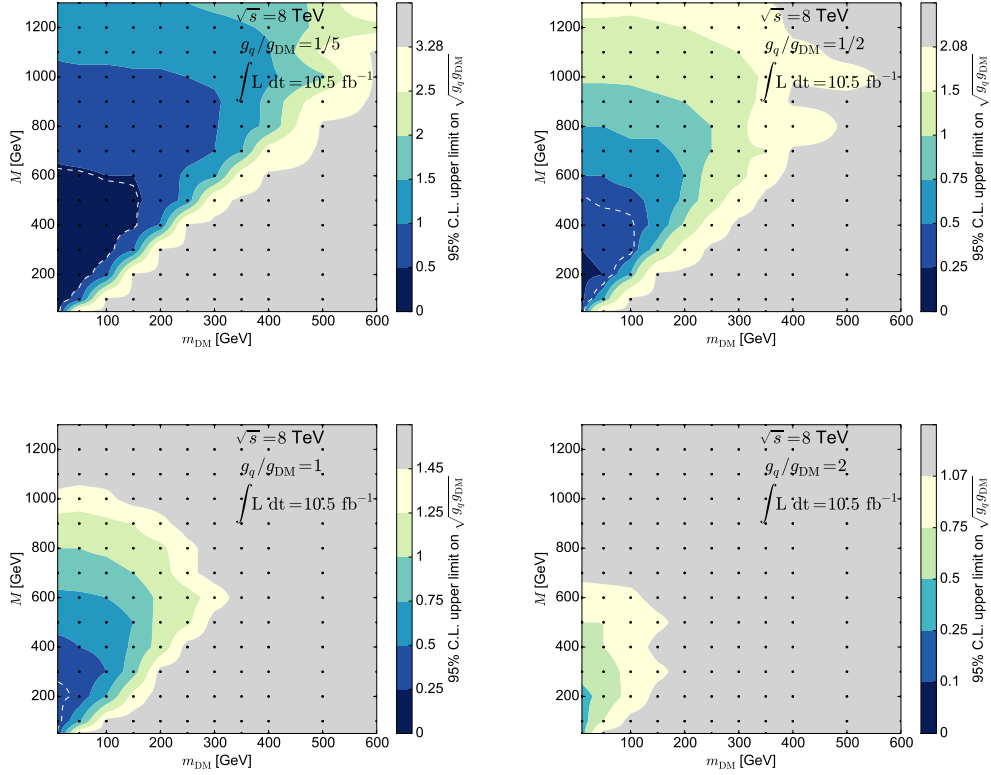
Figure 4.3: Our results using interpolation in $M - m_\chi$ space and the cross section approximations detailed in the text. The dashed white line shows where $\Gamma_{\mathrm{OS}}/M = 0.05$. The black dots are interpolation knots in $M - m_\chi$ space. See the text for further details. Note $g_{\mathrm{DM}} = g_\chi$, $m_{\mathrm{DM}} = m_\chi$ in our notation.

ered here (*e.g.* to leptons), this constraint is relaxed. Therefore this contour does not strictly rule out any region, but rather indicates that the 'simplest' implementation of DM using this model is expected to lie outside this contour. Limitations aside, this is a useful way to compare collider measurements to cosmological observations, and can be elegantly implemented in a simplified model context as we show here. This crucially relies on knowledge of the full parameter space: only considering a single slice will only allow a line which gives the correct relic density to be drawn, greatly reducing the overall information provided.

4.9.2   Limits from dijet resonance searches

Since our Z' couples to quarks one could attempt to make use of limits from dijet resonance searches [147–150] to further constrain the model as done in for example
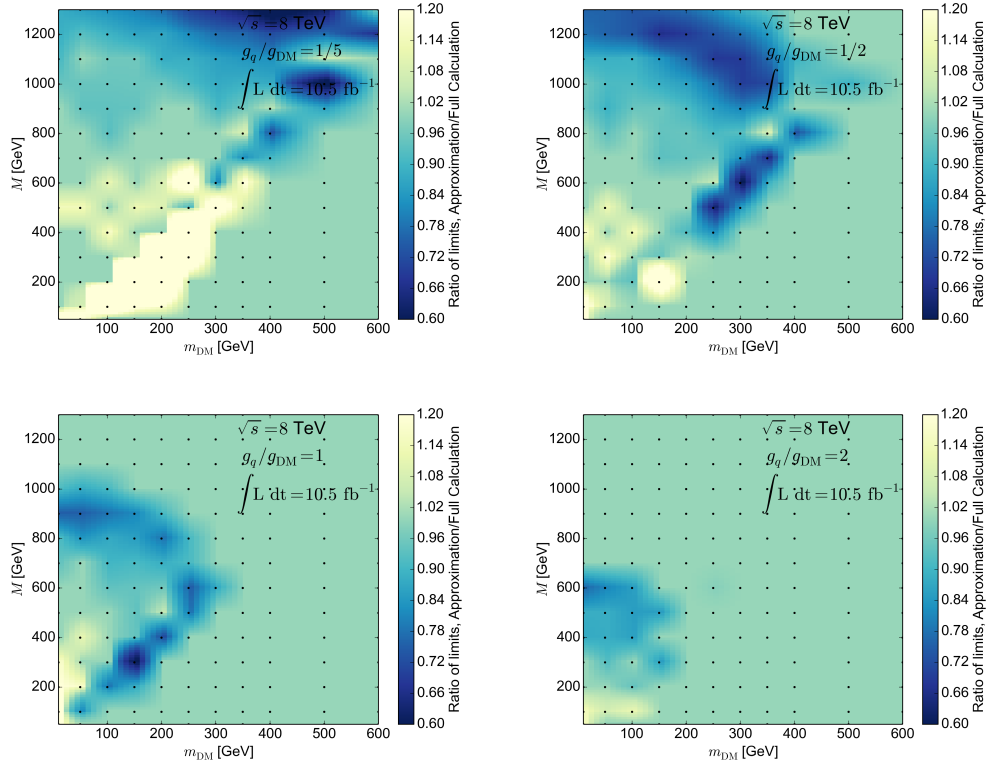
Figure 4.4: Ratio of the results using interpolation in $M - m_\chi$ space and the narrow width cross section approximation detailed in the text to using a full interpolation in $M - m_\chi - g_\chi \cdot g_q$ space. The cross section approximation is conservative in the bright yellow (light) areas, and overestimates the limit in the dark blue (dark) areas. The black dots are interpolation knots in $M - m_\chi$ space. Note the ratio takes values higher than 1.2 in some parts of parameter space but the colourbar is restricted since the approximations are conservative there. See the text for further details. Note $g_{DM} = g_\chi$, $m_{DM} = m_\chi$ in our notation.

[151]. This certainly gives much stronger constraints when $g_q/g_\chi > 1$ which is why we ignore this part of parameter space (we show results for $g_q/g_\chi = 2$ in our validation study in Section 4.8). For lower ratios of couplings we need to be careful since dijet resonance searches generally assume narrow resonances and in this part of parameter space the dark sector branching starts contributing to the width considerably. The dashed white line on the plots show where the width of the mediator becomes narrow enough to potentially violate such constraints assuming no additional dark sector decays (we take this to be $\Gamma_{OS}/M \lesssim 0.05$ to be conservative, but note that there are recent searches [150] which have constrained much wider
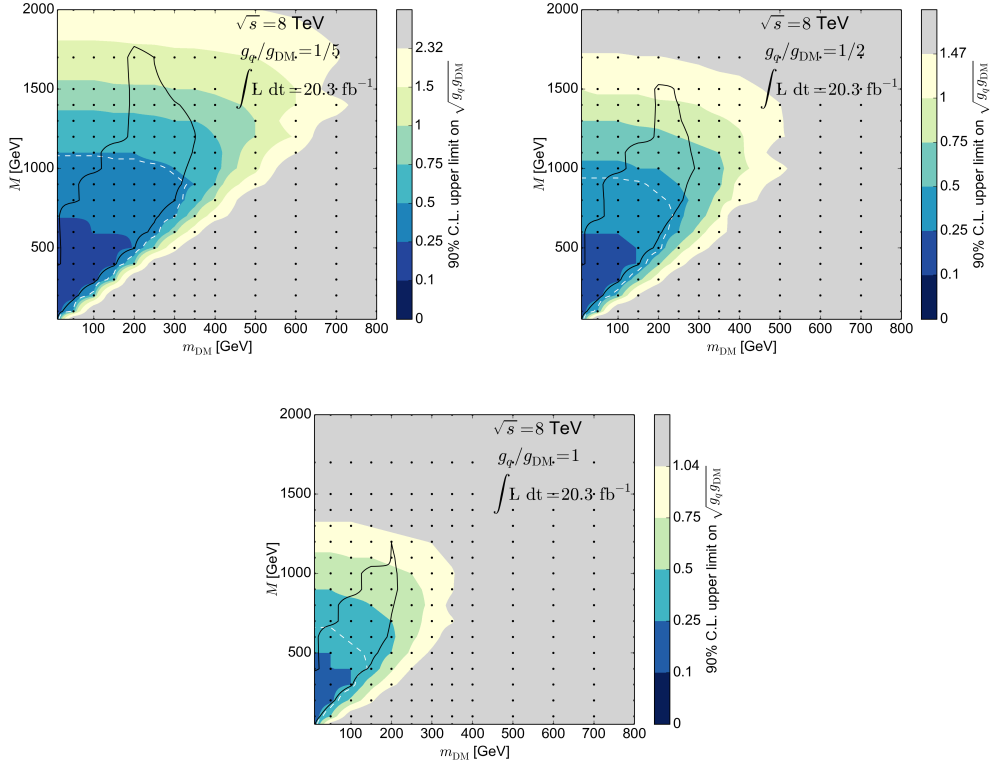
Figure 4.5: Current ATLAS monojet constraints at 90% C.L. on our model with the full 8 TeV dataset. The dashed white line shows where $\Gamma_{\rm OS}/M = 0.05$. The black dots are interpolation knots in $M - m_\chi$ space. The region inside the black line is naively ruled out by relic density contraints. For details see text. Note $g_{\rm DM} = g_\chi$, $m_{\rm DM} = m_\chi$ in our notation.

resonances). Comparing to the results from the detailed Z' dijet analysis in [152], presented in Figure 4.6, and assuming the results won't change drastically when using an axial-vector coupling compared to a vector one, we see (note the difference of a factor of 6 in the definition of g_q) that the values of g_q for which $\Gamma_{\rm OS}/M \lesssim 0.05$ for $g_q/g_\chi = 1/2, 1/5$ in our model typically are smaller than the values currently constrained by dijet searches, but $g_q/g_\chi = 1$ might be better constrained by dijet searches in the part of parameter space inside the dashed white line.

Realistically the dijet resonance constraints will apply for much wider resonances than we allow here once you perform a proper analysis instead of relying on constraints set assuming narrow widths, as done in [151] at parton level which suggests that monojet searches give the strongest constraints for light mediators but dijet searches are more constraining for heavy mediators even for low values of g_q/g_χ.
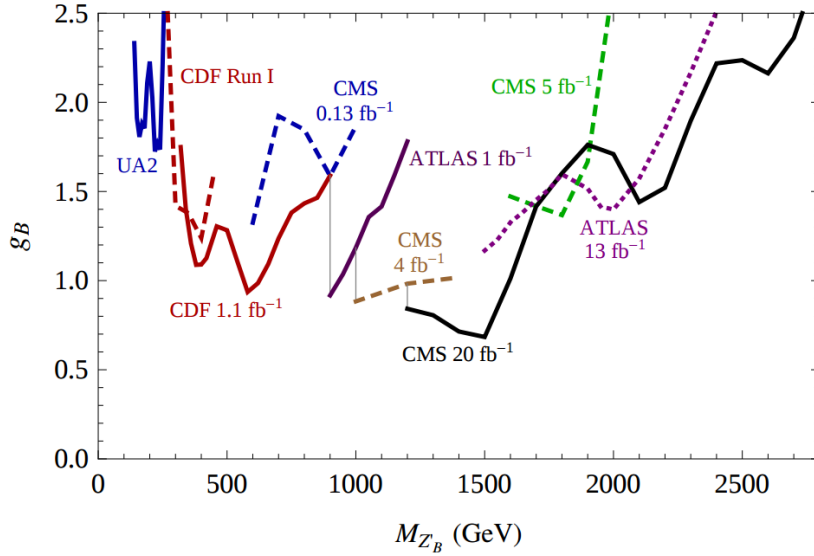
Figure 4.6: Limits set on a generic Z' model coupling equally to all quarks in [152]. Note that $g_B = 6g_q$ and $M_{Z_B} = M$ in our notation.

Due to the sensitive dependence on the width it is however worth stressing that since the model we assume here has no additional dark sector or standard model decays for the mediator, constraints set on dark matter mediators with dijet resonance searches in this part of parameter space can not be considered conservative: the width we use is the minimum width assuming equal coupling to each generation of quarks, and small changes to the dark sector can make a large difference to this width. This problem is not as pronounced when $g_q/g_\chi > 1$ since the width then is dominated by SM decays, which further motivates using dijet constraints over monojet ones in this part of parameter space. We also note that since the width can be large, interference effects with Z/γ^* should be properly taken into account when using dijet searches to constrain these models – we expect interference to play a similar role as in Drell-Yan [153] and have checked that this appears to be the case but a detailed analysis is outside the scope of this study.

It is also possible to make use of dijet angular distributions which are sensitive to wider resonances than the dijet mass spectrum [154, 155] and therefore can be considered more robust than dijet resonance contraints. As shown in the parton level study in [151] these can also be competetive with resonance searches in some parts of parameter space, but we won't consider them further here.

Signal Region	SR1	SR2	SR3
$E_T^{\mathrm{miss}} > $ [GeV]	400	600	800
ATLAS $\sigma_{\mathrm{vis}}^{\mathrm{exp.~95\%~CL}}$ [fb]	28	4.5	1.5

Table 4.4: Signal region definitions in the 14 TeV analysis and expected 95 % CL exclusion limits on the visible cross section from BSM contributions.

4.10   14 TeV Predictions

We make use of the public results in [112] as estimations for the expected backgrounds and hence expected cross section limits at 14 TeV with 20 fb^{-1} of data from the ATLAS detector assuming a low average number of pile-up collisions ($\mu = 60$)*. Our event generation and detector simulation is the same, but our analysis is changed to mirror that in [112]: we use a constant leading jet p_T cut of 300 GeV and the signal regions have been redefined as detailed in Table 4.4. The estimated reach with 20 fb^{-1} of 14 TeV data for $g_q/g_\chi = 1/5, 1/2, 1$ is presented in Figure 4.7. The black line again indicates the correct relic density as discussed in Section 4.9.1.

4.11   Comparison to ATLAS 13 TeV results

A monojet analysis using 36.1 fb^{-1} of 13 TeV ATLAS data have recently been made public in [156]. The analysis strategy is similar enough that it is possible to compare to our 14 TeV predictions, keeping in mind there's a small difference in center-of-mass energy and a factor of two difference in the available luminosity. The ATLAS result for a single parameter point in our signal model is presented in Figure 4.8 and shows very good agreement with the closest parameter point in our scan. This further confirms that our strategy is very robust and could be employed in realistic experimental limit-setting.

4.12   Conclusion

During the LHC Run II there has been a clear move towards supplementing EFT analyses with simplified models, as a stronger and more robust way to constrain the dark sector. These same arguments apply to Run I data, and thus it is useful to reinterpret existing constraints on the dark sector in the simplified model framework.

---

*We thank David Salek for providing us with the exact numbers for the background estimates and expected limits.
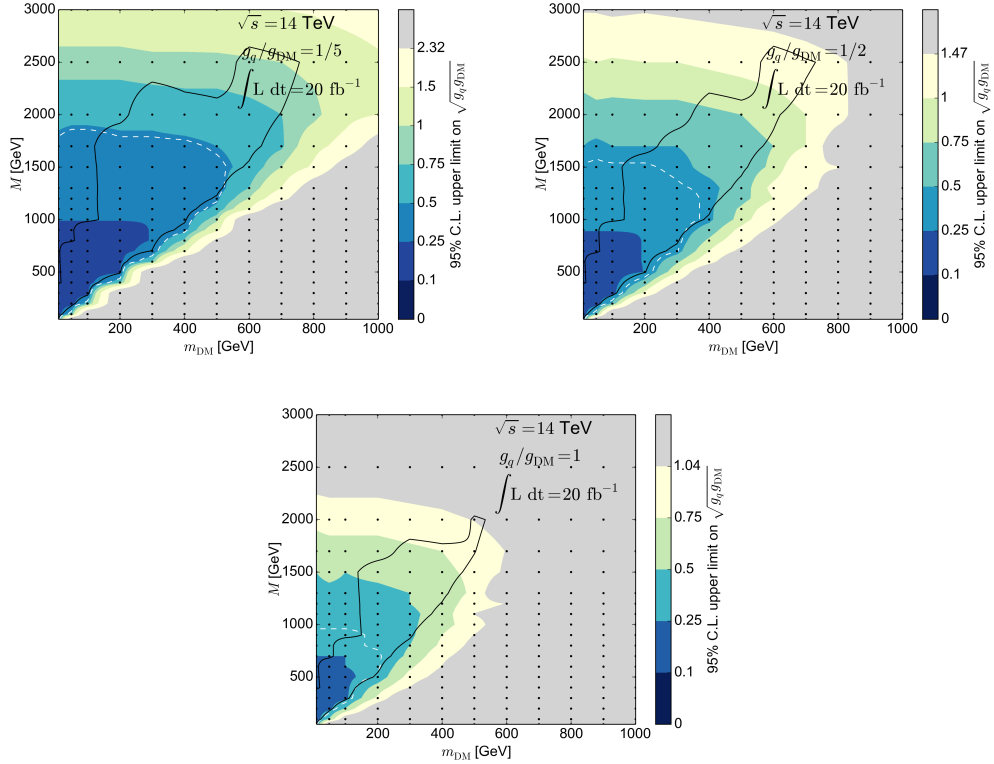
Figure 4.7: Predictions for the reach of the ATLAS experiment at 95% C.L. with 20fb^{-1} of 14 TeV data with $\mu = 60$. The dashed white line shows where $\Gamma_{\mathrm{OS}}/M = 0.05$. The black dots are interpolation knots in $M - m_\chi$ space. The region inside the black line could naively be ruled out by relic density contraints. For details see text. Note $g_{\mathrm{DM}} = g_\chi$, $m_{\mathrm{DM}} = m_\chi$ in our notation.

This has the added benefit of allowing us to validate a narrow width approximation for facilitating a wider parameter scan, and gives a clear benchmark for simplified models to be compared to results at higher LHC energies and luminosities. We have demonstrated this through constraints on a simple Z' model, with an axial-vector coupling. The parameter space for our simplified model spans four dimensions, making the parameter scan and visualisation of the subsequent constraints more challenging than for EFTs. The common restriction to 2-D slices of parameter space allows for easy comparison between several constraints, but does not tell us how these different constraints interact as we move to different parts of the parameter space. Here we instead scan over the full 4-D parameter space, presenting results as contours, allowing us to retain the maximum information possible on constraints. By making a well-motivated narrow width approximation we can perform such scans
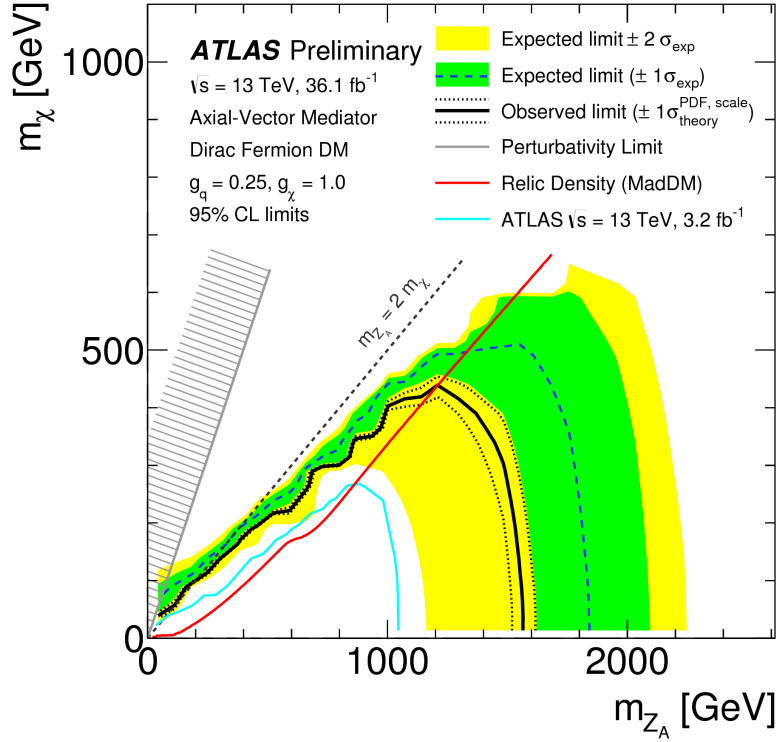
Figure 4.8: Limits set on our model by ATLAS [156]. Their chosen parameter point is close to the $\sqrt{g_q g_\chi} = 0.5$ contour on the $g_q/g_\chi = 1/5$ plot in Figure 4.7 and shows excellent agreement, taking the small difference in center-of-mass energy and factor of two in luminosity into account.

in an accurate and computationally reasonable way.

This allows for a more complete understanding of the strengths of the monojet channel for constraining dark sectors and facilitates comparison to contraints from other experiments and astronomical observations, as shown here by comparing to dijet and a simultaneous scan over relic density constraints. Whilst the scope of this analysis is limited to a single simplified model, this technique shows good prospects for the (re)interpretation of constraints across a broader model-space.

Having discussed the phenomenology of a Simplified Dark Matter model which falls squarely in the WIMP paradigm of dark matter, we will spend the next chapter investigating the collider phenomenology of an enlarged dark sector with a dark, potentially confining, gauge group.

Strongly-interacting Dark Sectors at Hadron Colliders

5.1 Attribution Notice

This chapter is based on results first published in [2] which I wrote together with Dr. Christoph Englert and Dr. Michael Spannowsky. I performed the calculations together with Dr. Christoph Englert and was responsible for all results except for those in Section 5.6 which are due to Dr. Christoph Englert, and created all of the original figures except for Figures 5.3, 5.4 which were created by Dr. Christoph Englert.

Contents

5.2   Summary

As outlined in Section 3.2.1.2, the ΛCDM paradigm suffers from a number of issues related to relatively small-scale structures, including the core vs cusp [92], too-big-to-fail [93], missing satellite [94] and Tully-Fisher Galaxy Halo [95–97] problems. These could be ameliorated if there were self-interactions among the dark matter particles. The self-interaction cross section required to fit observations without being excluded by others is of the same order-of-magnitude as nuclear interactions, $0.1 \text{ cm}^2/\text{g} \leq \sigma/m_\chi \leq 10 \text{ cm}^2/\text{g} \sim \text{barn/GeV}$ [157–160]. The observation of the Bullet Cluster called cross sections of this magnitude into question, as they would cause drag on the dark matter density distribution compared to the visible component of the cluster which was not observed [161]. However recent work has shown that such an analysis is sensitive to the details of both the model used for the dark matter density distribution of the bullet halo and the observational method used to infer the (non)-existence of any drag, and in fact a self-interaction cross section of $2 \text{ cm}^2/\text{g}$ can be completely consistent with the data [162, 163]. Dark sectors with strong interactions are therefore still a viable alternative to the ΛCDM paradigm which can solve many of its apparent shortcomings, and have seen considerable interest in the particle dark matter community. Here we will assume the existence of a minimally-coupled dark sector which runs to strong interactions in the infrared, and address the question of whether the scaling behavior of this dark sector can be observed in missing energy signatures at present and future hadron colliders. We compare these findings to the concrete case of self-interacting dark matter and demonstrate that the energy-dependence of high momentum transfer final states can in principle be used to gain information about the UV structure of hidden sectors at future hadron colliders, subject to large improvements in systematic uncertainties, which could complement proof-of-principle lattice investigations. We also comment on the case of dark abelian $U(1)$ theories.

5.3   Enlarged Dark Sectors

In the last chapter we considered a Simplified Dark Matter model with a massive, weakly interacting particle which freezes out through an interaction with the Standard Model quarks mediated by a heavy Z'. While such WIMP models offer a realistic mechanism for generating the relic density and lead to the correct bottom-up structure formation, there are other ways to achieve this.

A popular alternative to the WIMP paradigm of dark matter is to consider the existence of a mostly secluded larger dark sector which contains multiple particles that are not charged under the SM gauge interactions. The interactions of the dark sector can be protected by global symmetries and some of the particles can have a long lifetime, thus providing plausible dark matter candidates. Collider-relevant theories do not completely decouple the dark sector, but introduce interactions with the Standard Model fields through the exchange of a mediator of a yet unknown force. One reason to expect these to exist is that they in many cases can help cool down the dark sector and hence lead to the correct bottom-up structure formation [89]. From a quantum field theory perspective portal interactions are often motivated since they are allowed under the symmetries imposed and hence should exist, modulo fine-tuning. At the renormalisable level such an interaction can be facilitated by $U(1)$ mixing [164–166] or a so-called Higgs portal interaction [167–169].

A Higgs portal-like interaction is of particular interest, since we can argue for its existence on general grounds in a wide class of models: if we introduce a dark sector with particles which acquire their masses through a Higgs mechanism, this can either be achieved through a Yukawa coupling to the Standard Model Higgs H (this option requires the massive particles to not be singlets under $\mathcal{G}_{SM}$, and care needs to be taken to ensure interactions with the Standard Model are sufficiently suppressed [170]) or through a Yukawa coupling to a new scalar with a vev, ϕ. A new (real or complex) scalar ϕ will in general allow a mixing term $H^\dagger H \phi^\dagger \phi$ to be written down. Either way the Higgs provides a window into the dark sector.

Due to the issues the with ΛCDM paradigm outlined above, dark sectors with strong self-interactions have recently become of interest. One avenue to introduce self-interactions is to use the structure of the visible Standard Model sector as inspiration and consider the existence of a larger, potentially confining dark sector. The existence of complex dark sectors is further motivated by the fact that there is no a priori reason why dark matter interactions should exhibit the simple structure usually considered in WIMP scenarios.

While the very existence of dark matter is a strong indication of the presence of a secluded sector, dark sectors are also motivated beyond the realm of dark matter. Portal-type interactions have been motivated in generic hidden valley scenarios [171, 172], dark energy model building [173, 174], as well as conformal SM extensions to tackle the hierarchy problem [175–178] with potential links to leptogenesis [179] and inflation [180]. Dark sectors and their interaction with the SM spectrum can

therefore be considered as versatile tools to tackle apparent shortcomings of the SM, typically leading to the production of new states in high-energy interactions.

Irrespective of their motivation, we are faced with the question of how much we can learn about dark sectors by the very fact that their interaction with visible sectors is suppressed. How much can present and future high-energy colliders contribute to a resolution of this question?

It is known that inclusive rates of Z and Higgs boson interactions, as well as new resonances in multi-Higgs final states, can be indicative of mixing effects with dark sectors [181–183]. However, depending on the complexity of mediator interactions and dark sectors, it proves very difficult to enable a comprehensive dark sector "spectroscopy" [184, 185]. In this chapter we show that some information about the strong dynamics of a hidden sector can be gained by studying the momentum dependence of telltale E_T^{miss} events. Although we limit ourselves to $H +$ jet final states in the following, our arguments apply to any process that involves mediator production at high-energy colliders.

The chapter is organised as follows: we first review typical mediator scenarios and discuss the extent to which strong dynamics in the dark sector can leave measureable imprints on mediator production through renormalisation group effects at colliders in Sec. 5.4, before we focus on a minimal scenario based on Higgs portal interactions. In Section 5.5 we will provide sensitivity estimates of dark sector spectroscopy at the 14 TeV LHC and a hypothetical future 100 TeV hadron collider and comment on the expected performance of a future lepton collider. As we will see, this will crucially depend on improved experimental systematics. In Section 5.6 we connect the general discussion of Sections 5.4 and 5.5 to the concrete case of self-interacting dark matter and demonstrate that aspects of dark sectors can in principle be revealed by studying high-energy collisions. In case a state will be discovered that can be interpreted as a dark sector-mediator, such measurements can complement the on-going effort to construct realistic composite dark matter scenarios using lattice simulations. We summarise and conclude in Section 5.7.

5.4   Model

How can the dynamics of a strong sector influence the mediator phenomenology? The answer to this question is directly related to the UV properties of a particular mediator model and, to this end, we therefore focus on UV-complete models

with scalar and vector mediators. As is well known from studies of simplified dark matter models [110, 118, 119, 186], collider experiments are typically better suited to discover vector mediators with gauge-like interactions to quarks and the dark sector than scalar mediators with Yukawa-like couplings. In the vectorial case, however, the coupling to both visible and hidden sectors has to be a gauge coupling while the mass of the mediator is realised through spontaneous symmetry breaking (or a Stückelberg approach). The only possibility, therefore, is to understand the mediator interactions as part of a (Higgsed) product-group gauge theory, e.g. $SM \times U(1)_{\mathrm{mediator}} \times SU(N)_{\mathrm{dark}}$. Resumming the logarithmic enhancements of mediator production with a monojet signature can be estimated through a leading order (LO)-improved renormalisation group calculation that replaces the fixed LO value of g' with running parameter as function of the probed energy scale. The behaviour of the mediator coupling g' in the vectorial case, however, is protected through Ward identities which gives rise to a one loop renormalisation group equation (RGE)

$$\mu \frac{\mathrm{d}g'}{\mathrm{d}\mu} \propto \frac{(g')^3}{16\pi^2} \,, \tag{5.1}$$

irrespective of the dynamics in either the visible or hidden sector, as evident from the Standard Model one loop gauge beta functions presented in Section 2.4.6. Moreover, the mediator production cross section would only reflect the total contributing number of degrees of freedom to the running of g' but not their interaction properties (this is exactly the situation we encounter for the SM gauge couplings). On the one hand, such effects are difficult to observe in the LHC's (and a future 100 TeV collider's) energy range unless the value of g' was large enough to make the validity of perturbation theory questionable and potentially introduce a low-scale Landau pole. On the other hand the monojet cross section dominantly probes the mediator sector only, which is not the question we would like to see addressed by the measurement.

The LO RGE characteristics of gauge couplings are not present for scalar mediators. This already becomes transparent from the SM RGEs, where the top Yukawa interaction behaves as (Equation 2.94d):

$$\mu \frac{\mathrm{d}y_t}{\mathrm{d}\mu} = \left(\frac{9y_t}{2} - \frac{17g_1^2}{12} - \frac{9g_2^2}{4} - 8g_s^2 \right) \frac{y_t}{16\pi^2} \,. \tag{5.2}$$

As a consequence the top Yukawa RGE probes the strong QCD dynamics through the dependence on g_s, which runs as in Equation 2.94c. Therefore the combined solution of one loop RGEs indeed dials sensitivity from the QCD sector into the

behaviour of the Higgs-top interactions. This only happens at two loop order for gauge couplings and is hence a higher order effect for vector mediators.

We will therefore limit ourselves to scalar mediators, which can potentially allow us to observe an echo of the strong sector dynamics in the mediator cross sections. Our focus is a scenario consisting of a real SM-singlet scalar ϕ which obtains a vev x (similar to the singlet-extended Standard Model [167, 187, 188]), generating mass terms for three generations of SM-singlet fermion dark quarks ψ through Yukawa interactions. These mass terms can be small since we assume most of the mass in the dark sector results from confinement, however they need to be non-zero to keep all the dark pions massive in order to avoid strong long-range self-interactions in the $SU(N)$ case. We will in general assume a SM-like hierarchy structure in the generation masses in order to keep one of the Yukawa terms large. The full scalar potential is given by[*]:

$$V(H, \phi) = -\tilde{\mu}^2 H^\dagger H - \frac{m_\phi^2}{2}\phi^2 + \lambda_1 (H^\dagger H)^2 + \frac{\lambda_2}{4}\phi^4 + \frac{\lambda_3}{2}\phi^2 H^\dagger H. \qquad (5.3)$$

The λ_3 induced mixing between ϕ and H generically results in interactions between the visible and dark sector mediated by the two scalar mass eigenstates h and h', and we denote the mixing angle θ[†]. In unitary gauge:

$$H = \begin{pmatrix} 0 \\ (v + h_1)/\sqrt{2} \end{pmatrix}, \quad \phi = (x + h_2), \quad \begin{pmatrix} h \\ h' \end{pmatrix} = \begin{pmatrix} \cos\theta & -\sin\theta \\ \sin\theta & \cos\theta \end{pmatrix} \begin{pmatrix} h_1 \\ h_2 \end{pmatrix}, \quad (5.4)$$

θ is expressed in terms of the Lagrangian parameters by:

$$\tan 2\theta = \frac{\lambda_3 v x}{\lambda_2 x^2 - \lambda_1 v^2}. \qquad (5.5)$$

In principle we have five free parameters in the scalar sector, which we choose as $m(h), m(h'), v, x, \theta$, but we identify h as the Higgs-like particle discovered at the LHC which fixes $m(h) \simeq 125$ GeV and $v \simeq 246$ GeV.

5.4.1   The confining $SU(N)$ case

Since we are interested in dark sectors with nontrivial gauge structure we introduce a new $SU(N)$ gauge group (under which the SM transforms as a singlet) and let the dark quarks transform in the **M** representation. We consider the $U(1)$ case below.

---

[*]We impose a Z_2 symmetry to forbid any additional terms for simplicity.

[†]This notation supercedes the use of θ for the QCD-induced component of the $\mathcal{CP}$ violating angle involving $SU(3)_C$ field strengths.
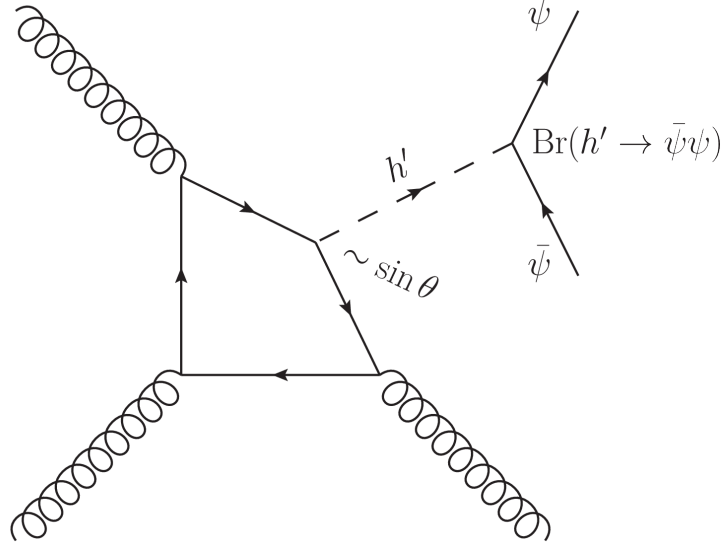
Figure 5.1: Example diagram contributing to the process. The dependence on the dark gauge group enters through the running of θ as explained in the text.

The dark sector Lagrangian then reads

$$\mathcal{L}_{\text{dark}} = -Y_\psi^{i,j} \phi \bar{\psi}^i \psi^j + \text{h.c.} + i\bar{\psi}\gamma^\mu D_\mu \psi - X_{\mu\nu}^a X^{a,\mu\nu} \,. \tag{5.6}$$

The mixing of the scalars will modify the interaction strength of the mass eigenstates with the two matter sectors: h couplings to the Standard Model are scaled by $\cos\theta$ compared to the Standard Model expectation and dark sector couplings are scaled by $\sin\theta$ compared to the ϕ, and vice versa for h'. This means $\bar{\psi}\psi$ production is allowed through both h and h' when kinematically possible . We assume Y_ψ is diagonal which means we have four new free parameters (with the dark gauge group coupling g_d) but motivated by the structure of the Yukawa terms in the SM we assume the third generation of dark quarks is considerably heavier than the two first ones and set the other Yukawa terms to 0 for the purposes of calculating the RGEs, which leaves us with $Y_\psi^{3,3}$ and g_d as free parameters. Showering and hadronisation can then occur as in QCD [171, 172] and decay to low-lying states can be achieved through additional weak interactions which will not impact the qualitative scaling behavior induced by the strong interactions in the dark sector (like in the SM sector). In total the free parameters for our study are:

$$Y_\psi^{3,3}, g_d, \theta, m(h'), x \,. \tag{5.7}$$

(a)

(b)

(c)
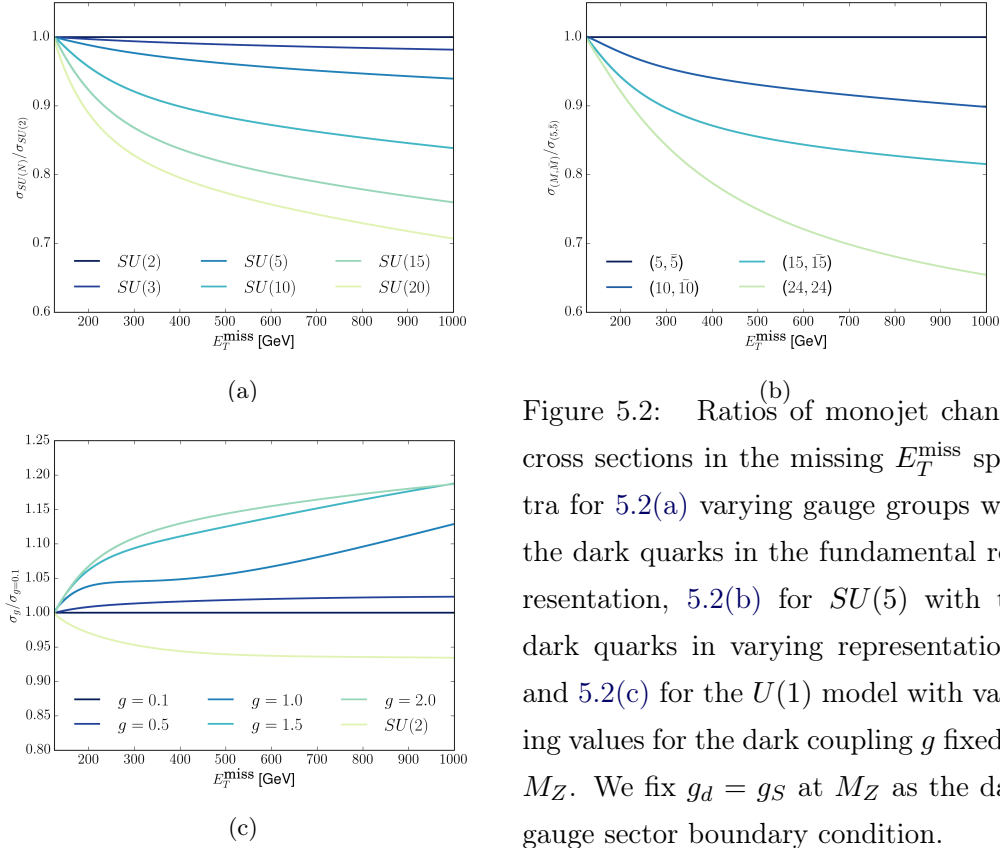
Figure 5.2:   Ratios of monojet channel cross sections in the missing E_T^{miss} spectra for 5.2(a) varying gauge groups with the dark quarks in the fundamental representation, 5.2(b) for $SU(5)$ with the dark quarks in varying representations, and 5.2(c) for the $U(1)$ model with varying values for the dark coupling g fixed at M_Z. We fix $g_d = g_S$ at M_Z as the dark gauge sector boundary condition.

To illustrate the effects of RGE running from different N and $\mathbf{M}$ we fix most of these to generic values inspired by their SM equivalents (defined at the h pole): $x = 100$ GeV, $Y_\psi^{3,3} = 0.7$, $\theta = 0.5$, and $m(h') = 150$ GeV. This parameter point is in agreement with current constraints [189]. For our chosen benchmark of a mass of 70 GeV for the heavy dark quark, production through h is kinematically suppressed and we will ignore it from now on. Also, since $\text{Br}(h' \to \psi\bar\psi) \approx 1$ current constraints from additional Higgs searches in visible channels are easily evaded.

We fix g_d in two different ways: first, by setting $g_d = g_S$ at the Z pole in order to map out the general features of the solutions in Section 5.5, and second, by requiring the dark IR Landau pole to be ~ 0.5 GeV in order to make Λ_d fall in a relevant part of parameter space for self-interacting dark matter in Section 5.6. This second requirement could be refined by using auxiliary measurements (e.g. on the lattice) but should capture the main features we are interested in; relevant to our analysis is the comparison of the different dark sectors.

Much like the top Yukawa in the Standard Model, the β function of $Y_\psi^{3,3}$ will be sensitive to the dark gauge group already at one loop level, which is the source of the dependence on the precise form of the group of the mixing angle θ in Equation (5.5), as the one loop β functions for λ_2, λ_3 and x all have a dependence on $Y_\psi^{3,3}$. Additionally these also depend on $\mathbf{M}$ [48–50]

$$\mu \frac{\mathrm{d}g_d}{\mathrm{d}\mu} = -\left(\frac{11}{3}C(\mathbf{A}) - 4\,T(\mathbf{M}) \right) \frac{g_d^3}{16\pi^2}\,, \tag{5.8a}$$

$$\mu \frac{\mathrm{d}Y_\psi^{3,3}}{\mathrm{d}\mu} = \left(-6\,C(\mathbf{M})\,g_d^2 + (2\,\mathrm{Dim}(\mathbf{M}) + 3)(Y_\psi^{3,3})^2 \right) \frac{Y_\psi^{3,3}}{16\pi^2}\,, \tag{5.8b}$$

$$\mu \frac{\mathrm{d}\lambda_2}{\mathrm{d}\mu} = \left(18\lambda_2^2 + 2\lambda_3^2 + 8\,\mathrm{Dim}(\mathbf{M})\,\lambda_2(Y_\psi^{3,3})^2 - 8\,\mathrm{Dim}(\mathbf{M})\,(Y_\psi^{3,3})^4 \right) \frac{1}{16\pi^2}\,, \tag{5.8c}$$

$$\mu \frac{\mathrm{d}\lambda_3}{\mathrm{d}\mu} = \left(-\frac{3}{2}g_1^2 - \frac{9}{2}g_2^2 + 12\lambda_1 + 6\lambda_2 + 4\lambda_3 + 4\,\mathrm{Dim}(\mathbf{M})\,(Y_\psi^{3,3})^2 + 6y_t^2 \right) \frac{\lambda_3}{16\pi^2}\,, \tag{5.8d}$$

$$\mu \frac{\mathrm{d}x}{\mathrm{d}\mu} = -2\,\mathrm{Dim}(\mathbf{M})\,(Y_\psi^{3,3})^2 \frac{x}{16\pi^2}\,. \tag{5.8e}$$

Here $C(\mathbf{A})$ is the quadratic Casimir of the adjoint representation ($= N$), $T(\mathbf{M})$ is the index of $\mathbf{M}$, and $C(\mathbf{M})$ the quadratic Casimir of $\mathbf{M}$.

Taking the Standard Model as a guiding example, it is also reasonable to expect an $SU(N)$ to capture the most important RGE effects even when the gauge group is enlarged, and hence this study should have some applicability beyond the simple scenario we consider here.

5.4.2 Dark $U(1)$s

We also consider a model with a dark $U(1)$ symmetry. In order to keep this force short-ranged ϕ must be complex and charged under this $U(1)$ in order to break the gauge symmetry by generating a mass term for the new gauge boson using the extra scalar degree of freedom. To avoid anomalies we will use three Weyl fermions and choose the charges as $q_{d,L} \sim 0$, $u_{d,R} \sim 1/2$, $d_{d,R} \sim -1/2$, $\phi \sim 1/2$. The dark sector Lagrangian is then:

$$\mathcal{L}_\mathrm{dark} = -Y_u^{i,j}\phi(u_{d,R}^\dagger)^i q_{d,L}^j - Y_d^{i,j}\phi^\dagger(d_{d,R}^\dagger)^i q_{d,L}^j + \mathrm{h.c.}$$
$$+ iq_{d,L}^\dagger \bar{\sigma}^\mu D_\mu q_{d,L} + iu_{d,R}^\dagger \sigma^\mu D_\mu u_{d,R} + id_{d,R}^\dagger \sigma^\mu D_\mu d_{d,R} - X_{\mu\nu}X^{\mu\nu}\,. \tag{5.9}$$

This gives us a theory which is similar to the one introduced above, with mass-mixing in the dark fermion sector[*], and which is not confining and has a Yukawa-like interaction potential between the dark fermion fields thanks to the vacuum being charged under the dark $U(1)$. Note that we will refer to the gauge coupling in the $U(1)$ model as g in contrast to g_d in the non-Abelian case. Much like in the non-Abelian case we assume only the largest Yukawa term is relevant and set $Y_u^{3,3} = 0.7$ and the rest to 0. This gives a mass eigenstate with a mass of ≈ 70 GeV for the purposes of the branching ratio calculation just like in the $SU(N)$ case. We keep all other parameters the same. We also assume there is no kinetic mixing between the dark $U(1)$ and $U(1)_Y$. The renormalisation group equations for this model are given below. Note that we have changed the normalisation of the ϕ field to that of a complex scalar field, and include a factor of $1/\sqrt{2}$ when expanding around x (leading to factor of 2 difference for terms involving squared Yukawas).

The RGEs for this model read [48–50]

$$\mu\frac{\mathrm{d}g}{\mathrm{d}\mu} = \frac{13}{12}\frac{g^3}{16\pi^2}\,, \tag{5.10a}$$

$$\mu\frac{\mathrm{d}Y_u^{3,3}}{\mathrm{d}\mu} = \left(-\frac{3}{4}g^2 + 2(Y_u^{3,3})^2\right)\frac{Y_u^{3,3}}{16\pi^2}\,, \tag{5.10b}$$

$$\mu\frac{\mathrm{d}\lambda_2}{\mathrm{d}\mu} = \left(20\lambda_2^2 + 2\lambda_3^2 + \frac{3}{8}g^4 - 3g^2\lambda_2 + 4\lambda_2(Y_u^{3,3})^2 - 2(Y_u^{3,3})^4\right)\frac{1}{16\pi^2}\,, \tag{5.10c}$$

$$\mu\frac{\mathrm{d}\lambda_3}{\mathrm{d}\mu} = \left(-\frac{3}{2}g_1^2 - \frac{9}{2}g_2^2 - \frac{3}{2}g^2 + 12\lambda_1 + 8\lambda_2 + 4\lambda_3 + 2(Y_u^{3,3})^2 + 6y_t^2\right)\frac{\lambda_3}{16\pi^2}\,, \tag{5.10d}$$

$$\mu\frac{\mathrm{d}x}{\mathrm{d}\mu} = -(Y_u^{3,3})^2\frac{x}{16\pi^2}\,. \tag{5.10e}$$

5.5   Results

We use implementations of our models in the Mathematica-based package SARAH [190] to obtain the relevant β functions at one loop for the described scenarios (checked against the general forms given in [50]), and solve these for the given boundary conditions using a slightly modified implementation of the RGE solver in SARAH which allows for boundary conditions to be defined at other points than the lowest scale considered.[†] These are then used to calculate the running of the

---

[*]We will only work in the interaction eigenstates here.

[†]SARAH also calculates the two loop β functions on demand but we do not use these to keep the dependence on N and $\mathbf{M}$ completely transparent as detailed in 5.8a-5.8e and 5.10a-5.10e. We

Cut	$U(1)$	$SU(2)$	$SU(25)$	Bgd.
$E_T^{\mathrm{miss}} > 200$ GeV	1.84 pb	1.70 pb	1.45 pb	432 pb
$E_T^{\mathrm{miss}} > 500$ GeV	0.0411 pb	0.0359 pb	0.0271 pb	18.0 pb
Ratio	44.8 ± 1.47	47.3 ± 1.78	53.5 ± 2.66	

Table 5.1: Cross sections of the signal at 100 TeV and expected measurements of the scaling with E_T^{miss} using 10 ab^{-1} of data. The $U(1)$ result uses $g(M_Z) = 0.1$. The statistics-only uncertainty on the ratio is calculated by estimating the statistical uncertainty on the signal strength in both cases and propagating these through to the ratio. For a CLs test based on the missing energy distribution see below.

mixing angle using the definition in Equation 5.5, which we numerically fit using built-in Mathematica functions. This fitted function is then passed on to a FOR-TRAN implementation of a full leading-order $pp \to h'j$ parton level event generator based on VBFNLO [191] with the analytic form of the matrix element evaluated using FORMCALC [192, 193], arriving at a one loop RGE-improved parton level calculation which is typically used in QCD LO calculations. Finally we take the branching ratio $\mathrm{Br}(h' \to \psi\bar{\psi})$ into account as a flat rescaling at the Higgs masses, which corresponds to the advocated prescription of the Higgs Cross Section Working Group [194]. In the matrix element calculation the renormalisation scale is set to $p_T(h')$, which is a motivated relevant scale for the logarithmically enhanced modifications of the cross section at large momentum transfers.

5.5.1 14 and 100 TeV hadron colliders

We estimate the monojet background by generating $pp \to (Z \to \nu\nu)j$ parton level events and scaling this by a factor of 1.5 to get an estimate of the total background following [113].*

In order to get a handle on the strong sector dynamics, we need to study the energy dependence of exclusive cross sections. Concretely this means we need to determine how an excess in the monojet channel scales as a function of E_T^{miss} when such a signal can be extracted from the background. This will allow us to make a statement about the likely gauge structure of the dark sector if different dark gauge

---

have checked that including two loop effects does not change the results presented here.

*While mismeasured lepton $(W \to \nu l)j$ events are important and slightly change the scaling with energy of the background, this rescaling should be conservative for our purposes as backgrounds at larger E_T^{miss} will be over-estimated.
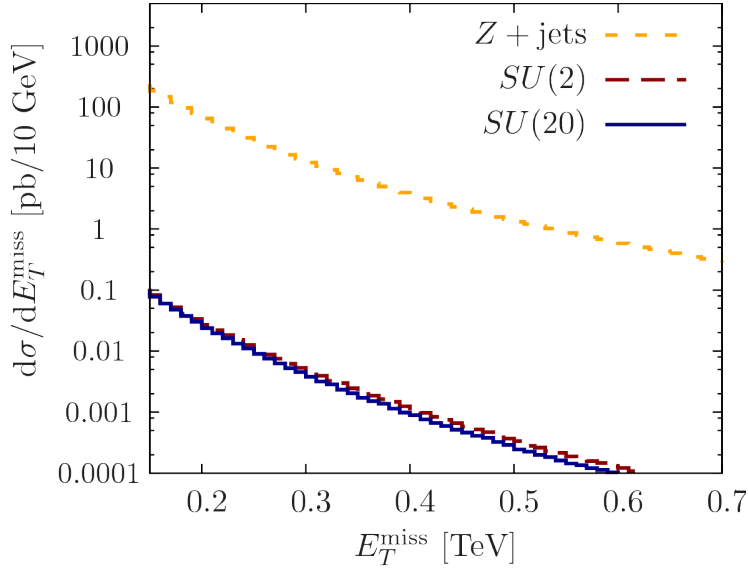
Figure 5.3:   100 TeV signal and background distributions that feed into the confidence level calculation detailed in the text.

groups indeed predict a statistically relevant deviation in a comparison. The relative scaling of the cross section as a function of missing E_T^{miss} for different gauge groups and different representations of $SU(5)$ is given in Figure 5.2. Due to our choice of scale the behaviour will be exactly the same at all center-of-mass energies.

The constraints from single Higgs phenomenology enforce a small mixing angle for SM-like Higgs measurements, which act as a boundary condition to the RGE flow. We therefore find for our parameter point that the absolute cross sections at 14 TeV are too small for a measurement to be made even with the full HL-LHC data set.[*]

The cross sections at a 100 TeV proton-proton collider given in Table 5.1 are large enough to offer an opportunity to make a measurement of the running of θ using a data set of 10 ab^{-1}. Given the expected small mixing angle, the largest experimental challenge will undoubtedly be the reduction of the systematic uncertainties of the measurements by over an order of magnitude compared to the recent 8 and 13 TeV monojet analyses by ATLAS and CMS [113, 146, 195, 196]. The impeding factor of a 14 TeV analysis, i.e. the smallness of the expected signal cross

---

[*]By changing the parameters, however, we could indeed maximise the potential sensitivity at the HL-LHC at the price of creating further tension with Higgs signal strength measurements. We do not discuss this case in detail as it would require additional dynamics in order to remain viabl.e
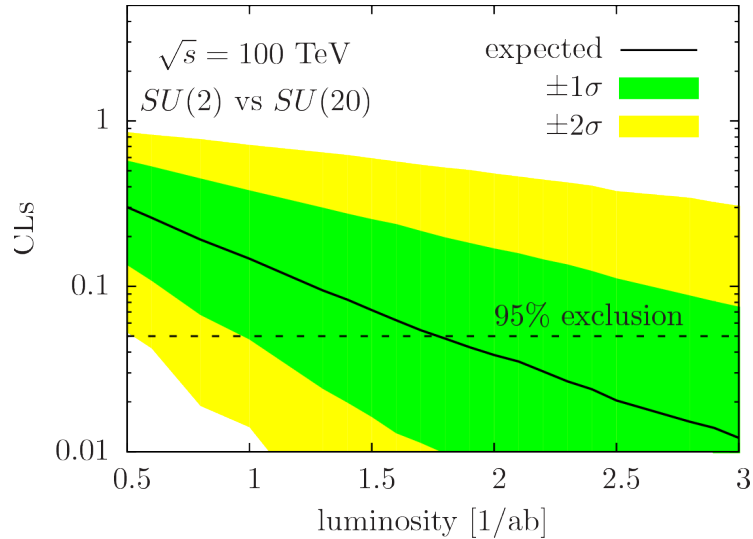
Figure 5.4: CLs hypothesis test detailed in the text, only assuming statistical uncertainties.

section as well as a limited data set will be overcome at a 100 TeV machine, where the signal cross sections are large enough to gather very large statistics with the aim to use data-driven, as well as multivariate techniques, which essentially remove the background uncertainties to a very large extent. Using an extrapolation from the low-missing-energy regime is not straightforwardly possible since the low-missing-energy phase space region receives a contribution from signal events, and is not entirely background dominated. However, Z boson data can be extrapolated from visible $Z \to e^+e^-$ and $\gamma + $ jet subsidiary measurements at essentially zero statistical uncertainty (note that all involved couplings are gauge couplings following 5.1), which essentially allows us to directly infer the dominant $Z(\to \nu\bar{\nu}) + $jet distribution completely using data-driven techniques. Similar techniques were used already for 8 TeV analyses, e.g. [197] . Since the detector layout of a 100 TeV machine is likely to change towards an improved electromagnetic calorimeter coverage [198, 199], this mapping from $(Z \to e^+e^-) + $jet and $\gamma + $jet could also be performed without relying on an extrapolation into the jet-acceptance region beyond the lepton and photon acceptance regions $|\eta| < 2.5$ that is imposed by the current LHC setup.

In the likely case that we can gain excellent control over the background distribution in a data-driven approach (i.e. assuming only statistical uncertainties), we can expect a 5σ discovery threshold of $\gtrsim 100$ fb^{-1} using a binned log-likelihood

approach (as detailed in Refs. [99, 200]) based on the missing energy distribution for the $SU(2)$ running, although the signal vs. background ratio is small. Discriminating the $SU(2)$ from the $SU(20)$ hypothesis, for instance, should then be possible at 95% CLs [100] for $\mathcal{L} \gtrsim 1.6$ ab^{-1} (assuming statistical uncertainties only, Figure 5.4). Similar conclusions hold for discriminating large non-Abelian groups against the $U(1)$ scenario (at slightly smaller integrated luminosities).

5.5.2 Probing dark sectors through h couplings

Since our SM-like scalar h has its couplings scaled by $\cos(\theta)$ we could in theory also use these to investigate the structure of the dark sector. Measuring θ at m_h is straightforward (current measurements already put some tension on our parameter point), after which the scaling could be investigated through a similar analysis as above but using cleaner and better understood visible decay channels, with larger cross sections. However, the issue with such a measurement is that θ generically runs to smaller values and hence towards the maximum of $\cos\theta$ where derivatives vanish; at small $\theta_{1,2}$, $\cos(\theta_1)/\cos(\theta_2) \sim 1$. At our parameter point we find cross section differences of up to 30% between $SU(2)$ and $SU(20)$ at a scale of 1 TeV when looking at production scaled by $\sin(\theta)^2$ (running away from the minimum), but these differences shrink to about 1% when scaling by $\cos(\theta)^2$. At smaller values of $\theta(m_h)$ this problem is further worsened and already with $\theta(m_h) = 0.1$ one needs to investigate differences of $\mathcal{O}(0.01\%)$, which is challenging the sensitivity range of a future lepton collider [201, 202].

5.5.3 A note on future lepton colliders

At a future lepton collider the two dominant production mechanisms for h' would be h'-strahlung and WW fusion. h'-strahlung is a threshold effect and would as such be inherently insensitive to the running of θ. WW fusion dominates at higher $\sqrt{s}$ and does in theory feel the running of θ but since the final state would be $h'\nu\bar{\nu}$, a measurement would have to rely on a radiated photon leading to cross sections of the order of $O(1-10$ fb) for $\sqrt{s} = 500 - 1000$ GeV for unpolarised e^+e^- beams, making a measurement dependent on extremely large integrated luminosities. However, thanks to the controlled kinematics at a lepton collider, the dominant background $(Z \to \nu\bar{\nu})\gamma$ peaks strongly at $E_\gamma = E_Z = E_{\text{beam}}$ for $E_{\text{beam}} \gg m_Z$, whereas the signal peaks below $E_\gamma < m_{h'}$, which allows for an almost background-free analysis before detector effects are taken into account. The choice of scale here is not straightforward

and we can expect non-RGE electroweak effects to play a significant role. Although this channel provides a clean avenue to test the hypothesis, RGE analyses alone cannot obtain a reliable estimate of the sensitivity.

5.6 Potential Relation with self-interacting dark matter

As discussed at the start of the chapter, there are measurements which point towards a large DM self-interaction cross section of the order $\sigma/m \simeq 1.3$ b/GeV [161]. Such a large cross section can of course be achieved by going to very small mass scales in the perturbative regime (see e.g. [203]) and our $U(1)$ discussion of the previous section is therefore directly relevant for these scenarios.

Cross sections of this size are not unusual in strongly interacting confined theories such as QCD, and we focus on this possibility in the following in detail. While the non-Abelian theories we have discussed so far are asymptotically free, explaining the relatively large characteristic decrease in cross section at large momentum transfers, they will confine at low scales which gives rise to a series of hadronic states in the dark sector. The details are highly dependent on the respective fermion and gauge symmetry content and the details as well as the existence of realistic confining theories can only be clarified by lattice simulations. However, we can obtain a qualitative estimate of whether such theories can reproduce self-interacting dark matter scenarios by means of chiral perturbation theory (χPT). To this end we assume that the self-interaction cross section is dominated by nonrelativistic pion scattering, well below the energy scales of other dark hadronic resonances. This will provide an estimate of the validity range of such scenarios and give us an idea if our previous discussion is relevant for self-interacting dark matter scenarios without making a particular reference to modified velocity distributions of the dark matter halo, which are likely to be found in theories with complex interactions [204,205,205]. Modifications from both corrections due to additional hadronic contributions to the cross section as well as a modified dark matter profile will change our numerical outcome, but can be compensated at least numerically by changing the fundamental parameters of χPT, which needs to be confirmed by lattice investigations.

The pion dynamics is completely determined by the $[SU(N) \times SU(N)]/SU(N)$ nonlinear sigma model describing the coset field $\Phi(x)$ with dark pion decay constant $f_{\tilde{\pi}}$:

$$U(x) = \exp\left(\frac{i\Phi(x)}{f_{\tilde{\pi}}}\right) . \tag{5.11}$$

Analogous to QCD we assume the pion to be the lightest hadronic state in the spectrum; if no additional gauged $U(1)$ symmetry is present in the dark sector this state will remain stable. The interactions that we consider follow from expanding the non-linear sigma model using the CCWZ prescription (see Section 2.4.2.1):

$$\mathcal{L}_{\text{dark},\chi} = \frac{f_{\tilde{\pi}}^2}{4}\text{Tr}\left(\partial_\mu U \partial^\mu U^\dagger\right) \tag{5.12}$$

and by identifying the dark pion with the uncharged pion analogous to QCD we arrive at

$$\mathcal{L}_{\text{dark},\chi} = \frac{1}{2}(\partial\pi)^2 + \frac{1}{f_{\tilde{\pi}}^2}\pi^2(\partial\pi)^2 + \dots, \tag{5.13}$$

where the ellipsis refers to higher-order terms in the χPT expansion as well as interactions of other states. With this Lagrangian we can compute the self-interaction cross section straightforwardly (we have cross-checked our results against implementations with FEYNRULES [127] and FORMCALC [192, 193]) and obtain in the nonrelativistic limit

$$\frac{\sigma}{m} = \frac{m}{4\pi f_{\tilde{\pi}}^4}, \tag{5.14}$$

which we can use to gauge whether self-interaction cross sections can be obtained from theories that show similarities with QCD (we assume the mass to be generated through a small explicit chiral symmetry violation analogous to QCD, as explained in Section 5.4). With naive dimensional analysis [206] (NDA), we can furthermore limit the parameter range of the dark pion decay constant given its mass. The mass needs to be smaller than the NDA cutoff $m < \Lambda_d \simeq 4\pi f_{\tilde{\pi}}$ and pion scattering needs to be in agreement with the observed self-interaction cross section of $\sigma/m \simeq 1.3$ b/GeV. This locates the cutoff of the theory between 0.2 GeV $\lesssim 4\pi f_{\tilde{\pi}} \lesssim 0.8$ GeV for pion masses $m < 0.8$ GeV. Matching the Landau pole of the running of the dark sector strong interaction to this energy scale then allows us to make a projection of the impact of the running at large momentum transfers in the light of our discussion of Sec. 5.5. The results are given in Figure 5.5.

As can be seen from Equation 5.14, if the self-interaction cross section is indeed dominated by the low-energy pion interactions, the cross section alone does not contain information about the strong dynamics as such (provided that the symmetry-breaking pattern indeed produces a spectrum that matches our assumptions). If this is the case, the only way to perform spectroscopy of the described scenario is through studies of the momentum dependence of the fundamental parameters of the dark sector UV theory. Since dark-gluon production is not directly accessible, an

(a) (b)
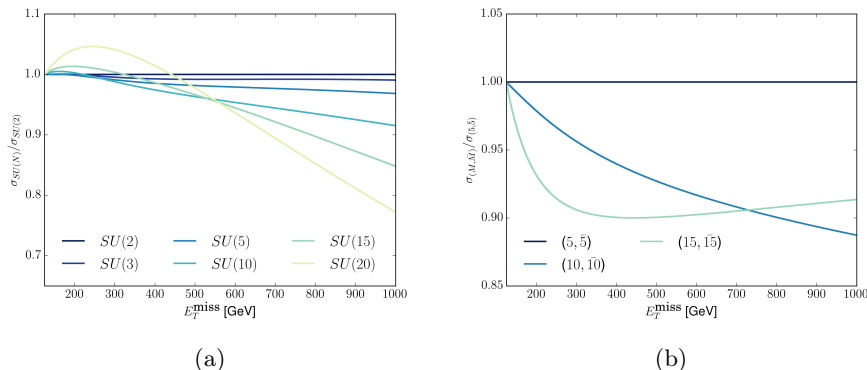
Figure 5.5: Ratios of monojet channel cross sections in the missing E_T^{miss} spectra for 5.5(a) varying gauge groups with the dark quarks in the fundamental representation, 5.5(b) for $SU(5)$ with the dark quarks in varying representations. The value of g_d was fixed by requiring $\Lambda_d \simeq 0.5$ GeV.

investigation through portal-interactions whose presence can be established through additional resonance searches is vital to gain information about the potential presence of such a sector given the discovery of an additional scalar which is compatible with a Higgs mixing scenario.

Although our main focus is the general behavior of strongly interacting dark sectors and their spectroscopy using Higgs mixing, models with self-interacting hidden sectors should also reproduce the correct measured relic density $\Omega_d h^2 \approx 0.12$ to be viable dark matter candidates. Our setup is flexible and allows for thermal freeze-out to occur either through standard annihilation into the SM as outlined in Section 3.2.1.1, through number-changing $3 \to 2$ interactions between the dark pions as in [89,207] (subject to the conditions detailed in this work), or a combination of the two, depending on the details of the chosen parameter point.

There is also the possibility that glueballs make up most of the relic density instead of the pions as qualitatively discussed above. Since our discussion involves asymptotically free dark sectors, the analyses of [208,209] are applicable in this case: on the one hand, the correct relic density can be achieved by tuning the ratio of the visible and dark sector temperatures, which, however, requires an extremely small mixing. Under these circumstances the discovery of the additional scalar becomes impossible. On the other hand, if both sectors are in thermal contact through non-negligible mixing angles, we need to rely on additional (supersymmetric) dynamics to make the model cosmologically viable [208]. Our discussion does not apply in these cases straightforwardly and we leave an analysis of supersymmetric extensions

to future work.[*]

5.7   Conclusions

Dark sectors are SM extensions motivated to tackle a plethora of unexplained phenomenological observations that require physics beyond the SM. Their appeal from a model-building perspective comes at the price of a naturally suppressed phenomenological sensitivity yield in terrestrial experiments such as colliders. In this study, using RGE-improved calculations, we have motivated that studying the energy dependence of scalar mediators, produced at a future hadron collider and decaying invisibly, can be utilised to gain some insights into the nature of the hidden sector, in particular because data-driven methods will be available for large data sets of 10 ab^{-1}. Gaining excellent systematic control over the backgrounds well beyond the current expectations of theoretical as well as experimental uncertainties will be crucial to obtain these insights into strongly interacting dark sectors, which can complement other lattice investigations.

We have used this rather general observation for the concrete case of self-interacting dark matter, whose large cross section can be naturally explained by strong dynamics. If the strongly interacting dark matter scenario turns out to be true and its relation to the TeV scale through e.g. Higgs mixing becomes favoured, then the described approach will be a unique collider-based strategy that provides insight into a strongly interacting sector (supplied by calculations of finite corrections which are not governed in our RGE-based approach), albeit remaining experimentally challenging.

---

[*]It is worthwhile mentioning that the authors of [208] found that the number of colours is required to be small, which decreases the relative impact of the RGE running when the mixing angle interactions of hidden and visible sectors are non-neglible.

$hhjj$ production and the $\mathcal{CP}$ nature of the Higgs sector

6.1 Attribution Notice

This chapter is based on results first published in [3] which I wrote together with Dr. Matthew Dolan, Dr. Christoph Englert, Dr. Nicolas Greiner, and Dr. Michael Spannowsky, and [4] which I wrote together with Dr. Christoph Englert, Dr. Kazuki Sakurai, and Dr. Michael Spannowsky. I performed the main analysis of [3] which is the focus of the chapter, relying on a calculation of the gluon fusion contribution performed by the co-authors and first presented in [210]. The same analysis was later also utilised in [4] and the relevant results are presented here. All work was done by me except for the calculations in Section 6.8 which were done by Dr. Christoph Englert and Dr. Kazuki Sakurai. All figures were created by me except for Figures 6.1, 6.5 which are due to Dr. Nicolas Greiner and Figures 6.11, 6.12, 6.13 which are due to Dr. Christoph Englert and Dr. Kazuki Sakurai.

Contents

6.2   Summary

As outlined in Sections 2.4.2.2 and 3.1.1, the search for di-Higgs production at the LHC in order to measure the Higgs trilinear coupling and set constraints on or discover new physics is one of the major goals of the LHC high luminosity phase. Experimental feasibility studies [211, 212] suggest that such analyses will only be successful if information from a range of channels is included. We will therefore here investigate di-Higgs production in association with two hadronic jets and give a detailed discussion of both the gluon- and weak boson fusion contributions, with a particular emphasis on the phenomenology with modified Higgs trilinear and quartic $hhV^{\dagger}V$ gauge couplings. We perform a detailed investigation of the full hadronic final state and find that $hhjj$ production should add sensitivity to a di-Higgs search combination at the HL-LHC with 3 ab^{-1}. Since the WBF and GF contributions are sensitive to different sources of physics beyond the Standard Model, we devise search strategies to disentangle and isolate these production modes. While gluon fusion remains non-negligible in WBF-type selections, sizeable new physics contributions to the latter can still be constrained. We demonstrate this by investigating the sensitivity that can be obtained for a measurement of the quartic Higgs-gauge boson couplings, which can be interpreted as a proxy for the Higgs self-energy and therefore can potentially be related to solutions to the hierarchy problem, as outlined in Section 3.1.1.

We also consider the phenomenology of $\mathcal{CP}$ violating extended Higgs sectors by investigating a subset of $\mathcal{CP}$-odd effective field theory operators, and show that perturbative unitarity arguments together with the non-observation of any new resonant states in the LHC's energy range thus far can be used to strongly constrain the low-energy Wilson coefficients of many of these. Extending our discussion to an operator which can be generated in a simplified model of a $\mathcal{CP}$ violating Two Higgs Doublet potential with a portal-like real scalar, we show that there is still space for
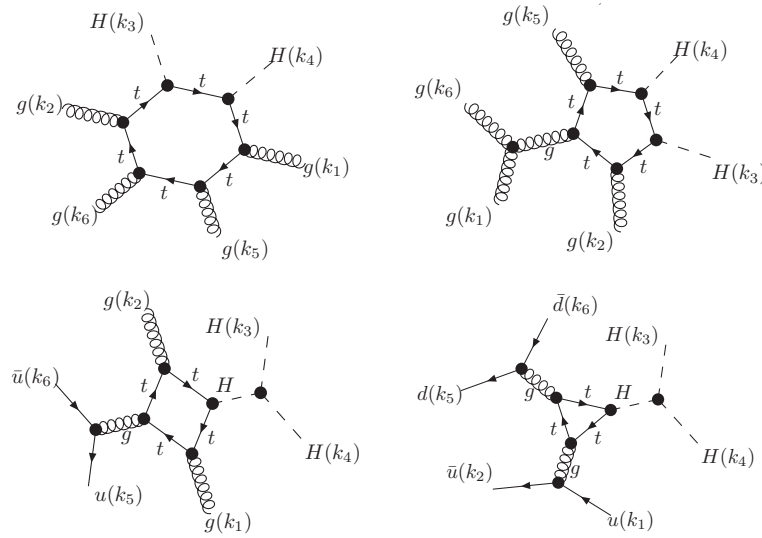
Figure 6.1: Sample Feynman diagrams contributing to $pp \to hhjj$ via gluon fusion.

$\mathcal{CP}$ violating effects in the Higgs sector. We then return to our discussion of *hhjj* production and show that the weak boson fusion component is highly sensitive to this operator.

6.3 *hhjj* production as a precision test of the Standard Model

A measurement of the Higgs trilinear self-coupling would provide both a precision test of the Standard Model and a sensitive probe of beyond Standard Model physics. This Higgs self-coupling manifests itself primarily in a destructive interference in gluon fusion-induced di-Higgs production [213–215] through feeding into the trilinear Higgs interaction with strength $\lambda_{\mathrm{SM}}^3 = m_h \sqrt{\eta/2}$ in the SM. The latter relation can be altered in BSM scenarios, for example the SM coupling pattern can be distorted by the presence of a dimension six operator $\sim (H^\dagger H)^3$, and di-Higgs production is the only channel with direct sensitivity to this interaction [216, 217]. A modification solely of the Higgs trilinear coupling, which is typically invoked in di-Higgs feasibility studies, is predicted in models of $\tilde{\mu}^2$-less electroweak symmetry breaking [218].

After the Higgs discovery, analyses of the di-Higgs final state at the high-luminosity LHC and beyond have seen considerable attention. Feasibility studies by ATLAS and CMS [211, 212] have highlighted the complexity of these analyses and

the necessity to explore different production mechanisms to obtain the strongest constraints possible.

Di-Higgs production in association with two jets is a particularly important channel in this regard since this final state receives contributions from the weak boson fusion (WBF) production mode. The phenomenological appeal of the WBF mode is twofold. Firstly, the weak boson fusion component of $pp \to hhjj$ is sensitive to modifications of the gauge-Higgs sector [210, 219], which can lead to large cross section enhancements. Secondly, the QCD uncertainties for the WBF topologies are known and under theoretical control [220, 221], such that a search for BSM electroweak-induced deviations is not hampered by QCD systematics. This situation is very different from QCD-induced production [222–225], and can be attributed to the particular phenomenology of WBF-like processes [226–231].

However, an additional source of uncertainty that was neglected until the calculation in [210] is the correct inclusion of the gluon fusion contribution to $pp \to hhjj$ analyses. Similar to single Higgs + 2 jet production [232, 233], the correct inclusion of massive fermion thresholds is crucial to a reliable prediction of QCD-induced $pp \to hhjj$ [41].

Given that the cross sections in WBF $hhjj$ production are very suppressed compared to WBF hjj production (the WBF $hhjj$ cross section is ~ 750 times smaller at 14 TeV), we have to rely on the dominant hadronic Higgs decay modes to be able to observe this final state. This rules out one of the most crucial single Higgs WBF selection tools - the central jet veto [234]. The observation of WBF-induced $pp \to hhjj$ production is further hampered by the top threshold in the QCD-mediated process. Since the top threshold sets the scale of the di-Higgs subsystem, an analysis that tries to retain as many low p_T Higgs bosons as possible leads to a QCD contribution that dominates over the WBF component when minimal WBF-like cut requirements are imposed [210].

In this chapter we perform a detailed comparison of EFT-approaches to QCD-mediated $pp \to hhjj$ against a calculation keeping the full mass dependencies of top and bottom quarks in Section 6.4. We compare the QCD-induced $pp \to hhjj$ phenomenology to the WBF signature in Section 6.5 before we discuss general approaches to isolate the signal from the dominant top backgrounds in a hadron level analysis in Section 6.6. This sets the stage for a discussion about the prospects to isolate the WBF and GF components in Sections 6.6.1 and 6.6.2, followed by a study on constraining $V^\dagger Vhh$ couplings using the WBF induced signal in Section 6.6.3.

λ^3	$0 \cdot \lambda^3_{\mathrm{SM}}$ [fb]	$1 \cdot \lambda^3_{\mathrm{SM}}$ [fb]	$2 \cdot \lambda^3_{\mathrm{SM}}$ [fb]
GF	10.73	5.502	2.669
WBF	4.141	2.010	0.9648

Table 6.1: Cross section normalisations for the GF and WBF samples at 14 TeV, for details see text. The WBF normalisation follows from [220] and includes higher order QCD effects.

To complement the interpretation in terms of λ^3 and $V^\dagger V h h$ measurements, we also consider perturbative unitarity constraints on $\mathcal{CP}$ violating effects in the Higgs sector in Section 6.7, and ultimately show that a $hhjj$ measurement strongly constrains an operator which is unaffected by such theoretical considerations in Section 6.9. We focus on collisions with 14 TeV throughout.

6.4 The gluon fusion contribution

6.4.1 Finite top mass effects

Effective field theory approximations in the $m_t \to \infty$ limit, as introduced in Section 2.4.5.1, can not be invoked to study di-Higgs final states at colliders in a reliable way due to the effects of the top-quark threshold [235, 236]. Additionally the breakdown of the $m_t \to \infty$ approximation is worsened in the presence of additional jet emission [41, 237]. Finite m_t effects must therefore be considered for all QCD di-Higgs production channels. This is crucially important when considering WBF-induced $hhjj$ production as signal as the GF-induced component will act as a non-reducible background.

The computational challenges in QCD-mediated $hhjj$ production are significant, with the gluon-fusion channels particularly time consuming. The standard method of simulating a differential cross section from unweighted events is not feasible in this case, and we instead use a reweighting technique that is exploited in higher order calculations and experimental analyses (see for example [238]).

We generate GF $hhjj$ events by implementing the relevant higher dimensional operators in the $m_t \to \infty$ limit obtained by expanding the low-energy effective theory discussed in Section 2.4.5.1,

$$\mathcal{L}_{\mathrm{eff}} = -\frac{1}{4}\frac{\alpha_S}{3\pi} G^a_{\mu\nu} G^{a\,\mu\nu} \log(1 + h/v) \tag{6.1}$$

in MADEVENT v5.1 [239] using the FEYNRULES/UFO [240] framework.[*] This allows us to sample a weighted set of events that we subsequently feed into our analysis solely depending on their final state kinematics. If an event passes the selection requirements of a certain search region, we correct for the full mass dependence using the reweighting library based on GOSAM package [241, 242] at this stage. The reweighting employs exactly the same matrix elements used for the event generation and the trilinear coupling is steered through a modification of the GOSAM matrix element, i.e. variations of the trilinear coupling are part of the reweighting. A selection of Feynman diagrams which contribute to the gluon fusion signal are illustrated in Figure 6.1. The GOSAM code used for the reweighting is based on a Feynman diagrammatic approach using QGRAF [243] and FORM [244, 245] for the diagram generation, and SPINNEY [246], HAGGIES [247] and FORM to write an optimised fortran output. The reduction of the one loop amplitudes was done using SAMURAI [248], which uses a d-dimensional integrand level decomposition based on unitarity methods [249–253]. The remaining scalar integrals have been evaluated using ONELOOP [254]. Alternative reduction techniques can be used employing NINJA [255–257] or GOLEM95 [258–260]. To validate the reweighting procedure we have performed a full phase space integration and we find full agreement within the statistical uncertainties between the result obtained from reweighting and the result from the full phase space integration.

6.4.2   Phenomenology of QCD-mediated *hhjj* production

Top thresholds are particularly prominent in the di-Higgs invariant mass distribution, which makes it well-suited to show the improvements of our finite m_t calculation compared to the effective theory of Equation 6.1. Other observables constructed from the six particle final state are also relevant when performing a targeted phenomenological analysis so we will discuss a number of them here.

In Figures 6.2, 6.3, and 6.4 we show a selection of *hhjj* final state observables for inclusive cuts $p_{T,j} > 20$ GeV and $|\eta_j| < 5$, no cuts on Higgs bosons are imposed. We label Higgs bosons and jets according to their hardness, i.e. $p_{T,h1} > p_{T,h2}$ and $p_{T,j1} > p_{T,j2}$. The cross sections are given in Table 6.1. The inclusive gluon fusion cross section is about 2.5 times larger than the WBF cross section approximately

---

[*]The effective theory implementation can be modified in the sense that only one effective vertex insertion is allowed. This is gives only a mild $\sim 10\%$ effect in the tail of the distribution, and is not relevant for an order one EFT/full theory rescaling, see below.

(a)   (b)
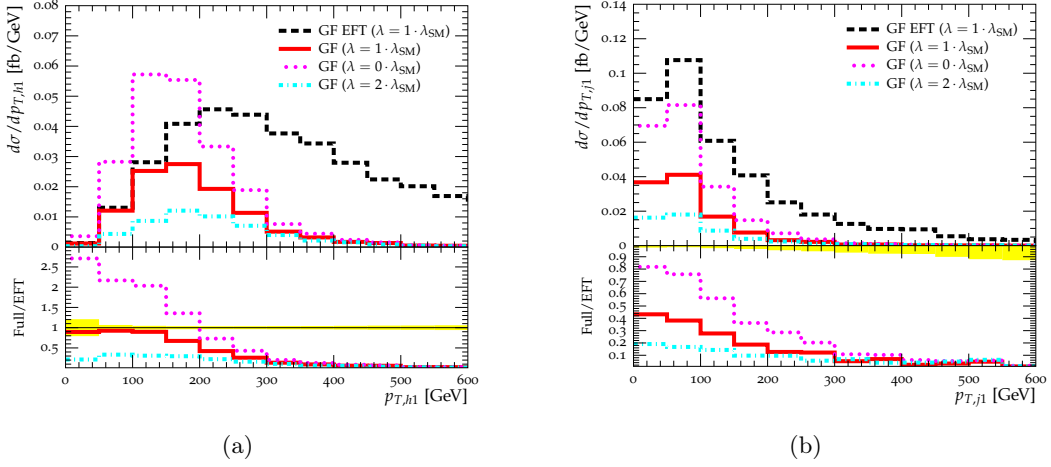
Figure 6.2: Maximum Higgs and jet transverse momenta in QCD-mediated $hhjj$ production, including the ratio of full theory to the effective theory calculation for three different values of the Higgs trilinear coupling. $\lambda = \lambda^3$ in our notation.

(a)   (b)
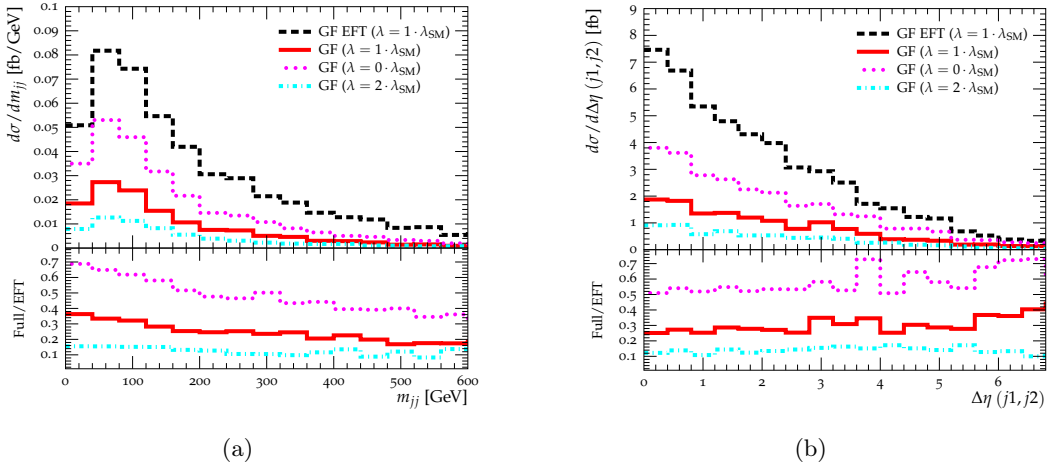
Figure 6.3: Invariant mass and pseudo-rapidity distributions of the jet system in QCD-mediated $hhjj$ production. We show the effective theory and full theory results for three values of the trilinear Higgs coupling, applying only generator-level cuts of $p_{T,j} \geq 20$ GeV and $|\eta_j| < 5$. $\lambda = \lambda^3$ in our notation.

independent of the value of the Higgs trilinear coupling.

As previously established in [41, 210, 235] the di-Higgs system is badly modelled by the effective theory which overshoots the full theory cross section at high momenta. The m_{hh} distribution in Figure 6.4(a) is the crucial observable which parametrises the finite top quark mass effects, and agrees well at small invariant

(a)   (b)
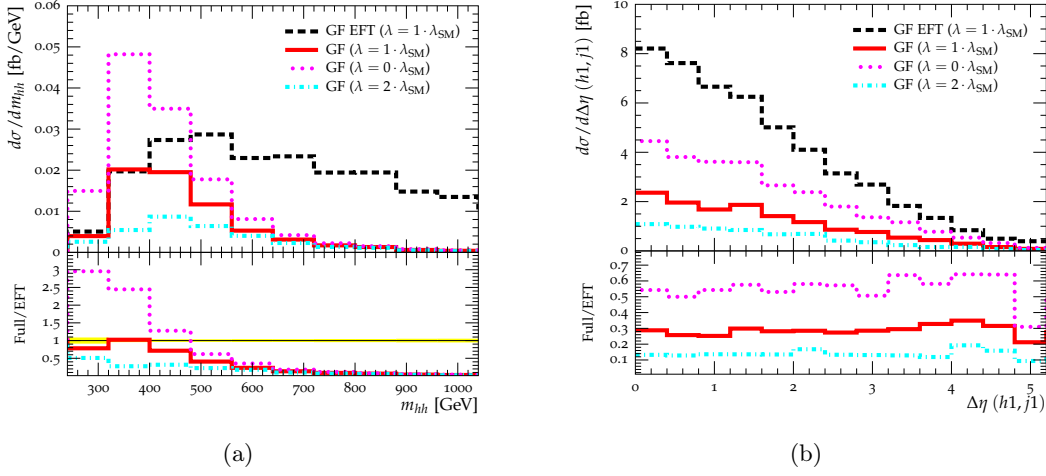
Figure 6.4:   Invariant mass of the di-Higgs system and pseudo-rapidity difference
between the leading Higgs and the leading jet in QCD-mediated $hhjj$ production.
We show the effective theory and full theory results for three values of the trilinear
Higgs coupling, applying only generator-level cuts of $p_{T,j} \geq 20$ GeV and $|\eta_j| < 5$.
$\lambda = \lambda^3$ in our notation.

masses. The EFT describes low maximum transverse Higgs momenta $p_{T,h1}$ reason-
ably well, as shown in Figure 6.2(a). The jet emission on the other hand integrates
over a considerable range of m_{hh}, and the ratio of full theory vs effective theory is
less than one for the entire range of $p_{T,j1}$, Figure 6.2(b).

Considering just the dijet system in Figure 6.3, we observe that the jet kinemat-
ics is not severely impacted by the reweighting procedure upon marginalising over
the di-Higgs kinematics. The phase space dependence of the dijet invariant mass
Figure 6.3(a) is relatively mild aside from the total rescaling of the inclusive cross
sections, and the ratio for the pseudo-rapidity distribution of the jets is nearly flat,
Figure 6.3(b). This is also true for the azimuthal angle difference $\Delta\phi_{jj}$. The angular
distributions of the leading members of the jet-Higgs system are relatively mildly
impacted by the reweighting too Figure 6.4(b) and can be approximated by a total
reweighting by a K-factor. This agrees with the m_{hh} being the observable most
sensitive to the top threshold, as suggested by the large impact of the reweighting
on m_{hh} in Figure 6.4(a). A reweighting based on m_{hh} to correct for finite top mass
effects could therefore potentially be used as a time-saving approach with reasonable
accuracy in future analyses.

6.5 The weak boson fusion contribution

The weak boson fusion contribution to $pp \to hhjj$ has received considerable attention and precise higher-order QCD corrections are provided in [220,221,231]. Due to the sensitivity of the WBF contribution to both the trilinear coupling and the quartic $V^\dagger Vhh$ ($V = W, Z, \gamma$) vertices, as shown in the Feynman diagrams in Figure 6.5, weak boson fusion to two Higgs bosons can, in principle, provide complementary information about BSM physics which remains uncaptured in other associated di-Higgs production channels.

We generate WBF samples with varying λ^3 using MADEVENT v4 [261] and normalise the cross section to NLO accuracy [220]. The WBF $hhjj$ contribution shares the QCD properties of WBF hjj production [226] which means it shares the distinctive $\Delta\eta(j1, j2)$ distribution shown in Figure 6.6(a): to produce the heavy di-Higgs pair we probe the initial state partons at large momentum fractions. This together with a colour-neutral t-channel exchange of the electroweak bosons leads to energetic back-to-back jet configurations at large rapidity separation and moderate transverse momenta with a centrally produced Higgs pair. The production of an additional Higgs boson in comparison to single Higgs production via WBF leads to a cross section reduction by three orders of magnitude (see Table 6.1) in the SM. Such a small inclusive production cross section highlights the necessity of considering dominant Higgs decay channels such as $h \to b\bar{b}$ and $h \to \tau^+\tau^-$ which makes it impossible to use central jet vetos [234] as a means to control the background *and* GF contribution in a targeted analysis.

The gluon fusion contribution is bigger by a factor of 2.5 than the WBF component of $hhjj$ production. However with increasing invariant di-Higgs mass the WBF contribution is enhanced relative to GF production as a consequence of the suppression above the $2m_t$ threshold, as shown in Figure 6.6(b).

Since we cannot rely on vetoing hadronic activity in the central part of the detector, a potential discrimination of GF from WBF needs to be built on the following strategy, which we will investigate in Section 6.6:

- To isolate the di-Higgs (WBF+GF) signal we can exploit the relative hardness of the di-Higgs pair which peaks around $\sim 2m_t$. Such hard events are less likely to be produced by (ir)reducible backgrounds.

- Focussing on large m_{hh} we can enhance WBF over GF by stringent cuts on the jet rapidity separation. This will also imply a significant decrease of QCD-
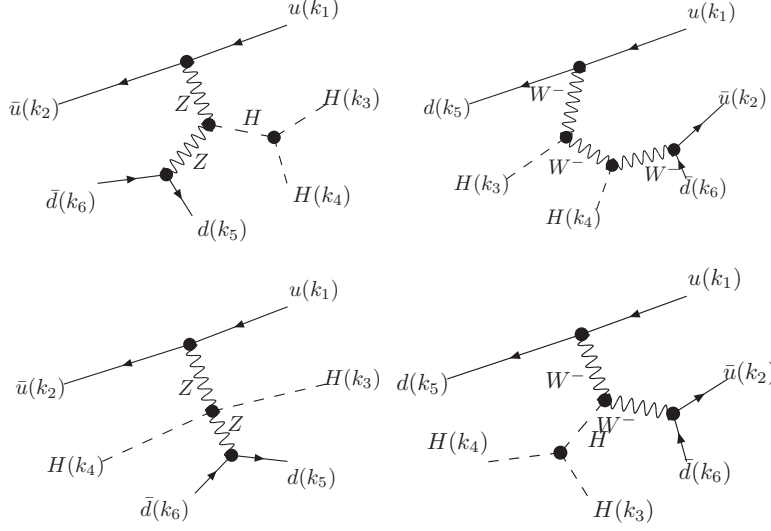
Figure 6.5: Sample Feynman diagrams contributing to $pp \rightarrow hhjj$ in weak boson fusion.

(a)	(b)
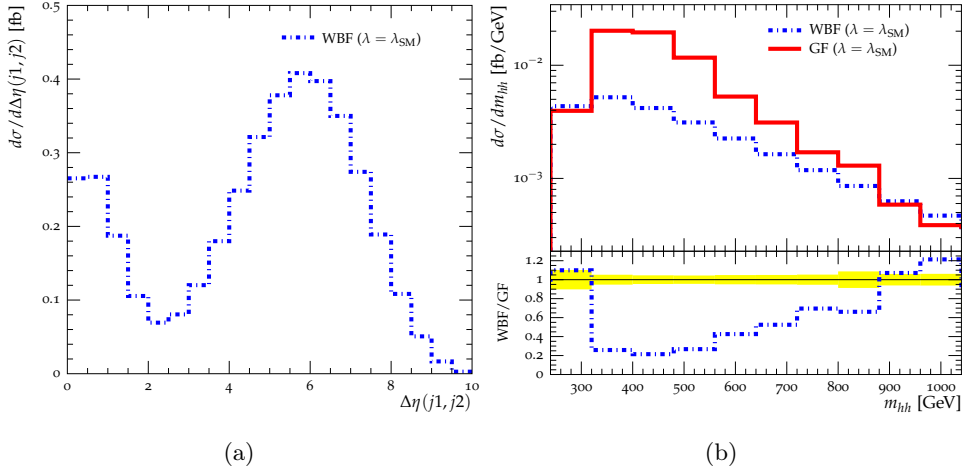
Figure 6.6: The $\Delta\eta(j1, j2)$ distribution of the weak boson fusion contribution at parton level (a) and the m_{hh} distribution of the weak boson fusion and gluon fusion contributions compared with correct cross section normalisation (b), both satisfying generator-level cuts of $p_{T,j} \geq 20$ GeV and $|\eta_j| < 5$. $\lambda = \lambda^3$ in our notation.

dominated backgrounds.

- By explicitly allowing central jet activity, we can exploit the colour correlation differences in WBF vs GF to further purify our selection. Since colour flow
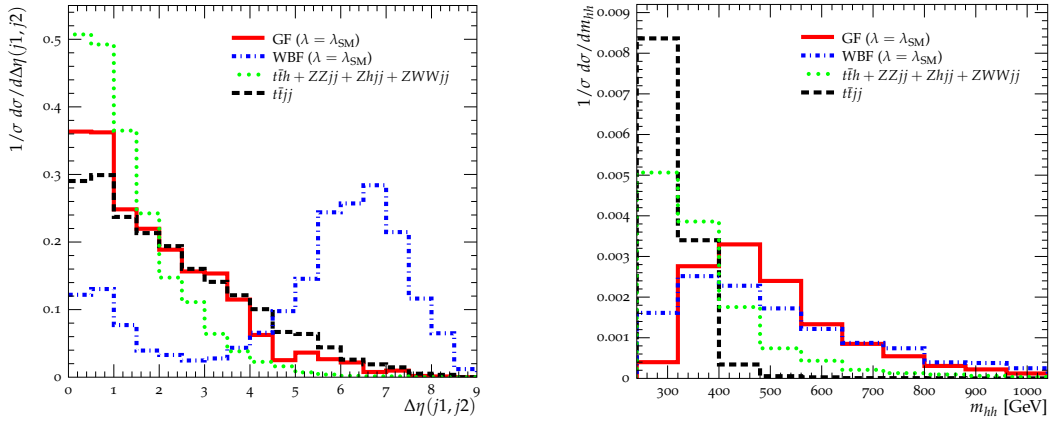
Figure 6.7: Shape comparison of $\Delta\eta(j1, j2)$ and m_{hh} distributions for our two sources of signal (GF and WBF), the dominant background $t\bar{t}jj$ and the rest of the backgrounds (stacked scaled by relative cross sections), after the Base Selection of Section 6.6 has been applied. $\lambda = \lambda^3$ in our notation.

is tantamount to energy flow in the detector, event shapes are particularly well-suited observables for unravelling the colour correlations in the final state once the reconstructed di-Higgs pair has been removed[*].

---

[*]Detailed discussions of event shapes at hadron colliders can be found in [262, 263].

Cut setup	Base Selection [fb]	GF Selection [fb]	WBF Selection [fb]	Normalisation* [fb]
GF ($\lambda = 1 \cdot \lambda_{\text{SM}}$)	1.396×10^{-2}	5.722×10^{-3}	5.378×10^{-4}	4.013×10^{-1}
GF ($\lambda = 0 \cdot \lambda_{\text{SM}}$)	2.562×10^{-2}	8.122×10^{-3}	8.767×10^{-4}	7.831×10^{-1}
GF ($\lambda = 2 \cdot \lambda_{\text{SM}}$)	7.167×10^{-3}	3.906×10^{-3}	3.034×10^{-4}	1.947×10^{-1}
WBF ($\lambda = 1 \cdot \lambda_{\text{SM}}$)	3.292×10^{-3}	4.999×10^{-4}	1.485×10^{-3}	1.466×10^{-1}
WBF ($\lambda = 0 \cdot \lambda_{\text{SM}}$)	7.706×10^{-3}	7.154×10^{-4}	2.820×10^{-3}	3.020×10^{-1}
WBF ($\lambda = 2 \cdot \lambda_{\text{SM}}$)	1.103×10^{-3}	1.815×10^{-4}	3.912×10^{-4}	7.037×10^{-2}
$t\bar{t}jj$	5.712	3.390×10^{-2}	1.801×10^{-2}	1.0130×10^{4}
$t\bar{t}h$	6.229×10^{-2}	7.047×10^{-3}	5.658×10^{-5}	3.862×10^{1}
$Zhjj$	5.118×10^{-3}	1.278×10^{-3}	1.026×10^{-4}	4.737×10^{1}
$ZZjj$	1.171×10^{-3}	6.659×10^{-5}	7.639×10^{-7}	2.257×10^{2}
$ZWWjj$	1.888×10^{-5}	5.461×10^{-6}	2.039×10^{-7}	5.368×10^{-1}
total background	5.781	4.230×10^{-2}	1.817×10^{-2}	-
S/B ($\lambda = 1 \cdot \lambda_{\text{SM}}$)	$1/335.1$	$1/6.799$	$1/8.983$	
S/B GF† ($\lambda = 1 \cdot \lambda_{\text{SM}}$)	$1/414.3$	$1/7.480$	$1/36.55$	
S/B WBF† ($\lambda = 1 \cdot \lambda_{\text{SM}}$)	$1/1760$	$1/96.06$	$1/12.60$	
$S/\sqrt{B}$ (3 ab^{-1}, $\lambda = 1 \cdot \lambda_{\text{SM}}$)	0.3930	1.657	0.8219	

∗ branchings included in normalisation

† considering only this as signal

Table 6.2: Cross sections for the two sources of signal, and backgrounds, after the various selections described in the text are applied, together with various measures of significance in the bottom four rows.

6.6 Taming the background

For our hadron level analysis we shower our signal samples with HERWIG++ [264] and generate backgrounds as follows: $t\bar{t}jj$, $t\bar{t}h$, $Zhjj$, and $ZZjj$ with SHERPA [265], and $ZWWjj$ with MADEVENT v5. We find the dominant backgrounds to be $t\bar{t}jj$ and $t\bar{t}h$ production, for which next-to-leading order results are available [266–277] and we use inclusive K factors $K_{t\bar{t}jj} \simeq 1$ and $K_{t\bar{t}h} \simeq 1.5$ to estimate the higher order contributions to these backgrounds. Higgs branching ratios are set to the values agreed upon by the Higgs Cross Section Working Group [194].

We begin the hadron level analysis implemented in Rivet [137] by recreating a base selection similar to [210]:

1.) We require two tau leptons using a two tau-trigger based on staggered transverse momentum selection cuts $p_T \geq 29, 20$ GeV in $|\eta_\tau| < 2.5$ and assume a flat tau tagging efficiency of 70% with no fakes.

    Jets are constructed by clustering $R = 0.4$ anti-k_T jets using FASTJET [138] with $p_{T,j} \geq 25$ GeV and $|\eta_j| \leq 4.5$.

2.) The two leading jets are b-tagged with an acceptance of 70% and fake rate of 1% [278] in the central part of the detector $|\eta_j| < 2.5$. We remove events if either of the two leading jets overlaps with a tau. Any additional jets which do not overlap with a tau are considered as potential "tagging jets", of which we require at least two.[*]

3.) As a final step of this base selection we require the b jet and tau pairs to reproduce the Higgs mass of 125 GeV within ± 15 and ± 25 GeV respectively.[†]

The signal and background cross sections after these cuts are presented in the Base Selection column of Table 6.2. We find that the background contribution of $t\bar{t}jj$ dominates with $t\bar{t}h$ also providing a larger-than-signal background resulting in $S/B \sim 1/300$, making a study based only on these selections extremely challenging. Since we only have ~ 40 expected gluon fusion and ~ 10 expected weak boson fusion events at 3 ab^{-1} luminosity, additional selections must also be careful to retain enough signal cross section to allow statistically meaningful statements to be made with a finite amount of data.

---

[*]It was argued recently [279] that single jet tagging [280] could provide an alternative at high luminosity for single Higgs production at lost WBF/GF purity.

[†]A high mass resolution is a crucial cornerstone of any successful di-Higgs analysis to assure a minimum pollution of Z boson decay backgrounds [281].

(a)   (b)
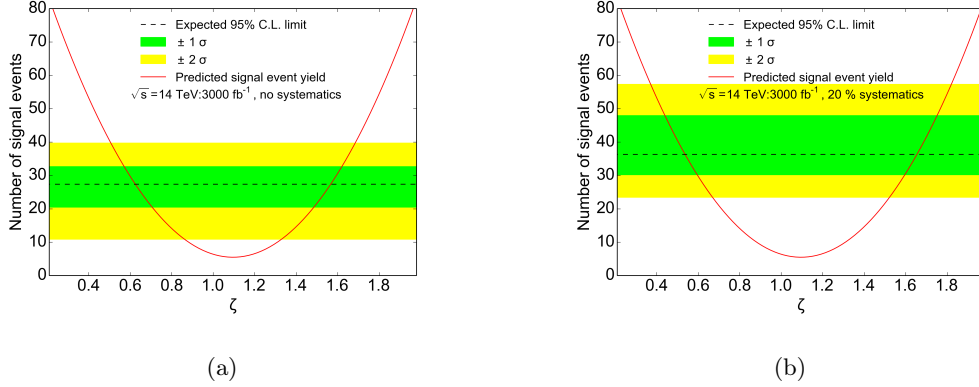
Figure 6.8:   Expected limits on the gauge-Higgs quartic couplings $\zeta = g_{V^\dagger Vhh}/g_{V^\dagger Vhh}^{\mathrm{SM}}$ under the assumption of no systematic uncertainties (a) and 20% systematic uncertainties (b). The 95% C.L. limit on ζ is defined by the value for which the expected number of theory events intersects with the experimental limit.

Shape comparisons for the rapidity and di-Higgs invariant mass distributions as motivated in the previous section are shown in Figure 6.7. Indeed, as expected, cutting on the rapidity distance between the jets will serve to purify towards a WBF-only selection at a reduced background rate. The dominant backgrounds are unlikely to produce a large invariant mass m_{hh}. However the WBF contribution, due to the lack of the $2m_t$ threshold peaks at a considerably lower invariant mass, leading to significant decrease of the WBF contribution for a reasonably strong cut on m_{hh}, which is required to observe the $hhjj$ signal at the given low signal yield, even at 3 ab^{-1} luminosity.

6.6.1 Prospects to isolate gluon fusion

We can extend the analysis outlined in Section 6.6 with the aim to purify the selection towards the GF component.* We make use of the hard Higgs candidates to greatly reduce the backgrounds by requiring $m_{hh} \geq 500$ GeV and additionally require $\Delta\eta(j1, j2) \leq 5$ to minimise the weak boson fusion contribution. The signal and background cross sections after these cuts are applied are presented in the 'GF Selection' column of Table 6.2.

The total background is reduced by a factor of ~ 100 while the gluon fusion contribution only is reduced by a factor of ~ 2.5 which allows for an encouraging

---

*Following the analysis of [282], we can expect negligible interference between WBF and GF and which allows us to make this distinction.
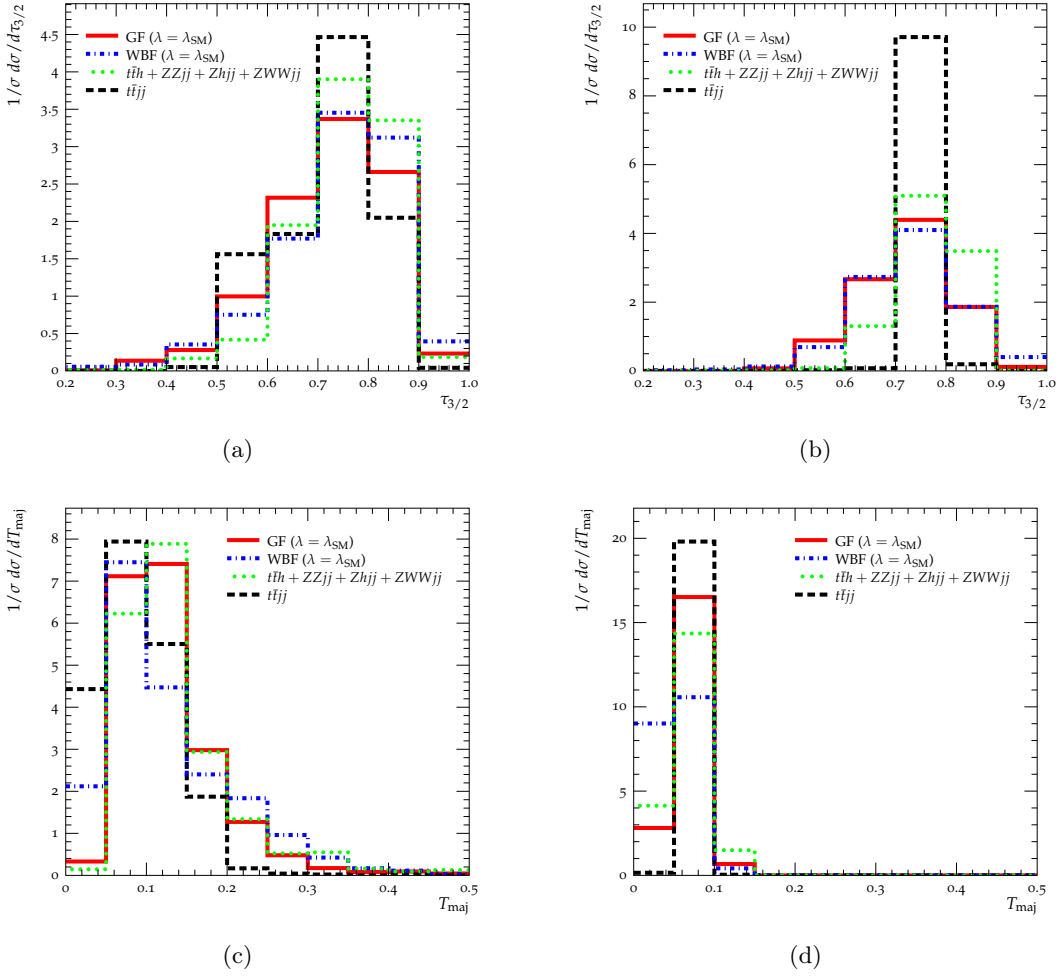
Figure 6.9: Shape comparisons of N-jettiness and thrust calculated in the major direction after the gluon fusion selection of Section 6.6.1 (a,c) and WBF Selection of Section 6.6.2 (b,d) have been applied. $\lambda = \lambda^3$ in our notation.

$S/\sqrt{B} \sim 1.7$ with 3 ab^{-1} of data. The weak boson fusion contribution is also suppressed compared to GF which allows for a clean probe of the physics accessible in the gluon fusion contribution.

6.6.2 Prospects to isolate weak boson fusion

Similarly we can extend the analysis towards isolating the WBF component. Since it has slightly softer Higgs candidates we require $m_{hh} \geq 400$ GeV and $\Delta\eta(j1, j2) \geq 5$ to reduce both the gluon fusion and background contributions. The signal and background cross sections after these cuts are applied are presented in the 'WBF Selection' column of Table 6.2.

The total background is reduced by a factor of $\sim$ 300 while three times more of the weak boson fusion contribution is retained compared to the GF selection, resulting in $S/\sqrt{B} \sim 0.8$ with 3 ab^{-1} of data due to the large reduction in the gluon fusion contribution. However even so the WBF selection is composed of one-to-three parts GF to WBF, which means measurements of physics that only enters the weak boson fusion contribution will need to take this gluon fusion "pollution" into account. This suggests a proper treatment of the gluon fusion component, as we have provided here, is crucial for any analysis relying on the WBF production mode.

6.6.3   Constraining the quartic $V^{\dagger}Vhh$ contribution

As mentioned in Section 6.5 there is a contribution from quartic $V^{\dagger}Vhh$ vertices to the WBF induced signal, and modifications of the corresponding $g_{V^{\dagger}Vhh}$ couplings away from their SM values using the Higgs Cross Section Working Group κ framework [194] will greatly enhance the signal cross section. This allows us to constrain ζ defined by $g_{V^{\dagger}Vhh} = \zeta \times g_{V^{\dagger}Vhh}^{\mathrm{SM}}$. To achieve this we have generated events with varying ζ using MADEVENT v5 and applied the WBF selections described in Section 6.6.2 to estimate the enhancement of the signal, which is compared to expected cross section limits on the signal with 3 ab^{-1} of data in the WBF selection under the assumptions of no systematic uncertainties and 20% total systematic uncertainties for comparison. The results are presented in Figure 6.8. We find that in the more realistic scenario of 20% systematic uncertainties the expected constraint on the $g_{V^{\dagger}Vhh}$ couplings is $0.55 < \zeta < 1.65$ at the 95% confidence level. A measurement of $pp \rightarrow hhjj$ is therefore crucial to constrain new physics which enters predominantly through enhancements to $g_{V^{\dagger}Vhh}$, which can be used as a proxy for investigating the nature of electroweak symmetry breaking as outlined in Section 3.1.1.

6.6.4   Event shapes of the tagging jets system

The analysis strategies outlined so far have mainly relied on exploiting correlations in the di-Higgs system, with only $\Delta\eta(j1, j2)$ carrying information about the tagging jets. Following similar applications in the context of single Higgs production [283], we have also investigated a range of event shapes in the tagging jets system. These could offer additional discriminating power through capturing colour correlations in the different signal contributions beyond angular dependencies. More specifically, we will present results for N-jettiness [284,285] and the thrust major which provided

the best results.

We calculate N-jettiness by minimising:

$$\tau_N = C \sum_k p_{T,k} \min(\Delta R_{k,1}, \ldots, \Delta R_{k,N}),\tag{6.2}$$

where C is a normalisation which cancels when taking the ratio of two τs, the sum is taken over all visible momenta which do not belong to one of the identified Higgs candidates within $|\eta| < 5$, and $\Delta R_{k,n}$ is the distance in the $\eta - \phi$ plane between the k-th momentum and the n-th reference vector (which are collectively defined such that they minimise Equation 6.2). $\tau_{3/2}$ is then explicitly given by τ_3/τ_2.

Thrust major is defined by maximising the scalar product with radiation in the plane perpendicular to the direction of the thrust vector:

$$T_{\mathrm{maj}} = \max_{\vec{n} \cdot \vec{n}_T = 0} \frac{\sum_k |\vec{p}_k \cdot \vec{n}|}{\sum_k |\vec{p}_k|}\ .\tag{6.3a}$$

Here $\vec{n}_T$ is the normalised thrust vector:

$$\vec{n}_T = \max_{\vec{n}} \frac{\sum_k |\vec{p}_k \cdot \vec{n}|}{\sum_k |\vec{p}_k|}\ .\tag{6.3b}$$

Again the sums run over all visible momenta which do not belong to one of the identified Higgs candidates within $|\eta| < 5$.

Both of these observables are very sensitive to radiation away from the jet axes in the event, and thus non-trivial colour connections in the underlying hard matrix element which generate such radiation.

We find $\tau_{3/2}$ and T_{maj} show promise for improving the WBF selection, but the signal cross section is already too low for us to be able to make meaningful use of this insight. The $\tau_{3/2}$ and T_{maj} distributions after the GF and WBF selections have been applied are presented in Figure 6.9. Cutting, for example, on $T_{\mathrm{maj}} < 0.05$, the gluon fusion contribution is reduced by 80%, while the WBF contribution is reduced by only 55% amounting to a total of 2 expected WBF and 0.3 expected GF events, with backgrounds very strongly suppressed. This means that WBF can in principle be observed at a small rate that can be used to set constraints on new physics in an almost GF-free selection with greatly reduced backgrounds.

The event shape distributions can also be used to greatly reduce the background in the GF selection as evident from Figure 6.9(c). It should be noted that these improvements of GF vs WBF vs background ultimately depend on underlying event and pile up conditions and have to be taken with a grain of salt in this hadron level analysis. However the clear separation that can be achieved with these observables

indicate that an analysis employing multivariate analysis techniques could, at least in theory, significantly improve the results presented here. These techniques may also prove useful at a 100 TeV collider where the di-Higgs production cross section is substantially higher [286].

6.7 $\mathcal{CP}$ structure of the Higgs sector

Having shown the potential of a measurement of $hhjj$ production to constrain λ^3 and $V^\dagger V hh$ vertices, we will also demonstrate its utility in constraining new operators in the Higgs-gauge sector. These can arise for example as the result of an enlarged Higgs sector. Here we will consider the case of $\mathcal{CP}$ violating effects from such an enlarged sector.

There is strong evidence that h can be characterised by a dominant $\mathcal{CP}$-even coupling pattern to gauge bosons [287, 288]. The sensitivity of this measurement is driven by large modified production rates compared to the Standard Model (SM) if $\mathcal{CP}$-odd couplings were dominant [289–291], as well as different kinematics if cross section information is not included in the analysis [288, 292–294].

The experimental observations of Higgs boson decays to electroweak bosons $h \to ZZ, WW$ outlined in Table 2.4 are already a strong indication of a $\mathcal{CP}$-even character of the gauge-Higgs interactions. A $\mathcal{CP}$-odd interaction parameterised by $\mathcal{L} \supset g_{Z\tilde{Z}h}/v\, hZ^{\mu\nu}\tilde{Z}_{\mu\nu}$ which overpowers the $\mathcal{L} \supset g_{hhZ}\, m_Z\, hZ^\mu Z_\mu$ term that follows from gauge boson mass generation through electroweak symmetry breaking (EWSB) would imply the breakdown of perturbation theory, only avoided if the longitudinal gauge boson degrees of freedom are generated by a mechanism which is not directly related to the observed Higgs boson with $m_h \simeq 125$ GeV. This would be difficult to reconcile with the otherwise successful description of the physics at this scale using perturbation theory. Taking the measurements in the ZZ channel at face value, the latter would need to be accompanied by a low scale of perturbative unitarity violation, well below the TeV scale, which is typically mended by either resolving a potential substructure responsible for the TeV scale or by accessing new resonant degrees of freedom. However, the LHC has already explored regions well beyond this regime without any evidence of neither weakly nor strongly-coupled degrees of freedom, as discussed in Section 2.4.2. In this sense, the statistically signifi-cant observation of $pp \to h \to ZZ$ alone does cement the very character of mostly $\mathcal{CP}$-even couplings to vector bosons, which is a generic property of spontaneous

symmetry breaking directly linked with perturbative unitarity of the Higgs-gauge sector [295, 296].

Strong constraints on $\mathcal{CP}$ violating interactions are typically inferred from flavor and electric dipole measurements [297–303]. These indirect probes of $\mathcal{CP}$ violation (which in the EDM context are strongest for interactions with first or second generation fermions) need to be contrasted with direct searches as performed by ATLAS and CMS. It is therefore natural to ask how $\mathcal{CP}$ violation can be accommodated by current Higgs measurements, in particular by the Run I combination of ATLAS and CMS data [34]. Given the absence of any conclusive hints for new resonant physics around the TeV scale, and taking into account the aforementioned unitarity-related issues, we can expect that a low energy effective formulation of TeV scale physics will reflect the imprint of a "good" probabilistic behavior of the underlying UV model. Understanding an effective theory formulation as the tool of mediating measurements between theories with widely separated scales, large fundamental $\mathcal{CP}$ violating effects at a scale that lies well above the electroweak scale could therefore present themselves at low scales in the guise of operators that do not immediately imply unitarity violation close to the TeV scale. Another possibility is the presence of additional intermediate degrees of freedom which could mend whatever unitarity violation that seems to be present above the TeV scale. Put differently, if no new particles are present, unitarity imposes a well-defined bias on the perturbative expansion of new physics effects in terms of a dimension six extended SM effective field theory framework [27]:

$$\mathcal{L} = \mathcal{L}_{\text{SM}} + \sum_i \frac{C_i(\mu^2)}{\Lambda_i^2} \mathcal{O}^i \,. \tag{6.4}$$

This hierarchy will be fully reflected by the Wilson coefficients if we choose all $\Lambda_i \equiv \Lambda \gg v$ in Equation 6.4 and limit ourselves to weakly-coupled UV theories. The latter point is required to give perturbative unitarity violation a well-defined meaning.

We will analyse the tree-level interplay of $\mathcal{CP}$ violation in the fermion-Higgs and gauge-Higgs sectors and unitarity using the tools of effective field theory. Assuming that amplitudes are well-behaved to high energies, we identify operators in Section 6.8 which are largely unconstrained by tree-level unitarity requirements. Using recent signal strength measurements as reported by ATLAS and CMS in [34], we analyse the direct phenomenological implications of allowed $\mathcal{CP}$ violation in the Higgs sector for future LHC exotics searches in Section 6.9. We provide a summary

of this work and offer conclusions in Section 6.10.

6.8 Unitarity and $\mathcal{CP}$ violating Operators

We consider the lowest order $\mathcal{CP}$-odd operators involving the physical Higgs field, which lead to CP-violation in conjunction of the CP-even operators in the Standard Model. A comprehensive list of operators has been presented in [304], for the purpose of this study we limit ourselves to a few key operators, which, on the one hand, are relevant to the dimension-6 framework. On the other, we also discuss the particular example of an operator which arises in the EFT expansion of Two Higgs Doublet Models, and allows us to make a connection to the dark matter-motivated extensions considered in Chapters 4 and 5.

In this study we work in the broken phase of $SU(2)_L \times U(1)_Y$ and consider $\mathcal{CP}$ violating operators effectively up to dimension 5. With this condition, we have the unique operator in the fermion-Higgs sector:

$$\mathcal{O}_4^{hff} = h\bar{\psi}_f\gamma_5\psi_f \,, \tag{6.5a}$$

with f denoting the Standard Model fermions ($f = u, d, s, c, b, t$).

In the gauge-Higgs sector, we consider the following operators:

$$\mathcal{O}_5^{hF\tilde{F}} = hF^{\mu\nu}\tilde{F}_{\mu\nu} \,. \tag{6.5b}$$

We use $F = (A, Z, W, G)$ as the (dual) field strengths of the photon, Z-boson, $W^{\pm}$-boson and gluon here. These operators can be generated by integrating out massive fermions with $\mathcal{CP}$-odd Yukawa couplings as in Equation 6.5a, and arise in general in non-linear Higgs EFT [305]. We also consider an alternative new dimension 4 operator in the gauge-Higgs sector:

$$\mathcal{O}_4^{hhZ} = h(\partial_\mu h)Z^\mu \,. \tag{6.5c}$$

This operator deserves a special comment as its appearance is linked to extending the dimension six EFT framework to a simplified multi-Higgs model, based on a two Higgs doublet model potential. If EWSB is triggered by more than one Higgs doublet, in the Georgi basis [306]* the kinetic term,

$$\mathcal{L}_{\text{kin}} = |D_\mu H_1|^2 + |D_\mu H_2|^2 \,, \tag{6.6}$$

---

*Given by $H_1 = [G^+, (v + h_1 + iG^0)/\sqrt{2}]^T$, $H_2 = [H^+, (h_2 + iA)/\sqrt{2}]^T$.

leads to the massless would-be Goldstone boson G^0 to be eaten by the Z boson,

$$\mathcal{L}_{\text{kin}} \supset m_Z \left(\partial_\mu G^0\right) Z^\mu . \tag{6.7}$$

This term is removed by R_ξ gauge fixing, while the $\mathcal{CP}$-odd A couples as:

$$\mathcal{L}_{\text{kin}} \supset \frac{gz}{2} h_2 (\partial_\mu A) \, Z^\mu - \frac{gz}{2} \left(\partial_\mu h_2\right) A \, Z^\mu . \tag{6.8}$$

If there is mass mixing between the $\mathcal{CP}$-even h_1, h_2 and odd A states as would be induced by a non-zero Im $\lambda_5^* \lambda_6^2$ in the 2HDM potential[*] [307] we have $\mathcal{CP}$ violation in the Higgs sector: the situation is similar to the neutral kaon K^0 system in the Standard Model. However we would not immediately induce the operator in Equation 6.5c as the expression in Equation 6.8 would disappear for $A, h_2 \to h_1$ after diagonalising since it is anti-symmetric. However if we allow dimension-6 operators,

$$\mathcal{L}_6 \supset \frac{c_6}{\Lambda^2} (H_1^\dagger D_\mu H_2)(H_2^\dagger D^\mu H_1) \supset \frac{c_6 v^2 \, g_Z \, i}{8\Lambda^2} \left[h_2 \left(\partial_\mu h_2\right) Z^\mu + A \left(\partial_\mu A\right) Z^\mu \right], \quad (6.10)$$

it becomes clear that Equation 6.5c is generically induced by an EFT expansion of a $\mathcal{CP}$ violating 2HDM. While the operator in Equation 6.5c therefore can be connected to $\mathcal{CP}$ violation in a 2HDM potential straightforwardly, we will also show how it can arise in a dark matter-inspired extension to a $\mathcal{CP}$ violating 2HDM. If there is in addition to the two Higgs doublet potential a portal-type real singlet scalar S we can postulate a dimension 5 operator:

$$\mathcal{L}_5 \supset \frac{c_S}{\Lambda} S \, (D_\mu H_1)^\dagger (D_\mu H_2) . \tag{6.11}$$

We then have additional interactions in unitary gauge:

$$\mathcal{L}_5 \supset \frac{c_S v \, g_Z}{4\Lambda} \left[S \left(\partial_\mu A\right) Z^\mu + i \, S \left(\partial_\mu h_2\right) Z^\mu \right] . \tag{6.12}$$

If we also introduce a portal interaction

$$V(H_1, S) \supset \eta \, |H_1|^2 \, S \supset \frac{\eta v_1 \, h_1 S}{2} , \tag{6.13}$$

we can see that mass mixing among the scalars in Equation 6.12 will induce Equation 6.5c.

---

[*]We use the standard conventions for the 2HDM potential in this section:

$$V(H_1, H_2) \supset \frac{1}{2}\lambda_5(H_1^\dagger H_2)(H_1^\dagger H_2) + \lambda_6(H_1^\dagger H_1)(H_1^\dagger H_2) + \lambda_7(H_2^\dagger H_2)(H_1^\dagger H_2) + \text{ h.c.} \tag{6.9}$$

While we only consider $\mathcal{CP}$ violation through mass-mixing here, it can also be introduced through interactions by non-zero Im $\lambda_5^* \lambda_7^2$ and Im $\lambda_7^* \lambda_6$.

$\mathcal{CP}$-mixing in the two Higgs doublet potential will then again link the operator in Equation 6.5c to $\mathcal{CP}$ violation in the Higgs sector. If $c_S v \sim \Lambda$, the operator in Equation 6.12 is not heavily mass suppressed and could potentially greatly enhance the amount of $\mathcal{CP}$ violation present thanks to the 2HDM potential.

While this setup appears somewhat contrived it is not unjustified from a BSM perspective: the singlet scalar portal is well-motivated in dark sector models as outlined in Section 5.3, and introducing a second Higgs doublet allows the couplings to quarks in a generic Z'-mediated simplified dark matter model to be completely spin-dependent which ameliorates tension with direct dark matter detection constraints, as discussed in Section 4.4. In this sense this model could arise naturally as a so-called Two Mediator Dark Matter Simplified Model [308] generalisation of the model presented in Chapter 4, where S is interpreted as the dark Higgs.

Since we are not interested in the effects of other new operators we assume that the additional states are sufficiently heavy to not immediately influence the Higgs decay phenomenology as well as unitarisation rules through additional channels opening up. We therefore assume h is dominantly composed of h_1 in the following.[*] We will see that this particular coupling is perturbatively unconstrained.

In order to respect the stringent flavor constraints which exist we only consider flavour diagonal operators as in Equation 6.5a. With these operators we can calculate the high energy behavior of $2 \rightarrow 2$ scattering amplitudes from an initial state i to a final state f, using the partial wave decomposition introduced in Section 2.4.2.1. As discussed there, unitarity together with perturbativity (which we also have to impose for an expansion of the operators in Equation 6.5 to be meaningful) requires the partial waves to be small compared to unity and we will define the critical value of the Wilson coefficients in our theory by saturating

$$|a_j^{fi}(\Lambda)| = 1 \,. \tag{6.14}$$

Λ should here be read as the highest scale at which we require our EFT to be consistent.

We will consider the following Lagrangian:

$$\mathcal{L} = \mathcal{L}^{\mathrm{SM}} + C_{hhZ} \, h(\partial_\mu h) Z^\mu + C_{htt} \, h \bar{t} \gamma^5 t + \sum_{F,\tilde{F}} \frac{C_{hF\tilde{F}}}{v} \, \mathcal{O}_5^{hF\tilde{F}} \,. \tag{6.15}$$

---

[*]It should also be noted that the presence of multiple mixings typically yields a more SM-like phenomenology of the lightest state in terms of signal strengths as compared to minimal Higgs portal scenarios [182].
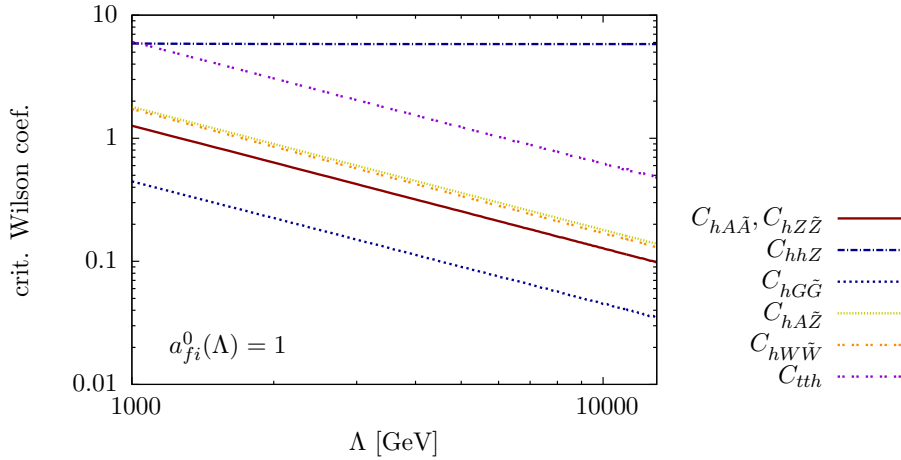
Figure 6.10: Saturation value of the Wilson coefficients of the operators in Equation 6.15 for the zeroth partial wave in $2 \to 2$ scattering. Λ should here be interpreted as the intended cutoff scale of the effective theory: if $C_i(\Lambda)$ is greater than the critical value, the effective theory is not perturbatively unitary. In this sense the critical value can be seen as a theoretical limit on the allowed contributions from these operators as a function of the cutoff scale of the Standard Model.

We focus on the top quark for the reasons outlined in Section 3.1.1 and choose the electroweak vacuum expectation value as reference scale where necessary. Typically the partial waves exhibit a hierarchy in the angular momentum J.

We have surveyed the list of processes relevant for unitarity violation at tree-level. These include vector, Higgs and fermion scattering, as well as combinations of the different particle species [309, 310]. We find that the tightest constraints follow from the $J = 0$ projections and will focus on the most constraining channels, but also mention other channels that are relevant for the discussion of the remainder of this study. Our results are collected in Figure 6.10 and we detail them below:

$\mathcal{O}_4^{hff}$: We first consider fermion-fermion scattering $t\bar{t} \to t\bar{t}$, which receives contributions from the operator in Equation 6.5a. We include the (modified) Higgs, Z boson and photon intermediate states and discard the gluon contribution as it corresponds to a non-trivial colour configuration, which does not interfere with the colour singlet exchange. The zeroth partial wave of $t\bar{t} \to t\bar{t}$ for identical helicity (zero total angular momentum) gives rise to only weak constraints on the Wilson coefficient $|C_{htt}| \simeq 7.1$, not dependent on the scale Λ. The amplitude also quickly approaches an asymptotic value as a consequence of

energy scales cancelling between the spinor normalisations and the *s*-channel suppression leading to an energy-independent value.

Superior bounds can be obtained from $t\bar{t} \to V_L V_L$. Note that due to the vertex structure induced by the operators of Equation 6.5, the Wilson coefficients $C_{hF\tilde{F}}$ do not contribute to scattering processes involving longitudinally polarized vector bosons.* Hence, the limit obtained from inelastic fermion scattering to gauge bosons provides a way to derive stringent unitarity constraints on C_{tth} without the influence of accidental cancellations between the interactions in the lagrangian 6.15. It is worth noting that the $\mathcal{CP}$-odd Higgs interactions therefore also exhibit a completely different unitarity-related behavior than their $\mathcal{CP}$-even counterparts [40]. Numerically we find that $t\bar{t} \to W_L^+ W_L^-$ provides the most stringent constraint among these channels as the amplitude shows a $\sim C_{tth}\sqrt{s}$ behavior.

$\mathcal{O}_5^{hF\tilde{F}}$: We derive unitarity bounds on the Wilson coefficients $C_{hA\tilde{A}}, C_{hZ\tilde{Z}}$, and $C_{hg\tilde{g}}$ through investigating $VV \to VV$ scattering for transverse polarisations of the participating vector bosons $V = A, Z, g$. For equal helicity and transverse ZZ scattering we obtain, for example,

$$\mathcal{M}(Z_T Z_T \to Z_T Z_T) = -\frac{4C_{hZ\tilde{Z}}^2}{v^2} \frac{s\left(s - 4m_Z^2\right)}{s - m_h^2} + \{\text{SM}\}, \qquad (6.16)$$

where {SM} refer to the well-known results of the SM [40], which do not give rise to unitarity violation. For the massless gluons and photons we find a similar relation for the unitarity violation-driving part.

The channels involving both A and Z introduces a cross-talk between the $C_{hA\tilde{A}}, C_{hA\tilde{Z}}$ and $C_{h\tilde{A}Z}$ channels and the results quoted in Figure 6.10 are calculated assuming $C_{hA\tilde{A}}, C_{h\tilde{A}Z} = 0$, which allows us to set constraints on $C_{hA\tilde{Z}}$ individually.

$\mathcal{O}_4^{hhZ}$: $J = 0$ unitarity constraints on this operator are calculated from multi-Higgs scattering. For $t\bar{t} \to hh$ in the equal helicity case, we obtain

$$\mathcal{M}(t\bar{t} \to hh) = \frac{e}{2s_W c_W} \frac{m_t \sqrt{s}}{s - m_Z^2} C_{hhZ} + \{\text{SM}\}, \qquad (6.17)$$

---

* The Feynman rule for the vertex induced by the operator in Equation 6.5 is given as $\propto \varepsilon_{\alpha\beta\mu\nu} p_1^\mu p_2^\nu$, which vanishes when contracting with the longitudinal polarization vectors of external gauge bosons: $\varepsilon_{\alpha\beta\mu\nu} p_1^\mu p_2^\nu \varepsilon_L^\alpha(p_1) \varepsilon_L^\beta(p_2) = 0$.

Wilson coefficient	Most sensitive channel	Scaling of $\lvert\mathcal{M}\rvert$ at large s	limit at $\Lambda = 5\,\mathrm{TeV}$
C_{tth}	$t\bar{t} \to W_L^+ W_L^-$	$C_{tth}\sqrt{s}$	1.24
$C_{hF\tilde{F}}$	$V_T V_T \to V_T V_T$	$C_{hF\tilde{F}}^2 s$	0.26
$C_{hG\tilde{G}}$	$g_T g_T \to g_T g_T$	$C_{hG\tilde{G}}^2 s$	0.09
$C_{hA\tilde{Z}}$	$Z_T A_T \to Z_T A_T$	$C_{hA\tilde{Z}}^2 s$	0.36
C_{hhZ}	$hh \to hh$	C_{hhZ}^2	5.82

Table 6.3: Representative values of perturbative unitarity constraints of the operators considered in this work at $\Lambda = 5\,\mathrm{TeV}$, in addition to the most sensitive channel to unitarity constraints.

which shows that only weak constraints can be derived from this channel as the amplitude becomes quickly negligible at energies $\sqrt{s} \gg m_Z$ even when $C_{hhZ} \neq 0$. This result also shows that unitarity constraints from the fermion sector are parametrically suppressed by the quark mass and that the top-quark sector will provide the most dominant unitarity constraints.

$hh \to ZZ$ and $hh \to WW$ induced by $\mathcal{O}_4^{hhZ}$ vanish, irrespective of helicities. This also holds for $hh \to hZ_L$, leaving only $hh \to hh$ as a potentially sensitive channel to C_{hhZ} for $J = 0$. In this channel, however, crossing symmetry guarantees that the amplitude can only have a small sensitivity on the energy of the scattering process for $s \gg m_Z^2, m_H^2$. With $s + t + u = 4m_h^2$ and this cancellation only slightly affected by the different propagators of the s, t, u channels for large enough energy, the unitarity constraint becomes largely insensitive to the probed energy (Figure 6.10). Amplitudes for $ZZ \to hZ$ vanish irrespective of polarisations; $WW \to hh$ does not receive contributions from $\mathcal{O}_4^{hhZ}$ insertions, and $hh \to hZ_L$ is suppressed by an order of magnitude compared to $hh \to hh$ at the amplitude level.

Table 6.3 summarises the constraints on the Wilson coefficients we've found in this section based on the perturbative unitarity argument. Out of the operators we consider in this work, $\mathcal{O}_4^{hhZ}$ is special in the sense that perturbative unitarity arguments do not limit the associated Wilson coefficient's range. This means that a
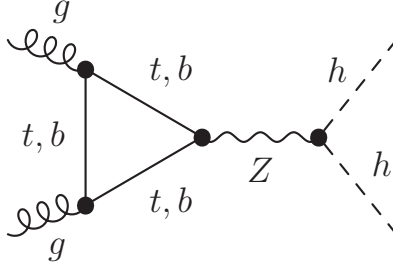
Figure 6.11: New contribution to Higgs pair production from gluon fusion $gg \to hh$, induced by the operator $\mathcal{O}_4^{hff}$. We suppress the fermion flow directions as well as SM contributions.

potentially large $\mathcal{CP}$ violation with this term could be induced by a non-perturbative or perturbative UV completion.

6.9   *hhjj* as a window into the $\mathcal{CP}$ violating Gauge-Higgs sector

Considering $\mathcal{CP}$ violation in the Higgs-gauge sector in a collider phenomenology context, we will therefore focus on the operator $\mathcal{O}_4^{hhZ}$ which is weakly constrained by unitarity arguments. Such an operator will impact multi-Higgs final states. The dominant process of this type is Higgs pair production through gluon fusion $gg \to hh$, which can receive a new Z boson-mediated contribution from $\mathcal{O}_4^{hhZ}$.[*] However, since $t\bar{t} \to hh$ does not give rise to an energy-dependent unitarity constraint, we can already anticipate that the absorptive parts of the $gg \to hh$ amplitude will be largely unaffected.

In Figure 6.12 we compare sensitivity estimates for di-Higgs productions from ATLAS [311] and CMS [312] with the expected enhancement of $pp \to hh$ at the LHC due to the operator $\mathcal{O}_4^{hhZ}$. The most optimistic constraints that can be set from this channel result from the 1.9-σ significance reported by CMS for the $b\bar{b}\gamma\gamma + b\bar{b}\tau^+\tau^-$ combination [312], which translates into a Wilson coefficient constraint

$$|C_{hhZ}| \lesssim 16.5 > 4\pi\,. \tag{6.18}$$

This constraint is weaker than the perturbative limit and does not probe the unitarity limit imposed by $hh \to hh$ scattering from Figure 6.10. This result is expected in

---

[*]Note that the bottom contribution needs to be included to avoid spurious loop singularities related to $SU(3)^2 \times SU(2)$ anomaly cancellations.

the light of our unitarity discussion of Section 6.8 and means the dominant di-Higgs production channel can not be used to constrain the operator.

The observed sensitivity of $pp \to hh$ to $\mathcal{O}_4^{hhZ}$ dominantly arises from contributions of Equation 6.17, which contribute to the imaginary part of the loop-induced $gg \to hh$ amplitude near the the threshold $m(hh) \simeq 2m_t$ through modifying the interference pattern that exists in gluon fusion between the box- and triangle-induced amplitude contributions (see Section 2.4.2.2). While the interference is modified, the magnitude of this change induced by $\mathcal{O}_4^{hhZ}$ quickly dies out for larger di-Higgs invariant masses. This kinematic suppression cannot be circumvented, but it points to a different channel that accesses a distinct kinematic configuration of $\mathcal{O}_4^{hhZ}$, which is not probed by the unitarity constraints of Figure 6.10 - di-Higgs production through weak boson fusion (WBF), which accesses t-channel virtual massive gauge bosons, Figure 6.13.

This leads to a sizeable contribution to WBF-induced di-Higgs production, which can be investigated through the $hhjj$ final state as outlined in Section 6.6.2 above. We make a projection of the HL-LHC's expected sensitivity to C_{hhZ} by generating
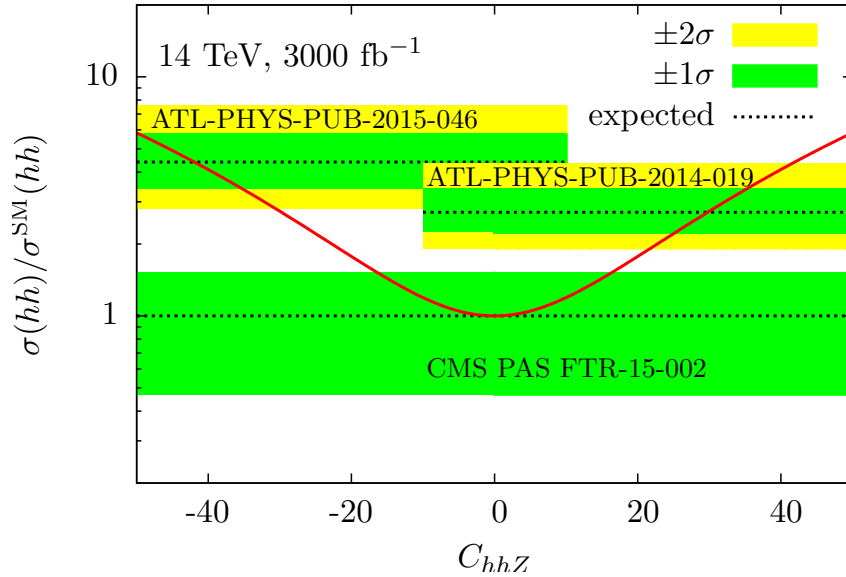
Figure 6.12: The expected exclusions of ATLAS [211, 311] and CMS [312] for the high-luminosity (HL)-LHC (3000 fb^{-1}, 14 TeV) for $pp \to hh + X$, overlaid by the di-Higgs cross section as a function of C_{hhZ} relative to the SM expectation. To highlight the different ATLAS exclusions, we do not plot them across the entire Wilson coefficient range.
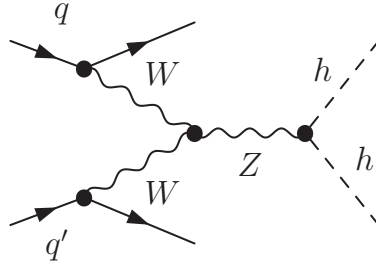
Figure 6.13: Representative Feynman diagram contributing to Higgs pair production from weak boson fusion $pp \to hhjj$, induced be the operator $\mathcal{O}_4^{hhZ}$.
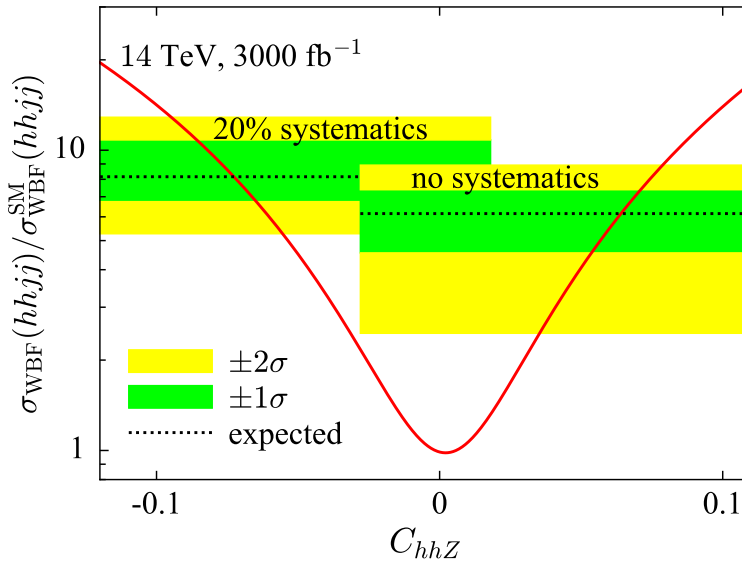
Figure 6.14: The expected exclusion for the high-luminosity (HL)-LHC (3000 fb^{-1}, 14 TeV) for the WBF-induced component of $pp \to hhjj$ using the analysis detailed in the text, overlaid by the cross section as a function of C_{hhZ} relative to the SM expectation. Two different systematics scenarios are assumed.

hadron level $hhjj$ events using MadEvent [128] and Herwig [313], and use the results from Section 6.6.2 to make a projected sensitivity estimate using the CLs method [314, 315]. To show the impact of uncertainties we again provide limits based on using 20% flat background systematics as well as excluding systematics for comparison in Figure 6.14.

Accessing the t-channel W and Z bosons in the initial state enhances the sensi-

tivity to C_{hhZ} way below the unitarity limit, with the expected constraints

$$|C_{hhZ}| \lesssim 0.06 \,, \tag{6.19}$$

well within the validity of the perturbative expansion of Equation 6.15.

6.10 Conclusions

After discovering single Higgs production at the Large Hadron Collider, new analysis strategies need to be explored to further constrain the presence of new physics beyond the Standard Model. Higgs pair production is pivotal in this regard as constraints from multi-Higgs production contain complementary information, in particular with respect to the Higgs boson's self-interaction. Cross sections for di-Higgs production are generically small at the LHC, which highlights the necessity to explore other viable channels than $pp \to hh$ to enhance sensitivity in a combined fit at high luminosity. To this end, we have investigated $pp \to hhjj$ production in detail in this study. Keeping the full top and bottom mass dependencies, we find sensitivity of $pp \to hhjj$ searches at the LHC for production in the SM and beyond. The gluon fusion contribution remains important at high invariant di-Higgs masses where the dominant backgrounds can be suppressed to facilitate a reasonable signal vs background discrimination. It remains large even for selections that enhance the weak boson fusion fraction of $pp \to hhjj$ events. This "pollution" is important when such selections are employed to set constraints on new physics effects that enter in the WBF contribution exclusively. Large new physics effects in the WBF contribution can still be constrained, which we have illustrated through an investigation of the constraints that can be set on deviations of the quartic $V^\dagger V hh$ couplings from their SM values with the HL-LHC, demonstrating that a measurement of $pp \to hhjj$ will provide a powerful probe of these. Employing observables which are intrinsically sensitive to the different colour correlation of WBF compared to GF, the discrimination between GF, WBF, and background can be further improved. However, the signal cross section is typically already too small to use such a strategy to constrain the presence of new physics if those effects are only a small deviation around the SM. If new physics effects are sizable, such an approach will remain a well-adapted strategy to minimise GF towards a pure WBF selection.

We have also considered $\mathcal{CP}$ violating effects in extensions to the Higgs sector, and shown that many such extensions can be strongly constrained by requiring their general description in terms of an effective theory to be perturbatively unitary at

the cutoff scale of the effective theory. A particular operator, $\mathcal{O}_4^{hhZ} = h\partial_\mu h Z^\mu$, which will arise in for example $\mathcal{CP}$ violating 2HDM models and extended simplified dark matter models, turns out to not be sensitive to such theoretical constraints. We have also shown that this operator is difficult to constrain with a measurement of $pp \to hh$ production, but that $hh \to hhjj$ production offers a highly sensitive probe.

Constraining resonances in the $t\bar{t}$ spectrum using polarisation information

7.1 Attribution Notice

This chapter is based on results first published in [5] which I wrote together with Dr. Christoph Englert and Dr. James Ferrando. I performed all calculations and created all figures.

Contents

7.2 Summary

As outlined in Sector 3.1.1, the large top Yukawa coupling suggests the top quark could play a special role in electroweak symmetry breaking. In this chapter we will

present a comprehensive study of the BSM applications of measuring the polarisation of top quarks in a top resonance search context, and interpret constraints that can be derived from such an analysis in terms of a Randall-Sundrum model where the right-handed top quark plays such a privileged role. We focus on kinematically challenging regions of the parameter space where ATLAS and CMS start losing sensitivity due to the width of the expected resonance. Following the general modeling and analysis strategies pursued by the experiments, we analyse the semi-leptonic and the di-lepton $t\bar{t}$ channels and show that including polarisation observables can provide considerable shape information with large data sets. This will allow us to set limits for parameter choices where sensitivity from $m(t\bar{t})$ is not sufficient. In a wider context we use this to point out the importance of spin observables as part of a more comprehensive set of observables to gain sensitivity to BSM resonance searches.

7.3 Spin observables for top resonance searches at the LHC

Given the lack of any conclusive hint for new physics beyond the Standard Model at the Large Hadron Collider so far, it is interesting to consider avenues to enhance the sensitivity of searches that target new states and interactions which are kinematically accessible.

Observables which directly reflect the final state momentum transfer, such as invariant mass or transverse momentum distributions, are obvious choices for searches for new resonant states. However, if the new physics production cross section is small, these observables might not have enough shape information to isolate the signal from the competing backgrounds satisfactorily. In these circumstances, the LHC experiments typically favor multivariate techniques over rectangular cut flows. While this approach can increase the sensitivity dramatically, care needs to be taken during the training stage of the analysis. In particular, experimental constraints (such as the detector's granularity, response effects and so on) need to be included and understood precisely in order to formulate a realistic sensitivity estimate. The optimisation of these methods lies firmly within the remit of the expertise of the experimental community. Observables which enhance the sensitivity in a cut-flow based analysis will retain their power when used in such a context, so from this perspective it is still useful to investigate individual observables. Additionally this also allows us to gain a physical understanding of where the shape information comes

from which can be absent in high-dimensional multivariate analyses.

For instance, constraints on the production cross section of new resonant states derived from mass resonance searches are strongly dependent on the assumed width of the new state. Larger widths reduce the shape information the pole of the resonance provides when in the energy range of a collider as the signal increasingly resembles a continuum excess rather than a localised peak. We will show that spin polarisation observables are precisely observables which can provide complementary shape information in such a case.

In this study we will focus on an extra-dimensional model used as a benchmark for top resonance searches by both ATLAS and CMS, see for example [316, 317]. This compactified Randall-Sundrum (RS) model [22] introduces a series of isolated graviton resonances into the 4D effective theory. If SM fields propagate in the entire five-dimensional Anti-de Sitter (AdS) background geometry, the 4D theory will also contain Kaluza-Klein copies of the low energy states that are identified with the SM.

The ATLAS study in [316] demonstrates that the constraint on the production cross section of a 3 TeV gluon g_{KK} decaying to $t\bar{t}$ weakens by almost an order of magnitude when going from $\Gamma/m = 10\%$ to $\Gamma/m = 40\%$. Such large widths can be problematic from a modeling perspective, as discussed in Section 4.4, but are not unexpected in strongly-coupled theories inherent to the dual formulation of RS-type theories. In fact, one of the coupling choices we will make in our analysis corresponds to a width of $\Gamma/m = 37.5\%$, to be compared to $\Gamma/m \approx 15\%$ for the default coupling choice made for the standard ATLAS and CMS benchmark point. This does not require the presence of additional strongly coupled states in the direct vicinity as these are given by the higher Kaluza-Klein modes which still are well-separated in mass, although the convolution with parton densities could in practice produce a non-negligible contribution at lower masses as their widths also get large. We will assume such contributions are not relevant for the purposes of this study.

From the AdS/CFT [318–321] perspective, the top quark being the heaviest particle discovered so far plays a special role as its mass could be direct evidence of (at least partial) compositeness. A potential composite structure of extra resonances could therefore be reflected in the analysis of the associated top quark spin observables, while a $t\bar{t}$ bump search alone does not access this level of detail.

These BSM-induced effects can be contrasted with the fact that $t\bar{t}$ production in the SM at the LHC is dominated by parity-invariant QCD processes. We therefore

can expect to produce almost unpolarised tops. At the high invariant masses we consider there is a sizeable contribution from weak processes which makes the SM expectation slightly left-handed: for $m(t\bar{t}) > 3$ TeV, $P_t \approx -0.15$ where $P_t = +(-)1$ correspond to completely right-(left-)handed tops. This fact has inspired many studies of top polarisation as a probe into BSM physics, both in pair [322–324] and single [325–328] production. As the decays of Kaluza-Klein gluons g_{KK} and gravitons G_{KK} in our model are dominated by right-handed tops these distributions are modified for the signal component as pointed out in for example [329, 330].

The crucial point which motivates our expectation that spin observables will carry additional shape information is that increasing the width of a parent particle only has a modest effect on the spin observables of its decay products. Therefore, they should offer a great opportunity to not only access more shape information generically, but also maintain this shape information when considering wider signal models. We will show that this allows enhancements to the sensitivity of analyses like [316].

In this study we consider $pp \to g_{KK}/G_{KK} \to t\bar{t}$ production and focus on both the semi-leptonic and di-leptonic final states of the top decays in the region where the reported sensitivity is low. Our goal is to determine to what extent top polarisation and spin correlation measurements allow us to make stronger empirical statements for the models studied in for example [316].* Our results can be considered as a litmus test which motivates the inclusion of such observables in analyses based on the aforementioned multivariate techniques pursued by the experiments, and gives a solid theoretical basis for the gains in sensitivity that can be achieved by doing so.

This chapter is organised as follows: in Section 7.4 we introduce the model and discuss relevant parameter choices for our analysis to make this study self-consistent. In Section 7.5.1 we discuss the semi-leptonic final state, while Section 7.5.2 focuses on the di-leptonic final state. In Section 7.6 we summarise our results and we present our conclusions in Section 7.7.

7.4   The Model

In RS1 models [22] the hierarchy problem is solved by introducing an extra compactified dimension $r_{\mathrm{UV}} < z < r_{\mathrm{TeV}}$ with a warped anti-de Sitter geometry AdS_5. This

---

*While our search focuses specifically on the Randall-Sundrum model as it allows us to investigate the interplay of spin observables and cross sections in a theoretically self-consistent way, they directly generalise to a Z' case with chiral couplings to 3rd generation fermions.

explains fine-tuning in $M_{\mathrm{Planck}}/M_{\mathrm{Weak}}$ in terms of the localisation of the 4D graviton near the "Planck" brane, $z = r_{\mathrm{UV}}$ with a fundamental scale of M_{Planck} and the Higgs sector near the "TeV" brane, $z = r_{\mathrm{TeV}}$, with a fundamental scale of M_{Weak}. Thanks to the warped geometry we then expect $M_{\mathrm{Planck}}/M_{\mathrm{Weak}} \sim \exp\{\pi k(r_{\mathrm{TeV}} - r_{\mathrm{UV}})\}$, where k is the AdS curvature scale and $r_C = r_{\mathrm{TeV}} - r_{\mathrm{UV}}$ is the size of the extra dimension. This is solved by $kr_C \sim 11$ for the observed values of the Planck and weak scales, and hence massively reduces the required fine-tuning.

If the SM fermions propagate in all five dimensions, we can additionally explain the structure of the Standard Model Yukawa sector through localisation [23]. The profile of the fermions' wave function is determined by a localisation factor ν which exponentially peaks towards the Planck brane for $\nu < -1/2$ and towards the TeV brane for $\nu > -1/2$ (this can be understood as mixing with CFT bound state in the dual picture). To avoid electroweak constraints from $Z \to b_L \bar{b}_L$ while reproducing the correct Yukawa structure we will set $\nu_{t_R} > \nu_{Q3_L} > \nu_{\mathrm{other}}$ following [331]. In general we will keep $\nu_{\mathrm{other}} < -1/2$.

Setups with the right-handed top quark localised close to the TeV brane, a flat third generation left-handed quark doublet profile, and the other fermions localised close to the Planck brane are phenomenologically viable [331]. Thanks to t_R living on the TeV brane and $(t,b)_L$ being almost flat, the dominant decay mode of g_{KK} and G_{KK} is to $t_R \bar{t}_R$.

These are typical parameter choices that underpin the experimental analyses. For the graviton, branching fractions to hh and $V_L V_L^\dagger$ are also sizeable as the Higgs and therefore also the longitudinal modes of the weak bosons are located on the TeV brane, but strong constraints on the masses of both particles $m(g_{KK})$ and $m(G_{KK})$ can be derived from top resonance searches [316, 317].

Our model setup therefore follows ATLAS and CMS [316, 317] but varies slightly between the gluon and graviton signals. In general the gluon will always be easier to discover due to much larger cross sections as it can be produced efficiently through $u\bar{u}$ and $d\bar{d}$ annihilation, whereas graviton production is dominated by gluon fusion. As such it does not make sense to compare identical parameter points and we focus on choices which give a (relatively) narrow and a wide resonance for each signal model.

For our graviton samples we use the model file from [332] and consider the above extreme case where t_R is localised on the TeV brane (i.e. being fully composite), $Q3_L$ is very close to flat, and the decay widths of the lightest KK graviton resonance

therefore are:

$$\Gamma(G^1 \to t_R \bar{t}_R) = 9\frac{(3.83c)^2 m_{G^1}}{960\pi} \, , \tag{7.1}$$

$$\Gamma(G^1 \to \phi\phi) = 4\frac{(3.83c)^2 m_{G^1}}{960\pi} \, , \tag{7.2}$$

with $c = k/M_{\text{Planck}}$. The factor of 3.83 is the first root of the Bessel function J_1 which is encountered in RS models for the wave function along the compactified direction, and which stems from the boundary condition for gravitons. ϕ here sums over the components Z_L, W_L, and h of ϕ as outlined in Section 2.4.2. Decays to right-handed tops are therefore dominant at $\sim 70\%$ and offer good prospects for detection, however, both ZZ [333] and WW searches offer additional information [334, 335]. We consider two values of $c = \{1, 2\}$ which correspond to widths of $\Gamma_{G^1}/m_{G^1} = \{6.2\%, 25\%\}$. While $c = 2$ is in the upper end of the range where we can trust our assumption that higher curvature terms can be neglected in our calculations [333] this is a useful point to consider in order to have a wide, fully polarised resonance as one of our benchmark points. Note that our model setup has $m_{G^1} \approx 1.5 m_{g^1}$ which would put our chosen mass points in tension with current constraints on m_{g^1}, however our intention is to show the value of adding polarisation information to searches and G^1 is a useful example of a source of a fully polarised resonance: searches for g^1 will in general always be more sensitive due to the more efficient production mechanism.

For our gluon sample, generated with the model file introduced in [336], we soften the localisation requirement and set $\nu_{Q3_L} \sim -0.4$ and vary $\nu_{t_R} \sim \{-0.3, 0\}$ which corresponds to effective couplings of $g_{g^1 b_L \bar{b}_L} = g_{g^1 t_L \bar{t}_L} = g_S$, and $g_{g^1 t_R \bar{t}_R} = \{2, 6\}g_S$. These give widths of $\Gamma_{g^1}/m_{g^1} = \{6.2\%, 37.5\%\}$ and branching ratios to $t\bar{t} = \{78.5\%, 96.5\%\}$. While always dominated by right-handed tops, the fraction of right-handed to left-handed tops also changes which should be reflected in the polarisation observables.

7.4.1 Event Generation and Analysis

Our background is leading order semi- and di-leptonic $t\bar{t}$ samples generated using MADGRAPH 5 [128, 239] and reweighted to the NNLO cross section given in [337–339]. We focus on $\sqrt{s} = 14$ TeV collisions. Our signal samples are also generated with MADGRAPH using the UFO model format [240] to import models implemented in the FEYNRULES [127] language. These parton level samples are then showered in HERWIG 7.0.3 [264, 340] and analysed using the Rivet framework [137] which

we also use for applying smearing and efficiencies to the physics objects according to typical ATLAS Run II resolutions (where available, with Run I resolutions used otherwise) [341–343] at the beginning of the analysis routine.

7.5 Analyses

7.5.1 Semi-leptonic study

7.5.1.1 Analysis Selections and Reconstruction

The analysis of the semi-leptonic samples focuses on reducing non-$t\bar{t}$ backgrounds and reconstructing the individual tops, largely following the boosted approach detailed in [316]. We start by finding electrons with $p_T > 25$ GeV for $|\eta| < 2.47$ and muons with $p_T > 25$ GeV with $|\eta| < 2.7$. We then cluster narrow anti-k_T [63] $R = 0.4$ jets with $p_T > 25$ GeV inside $|\eta| < 2.8$ and fat Cambridge-Aachen [62, 344] $R = 1.2$ jets with $p_T > 250$ GeV inside $|\eta| < 2$, and require at least one of each after removing narrow jets which overlap with the leading fat jet.

Since we are interested in highly boosted tops, we have to accept some overlap between the lepton and b-jet on the leptonic side so we do not require these to be isolated and assume we can veto events with hard leptons from heavy flavour decays inside QCD-produced jets.* Following [346], we top-tag the leading fat jet with HEPTOPTAGGER [347, 348] mostly using the default setup of [348]. Note our choice of $R = 1.2$ is well-motivated compared to the choice of $R = 1.5$ in the benchmark study in [348] since we consider much heavier resonances. Our only deviations from the default setup is that we require the candidate to have a mass between 140 and 210 GeV and a $p_T > 250$ GeV, since widening the mass windows allows us to gain some statistics while still keeping non-$t\bar{t}$ backgrounds negligible and our signal tops are so highly boosted that there is no loss in efficiency in a slightly higher cut in p_T. This provides our hadronic top candidate and we require at least one of the narrow jets to be b-tagged with an efficiency of 70% and fake rate of 1%, see for example [278].

Our narrow jets tend to be quite hard since we are interested in the high-$m_{t\bar{t}}$ region but we have checked that the leading narrow jet p_T distribution peaks in the range from 50 GeV to 300 GeV where the MV1 algorithm used by ATLAS outperforms this naive estimate [349] for our signal samples. To reflect the degradation of

---

*See [345] for a proof-of-principle investigation using the muon final state.
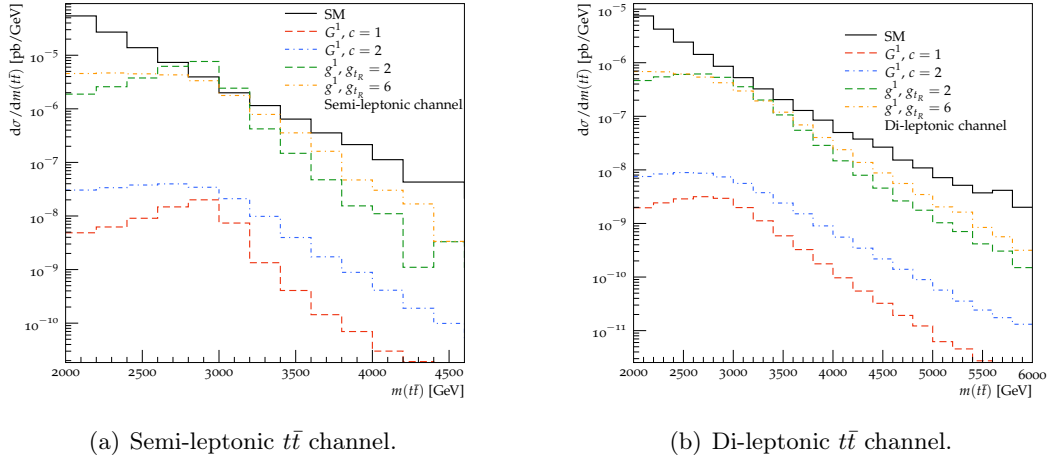
(a) Semi-leptonic $t\bar{t}$ channel.

(b) Di-leptonic $t\bar{t}$ channel.

Figure 7.1: Distributions of $m(t\bar{t})$ for the semi-leptonic (a) and di-leptonic (b) analyses for the background SM $t\bar{t}$ and signal samples after all analysis selections and detector effects. Note that the semi-leptonic analysis manages to reconstruct peaks for the narrow signal models, whereas the di-leptonic one smears out all of the signal models into something resembling continuum excesses.

performance at higher p_T, we use a fake rate for light quarks and gluons of 10% above 300 GeV. We have checked that combining the p_T-dependent b-tagging with contemporary top-tagging techniques renders the Wjj background negligible compared to SM $t\bar{t}$ production at our signal mass points. We expect other SM backgrounds to be negligible: we find lower signal Acceptance $\times$ Efficiencies than the 13 TeV ATLAS study in [350] thanks to our stricter top-tagging which further suppresses all non-$t\bar{t}$ backgrounds. The final sensitivity of our study could potentially be improved by using a more permissive top-tagging algorithm and taking care to estimate non-$t\bar{t}$ background contributions.

In the next step, we require missing transverse energy $\not{p}_T$ with $|\not{p}_T| > 20$ GeV and $|\not{p}_T| + m_T > 60$ GeV where $m_T = \sqrt{2p_{T,l}|\not{p}_T|(1 - \cos\phi_{l\not{p}})}$.

We reconstruct the leptonic W by assuming that its decay products are the leading lepton and a neutrino, which accounts for all of the reconstructed missing transverse momentum. The longitudinal component of the neutrino momentum is found by assuming the W is produced on-shell, and we choose between the two resulting solutions by picking the one which minimises $|m_{bl\nu} - m_t|$ after combining with the leading b-tagged jet. This object is our leptonic top candidate.

We extract $m(t\bar{t})$ by adding the found leptonic and hadronic top candidates and
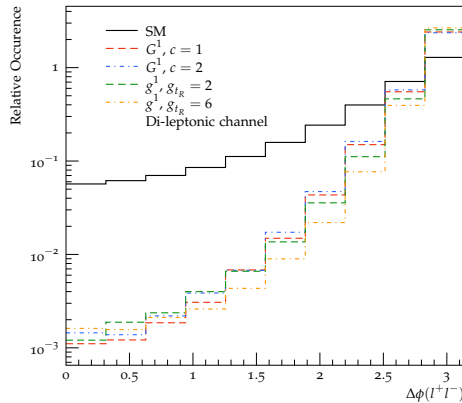
Figure 7.2: Distribution of $\Delta\phi(l^+l^-)$ for the considered scenarios for invariant masses $m(t\bar{t}) > 2$ TeV. The signal models all use $m(G^1/g^1) = 3$ TeV.

define $\theta_{l\pm}$ by boosting to the leptonic top's rest frame and taking the angle between the lepton and the top's direction of travel.[*] The final $m(t\bar{t})$ distribution is shown in Figure 7.1(a) and the $\cos\theta_{l\pm}$ distribution in Figure 7.3(a).

7.5.2 Di-leptonic study

The semi-leptonic final state discussed in Sec. 7.5.1 is naively much more attractive due to a six times larger branching fraction (since we are only considering electrons and muons) and a less involved reconstruction of the individual top momenta. Nonetheless, it is worthwhile to also consider the di-leptonic final state as it offers two clean final state leptons which enable a comparably straightforward measurement of spin correlations with increasing statistics.

When considering di-leptonic $t\bar{t}$ decays, however, we run into a qualitatively new issue related to the reconstruction of the individual top momenta: with two neutrinos in the final state, we will have to make an educated guess of how the single missing transverse energy vector decomposes into the transverse components of the neutrinos $p_{T,\nu/\bar{\nu}}$ before reconstructing the longitudinal momentum components. There are a number of approaches that we outline in the following.

The first method is to simply solve the full system of kinematic equations by assuming all intermediate particles are produced on-shell and that your measured

---

[*]Note that there are studies [351] that aim to extract the polarisation information from boosted hadronic tops but we do not attempt to do so here. We can expect the sensitivity of such a measurement to be smaller than that of the leptonic side measurement.

(a) Semi-leptonic channel.

(b) Di-leptonic channel.
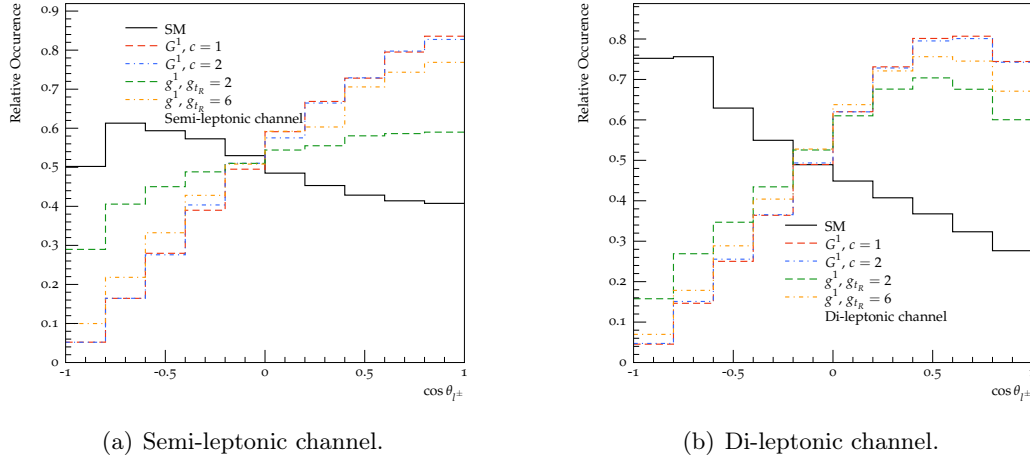
Figure 7.3: $\cos\theta_{l^{\pm}}$ distributions for the SM $t\bar{t}$ and signal samples for the semi-leptonic (a) and di-leptonic (b) analyses after all analysis selections and detector effects, in both for $m(t\bar{t}) > 2$ TeV. Since the signal produces right-handed tops we see a large modification of these lepton angle distributions when compared to the SM expectation which at these high invariant masses is slightly left-handed. Note that the polarisation of the tops from g^1 decays differs between the two coupling choices and this can be discerned in both analyses.

kinematic quantities are exact [352, 353]. This will in general provide up to eight sets of solutions, one of which being close to the true momenta assuming that the assumptions are valid. Using smeared kinematic quantities results in a larger mean number of solutions which causes large combinatorial uncertainties. CMS have made use of this approach together with a Matrix Element-method [354] to reduce the number of solutions on the basis of the matrix element weight.

A second method is to use so-called "neutrino weighting" [355, 356], which scans over a large number of proposed neutrino solutions and constructs and assigns individual weights for each guess based on how well the solution solves the kinematic equations. It is then possible to calculate observables for single events by either selecting the solution with the highest weight, or adding up the values for all solutions with correct weighting. This method is often used by ATLAS and has the advantage of only relying on kinematic information.

A third method, which is the one we will adopt in this work, uses kinematic insights from the M_{T2} [357] observable. The so-called M_{T2} Assisted On Shell (MAOS) method [358, 359] uses the solution for the transverse components of the two neu-
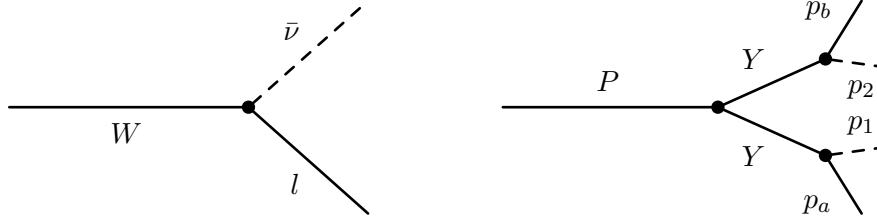
Figure 7.4: Kinematics for the m_T calculation (left) and M_{T2} calculation (right). The diagrams here should not be interpreted in the usual Feynman diagram sense: a solid line final state momentum indicates it is visible, and a dashed line final state momentum indicates it is invisible. Note that these should not be interpreted as particles: on the right-hand diagram p_a denotes all of the visible particles from the bottom Y decay, and p_1 denotes all of the invisible particles from the same decay. We can only hope to measure the total transverse component of all of the invisible particles in the final state at a hadron collider.

trino momenta which provides M_{T2}. The bisection method for calculating M_{T2} [360] and subsequent improvements of the algorithm [361–363] have made it possible to find the solution efficiently. The solutions for the neutrino momenta $k_{\nu/\bar{\nu}}^{\pm}$ (where $\pm$ denotes the remaining twofold ambiguity in the longitudinal components) will approach the true solutions for $M_{T2} \to m(t)$, with $k_{\nu/\bar{\nu}}^{\pm} = p_{\nu/\bar{\nu}}{}^*$ for $M_{T2} = m(t)$ with all kinematic quantities measured exactly and all intermediate particles on-shell. Therefore this approach provides an approach to improve the quality of the reconstruction if required by only using events with $m(t) - M_{T2} < C$ for some cut C. For completeness we will discuss the M_{T2} calculation in more detail below.

7.5.2.1 Estimating invisible momenta with M_{T2}

The transverse mass observable m_T is used to measure the W mass in leptonic decays. The relevant kinematics are presented in the left-hand diagram of Figure 7.4. The crucial point here is that since we do not know the fractions of the proton momenta the scattering partons carry in a proton-proton collision, we can not rely on momentum conservation along the beam line. Using the momenta as defined in this diagram, the transverse mass is given by:

---

*In this very particular situation we should find $k^+ = k^-$.

$$m_T^2 = m_l^2 + m_\nu^2 + 2\sqrt{E_T^l E_T^\nu - \vec{p}_T^{\,l}.\vec{p}_T^{\,\nu}} = (\alpha_l + \alpha_\nu)^2, \quad \alpha = (E_T, \vec{p}_T)\,. \qquad (7.3)$$

Here we've introduced the α notation to denote the $(2+1)$ dimensional momentum which drops the component along the beam line. The transverse component of the neutrino momentum can be calculated since we can assume (to a good approximation) momentum conservation in the transverse plane. Assuming no finite width effects, this suggests $m_T \leq m_W{}^*$ and allows m_W to be measured as the cutoff when a large number of events have been recorded. Generalising this to the situation with a parent particle P decaying to two daughters Y, which further decay semi-invisibly, will allow us to define the M_{T2} observable. The kinematics are shown in the right-hand diagram of Figure 7.4. Note we still can only measure the total invisible transverse momentum $\slashed{p}_T$, and have to deal with this ambiguity in the individual invisible momenta somehow. We will assume that the masses of the two Y particles are identical, and similarly that the masses of the two invisible momenta $p_{1/2}$ are identical. M_{T2} is then given by:

$$M_{T2}^2 = \min_{\vec{p}_{1,T}+\vec{p}_{2,T}=\slashed{p}_T} \left[\max\left(m_T^2(\alpha_1, \alpha_a), m_T^2(\alpha_2, \alpha_b)\right)\right]\,. \qquad (7.4)$$

The ambiguity in the individual invisible momenta is here dealt with by minimising over all possible values, keeping the sum equal to the observable $\slashed{p}_T$. Performing this min max using a naive, numerical approach is very computationally expensive and error-prone as there can be several local minima and a max distribution does not have a smooth first derivative. There is a more clever method thanks to Cheng & Han [360]: assuming the invisible momenta are single particles with the same mass m_i, we have:

$$p_1^2 = p_2^2 = m_i^2, \quad (p_{1/2}^2 + p_{a/b}^2)^2 = \mu_Y^2, \quad p_1^{x/y} + p_2^{x/y} = \slashed{p}^{x/y}\,. \qquad (7.5)$$

This allows us to calculate:

$$\mu_Y^2 = m_i^2 + m_a^2 + 2(E_1 E_a - p_1^x p_a^x - p_1^y p_a^y)$$

$$\Rightarrow E_1 = \frac{p_a^x}{E_a} p_1^x + \frac{p_a^y}{E_a} p_1^y + \frac{\mu_Y^2 - m_i^2 - m_a^2}{2E_a}\,, \qquad (7.6)$$

---

*The two are equivalent if the rapidity of the lepton and neutrino are the same.

where we have used that we expect M_{T2} to be invariant under boosts along the z-direction to set p_a^z to 0. The same can be done on the other side to find an expression for E_2 in terms of the momenta on the other side. A physical momentum must have $p_1^2 \geq 0$, which can be rewritten as:

$$(p_1^z)^2 = E_1^2 - (p_1^x)^2 - (p_1^y)^2 - m_i^2 \geq 0. \tag{7.7}$$

Combining Equations 7.6 and 7.7 we see that the physical solutions in the p_1^x, p_1^y–plane are given by an ellipse Ω_1. Doing the same thing on the other side of the decay, and remembering that $p_1^{x/y} + p_2^{x/y} = \not{p}^{x/y}$, we can express the requirement that both invisible momenta are physical as two ellipses Ω_1, Ω_2 in the p_1^x, p_1^y–plane, with the size set by μ_Y^2. M_{T2}^2 is then given by the value of μ_Y^2 which uniquely determines $\Omega_1 \cap \Omega_2$*. Therefore, by definition, this solution also provides unique values for $p_{1/2}^x, p_{1/2}^y$ which can be used together with an on-shell assumption for Y to fully reconstruct the invisible momenta, modulo a four-time combinatoric uncertainty in the longitudinal components.

As mentioned above, assuming all momenta are exact and all particles are on-shell, the solution for the neutrino momenta given by this method will be exact when $\mu_Y^2 = m_Y^2$.

7.5.2.2 Analysis Selections and Reconstruction

We begin the analysis by finding electrons with $p_T > 25$ GeV inside $|\eta| < 2.47$ and muons with $p_T > 25$ GeV inside $|\eta| < 2.7$. We then find anti-k_T $R = 0.4$ jets with $p_T > 25$ GeV with $|\eta| < 2.8$. Again we have to accept some overlap between the leptons and jets due to the large top boost, so we do not require these to be isolated and again assume we can separate very hard prompt leptons from a nearby jet. We then b-tag the jets within $|\eta| < 2.5$ with 70% efficiency and a 1% fake rate (10% for $p_T > 300$ GeV with the comments regarding this choice made in Section 7.5.1.1 also valid here), and require at least two b-tags. We also require missing transverse energy $\not{p}_T$ with $|\not{p}_T| > 60$ GeV.

While the high boost of our tops means that we can usually correctly pair b-jets to leptons by taking the ones closest to each other in $\eta - \phi$ space, we make

---

*Determining whether two ellipses overlap is non-trivial: a general solution using the roots of the characteristic polynomials calculated using Sturm-Habicht sequences [364] was first presented in [363], and an algorithm making use of this solution was only recently implemented in the M_{T2} context [362].

use of some standard approaches to further reduce the combinatorial uncertainty. Due to the large boost we consider, we do not gain much from cutting on $M_T^{t\bar{t}}(0)$, which is often considered in the literature [365–368], where $M_T^{t\bar{t}}(0)$ is defined as the transverse mass of the entire $t\bar{t}$ system when $m_{\nu\bar{\nu}} = 0$:

$$\left(M_T^{t\bar{t}}(0)\right)^2 = m_{\text{vis}}^2 + 2\left(\sqrt{|p_T|^2 + m_{\text{vis}}^2}|\not{p}_T| + p_T \cdot \not{p}_T\right). \tag{7.8}$$

We therefore select the candidate which minimises at least two out of three test variables: T_2, T_3, and T_4 defined in [367]. These correspond to how well the solution corresponding to each pairing reconstruct the W and top masses and the expected M_{T2} distribution. If either of the pairings returns complex solutions for the neutrino momenta we automatically select the other one. Once we have selected a pairing we veto the event if $M_{T2} > m(t)$ or $m_{bl} > \sqrt{m(t)^2 - m(W)^2}$.[*] We find that vetoing the entire event if neither pairing results in a viable-seeming solution suppresses the $WWjj$ background with little signal efficiency loss. We do not use m_{bl} for determining the correct pairing (referred to as the T_1 test variable in [367]) since this would make the total number of test variables even and it correlates strongly with T_2.

As discussed above we reconstruct the individual neutrinos using the MAOS method. We take the solution for the transverse momenta of the neutrinos which gives the correct M_{T2}, and solve the remaining kinematic constraints to give two solutions for the longitudinal component of each neutrino. This results in four final solutions for the complete kinematics of the event with equal weights. This technique has been used for example in phenomenological studies of production angle measurements in [358] and top polarisation measurements in [369]. Despite the fourfold combinatorial uncertainty which introduces a large smearing of the final $m(t\bar{t})$ distribution as shown in Fig 7.1(b), it reproduces truth-level angular observables well as this only affects the longitudinal neutrino momenta. The $\cos\theta_{l\pm}$ distribution in Figure 7.3(b) shows this in practice and confirms the final distributions are closer to their true shapes than in the semi-leptonic analysis. Unlike in the semi-leptonic case in Section 7.5.1.1 we can extract the lepton angle from both tops by again boosting to the individual rest frames and taking the angle of their decay lepton to the top direction of travel.

---

[*]Ignoring smearing, finite width effects, and $\mathcal{O}(m_b)$ corrections to m_{bl} these correspond to unphysical solutions.
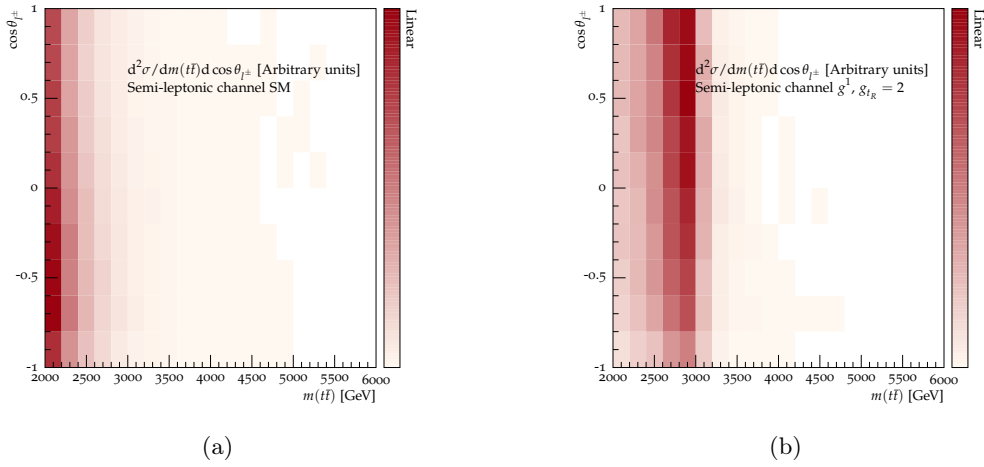
Figure 7.5: Two-dimensional shape distributions of $m(t\bar{t})$ and $\cos\theta_{l\pm}$ for the expected SM background (a) and a narrow $(g_{t_R} = 2)$ g^1 (b) in the semi-leptonic analysis. This corresponds to the worst-case scenario among our signal models from the perspective of gaining additional information from the polarisation measurement.
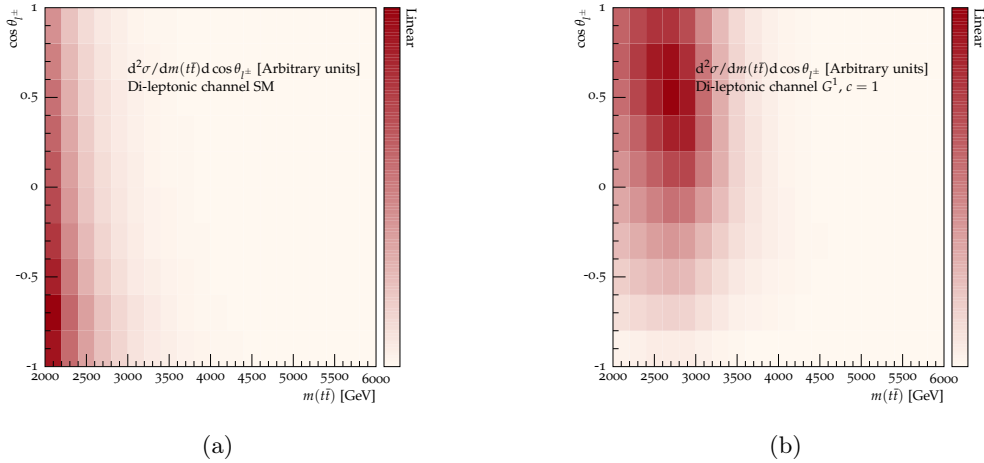
Figure 7.6: Two-dimensional shape distributions of $m(t\bar{t})$ and $\cos\theta_{l\pm}$ for the expected SM background (a) and a narrow $(c = 1)$ G^1 (b) in the di-leptonic analysis. This corresponds to one of the best scenarios among our signal models from the perspective of gaining additional information from the polarisation measurement.

(a)   (b)
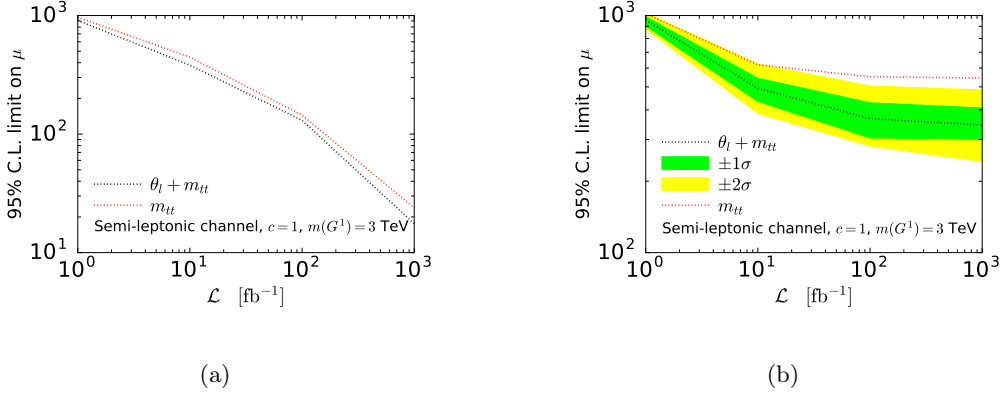
Figure 7.7: Limits on μ for a narrow ($c = 1$) G^1 assuming (a) no systematics and (b) 5% systematics (see text for details on how this is propagated to the individual bins) which can be set with different assumed total luminosities using $m(t\bar{t})$ and $\cos\theta_{l\pm}$ (black line) and only using $m(t\bar{t})$ (red line) with the semi-leptonic analysis. The $\pm\sigma$ bands are for the combined result. $\mu = 1$ corresponds to $\sigma \times \mathrm{Br}\,(G^1 \to t\bar{t}) = 0.3$ fb.

7.6 Discussion of Results

7.6.1 Signal vs Background discrimination

We estimate the limits that can be set on the signal strength $\mu = \sigma/\sigma_{\mathrm{expected}}$[*] for our model setups with the $m(t\bar{t})$ and combined $m(t\bar{t})$ - $\theta_{l\pm}$ distributions by using the CL_s method as outlined in Section 3.3: for each of the 2D-binned distributions (examples of which are shown in Figures 7.5, 7.6) we calculate the Poissonian likelihood ratio bin-by-bin. To avoid spurious exclusions we do not use bins which have no background events – this has a negligible effect as we have ensured there is sufficient statistics in all bins which are expected to contribute to the exclusion limit for our signal models.

When calculating limits we use a flat Gaussian systematic of 5% on the total cross section[†] of the background and only statistical uncertainties for the signal. To propagate the systematic uncertainty to individual bins we assume the fractional systematic error is the same in all bins, and calculate the correct uncertainty which would lead to the stated uncertainty on the total cross section when adding up all the

---

[*]Note this use of μ differs from that in from Chapter 2. For the rest of this chapter μ will refer to the signal strength.

[†]We can expect that data-driven methods, that use the low $m(t\bar{t})$ spectrum to extrapolate to our signal region become well-controlled with large data sets.

(a)   (b)
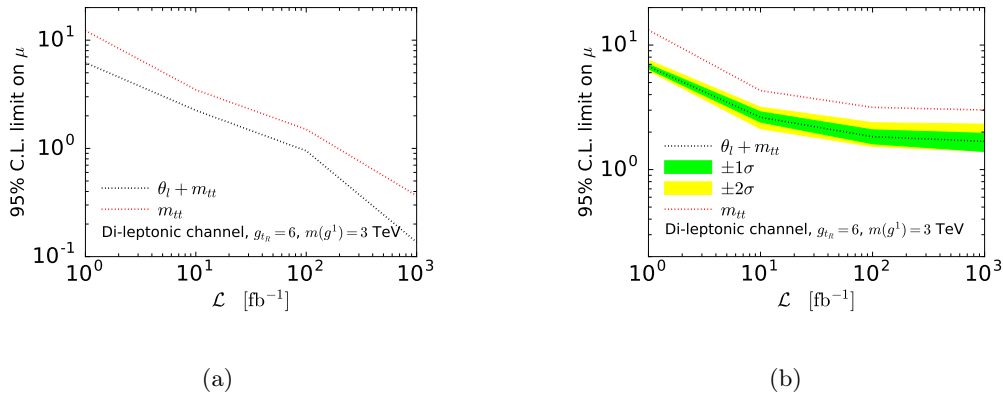
Figure 7.8: Limits on μ for a wide $(g_{t_R} = 6)$ g^1 assuming (a) no systematics and (b) 5% systematics on the total cross section (see text for details on how this is propagated to the individual bins) which can be set with different assumed total luminosities using $m(t\bar{t})$ and $\cos\theta_{l\pm}$ (black line) and only using $m(t\bar{t})$ (red line) with the di-leptonic analysis. The $\pm\sigma$ bands are for the combined result. $\mu = 1$ corresponds to $\sigma \times \mathrm{Br}\,(g^1 \to t\bar{t}) = 200$ fb.

bins assuming they are statistically independent. In general introducing systematic uncertainties and propagating these in a consistent manner always requires us to make an assumption of how this is to be done which introduces a large effect on the final limit on μ. In order to provide an estimate of the importance of the systematic uncertainty on our limits we also present a comparison to limits calculated with no systematic uncertainties in Figures 7.7 and 7.8.

7.6.2 Improvement from top polarisation observables

Before we comment on the shape information gain from including polarisation-sensitive observables let us quickly investigate the expected phenomenology in the model we consider. As can be seen from Figure 7.1, the reconstruction smears out the resonance so the signal appears very wide for all signal models in the semi-leptonic and di-leptonic analysis. For relatively narrow resonances our reconstruction of the semi-leptonic channel yields a better performance, however, for the wider parameter points the $m_{t\bar{t}}$ distribution quickly loses its peak-like features. In such a case, setting limits by using $m(t\bar{t})$ as a single discriminant effectively means constraining a continuum excess.

Considering directly-inferred angular quantities like $\Delta\phi(l^+l^-)$ from, for example,

(a)

(b)
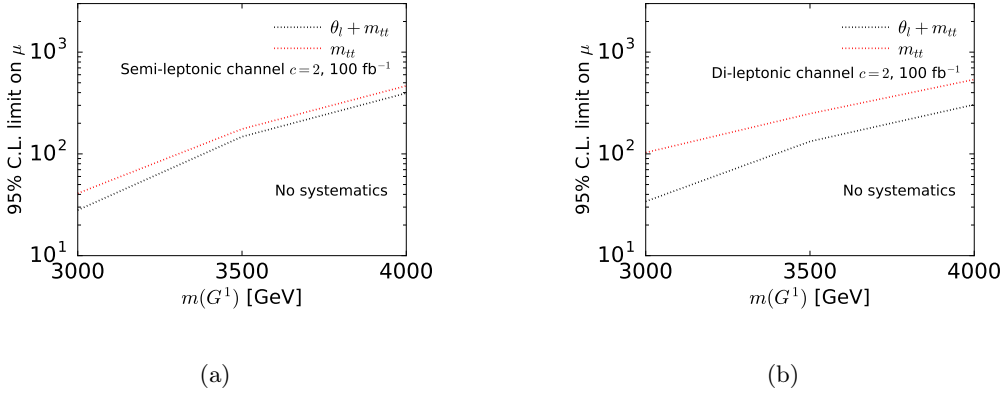
Figure 7.9: Limits on μ for a wide ($c = 2$) G^1 using the semi-leptonic (a) and di-leptonic (b) analyses for a fixed luminosity of 100 fb^{-1} with no systematics as a function of resonance mass using $m(t\bar{t})$ and $\cos\theta_{l\pm}$ (black line) and only using $m(t\bar{t})$ (red line). The $\pm\sigma$ bands are for the combined result.

(a)

(b)
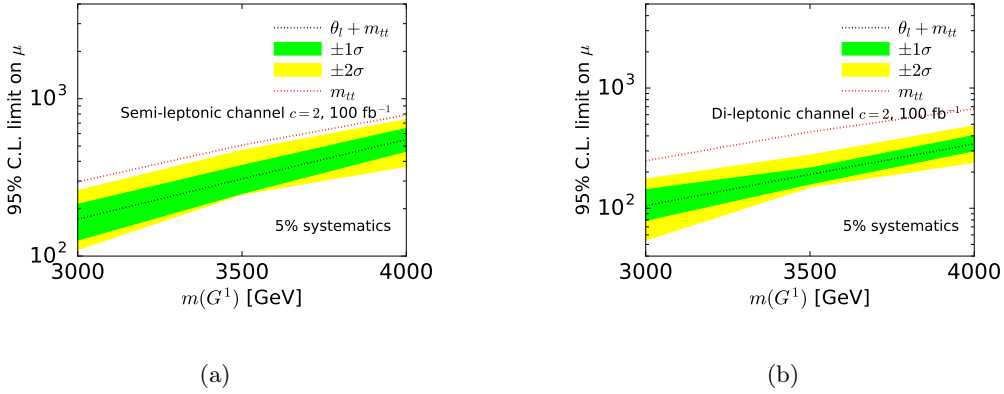
Figure 7.10: Limits on μ for a wide ($c = 2$) G^1 using the semi-leptonic (a) and di-leptonic (b) analyses for a fixed luminosity of 100 fb^{-1} with 5% systematics on the total cross section (propagated to bins as explained in the text) as a function of resonance mass using $m(t\bar{t})$ and $\cos\theta_{l\pm}$ (black line) and only using $m(t\bar{t})$ (red line). The $\pm\sigma$ bands are for the combined result.

the di-lepton final state offers limited shape information. This is in particular true when we would like to discriminate between different signal hypothesis once an excess has been discovered. The reason for the lack of information in $\Delta\phi(l^+l^-)$ is the large considered mass range of the $t\bar{t}$ resonance, which leads to back-to-back tops and leptons as a consequence.

It is exactly the boost to the top rest frame which lifts this degeneracy. And since the signal produces highly polarised tops, we see a large modification of these lepton angle distributions, which provides the additional shape information (Figure 7.3) which we can use to tighten the estimated constraint on μ when combined with $m(t\bar{t})$, Figures 7.5 and 7.6 (we also show the distribution of the expected SM background which exhibits no particular resonant features in the $m(t\bar{t}) - \cos\theta_{l\pm}$ plane). Note that the polarisation of the tops from g^1 decays differs between the two coupling choices and this is visible in both channels. The apparent difference in the difference in polarisation between the two coupling choices can be traced to the non-linear nature of the transfer functions from the truth distribution to the reconstructed distribution in the two cases.

Using the $m(t\bar{t}) - \cos\theta_{l\pm}$ correlation as the baseline of the limit setting outlined above we obtain a large improvement by a factor up to ~ 3 on the limit on μ with increasing luminosity compared to $m(t\bar{t})$ alone in Figure 7.9(b) for the ideal case of the di-leptonic analysis of a wide highly polarised resonance, as the large statistics available with 100 fb^{-1} provide an efficient sampling of the sensitivity unveiled in Figures 7.6. This relative improvement reduces for smaller reconstructed widths that can be reached in the semi-leptonic channel as shape information is gained in $m(t\bar{t})$, yet an improvement at large luminosity by a factor of $\sim \sqrt{2}$ is still possible for our benchmark narrow less-polarised gluon in Figure 7.7(a), which is the least sensitive of our parameter points.

It is exactly the additional shape information from including polarisation information which renders the analyses potentially sensitive – depending on systematics – to broad gluon-like resonances at $\mathcal{L} \sim 100$ fb^{-1} at our benchmark point. Discrimination solely based on $m(t\bar{t})$ flattens out and an analysis which focuses exclusively on resonant-like enhancements will have less sensitivity by factors up to 3.

The improvement is not too sensitive on the precise mass scale around our chosen benchmark, and becomes especially relevant at large widths as alluded to in the beginning of this work, Figures 7.8, 7.9, 7.10.

7.7   Conclusions

Resonance searches in the $t\bar{t}$ final state are a well-motivated strategy for discovering new physics beyond the Standard Model [316, 317]. While peaks in the mass spectrum are very powerful indicators of the presence of such new physics, we also

often expect to see large modifications to other distributions and including this shape information through multi-dimensional distributions often offers a good way to improve sensitivity. Additionally, if the resonance becomes wide, invariant mass distributions necessarily lose shape information. We have performed a detailed investigation of the semi-leptonic and di-leptonic $t\bar{t}$ final states for $\sqrt{s} = 14$ TeV and provide quantitative estimates of the information gain from including top polarisation information in the limit setting. Our results demonstrate that this information helps to ameliorate the loss of shape information in the invariant mass spectrum for wider signal models. To make our analysis comparable to the practice of the experiments we have focussed on the RS scenario as a particular candidate that provides a theoretically well-defined framework for such a phenomenological situation. For the fully-polarised scenarios we study in this work we find improvements of factors of up to 3 (2) on the limit of the signal strength for the di-(semi)-leptonic analysis at large luminosity, with larger improvements for wider signal models as expected. For our benchmark choice of 3 TeV resonances, including this information is crucial to exclude certain KK gluon resonances at 95%. Interestingly the larger improvement for the di-leptonic analysis allows this channel to become competitive with semi-leptonic one for resonance searches for these types of models, however we would like to note that this statement heavily depends on the systematics modelling and only a dedicated experimental analysis can fully assess the relative sensitivities.

While these improvements are specific to our parameter choices at face value, similar relative improvements can be expected for other, non-graviton or gluon resonances (not limited to RS models) that predict a net polarisation of the top pair. Polarisation information is therefore an important ingredient to a more comprehensive analysis strategy that builds upon the invariant top pair mass, using additional shape information through multivariate approaches.

Conclusions

In this thesis we have discussed the Standard Model of particle physics, its application and relevance to high energy hadron colliders, and some open questions that we hope can be answered by the experiments at the Large Hadron Collider. In particular we have focused on searches for microscopic models for dark matter, and methods for revealing the nature of electroweak symmetry breaking using the structure of the Higgs sector.

Chapter 2 reviewed the Standard Model and the calculational tools used to obtain the results in Chapters 5 and 6. In particular the Higgs sector of the Standard Model, the application of perturbative unitarity arguments for constraining parameters, and the calculation of renormalisation group equations were reviewed in detail. Chapter 3 focused in part on the Hierarchy problem of the Higgs sector in the Standard Model, and its connection to the question of what the underlying nature of electroweak symmetry breaking is. The second part focused on dark matter and in particular on how to connect quantum field theory dark matter models to the macroscopic observations which motivate them. To remain self-contained the Boltzmann equation which underlies the thermal freezeout mechanism for generating the relic density used in Chapter 4 was reviewed in detail, and the statistical framework employed throughout the thesis was similarly introduced.

In Chapter 4 we showed how to facilitate scans of the full parameter space of a Simplified Dark Matter Model, and demonstrated that this allows for a more meaningful comparison between collider constraints and the relic density to be made. This motivates the interpretation of future results using our method, especially if searches continue to return null results and we require a more complete picture of the status of the full parameter space of a model in order to target searches better. In Chapter 5 we considered the phenomenology of a strongly interacting dark sector at the Large Hadron Collider and future hadron colliders, and calculated the size of the leading logarithmic quantum corrections to dark matter production which could be used to disentangle the internal structure of a dark sector after a hypothetical

discovery. While such effects are hard to disentangle at the Large Hadron Collider, we show that our results could be used at a future 100 TeV Collider if a scalar mediator connected to a dark sector is discovered in the Large Hadron Collider energy range.

In Chapter 6 we presented a detailed study of $hhjj$ production, both through gluon fusion using the full leading order result and weak boson fusion, and showed that the weak boson fusion channel is uniquely sensitive to modifications of the quartic $VV^{\dagger}hh$ vertices from their Standard Model expectation. However the gluon fusion component remains sizeable even if we apply strict selections towards the weak boson fusion component, necessitating our detailed simulation. We further considered $\mathcal{CP}$ violation in the Higgs sector and again found that the weak boson fusion channel of $hhjj$ production is highly sensitive to an operator which appears generically in effective expansions of $\mathcal{CP}$ violating Two Higgs Doublet Models, but is insensitive to perturbative unitarity arguments and other production channels. Other leading $\mathcal{CP}$ violating effective operators are strongly constrained by perturbative unitarity arguments, as the absence of new resonant physics in the Large Hadron Collider energy range pushes the necessary completion to the TeV scale.

Finally, in Chapter 7 we investigated the use of shape information from top polarisation observables in searches for resonances decaying to top pairs. It was shown that including this information can greatly improve the statistical sensitivity of the searches towards signal models which predict polarised tops in both the di-leptonic and semi-leptonic final states. This was demonstrated with a well-motivated benchmark Randall-Sundrum model. Looking forward, as the Large Hadron Collider collects more data we can expect machine learning algorithms to become widespread in order to fully exploit shape information in observables towards signal and background discrimination, and a robust understanding of the underlying physics will be crucial both to guide the experiments towards interesting observables, and to avoid spurious discoveries and exclusions. Our study provides an example of an observable which is decorrelated from the hard kinematics underlying the resonant decay but still carries robust information about the underlying signal model. In the future it would be interesting to study such effects in a more systematic way.

List of Figures

List of Tables

Bibliography

[1] Thomas Jacques and Karl Nordström. Mapping monojet constraints onto Simplified Dark Matter Models. *JHEP*, 06:142, 2015. (Cited on pages 5 and 71.)

[2] Christoph Englert, Karl Nordström, and Michael Spannowsky. Towards resolving strongly-interacting dark sectors at colliders. *Phys. Rev.*, D94(5):055028, 2016. (Cited on pages 5 and 89.)

[3] Matthew J. Dolan, Christoph Englert, Nicolas Greiner, Karl Nordstrom, and Michael Spannowsky. *hhjj* production at the LHC. *Eur. Phys. J.*, C75(8):387, 2015. (Cited on pages 5 and 107.)

[4] Christoph Englert, Karl Nordström, Kazuki Sakurai, and Michael Spannowsky. Perturbative Higgs CP violation, unitarity and phenomenology. *Phys. Rev.*, D95(1):015018, 2017. (Cited on pages 5 and 107.)

[5] Christoph Englert, James Ferrando, and Karl Nordström. Constraining new resonant physics with top spin polarisation information. 2017. (Cited on pages 5 and 137.)

[6] Georges Aad et al. Observation of a new particle in the search for the Standard Model Higgs boson with the ATLAS detector at the LHC. *Phys.Lett.*, B716:1–29, 2012. (Cited on pages 1, 18 and 20.)

[7] Serguei Chatrchyan et al. Observation of a new boson at a mass of 125 GeV with the CMS experiment at the LHC. *Phys. Lett.*, B716:30–61, 2012. (Cited on pages 1, 18, 20, 22 and 159.)

[8] Atlas public luminosity tracker. Accessed: 2017-01-08. (Cited on page 1.)

[9] E. Wigner. On unitary representations of the inhomogeneous lorentz group. *Annals of Mathematics*, 40(1):149–204, 1939. (Cited on page 4.)

[10] P. A. M. Dirac. The quantum theory of the emission and absorption of radiation. *Proceedings of the Royal Society of London A: Mathematical, Physical and Engineering Sciences*, 114(767):243–265, 1927. (Cited on page 4.)

[11] Steven Weinberg. *The Quantum theory of fields. Vol. 1: Foundations.* Cambridge University Press, 2005. (Cited on page 4.)

[12] Richard P. Feynman, Robert B. Leighton, and Matthew Sands. *The Feynman lectures on physics. Vol. 3: Quantum mechanics.* Addison-Wesley Publishing Co., Inc., Reading, Mass.-London, 1965. (Cited on page 5.)

[13] E.C.G. Stueckelberg. Die wechselwirkungskräfte in der elektrodynamik und in der feldtheorie der kräfte. *Helv. Phys. Acta*, 11. (Cited on page 7.)

[14] H. Lehmann, K. Symanzik, and W. Zimmermann. Zur Formulierung quantisierter Feldtheorien. *Nuovo Cimento Serie*, 1:205–225, January 1955. (Cited on page 8.)

[15] Kenneth G. Wilson. The renormalization group: Critical phenomena and the kondo problem. *Rev. Mod. Phys.*, 47:773–840, Oct 1975. (Cited on pages 8 and 15.)

[16] W. Pauli and F. Villars. On the invariant regularization in relativistic quantum theory. *Rev. Mod. Phys.*, 21:434–444, Jul 1949. (Cited on page 9.)

[17] Curtis G. Callan. Broken scale invariance in scalar field theory. *Phys. Rev. D*, 2:1541–1547, Oct 1970. (Cited on page 10.)

[18] T. D. Lee and M. Nauenberg. Degenerate systems and mass singularities. *Phys. Rev.*, 133:B1549–B1562, Mar 1964. (Cited on page 11.)

[19] Toichiro Kinoshita. Mass singularities of feynman amplitudes. *Journal of Mathematical Physics*, 3(4):650–677, 1962. (Cited on page 11.)

[20] Antti Aarne. *The types of the folktale: a classification and bibliography.* 1961. (Cited on page 12.)

[21] Stith Thompson. *The Folktale.* 1977. (Cited on page 12.)

[22] Lisa Randall and Raman Sundrum. A Large mass hierarchy from a small extra dimension. *Phys. Rev. Lett.*, 83:3370–3373, 1999. (Cited on pages 13, 55, 139 and 140.)

[23] Tony Gherghetta and Alex Pomarol. Bulk fields and supersymmetry in a slice of AdS. *Nucl. Phys.*, B586:141–162, 2000. (Cited on pages 13, 55 and 141.)

[24] C. Patrignani et al. Review of Particle Physics. *Chin. Phys.*, C40(10):100001, 2016. (Cited on pages 14, 44, 160 and 167.)

[25] Christopher Balzereit, Thomas Mannel, and Benedikt Plumper. The Renormalization group evolution of the CKM matrix. *Eur. Phys. J.*, C9:197–211, 1999. (Cited on page 14.)

[26] Gerard 't Hooft and M. J. G. Veltman. Regularization and Renormalization of Gauge Fields. *Nucl. Phys.*, B44:189–213, 1972. (Cited on page 15.)

[27] B. Grzadkowski, M. Iskrzynski, M. Misiak, and J. Rosiek. Dimension-Six Terms in the Standard Model Lagrangian. *JHEP*, 10:085, 2010. (Cited on pages 16 and 125.)

[28] Matthew D. Schwartz. *Quantum Field Theory and the Standard Model*. Cambridge University Press, 2014. (Cited on pages 17 and 22.)

[29] L. D. Faddeev and V. N. Popov. Feynman Diagrams for the Yang-Mills Field. *Phys. Lett.*, 25B:29–30, 1967. (Cited on page 17.)

[30] F. Englert and R. Brout. Broken Symmetry and the Mass of Gauge Vector Mesons. *Phys. Rev. Lett.*, 13:321–323, 1964. (Cited on page 18.)

[31] Peter W. Higgs. Broken Symmetries and the Masses of Gauge Bosons. *Phys. Rev. Lett.*, 13:508–509, 1964. (Cited on page 18.)

[32] K. Fujikawa, B. W. Lee, and A. I. Sanda. Generalized Renormalizable Gauge Formulation of Spontaneously Broken Gauge Theories. *Phys. Rev.*, D6:2923–2943, 1972. (Cited on page 19.)

[33] Daniel Enrique De Florian Sabaris, Christophe Grojean, Fabio Maltoni, Chiara Mariotti, Alexandre Nikitenko, Marco Pieri, Pierre Savard, Markus Schumacher, and Rei Tanaka. Handbook of LHC Higgs cross sections: 4. Deciphering the nature of the Higgs sector. Sep 2016. (Cited on pages 20, 21 and 167.)

[34] Georges Aad et al. Measurements of the Higgs boson production and decay rates and constraints on its couplings from a combined ATLAS and CMS analysis of the LHC pp collision data at $\sqrt{s} = 7$ and 8 TeV. 2016. (Cited on pages 20, 125 and 167.)

[35] ATLAS Collaboration. Combined measurements of Higgs boson production and decay using $\sqrt{s} = 13$ TeV pp collision data collected with the ATLAS experiment. (ATLAS-CONF-2017-047), Jul 2017. (Cited on pages 20 and 167.)

[36] Charalampos Anastasiou, Claude Duhr, Falko Dulat, Franz Herzog, and Bernhard Mistlberger. Higgs Boson Gluon-Fusion Production in QCD at Three Loops. *Phys. Rev. Lett.*, 114:212001, 2015. (Cited on pages 20 and 167.)

[37] Georges Aad et al. Measurements of the Higgs boson production and decay rates and coupling strengths using pp collision data at $\sqrt{s} = 7$ and 8 TeV in the ATLAS experiment. *Eur. Phys. J.*, C76(1):6, 2016. (Cited on pages 21 and 167.)

[38] Curtis G. Callan, Sidney Coleman, J. Wess, and Bruno Zumino. Structure of phenomenological lagrangians. ii. *Phys. Rev.*, 177:2247–2250, Jan 1969. (Cited on page 27.)

[39] Michael S. Chanowitz and Mary K. Gaillard. The tev physics of strongly interacting w's and z's. *Nuclear Physics B*, 261:379 – 431, 1985. (Cited on page 28.)

[40] Benjamin W. Lee, C. Quigg, and H. B. Thacker. Weak Interactions at Very High-Energies: The Role of the Higgs Boson Mass. *Phys. Rev.*, D16:1519, 1977. (Cited on pages 29 and 130.)

[41] Matthew J. Dolan, Christoph Englert, and Michael Spannowsky. Higgs self-coupling measurements at the LHC. *JHEP*, 10:112, 2012. (Cited on pages 29, 30, 110, 111, 113 and 159.)

[42] Nicola Cabibbo. Unitary symmetry and leptonic decays. *Phys. Rev. Lett.*, 10:531–533, Jun 1963. (Cited on page 32.)

[43] Makoto Kobayashi and Toshihide Maskawa. CP Violation in the Renormalizable Theory of Weak Interaction. *Prog. Theor. Phys.*, 49:652–657, 1973. (Cited on page 32.)

[44] John R. Ellis, Mary K. Gaillard, and Dimitri V. Nanopoulos. A Phenomenological Profile of the Higgs Boson. *Nucl. Phys.*, B106:292, 1976. (Cited on page 36.)

[45] Mikhail A. Shifman, A. I. Vainshtein, M. B. Voloshin, and Valentin I. Za-kharov. Low-Energy Theorems for Higgs Boson Couplings to Photons. *Sov. J. Nucl. Phys.*, 30:711–716, 1979. [Yad. Fiz.30,1368(1979)]. (Cited on page 36.)

[46] Bernd A. Kniehl and Michael Spira. Low-energy theorems in Higgs physics. *Z. Phys.*, C69:77–88, 1995. (Cited on page 36.)

[47] Hiren H. Patel. Package-X: A Mathematica package for the analytic calcu-lation of one-loop integrals. *Comput. Phys. Commun.*, 197:276–290, 2015. (Cited on pages 37 and 53.)

[48] Marie E. Machacek and Michael T. Vaughn. Two-loop renormalization group equations in a general quantum field theory. *Nuclear Physics B*, 222(1):83 – 103, 1983. (Cited on pages 42, 97 and 98.)

[49] Marie E. Machacek and Michael T. Vaughn. Two-loop renormalization group equations in a general quantum field theory (ii). yukawa couplings. *Nuclear Physics B*, 236(1):221 – 232, 1984. (Cited on pages 42, 97 and 98.)

[50] Ming-xing Luo, Hua-wen Wang, and Yong Xiao. Two loop renormalization group equations in general gauge field theories. *Phys. Rev.*, D67:065019, 2003. (Cited on pages 42, 97 and 98.)

[51] Sidney Coleman and Erick Weinberg. Radiative corrections as the origin of spontaneous symmetry breaking. *Phys. Rev. D*, 7:1888–1910, Mar 1973. (Cited on page 43.)

[52] R. J. Crewther, P. Di Vecchia, G. Veneziano, and Edward Witten. Chiral Estimate of the Electric Dipole Moment of the Neutron in Quantum Chromo-dynamics. *Phys. Lett.*, 88B:123, 1979. [Erratum: Phys. Lett.91B,487(1980)]. (Cited on page 45.)

[53] Constantia Alexandrou. Parton distribution functions from Lattice QCD. *Few Body Syst.*, 57(8):621–626, 2016. (Cited on page 45.)

[54] John C. Collins, Davison E. Soper, and George F. Sterman. Factorization of Hard Processes in QCD. *Adv. Ser. Direct. High Energy Phys.*, 5:1–91, 1989. (Cited on page 45.)

[55] V. N. Gribov and L. N. Lipatov. Deep inelastic e p scattering in perturbation theory. *Sov. J. Nucl. Phys.*, 15:438–450, 1972. [Yad. Fiz.15,781(1972)]. (Cited on page 46.)

[56] Guido Altarelli and G. Parisi. Asymptotic Freedom in Parton Language. *Nucl. Phys.*, B126:298–318, 1977. (Cited on page 46.)

[57] Yuri L. Dokshitzer. Calculation of the Structure Functions for Deep Inelastic Scattering and e+ e- Annihilation by Perturbation Theory in Quantum Chromodynamics. *Sov. Phys. JETP*, 46:641–653, 1977. [Zh. Eksp. Teor. Fiz.73,1216(1977)]. (Cited on page 46.)

[58] Andy Buckley, James Ferrando, Stephen Lloyd, Karl Nordström, Ben Page, Martin Rüfenacht, Marek Schönherr, and Graeme Watt. LHAPDF6: parton density access in the LHC precision era. *Eur. Phys. J.*, C75:132, 2015. (Cited on page 46.)

[59] Richard D. Ball et al. Parton distributions for the LHC Run II. *JHEP*, 04:040, 2015. (Cited on pages 47 and 160.)

[60] Gavin P. Salam. Towards Jetography. *Eur.Phys.J.*, C67:637–686, 2010. (Cited on page 49.)

[61] Stephen D. Ellis and Davison E. Soper. Successive combination jet algorithm for hadron collisions. *Phys. Rev.*, D48:3160–3166, 1993. (Cited on page 49.)

[62] Yuri L. Dokshitzer, G. D. Leder, S. Moretti, and B. R. Webber. Better jet clustering algorithms. *JHEP*, 08:001, 1997. (Cited on pages 49 and 143.)

[63] Matteo Cacciari, Gavin P. Salam, and Gregory Soyez. The Anti-k(t) jet clustering algorithm. *JHEP*, 0804:063, 2008. (Cited on pages 50, 77 and 143.)

[64] Y. et al. Fukuda. Evidence for oscillation of atmospheric neutrinos. *Phys. Rev. Lett.*, 81:1562–1567, Aug 1998. (Cited on page 51.)

[65] Peter Minkowski. mu to e gamma at a rate of one out of 109 muon decays? *Physics Letters B*, 67(4):421 – 428, 1977. (Cited on page 52.)

[66] James D. Wells. Higgs naturalness and the scalar boson proliferation instability problem. *Synthese*, 194(2):477–490, 2017. (Cited on page 52.)

[67] G. C. Branco, P. M. Ferreira, L. Lavoura, M. N. Rebelo, Marc Sher, and Joao P. Silva. Theory and phenomenology of two-Higgs-doublet models. *Phys. Rept.*, 516:1–102, 2012. (Cited on pages 54 and 74.)

[68] Roberto Contino. The Higgs as a Composite Nambu-Goldstone Boson. In *Physics of the large and the small, TASI 09, proceedings of the Theoretical Advanced Study Institute in Elementary Particle Physics, Boulder, Colorado, USA, 1-26 June 2009*, pages 235–306, 2011. (Cited on page 54.)

[69] A. D. Sakharov. Violation of CP Invariance, c Asymmetry, and Baryon Asymmetry of the Universe. *Pisma Zh. Eksp. Teor. Fiz.*, 5:32–35, 1967. [Usp. Fiz. Nauk161,61(1991)]. (Cited on page 55.)

[70] R.P. Feynman, F.B. Morinigo, W. Wagner, and B. Hatfield. *Feynman Lectures on Gravitation*. Frontiers in Physics Series. Avalon Publishing, 2002. (Cited on page 56.)

[71] Adam G. Riess et al. Observational evidence from supernovae for an accelerating universe and a cosmological constant. *Astron.J.*, 116:1009–1038, 1998. (Cited on page 56.)

[72] Philippe Brax, Clare Burrage, and Christoph Englert. Disformal dark energy at colliders. *Phys. Rev.*, D92(4):044036, 2015. (Cited on page 56.)

[73] Philippe Brax, Clare Burrage, Christoph Englert, and Michael Spannowsky. LHC Signatures Of Scalar Dark Energy. *Phys. Rev.*, D94(8):084054, 2016. (Cited on page 56.)

[74] F. Zwicky. Republication of: The redshift of extragalactic nebulae. *General Relativity and Gravitation*, 41(1):207–224, Jan 2009. (Cited on page 56.)

[75] H. W. Babcock. The rotation of the Andromeda Nebula. *Lick Observatory Bulletin*, 19:41–51, 1939. (Cited on page 57.)

[76] J. P. Ostriker and P. J. E. Peebles. A Numerical Study of the Stability of Flattened Galaxies: or, can Cold Galaxies Survive? *Astro-Physical Journal*, 186:467–480, December 1973. (Cited on page 57.)

[77] Douglas Clowe, Marusa Bradac, Anthony H. Gonzalez, Maxim Markevitch, Scott W. Randall, Christine Jones, and Dennis Zaritsky. A direct empirical

proof of the existence of dark matter. *Astrophys. J.*, 648:L109–L113, 2006. (Cited on page 57.)

[78] Joel R. Primack. Dark matter and structure formation. In *Midrasha Mathematicae in Jerusalem: Winter School in Dynamical Systems Jerusalem, Israel, January 12-17, 1997*, 1997. (Cited on page 57.)

[79] Wayne Hu and Scott Dodelson. Cosmic microwave background anisotropies. *Ann. Rev. Astron. Astrophys.*, 40:171–216, 2002. (Cited on page 57.)

[80] M. Miyamoto and R. Nagai. Three-dimensional models for the distribution of mass in galaxies. *Publications of the Astronomical Society of Japan*, 27:533–543, 1975. (Cited on page 57.)

[81] Julio F. Navarro, Carlos S. Frenk, and Simon D. M. White. The Structure of cold dark matter halos. *Astrophys. J.*, 462:563–575, 1996. (Cited on page 58.)

[82] Yoshiaki Sofue. Pseudo rotation curve connecting the galaxy, dark halo, and local group. *Publications of the Astronomical Society of Japan*, 61(2):153, 2009. (Cited on pages 60 and 160.)

[83] N. Aghanim et al. Planck 2015 results. XI. CMB power spectra, likelihoods, and robustness of parameters. *Astron. Astrophys.*, 594:A11, 2016. (Cited on page 59.)

[84] Flip Tanedo. Defense against the dark arts - notes on dark matter and particle physics. (Cited on page 60.)

[85] Edward W. Kolb and Michael S. Turner. The Early Universe. *Front. Phys.*, 69:1–547, 1990. (Cited on page 61.)

[86] Xenon100 Collaboration, E. Aprile, K. Arisaka, F. Arneodo, A. Askin, L. Baudis, A. Behrens, E. Brown, J. M. R. Cardoso, B. Choi, D. Cline, S. Fattori, A. D. Ferella, K. L. Giboni, A. Kish, C. W. Lam, R. F. Lang, K. E. Lim, J. A. M. Lopes, T. Marrodán Undagoitia, Y. Mei, A. J. Melgarejo Fernandez, K. Ni, U. Oberlack, S. E. A. Orrigo, E. Pantic, G. Plante, A. C. C. Ribeiro, R. Santorelli, J. M. F. Dos Santos, M. Schumann, P. Shagin, A. Teymourian, E. Tziaferi, H. Wang, and M. Yamashita. The XENON100 dark matter experiment. *Astroparticle Physics*, 35:573–590, April 2012. (Cited on page 63.)

[87] Jalal Abdallah et al. Simplified Models for Dark Matter Searches at the LHC. *Phys. Dark Univ.*, 9-10:8–23, 2015. (Cited on page 63.)

[88] Lawrence J. Hall, Karsten Jedamzik, John March-Russell, and Stephen M. West. Freeze-In Production of FIMP Dark Matter. *JHEP*, 03:080, 2010. (Cited on page 63.)

[89] Yonit Hochberg, Eric Kuflik, Tomer Volansky, and Jay G. Wacker. Mechanism for Thermal Relic Dark Matter of Strongly Interacting Massive Particles. *Phys. Rev. Lett.*, 113:171301, 2014. (Cited on pages 63, 91 and 105.)

[90] C. S. Frenk and Simon D. M. White. Dark matter and cosmic structure. *Annalen Phys.*, 524:507–534, 2012. (Cited on page 64.)

[91] Max Tegmark et al. The 3-D power spectrum of galaxies from the SDSS. *Astrophys. J.*, 606:702–740, 2004. (Cited on pages 65 and 160.)

[92] W. J. G. de Blok. The Core-Cusp Problem. *Adv. Astron.*, 2010:789293, 2010. (Cited on pages 64 and 90.)

[93] Michael Boylan-Kolchin, James S. Bullock, and Manoj Kaplinghat. Too big to fail? The puzzling darkness of massive Milky Way subhaloes. *Mon. Not. Roy. Astron. Soc.*, 415:L40, 2011. (Cited on pages 64 and 90.)

[94] James S. Bullock. Notes on the Missing Satellites Problem. 2010. (Cited on pages 64 and 90.)

[95] R. B. Tully and J. R. Fisher. A New method of determining distances to galaxies. *Astron. Astrophys.*, 54:661–673, 1977. (Cited on pages 64 and 90.)

[96] B. Moore, S. Ghigna, F. Governato, G. Lake, Thomas R. Quinn, J. Stadel, and P. Tozzi. Dark matter substructure within galactic halos. *Astrophys. J.*, 524:L19–L22, 1999. (Cited on pages 64 and 90.)

[97] A. Burkert. The Structure of dark matter halos in dwarf galaxies. *IAU Symp.*, 171:175, 1996. [Astrophys. J.447,L25(1995)]. (Cited on pages 64 and 90.)

[98] Benjamin D. Wandelt, Romeel Dave, Glennys R. Farrar, Patrick C. McGuire, David N. Spergel, and Paul J. Steinhardt. Selfinteracting dark matter. In *Sources and detection of dark matter and dark energy in the universe. Proceedings, 4th International Symposium, DM 2000, Marina del Rey, USA, February 23-25, 2000*, pages 263–274, 2000. (Cited on page 64.)

[99] Thomas Junk. Confidence level computation for combining searches with small statistics. *Nucl. Instrum. Meth.*, A434:435–443, 1999. (Cited on pages 65 and 102.)

[100] Alexander L. Read. Presentation of search results: The CL(s) technique. *J. Phys.*, G28:2693–2704, 2002. [,11(2002)]. (Cited on pages 66 and 102.)

[101] Johann Brehmer, Kyle Cranmer, Felix Kling, and Tilman Plehn. Better Higgs boson measurements through information geometry. *Phys. Rev.*, D95(7):073002, 2017. (Cited on pages 66, 67, 68 and 161.)

[102] C. Radhakrishna Rao. Information and the accuracy attainable in the estimation of statistical parameters. *Bull. Calcutta Math. Soc.*, 37:81–91, 1945. (Cited on page 67.)

[103] Kyle Cranmer and Tilman Plehn. Maximum significance at the LHC and Higgs decays to muons. *Eur. Phys. J.*, C51:415–420, 2007. (Cited on page 68.)

[104] G. Cybenko. Approximation by superpositions of a sigmoidal function. *Mathematics of Control, Signals and Systems*, 2(4):303–314, Dec 1989. (Cited on page 69.)

[105] Andrew R Barron. Universal approximation bounds for superpositions of a sigmoidal function. *IEEE Transactions on Information theory*, 39(3):930–945, 1993. (Cited on page 69.)

[106] Alexandr Andoni, Rina Panigrahy, Gregory Valiant, and Li Zhang. Learning polynomials with neural networks. In Eric P. Xing and Tony Jebara, editors, *Proceedings of the 31st International Conference on Machine Learning*, volume 32 of *Proceedings of Machine Learning Research*, pages 1908–1916, Bejing, China, 22–24 Jun 2014. PMLR. (Cited on page 69.)

[107] Sarah Malik, Christopher McCabe, Henrique Araujo, A. Belyaev, Celine Boehm, et al. Interplay and Characterization of Dark Matter Searches at Colliders and in Direct Detection Experiments. 2014. (Cited on pages 72 and 73.)

[108] Oliver Buchmueller, Matthew J. Dolan, Sarah A. Malik, and Christopher McCabe. Characterising dark matter searches at colliders and direct detection experiments: Vector mediators. 2014. (Cited on pages 72, 73 and 77.)

[109] Patrick J. Fox, Roni Harnik, Joachim Kopp, and Yuhsin Tsai. Missing Energy Signatures of Dark Matter at the LHC. *Phys.Rev.*, D85:056011, 2012. (Cited on page 72.)

[110] O. Buchmueller, Matthew J. Dolan, and Christopher McCabe. Beyond Effective Field Theory for Dark Matter Searches at the LHC. *JHEP*, 1401:025, 2014. (Cited on pages 72 and 93.)

[111] Giorgio Busoni, Andrea De Simone, Johanna Gramling, Enrico Morgante, and Antonio Riotto. On the Validity of the Effective Field Theory for Dark Matter Searches at the LHC, Part II: Complete Analysis for the s-channel. 2014. (Cited on page 73.)

[112] Sensitivity to WIMP Dark Matter in the Final States Containing Jets and Missing Transverse Momentum with the ATLAS Detector at 14 TeV LHC. Technical Report ATL-PHYS-PUB-2014-007, CERN, Geneva, Jun 2014. (Cited on pages 73 and 86.)

[113] Georges Aad et al. Search for new phenomena in final states with an energetic jet and large missing transverse momentum in pp collisions at $\sqrt{s} = 8$ TeV with the ATLAS detector. 2015. (Cited on pages 73, 74, 80, 99 and 100.)

[114] D.J.H. Chung, L.L. Everett, G.L. Kane, S.F. King, Joseph D. Lykken, et al. The Soft supersymmetry breaking Lagrangian: Theory and applications. *Phys.Rept.*, 407:1–203, 2005. (Cited on page 73.)

[115] Nima Arkani-Hamed, Savas Dimopoulos, and G.R. Dvali. The Hierarchy problem and new dimensions at a millimeter. *Phys.Lett.*, B429:263–272, 1998. (Cited on page 73.)

[116] Jalal Abdallah, Adi Ashkenazi, Antonio Boveia, Giorgio Busoni, Andrea De Simone, et al. Simplified Models for Dark Matter and Missing Energy Searches at the LHC. 2014. (Cited on page 73.)

[117] Daniele Alves et al. Simplified Models for LHC New Physics Searches. *J.Phys.*, G39:105005, 2012. (Cited on page 73.)

[118] Philip Harris, Valentin V. Khoze, Michael Spannowsky, and Ciaran Williams. Constraining Dark Sectors at Colliders: Beyond the Effective Theory Approach. 2014. (Cited on pages 73 and 93.)

[119] Matthew R. Buckley, David Feld, and Dorival Goncalves. Scalar Simplified Models for Dark Matter. *Phys.Rev.*, D91(1):015017, 2015. (Cited on pages 73 and 93.)

[120] Marco Cirelli, Eugenio Del Nobile, and Paolo Panci. Tools for model-independent bounds in direct dark matter searches. *JCAP*, 1310:019, 2013. (Cited on page 74.)

[121] Georges Aad et al. Search for new phenomena in events with a photon and missing transverse momentum in pp collisions at $\sqrt{s} = 8$ TeV with the ATLAS detector. 2014. (Cited on page 74.)

[122] Felix Kahlhoefer, Kai Schmidt-Hoberg, Thomas Schwetz, and Stefan Vogl. Implications of unitarity and gauge invariance for simplified dark matter models. *JHEP*, 02:016, 2016. (Cited on page 74.)

[123] Georges Aad et al. Search for high-mass dilepton resonances in pp collisions at $\sqrt{s} = 8$TeV with the ATLAS detector. *Phys.Rev.*, D90(5):052005, 2014. (Cited on page 75.)

[124] Vardan Khachatryan et al. Search for physics beyond the standard model in dilepton mass spectra in proton-proton collisions at $\sqrt{s} = 8$ TeV. *JHEP*, 1504:025, 2015. (Cited on page 75.)

[125] Stefano Goria, Giampiero Passarino, and Dario Rosco. The Higgs Boson Lineshape. *Nucl.Phys.*, B864:530–579, 2012. (Cited on page 75.)

[126] Christoph Englert, Ian Low, and Michael Spannowsky. On-shell interference effects in Higgs final states. 2015. (Cited on page 75.)

[127] Adam Alloul, Neil D. Christensen, Céline Degrande, Claude Duhr, and Benjamin Fuks. FeynRules 2.0 - A complete toolbox for tree-level phenomenology. *Comput.Phys.Commun.*, 185:2250–2300, 2014. (Cited on pages 76, 104 and 142.)

[128] J. Alwall, R. Frederix, S. Frixione, V. Hirschi, F. Maltoni, et al. The automated computation of tree-level and next-to-leading order differential cross sections, and their matching to parton shower simulations. *JHEP*, 1407:079, 2014. (Cited on pages 76, 134 and 142.)

[129] Richard D. Ball, Valerio Bertone, Stefano Carrazza, Christopher S. Deans, Luigi Del Debbio, et al. Parton distributions with LHC data. *Nucl.Phys.*, B867:244–289, 2013. (Cited on page 77.)

[130] Torbjorn Sjostrand, Stephen Mrenna, and Peter Z. Skands. A Brief Introduction to PYTHIA 8.1. *Comput.Phys.Commun.*, 178:852–867, 2008. (Cited on page 77.)

[131] Search for new physics in monojet events in pp collisions at sqrt(s)= 8 TeV. (CMS-PAS-EXO-12-048), 2013. (Cited on page 77.)

[132] Ulrich Haisch, Felix Kahlhoefer, and James Unwin. The impact of heavy-quark loops on LHC dark matter searches. *JHEP*, 1307:125, 2013. (Cited on page 77.)

[133] Patrick J. Fox and Ciaran Williams. Next-to-Leading Order Predictions for Dark Matter Production at Hadron Colliders. *Phys.Rev.*, D87:054030, 2013. (Cited on page 77.)

[134] Ulrich Haisch, Felix Kahlhoefer, and Emanuele Re. QCD effects in mono-jet searches for dark matter. *JHEP*, 1312:007, 2013. (Cited on page 77.)

[135] Ian-Woo Kim, Michele Papucci, Kazuki Sakurai, and Andreas Weiler. , in preparation. (Cited on page 77.)

[136] Michele Papucci, Kazuki Sakurai, Andreas Weiler, and Lisa Zeune. Fastlim: a fast LHC limit calculator. *Eur.Phys.J.*, C74(11):3163, 2014. (Cited on page 77.)

[137] Andy Buckley, Jonathan Butterworth, Leif Lonnblad, David Grellscheid, Hendrik Hoeth, et al. Rivet user manual. *Comput.Phys.Commun.*, 184:2803–2819, 2013. (Cited on pages 77, 119 and 142.)

[138] Matteo Cacciari, Gavin P. Salam, and Gregory Soyez. FastJet User Manual. *Eur.Phys.J.*, C72:1896, 2012. (Cited on pages 77 and 119.)

[139] Georges Aad et al. Performance of Missing Transverse Momentum Reconstruction in ATLAS studied in Proton-Proton Collisions recorded in 2012 at 8 TeV. (ATLAS-CONF-2013-082), Aug 2013. (Cited on page 77.)

[140] Tao Han. Collider phenomenology: Basic knowledge and techniques. pages 407–454, 2005. (Cited on page 78.)

[141] Patrick J. Fox, Roni Harnik, Joachim Kopp, and Yuhsin Tsai. LEP Shines Light on Dark Matter. *Phys.Rev.*, D84:014028, 2011. (Cited on page 78.)

[142] Paolo Gondolo and Graciela Gelmini. Cosmic abundances of stable particles: Improved analysis. *Nucl.Phys.*, B360:145–179, 1991. (Cited on page 78.)

[143] Gianfranco Bertone, Dan Hooper, and Joseph Silk. Particle dark matter: Evidence, candidates and constraints. *Phys.Rept.*, 405:279–390, 2005. (Cited on page 78.)

[144] Giorgio Busoni, Andrea De Simone, Thomas Jacques, Enrico Morgante, and Antonio Riotto. Making the Most of the Relic Density for Dark Matter Searches at the LHC 14 TeV Run. 2014. (Cited on page 78.)

[145] Search for New Phenomena in Monojet plus Missing Transverse Momentum Final States using 10fb-1 of pp Collisions at sqrts=8 TeV with the ATLAS detector at the LHC. 2012. (Cited on pages 79, 80 and 168.)

[146] Vardan Khachatryan et al. Search for dark matter, extra dimensions, and unparticles in monojet events in proton-proton collisions at $\sqrt{s} = 8$ TeV. 2014. (Cited on pages 80 and 100.)

[147] Georges Aad et al. Search for new phenomena in the dijet mass distribution using pp collision data at $\sqrt{s} = 8$ TeV with the ATLAS detector. 2014. (Cited on page 82.)

[148] Serguei Chatrchyan et al. Search for narrow resonances using the dijet mass spectrum in pp collisions at $\sqrt{s}$=8TeV. *Phys.Rev.*, D87(11):114015, 2013. (Cited on page 82.)

[149] T. Aaltonen et al. Search for new particles decaying into dijets in proton-antiproton collisions at s**(1/2) = 1.96-TeV. *Phys.Rev.*, D79:112002, 2009. (Cited on page 82.)

[150] Vardan Khachatryan et al. Search for resonances and quantum black holes using dijet mass spectra in proton-proton collisions at $\sqrt{s}$=8 TeV. 2015. (Cited on pages 82 and 83.)

[151] Haipeng An, Xiangdong Ji, and Lian-Tao Wang. Light Dark Matter and Z' Dark Force at Colliders. *JHEP*, 1207:182, 2012. (Cited on pages 83, 84 and 85.)

[152] Bogdan A. Dobrescu and Felix Yu. Coupling-mass mapping of dijet peak searches. *Phys.Rev.*, D88(3):035021, 2013. (Cited on pages 84, 85 and 162.)

[153] Elena Accomando, Diego Becciolini, Alexander Belyaev, Stefano Moretti, and Claire Shepherd-Themistocleous. Z' at the LHC: Interference and Finite Width Effects in Drell-Yan. *JHEP*, 1310:153, 2013. (Cited on page 85.)

[154] Georges Aad et al. ATLAS search for new phenomena in dijet mass and angular distributions using pp collisions at $\sqrt{s} = 7$ TeV. *JHEP*, 1301:029, 2013. (Cited on page 85.)

[155] Vardan Khachatryan et al. Search for quark contact interactions and extra spatial dimensions using dijet angular distributions in proton-proton collisions at $\sqrt{s} = 8$ TeV. 2014. (Cited on page 85.)

[156] Search for dark matter and other new phenomena in events with an energetic jet and large missing transverse momentum using the ATLAS detector. Technical Report ATLAS-CONF-2017-060, CERN, Geneva, Jul 2017. (Cited on pages 86, 88 and 162.)

[157] Romeel Dave, David N. Spergel, Paul J. Steinhardt, and Benjamin D. Wandelt. Halo properties in cosmological simulations of selfinteracting cold dark matter. *Astrophys. J.*, 547:574–589, 2001. (Cited on page 90.)

[158] Mark Vogelsberger, Jesus Zavala, and Abraham Loeb. Subhaloes in Self-Interacting Galactic Dark Matter Haloes. *Mon. Not. Roy. Astron. Soc.*, 423:3740, 2012. (Cited on page 90.)

[159] Miguel Rocha, Annika H. G. Peter, James S. Bullock, Manoj Kaplinghat, Shea Garrison-Kimmel, Jose Onorbe, and Leonidas A. Moustakas. Cosmological Simulations with Self-Interacting Dark Matter I: Constant Density Cores and Substructure. *Mon. Not. Roy. Astron. Soc.*, 430:81–104, 2013. (Cited on page 90.)

[160] Annika H. G. Peter, Miguel Rocha, James S. Bullock, and Manoj Kaplinghat. Cosmological Simulations with Self-Interacting Dark Matter II: Halo Shapes vs. Observations. *Mon. Not. Roy. Astron. Soc.*, 430:105, 2013. (Cited on page 90.)

[161] Scott W. Randall, Maxim Markevitch, Douglas Clowe, Anthony H. Gonzalez, and Marusa Bradac. Constraints on the Self-Interaction Cross-Section of Dark Matter from Numerical Simulations of the Merging Galaxy Cluster 1E 0657-56. *Astrophys. J.*, 679:1173–1180, 2008. (Cited on pages 90 and 103.)

[162] Felix Kahlhoefer, Kai Schmidt-Hoberg, Mads T. Frandsen, and Subir Sarkar. Colliding clusters and dark matter self-interactions. *Mon. Not. Roy. Astron. Soc.*, 437(3):2865–2881, 2014. (Cited on page 90.)

[163] Andrew Robertson, Richard Massey, and Vincent Eke. What does the Bullet Cluster tell us about self-interacting dark matter? *Mon. Not. Roy. Astron. Soc.*, 465(1):569–587, 2017. (Cited on page 90.)

[164] Bob Holdom. Two U(1)'s and Epsilon Charge Shifts. *Phys. Lett.*, B166:196–198, 1986. (Cited on page 91.)

[165] R. Foot and S. Vagnozzi. Dissipative hidden sector dark matter. *Phys. Rev.*, D91:023512, 2015. (Cited on page 91.)

[166] Robert Foot and Sunny Vagnozzi. Solving the small-scale structure puzzles with dissipative dark matter. 2016. (Cited on page 91.)

[167] T. Binoth and J. J. van der Bij. Influence of strongly coupled, hidden scalars on Higgs signals. *Z. Phys.*, C75:17–25, 1997. (Cited on pages 91 and 94.)

[168] Robert Schabinger and James D. Wells. A Minimal spontaneously broken hidden sector and its impact on Higgs boson physics at the large hadron collider. *Phys. Rev.*, D72:093007, 2005. (Cited on page 91.)

[169] Brian Patt and Frank Wilczek. Higgs-field portal into hidden sectors. 2006. (Cited on page 91.)

[170] Anthony DiFranzo and Gopolang Mohlabeng. Multi-component Dark Matter through a Radiative Higgs Portal. *JHEP*, 01:080, 2017. (Cited on page 91.)

[171] Matthew J. Strassler and Kathryn M. Zurek. Echoes of a hidden valley at hadron colliders. *Phys. Lett.*, B651:374–379, 2007. (Cited on pages 91 and 95.)

[172] Tao Han, Zongguo Si, Kathryn M. Zurek, and Matthew J. Strassler. Phenomenology of hidden valleys at hadron colliders. *JHEP*, 07:008, 2008. (Cited on pages 91 and 95.)

[173] Lawrence M. Krauss and James B. Dent. A Higgs–Saw Mechanism as a Source for Dark Energy. *Phys. Rev. Lett.*, 111:061802, 2013. (Cited on page 91.)

[174] Clare Burrage, Edmund J. Copeland, and Peter Millington. Radiative screening of fifth forces. 2016. (Cited on page 91.)

[175] Krzysztof A. Meissner and Hermann Nicolai. Conformal Symmetry and the Standard Model. *Phys. Lett.*, B648:312–317, 2007. (Cited on page 91.)

[176] Christoph Englert, Joerg Jaeckel, V. V. Khoze, and Michael Spannowsky. Emergence of the Electroweak Scale through the Higgs Portal. *JHEP*, 04:060, 2013. (Cited on page 91.)

[177] Steven Abel and Alberto Mariotti. Novel Higgs Potentials from Gauge Mediation of Exact Scale Breaking. *Phys. Rev.*, D89(12):125018, 2014. (Cited on page 91.)

[178] Adam Latosinski, Adrian Lewandowski, Krzysztof A. Meissner, and Hermann Nicolai. Conformal Standard Model with an extended scalar sector. *JHEP*, 10:170, 2015. (Cited on page 91.)

[179] Valentin V. Khoze and Gunnar Ro. Leptogenesis and Neutrino Oscillations in the Classically Conformal Standard Model with the Higgs Portal. *JHEP*, 10:075, 2013. (Cited on page 91.)

[180] Valentin V. Khoze. Inflation and Dark Matter in the Higgs Portal of Classically Scale Invariant Standard Model. *JHEP*, 11:215, 2013. (Cited on page 91.)

[181] Matthew J. Dolan, Christoph Englert, and Michael Spannowsky. New Physics in LHC Higgs boson pair production. *Phys. Rev.*, D87(5):055002, 2013. (Cited on page 92.)

[182] S. Y. Choi, C. Englert, and P. M. Zerwas. Multiple Higgs-Portal and Gauge-Kinetic Mixings. *Eur. Phys. J.*, C73:2643, 2013. (Cited on pages 92 and 128.)

[183] Andreas Papaefstathiou and Kazuki Sakurai. Triple Higgs boson production at a 100 TeV proton-proton collider. *JHEP*, 02:006, 2016. (Cited on page 92.)

[184] Herbert Dreiner, Moritz Huck, Michael Krämer, Daniel Schmeier, and Jamie Tattersall. Illuminating Dark Matter at the ILC. *Phys.Rev.*, D87(7):075015, 2013. (Cited on page 92.)

[185] Valentin V Khoze, Gunnar Ro, and Michael Spannowsky. Spectroscopy of scalar mediators to dark matter at the LHC and at 100 TeV. *Phys. Rev.*, D92(7):075006, 2015. (Cited on page 92.)

[186] Ulrich Haisch and Emanuele Re. Simplified dark matter top-quark interactions at the LHC. *JHEP*, 06:078, 2015. (Cited on page 93.)

[187] Christoph Englert, Tilman Plehn, Dirk Zerwas, and Peter M. Zerwas. Exploring the Higgs portal. *Phys. Lett.*, B703:298–305, 2011. (Cited on page 94.)

[188] Tania Robens and Tim Stefaniak. LHC Benchmark Scenarios for the Real Higgs Singlet Extension of the Standard Model. 2016. (Cited on page 94.)

[189] Tania Robens and Tim Stefaniak. Status of the Higgs Singlet Extension of the Standard Model after LHC Run 1. *Eur. Phys. J.*, C75:104, 2015. (Cited on page 96.)

[190] Florian Staub. SARAH 4 : A tool for (not only SUSY) model builders. *Comput. Phys. Commun.*, 185:1773–1790, 2014. (Cited on page 98.)

[191] K. Arnold et al. VBFNLO: A Parton Level Monte Carlo for Processes with Electroweak Bosons – Manual for Version 2.5.0. 2011. (Cited on page 99.)

[192] T. Hahn and M. Perez-Victoria. Automatized one loop calculations in four-dimensions and D-dimensions. *Comput. Phys. Commun.*, 118:153–165, 1999. (Cited on pages 99 and 104.)

[193] Thomas Hahn. Generating Feynman diagrams and amplitudes with FeynArts 3. *Comput. Phys. Commun.*, 140:418–431, 2001. (Cited on pages 99 and 104.)

[194] J R Andersen et al. Handbook of LHC Higgs Cross Sections: 3. Higgs Properties. 2013. (Cited on pages 99, 119 and 122.)

[195] Morad Aaboud et al. Search for new phenomena in final states with an energetic jet and large missing transverse momentum in pp collisions at $\sqrt{s} = 13$ TeV using the ATLAS detector. 2016. (Cited on page 100.)

[196] Vardan Khachatryan et al. Search for dark matter production in association with jets, or hadronically decaying W or Z boson at $\sqrt{s} = 13$ TeV. 2016. (Cited on page 100.)

[197] Vardan Khachatryan et al. Search for new physics in final states with jets and missing transverse momentum in $\sqrt{s} = 13$ TeV pp collisions with the α_T variable. 2015. (Cited on page 101.)

[198] T. Golling et al. Physics at a 100 TeV pp collider: beyond the Standard Model phenomena. 2016. (Cited on page 101.)

[199] Nima Arkani-Hamed, Tao Han, Michelangelo Mangano, and Lian-Tao Wang. Physics Opportunities of a 100 TeV Proton-Proton Collider. 2015. (Cited on page 101.)

[200] F. James, Y. Perrin, and L. Lyons, editors. *Workshop on confidence limits, CERN, Geneva, Switzerland, 17-18 Jan 2000: Proceedings*, 2000. (Cited on page 102.)

[201] Michael E. Peskin. Comparison of LHC and ILC Capabilities for Higgs Boson Coupling Measurements. 2012. (Cited on page 102.)

[202] A. Blondel et al. LEP3: A High Luminosity e^+e^- Collider to study the Higgs Boson. 2012. (Cited on page 102.)

[203] P. Ko and Y. Tang. Self-interacting scalar dark matter with local Z_3 symmetry. *JCAP*, 1405:047, 2014. (Cited on page 103.)

[204] Matthew McCullough and Lisa Randall. Exothermic Double-Disk Dark Matter. *JCAP*, 1310:058, 2013. (Cited on page 103.)

[205] JiJi Fan, Andrey Katz, Lisa Randall, and Matthew Reece. Dark-Disk Universe. *Phys. Rev. Lett.*, 110(21):211302, 2013. (Cited on page 103.)

[206] Aneesh Manohar and Howard Georgi. Chiral Quarks and the Nonrelativistic Quark Model. *Nucl. Phys.*, B234:189–212, 1984. (Cited on page 104.)

[207] Yonit Hochberg, Eric Kuflik, Hitoshi Murayama, Tomer Volansky, and Jay G. Wacker. Model for Thermal Relic Dark Matter of Strongly Interacting Massive Particles. *Phys. Rev. Lett.*, 115(2):021301, 2015. (Cited on page 105.)

[208] Kimberly K. Boddy, Jonathan L. Feng, Manoj Kaplinghat, and Tim M. P. Tait. Self-Interacting Dark Matter from a Non-Abelian Hidden Sector. *Phys. Rev.*, D89(11):115017, 2014. (Cited on pages 105 and 106.)

[209] Amarjit Soni and Yue Zhang. Hidden SU(N) Glueball Dark Matter. *Phys. Rev.*, D93(11):115025, 2016. (Cited on page 105.)

[210] Matthew J. Dolan, Christoph Englert, Nicolas Greiner, and Michael Spannowsky. Further on up the road: $hhjj$ production at the LHC. *Phys. Rev. Lett.*, 112:101802, 2014. (Cited on pages 107, 110, 113 and 119.)

[211] Prospects for measuring Higgs pair production in the channel $H(\to \gamma\gamma)H(\to b\bar{b})$ using the ATLAS detector at the HL-LHC. Technical Report ATL-PHYS-PUB-2014-019, CERN, Geneva, Oct 2014. (Cited on pages 108, 109, 133 and 164.)

[212] O. Arnaez. Higgs Prospects for future (HL)LHC runs. (Cited on pages 108 and 109.)

[213] E. W. Nigel Glover and J. J. van der Bij. HIGGS BOSON PAIR PRODUCTION VIA GLUON FUSION. *Nucl. Phys.*, B309:282–294, 1988. (Cited on page 109.)

[214] Duane A. Dicus, Chung Kao, and Scott S. D. Willenbrock. Higgs Boson Pair Production From Gluon Fusion. *Phys. Lett.*, B203:457–461, 1988. (Cited on page 109.)

[215] T. Plehn, M. Spira, and P. M. Zerwas. Pair production of neutral Higgs particles in gluon-gluon collisions. *Nucl. Phys.*, B479:46–64, 1996. [Erratum: Nucl. Phys.B531,655(1998)]. (Cited on page 109.)

[216] Florian Goertz, Andreas Papaefstathiou, Li Lin Yang, and José Zurita. Higgs boson pair production in the D=6 extension of the SM. *JHEP*, 04:167, 2015. (Cited on page 109.)

[217] Aleksandr Azatov, Roberto Contino, Giuliano Panico, and Minho Son. Effective field theory analysis of double Higgs boson production via gluon fusion. *Phys. Rev.*, D92(3):035001, 2015. (Cited on page 109.)

[218] Florian Goertz. Electroweak Symmetry Breaking without the μ^2 Term. *Phys. Rev.*, D94(1):015013, 2016. (Cited on page 109.)

[219] G. Brooijmans et al. Les Houches 2013: Physics at TeV Colliders: New Physics Working Group Report. 2014. (Cited on page 110.)

[220] J. Baglio, A. Djouadi, R. Gröber, M. M. Mühlleitner, J. Quevillon, and M. Spira. The measurement of the Higgs self-coupling at the LHC: theoretical status. *JHEP*, 04:151, 2013. (Cited on pages 110, 111, 115 and 168.)

[221] R. Frederix, S. Frixione, V. Hirschi, F. Maltoni, O. Mattelaer, P. Torrielli, E. Vryonidou, and M. Zaro. Higgs pair production at the LHC with NLO and parton-shower effects. *Phys. Lett.*, B732:142–149, 2014. (Cited on pages 110 and 115.)

[222] Ding Yu Shao, Chong Sheng Li, Hai Tao Li, and Jian Wang. Threshold resummation effects in Higgs boson pair production at the LHC. *JHEP*, 07:169, 2013. (Cited on page 110.)

[223] Daniel de Florian and Javier Mazzitelli. Two-loop virtual corrections to Higgs pair production. *Phys. Lett.*, B724:306–309, 2013. (Cited on page 110.)

[224] Jonathan Grigo, Jens Hoff, Kirill Melnikov, and Matthias Steinhauser. On the Higgs boson pair production at the LHC. *Nucl. Phys.*, B875:1–17, 2013. (Cited on page 110.)

[225] Daniel de Florian and Javier Mazzitelli. Higgs Boson Pair Production at Next-to-Next-to-Leading Order in QCD. *Phys. Rev. Lett.*, 111:201801, 2013. (Cited on page 110.)

[226] T. Figy, C. Oleari, and D. Zeppenfeld. Next-to-leading order jet distributions for Higgs boson production via weak boson fusion. *Phys. Rev.*, D68:073005, 2003. (Cited on pages 110 and 115.)

[227] Jeppe R. Andersen and Jennifer M. Smillie. QCD and electroweak interference in Higgs production by gauge boson fusion. *Phys. Rev.*, D75:037301, 2007. (Cited on page 110.)

[228] J. R. Andersen, T. Binoth, G. Heinrich, and J. M. Smillie. Loop induced interference effects in Higgs Boson plus two jet production at the LHC. *JHEP*, 02:057, 2008. (Cited on page 110.)

[229] Mariano Ciccolini, Ansgar Denner, and Stefan Dittmaier. Electroweak and QCD corrections to Higgs production via vector-boson fusion at the LHC. *Phys. Rev.*, D77:013002, 2008. (Cited on page 110.)

[230] Paolo Bolzoni, Fabio Maltoni, Sven-Olaf Moch, and Marco Zaro. Higgs production via vector-boson fusion at NNLO in QCD. *Phys. Rev. Lett.*, 105:011801, 2010. (Cited on page 110.)

[231] Terrance Figy. Next-to-leading order QCD corrections to light Higgs Pair production via vector boson fusion. *Mod. Phys. Lett.*, A23:1961–1973, 2008. (Cited on pages 110 and 115.)

[232] Jeppe R. Andersen, Vittorio Del Duca, and Chris D. White. Higgs Boson Production in Association with Multiple Hard Jets. *JHEP*, 02:015, 2009. (Cited on page 110.)

[233] Jeppe R. Andersen, Ken Arnold, and Dieter Zeppenfeld. Azimuthal Angle Correlations for Higgs Boson plus Multi-Jet Events. *JHEP*, 06:091, 2010. (Cited on page 110.)

[234] Vernon D. Barger, R. J. N. Phillips, and D. Zeppenfeld. Mini - jet veto: A Tool for the heavy Higgs search at the LHC. *Phys. Lett.*, B346:106–114, 1995. (Cited on pages 110 and 115.)

[235] Ulrich Baur, Tilman Plehn, and David L. Rainwater. Measuring the Higgs boson self coupling at the LHC and finite top mass matrix elements. *Phys. Rev. Lett.*, 89:151801, 2002. (Cited on pages 111 and 113.)

[236] S. Dawson, A. Ismail, and Ian Low. What's in the loop? The anatomy of double Higgs production. *Phys. Rev.*, D91(11):115008, 2015. (Cited on page 111.)

[237] Philipp Maierhöfer and Andreas Papaefstathiou. Higgs Boson pair production merged to one jet. *JHEP*, 03:126, 2014. (Cited on page 111.)

[238] Georges Aad et al. Search for $t\bar{t}$ resonances in the lepton plus jets final state with ATLAS using 4.7 fb^{-1} of pp collisions at $\sqrt{s} = 7$ TeV. *Phys. Rev.*, D88(1):012004, 2013. (Cited on page 111.)

[239] Johan Alwall, Michel Herquet, Fabio Maltoni, Olivier Mattelaer, and Tim Stelzer. MadGraph 5 : Going Beyond. *JHEP*, 06:128, 2011. (Cited on pages 112 and 142.)

[240] Celine Degrande, Claude Duhr, Benjamin Fuks, David Grellscheid, Olivier Mattelaer, et al. UFO - The Universal FeynRules Output. *Comput.Phys.Commun.*, 183:1201–1214, 2012. (Cited on pages 112 and 142.)

[241] Gavin Cullen, Nicolas Greiner, Gudrun Heinrich, Gionata Luisoni, Pierpaolo Mastrolia, Giovanni Ossola, Thomas Reiter, and Francesco Tramontano. Automated One-Loop Calculations with GoSam. *Eur. Phys. J.*, C72:1889, 2012. (Cited on page 112.)

[242] Gavin Cullen et al. (Cited on page 112.)

[243] Paulo Nogueira. Automatic Feynman graph generation. *J. Comput. Phys.*, 105:279–289, 1993. (Cited on page 112.)

[244] J. A. M. Vermaseren. New features of FORM. 2000. (Cited on page 112.)

[245] J. Kuipers, T. Ueda, J. A. M. Vermaseren, and J. Vollinga. FORM version 4.0. *Comput. Phys. Commun.*, 184:1453–1467, 2013. (Cited on page 112.)

[246] Gavin Cullen, Maciej Koch-Janusz, and Thomas Reiter. Spinney: A Form Library for Helicity Spinors. *Comput. Phys. Commun.*, 182:2368–2387, 2011. (Cited on page 112.)

[247] Thomas Reiter. Optimising Code Generation with haggies. *Comput. Phys. Commun.*, 181:1301–1331, 2010. (Cited on page 112.)

[248] P. Mastrolia, G. Ossola, T. Reiter, and F. Tramontano. Scattering AMplitudes from Unitarity-based Reduction Algorithm at the Integrand-level. *JHEP*, 08:080, 2010. (Cited on page 112.)

[249] R. Keith Ellis, W. T. Giele, and Z. Kunszt. A Numerical Unitarity Formalism for Evaluating One-Loop Amplitudes. *JHEP*, 03:003, 2008. (Cited on page 112.)

[250] Giovanni Ossola, Costas G. Papadopoulos, and Roberto Pittau. Reducing full one-loop amplitudes to scalar integrals at the integrand level. *Nucl. Phys.*, B763:147–169, 2007. (Cited on page 112.)

[251] P. Mastrolia, G. Ossola, C. G. Papadopoulos, and R. Pittau. Optimizing the Reduction of One-Loop Amplitudes. *JHEP*, 06:030, 2008. (Cited on page 112.)

[252] Giovanni Ossola, Costas G. Papadopoulos, and Roberto Pittau. On the Rational Terms of the one-loop amplitudes. *JHEP*, 05:004, 2008. (Cited on page 112.)

[253] G. Heinrich, G. Ossola, T. Reiter, and F. Tramontano. Tensorial Reconstruction at the Integrand Level. *JHEP*, 10:105, 2010. (Cited on page 112.)

[254] A. van Hameren. OneLOop: For the evaluation of one-loop scalar functions. *Comput. Phys. Commun.*, 182:2427–2438, 2011. (Cited on page 112.)

[255] Pierpaolo Mastrolia, Edoardo Mirabella, and Tiziano Peraro. Integrand reduction of one-loop scattering amplitudes through Laurent series expansion. *JHEP*, 06:095, 2012. [Erratum: JHEP11,128(2012)]. (Cited on page 112.)

[256] Hans van Deurzen, Gionata Luisoni, Pierpaolo Mastrolia, Edoardo Mirabella, Giovanni Ossola, and Tiziano Peraro. Multi-leg One-loop Massive Amplitudes from Integrand Reduction via Laurent Expansion. *JHEP*, 03:115, 2014. (Cited on page 112.)

[257] Tiziano Peraro. Ninja: Automated Integrand Reduction via Laurent Expansion for One-Loop Amplitudes. *Comput. Phys. Commun.*, 185:2771–2797, 2014. (Cited on page 112.)

[258] T. Binoth, J. Ph. Guillet, G. Heinrich, E. Pilon, and T. Reiter. Golem95: A Numerical program to calculate one-loop tensor integrals with up to six external legs. *Comput. Phys. Commun.*, 180:2317–2330, 2009. (Cited on page 112.)

[259] G. Cullen, J. Ph. Guillet, G. Heinrich, T. Kleinschmidt, E. Pilon, T. Reiter, and M. Rodgers. Golem95C: A library for one-loop integrals with complex masses. *Comput. Phys. Commun.*, 182:2276–2284, 2011. (Cited on page 112.)

[260] J. Ph. Guillet, G. Heinrich, and J. F. von Soden-Fraunhofen. Tools for NLO automation: extension of the golem95C integral library. *Comput. Phys. Commun.*, 185:1828–1834, 2014. (Cited on page 112.)

[261] Johan Alwall, Pavel Demin, Simon de Visscher, Rikkert Frederix, Michel Herquet, Fabio Maltoni, Tilman Plehn, David L. Rainwater, and Tim Stelzer. MadGraph/MadEvent v4: The New Web Generation. *JHEP*, 09:028, 2007. (Cited on page 115.)

[262] Andrea Banfi, Gavin P. Salam, and Giulia Zanderighi. Resummed event shapes at hadron - hadron colliders. *JHEP*, 08:062, 2004. (Cited on page 117.)

[263] Andrea Banfi, Gavin P. Salam, and Giulia Zanderighi. Phenomenology of event shapes at hadron colliders. *JHEP*, 06:038, 2010. (Cited on page 117.)

[264] M. Bahr et al. Herwig++ Physics and Manual. *Eur. Phys. J.*, C58:639–707, 2008. (Cited on pages 119 and 142.)

[265] T. Gleisberg, Stefan. Hoeche, F. Krauss, M. Schonherr, S. Schumann, F. Siegert, and J. Winter. Event generation with SHERPA 1.1. *JHEP*, 02:007, 2009. (Cited on page 119.)

[266] G. Bevilacqua, M. Czakon, C. G. Papadopoulos, and M. Worek. Dominant QCD Backgrounds in Higgs Boson Analyses at the LHC: A Study of pp -> t anti-t + 2 jets at Next-To-Leading Order. *Phys. Rev. Lett.*, 104:162002, 2010. (Cited on page 119.)

[267] G. Bevilacqua, M. Czakon, C. G. Papadopoulos, and M. Worek. Hadronic top-quark pair production in association with two jets at Next-to-Leading Order QCD. *Phys. Rev.*, D84:114017, 2011. (Cited on page 119.)

[268] William J. Marciano and Frank E. Paige. Associated production of Higgs bosons with t anti-t pairs. *Phys. Rev. Lett.*, 66:2433–2435, 1991. (Cited on page 119.)

[269] W. Beenakker, S. Dittmaier, M. Kramer, B. Plumper, M. Spira, and P. M. Zerwas. Higgs radiation off top quarks at the Tevatron and the LHC. *Phys. Rev. Lett.*, 87:201805, 2001. (Cited on page 119.)

[270] L. Reina and S. Dawson. Next-to-leading order results for t anti-t h production at the Tevatron. *Phys. Rev. Lett.*, 87:201804, 2001. (Cited on page 119.)

[271] W. Beenakker, S. Dittmaier, M. Kramer, B. Plumper, M. Spira, and P. M. Zerwas. NLO QCD corrections to t anti-t H production in hadron collisions. *Nucl. Phys.*, B653:151–203, 2003. (Cited on page 119.)

[272] S. Dawson, C. Jackson, L. H. Orr, L. Reina, and D. Wackeroth. Associated Higgs production with top quarks at the large hadron collider: NLO QCD corrections. *Phys. Rev.*, D68:034022, 2003. (Cited on page 119.)

[273] Rikkert Frederix, Stefano Frixione, Valentin Hirschi, Fabio Maltoni, Roberto Pittau, and Paolo Torrielli. Scalar and pseudoscalar Higgs production in association with a top–antitop pair. *Phys. Lett.*, B701:427–433, 2011. (Cited on page 119.)

[274] M. V. Garzelli, A. Kardos, C. G. Papadopoulos, and Z. Trocsanyi. Standard Model Higgs boson production in association with a top anti-top pair at NLO with parton showering. *Europhys. Lett.*, 96:11001, 2011. (Cited on page 119.)

[275] Yu Zhang, Wen-Gan Ma, Ren-You Zhang, Chong Chen, and Lei Guo. QCD NLO and EW NLO corrections to $t\bar{t}H$ production with top quark decays at hadron collider. *Phys. Lett.*, B738:1–5, 2014. (Cited on page 119.)

[276] S. Frixione, V. Hirschi, D. Pagani, H. S. Shao, and M. Zaro. Electroweak and QCD corrections to top-pair hadroproduction in association with heavy bosons. *JHEP*, 06:184, 2015. (Cited on page 119.)

[277] Ansgar Denner and Robert Feger. NLO QCD corrections to off-shell top-antitop production with leptonic decays in association with a Higgs boson at the LHC. *JHEP*, 11:209, 2015. (Cited on page 119.)

[278] Georges Aad et al. Measurement of the b-tag Efficiency in a Sample of Jets Containing Muons with 5 fb1 of Data from the ATLAS Detector. 2012. (Cited on pages 119 and 143.)

[279] Amanda Kruse, Alan S. Cornell, Mukesh Kumar, Bruce Mellado, and Xifeng Ruan. Probing the Higgs boson via vector boson fusion with single jet tagging at the LHC. *Phys. Rev.*, D91(5):053009, 2015. (Cited on page 119.)

[280] Vernon D. Barger, King-man Cheung, Tao Han, and D. Zeppenfeld. Single forward jet tagging and central jet vetoing to identify the leptonic WW decay mode of a heavy Higgs boson. *Phys. Rev.*, D44:2701, 1991. [Erratum: Phys. Rev.D48,5444(1993)]. (Cited on page 119.)

[281] Alan J. Barr, Matthew J. Dolan, Christoph Englert, and Michael Spannowsky. Di-Higgs final states augMT2ed – selecting hh events at the high luminosity LHC. *Phys. Lett.*, B728:308–313, 2014. (Cited on page 119.)

[282] A. Bredenstein, Kaoru Hagiwara, and B. Jager. Mixed QCD-electroweak contributions to Higgs-plus-dijet production at the LHC. *Phys. Rev.*, D77:073004, 2008. (Cited on page 120.)

[283] Christoph Englert, Michael Spannowsky, and Michihisa Takeuchi. Measuring Higgs CP and couplings with hadronic event shapes. *JHEP*, 06:108, 2012. (Cited on page 122.)

[284] Iain W. Stewart, Frank J. Tackmann, and Wouter J. Waalewijn. N-Jettiness: An Inclusive Event Shape to Veto Jets. *Phys. Rev. Lett.*, 105:092002, 2010. (Cited on page 122.)

[285] Jesse Thaler and Ken Van Tilburg. Identifying Boosted Objects with N-subjettiness. *JHEP*, 03:015, 2011. (Cited on page 122.)

[286] Alan J. Barr, Matthew J. Dolan, Christoph Englert, Danilo Enoque Ferreira de Lima, and Michael Spannowsky. Higgs Self-Coupling Measurements at a 100 TeV Hadron Collider. *JHEP*, 02:016, 2015. (Cited on page 124.)

[287] Serguei Chatrchyan et al. Study of the Mass and Spin-Parity of the Higgs Boson Candidate Via Its Decays to Z Boson Pairs. *Phys. Rev. Lett.*, 110(8):081803, 2013. (Cited on page 124.)

[288] Georges Aad et al. Study of the spin and parity of the Higgs boson in diboson decays with the ATLAS detector. *Eur. Phys. J.*, C75(10):476, 2015. [Erratum: Eur. Phys. J.C76,no.3,152(2016)]. (Cited on page 124.)

[289] Christoph Englert, Dorival Goncalves-Netto, Kentarou Mawatari, and Tilman Plehn. Higgs Quantum Numbers in Weak Boson Fusion. *JHEP*, 01:148, 2013. (Cited on page 124.)

[290] Tyler Corbett, O. J. P. Eboli, J. Gonzalez-Fraile, and M. C. Gonzalez-Garcia. Constraining anomalous Higgs interactions. *Phys. Rev.*, D86:075013, 2012. (Cited on page 124.)

[291] John Ellis, Verónica Sanz, and Tevong You. Associated Production Evidence against Higgs Impostors and Anomalous Couplings. *Eur. Phys. J.*, C73:2507, 2013. (Cited on page 124.)

[292] Vardan Khachatryan et al. Constraints on the spin-parity and anomalous HVV couplings of the Higgs boson in proton collisions at 7 and 8 TeV. *Phys. Rev.*, D92(1):012004, 2015. (Cited on page 124.)

[293] Vardan Khachatryan et al. Combined search for anomalous pseudoscalar HVV couplings in VH(H → $b\bar{b}$) production and H → VV decay. *Phys. Lett.*, B759:672–696, 2016. (Cited on page 124.)

[294] CMS Collaboration. Measurements of properties of the Higgs boson and search for an additional resonance in the four-lepton final state at sqrt(s) = 13 TeV. 2016. (Cited on page 124.)

[295] John M. Cornwall, David N. Levin, and George Tiktopoulos. Uniqueness of spontaneously broken gauge theories. *Phys. Rev. Lett.*, 30:1268–1270, 1973. [Erratum: Phys. Rev. Lett.31,572(1973)]. (Cited on page 125.)

[296] John M. Cornwall, David N. Levin, and George Tiktopoulos. Derivation of Gauge Invariance from High-Energy Unitarity Bounds on the s Matrix. *Phys. Rev.*, D10:1145, 1974. [Erratum: Phys. Rev.D11,972(1975)]. (Cited on page 125.)

[297] B. C. Regan, E. D. Commins, C. J. Schmidt, and D. DeMille. New limit on the electron electric dipole moment. *Phys. Rev. Lett.*, 88:071805, 2002. (Cited on page 125.)

[298] C. A. Baker et al. An Improved experimental limit on the electric dipole moment of the neutron. *Phys. Rev. Lett.*, 97:131801, 2006. (Cited on page 125.)

[299] W. C. Griffith, M. D. Swallows, T. H. Loftus, M. V. Romalis, B. R. Heckel, and E. N. Fortson. Improved Limit on the Permanent Electric Dipole Moment of Hg-199. *Phys. Rev. Lett.*, 102:101601, 2009. (Cited on page 125.)

[300] Joachim Brod, Ulrich Haisch, and Jure Zupan. Constraints on CP-violating Higgs couplings to the third generation. *JHEP*, 11:180, 2013. (Cited on page 125.)

[301] Jacob Baron et al. Order of Magnitude Smaller Limit on the Electric Dipole Moment of the Electron. *Science*, 343:269–272, 2014. (Cited on page 125.)

[302] Y. T. Chien, V. Cirigliano, W. Dekens, J. de Vries, and E. Mereghetti. Direct and indirect constraints on CP-violating Higgs-quark and Higgs-gluon interactions. *JHEP*, 02:011, 2016. [JHEP02,011(2016)]. (Cited on page 125.)

[303] V. Cirigliano, W. Dekens, J. de Vries, and E. Mereghetti. Is there room for CP violation in the top-Higgs sector? *Phys. Rev.*, D94(1):016002, 2016. (Cited on page 125.)

[304] M. B. Gavela, J. Gonzalez-Fraile, M. C. Gonzalez-Garcia, L. Merlo, S. Rigolin, and J. Yepes. CP violation with a dynamical Higgs. *JHEP*, 10:044, 2014. (Cited on page 126.)

[305] Roberto Contino, Margherita Ghezzi, Christophe Grojean, Margarete Muhlleitner, and Michael Spira. Effective Lagrangian for a light Higgs-like scalar. *JHEP*, 07:035, 2013. (Cited on page 126.)

[306] Howard Georgi and D.V. Nanopoulos. Suppression of flavor changing effects from neutral spinless meson exchange in gauge theories. *Physics Letters B*, 82(1):95 – 96, 1979. (Cited on page 126.)

[307] Dorota Sokolowska, Konstantin A. Kanishev, and Maria Krawczyk. On distinguishing the direct and spontaneous CP violation in 2HDM. *PoS*, CHARGED2008:016, 2008. (Cited on page 127.)

[308] Michael Duerr, Felix Kahlhoefer, Kai Schmidt-Hoberg, Thomas Schwetz, and Stefan Vogl. How to save the WIMP: global analysis of a dark matter model with two s-channel mediators. *JHEP*, 09:042, 2016. (Cited on page 128.)

[309] Michael S. Chanowitz, M. A. Furman, and I. Hinchliffe. Weak Interactions of Ultraheavy Fermions. 2. *Nucl. Phys.*, B153:402–430, 1979. (Cited on page 129.)

[310] Michael S. Chanowitz, M. A. Furman, and I. Hinchliffe. Weak Interactions of Ultraheavy Fermions. *Phys. Lett.*, B78:285, 1978. (Cited on page 129.)

[311] Higgs Pair Production in the $H(\to \tau\tau)H(\to b\bar{b})$ channel at the High-Luminosity LHC. Technical Report ATL-PHYS-PUB-2015-046, CERN, Geneva, Nov 2015. (Cited on pages 132, 133 and 164.)

[312] Higgs pair production at the High Luminosity LHC. Technical Report CMS-PAS-FTR-15-002, CERN, Geneva, 2015. (Cited on pages 132, 133 and 164.)

[313] M. Bahr, S. Gieseke, M.A. Gigg, D. Grellscheid, K. Hamilton, et al. Herwig++ Physics and Manual. *Eur.Phys.J.*, C58:639–707, 2008. (Cited on page 134.)

[314] Alexander L. Read. Presentation of search results: The CL(s) technique. *J.Phys.*, G28:2693–2704, 2002. (Cited on page 134.)

[315] Alexander L. Read. Modified frequentist analysis of search results (The CL(s) method). *CERN-OPEN-2000-205*, 2000. (Cited on page 134.)

[316] Georges Aad et al. A search for $t\bar{t}$ resonances using lepton-plus-jets events in proton-proton collisions at $\sqrt{s} = 8$ TeV with the ATLAS detector. *JHEP*, 08:148, 2015. (Cited on pages 139, 140, 141, 143 and 155.)

[317] Vardan Khachatryan et al. Search for resonant $t\bar{t}$ production in proton-proton collisions at $\sqrt{s} = 8$TeV. *Phys. Rev.*, D93(1):012001, 2016. (Cited on pages 139, 141 and 155.)

[318] Juan Martin Maldacena. The Large N limit of superconformal field theories and supergravity. *Int. J. Theor. Phys.*, 38:1113–1133, 1999. [Adv. Theor. Math. Phys.2,231(1998)]. (Cited on page 139.)

[319] Edward Witten. Anti-de Sitter space and holography. *Adv. Theor. Math. Phys.*, 2:253–291, 1998. (Cited on page 139.)

[320] Nima Arkani-Hamed, Massimo Porrati, and Lisa Randall. Holography and phenomenology. *JHEP*, 08:017, 2001. (Cited on page 139.)

[321] R. Rattazzi and A. Zaffaroni. Comments on the holographic picture of the Randall-Sundrum model. *JHEP*, 04:021, 2001. (Cited on page 139.)

[322] David Krohn, Tao Liu, Jessie Shelton, and Lian-Tao Wang. A Polarized View of the Top Asymmetry. *Phys. Rev.*, D84:074034, 2011. (Cited on page 140.)

[323] Matthew Baumgart and Brock Tweedie. Transverse Top Quark Polarization and the ttbar Forward-Backward Asymmetry. *JHEP*, 08:072, 2013. (Cited on page 140.)

[324] Brock Tweedie. Better Hadronic Top Quark Polarimetry. *Phys. Rev.*, D90(9):094010, 2014. (Cited on page 140.)

[325] Jessie Shelton. Polarized tops from new physics: signals and observables. *Phys. Rev.*, D79:014032, 2009. (Cited on page 140.)

[326] Rohini M. Godbole, Lisa Hartgring, Irene Niessen, and Chris D. White. Top polarisation studies in H^-t and Wt production. *JHEP*, 01:011, 2012. (Cited on page 140.)

[327] Katri Huitu, Santosh Kumar Rai, Kumar Rao, Saurabh D. Rindani, and Pankaj Sharma. Probing top charged-Higgs production using top polarization at the Large Hadron Collider. *JHEP*, 04:026, 2011. (Cited on page 140.)

[328] Andreas Papaefstathiou and Kazuki Sakurai. Determining the Helicity Structure of Third Generation Resonances. *JHEP*, 06:069, 2012. (Cited on page 140.)

[329] Kaustubh Agashe, Alexander Belyaev, Tadas Krupovnickas, Gilad Perez, and Joseph Virzi. LHC Signals from Warped Extra Dimensions. *Phys. Rev.*, D77:015003, 2008. (Cited on page 140.)

[330] Ben Lillie, Lisa Randall, and Lian-Tao Wang. The Bulk RS KK-gluon at the LHC. *JHEP*, 09:074, 2007. (Cited on page 140.)

[331] Kaustubh Agashe, Antonio Delgado, Michael J. May, and Raman Sundrum. RS1, custodial isospin and precision tests. *JHEP*, 08:050, 2003. (Cited on page 141.)

[332] Oleg Antipin and Tuomas Hapola. Graviton model file. `http://cp3-origins. dk/research/units/ed-tools`. (Cited on page 141.)

[333] Kaustubh Agashe, Hooman Davoudiasl, Gilad Perez, and Amarjit Soni. Warped Gravitons at the LHC and Beyond. *Phys. Rev.*, D76:036006, 2007. (Cited on page 142.)

[334] Morad Aaboud et al. Searches for heavy diboson resonances in pp collisions at $\sqrt{s} = 13$ TeV with the ATLAS detector. *JHEP*, 09:173, 2016. (Cited on page 142.)

[335] Albert M Sirunyan et al. Search for massive resonances decaying into WW, WZ or ZZ bosons in proton-proton collisions at $\sqrt{s} = 13$ TeV. 2016. (Cited on page 142.)

[336] Rikkert Frederix and Fabio Maltoni. Top pair invariant mass distribution: a window on new physics. *Journal of High Energy Physics*, 2009(01):047, 2009. (Cited on page 142.)

[337] Michal Czakon and Alexander Mitov. NNLO corrections to top-pair production at hadron colliders: the all-fermionic scattering channels. *JHEP*, 12:054, 2012. (Cited on page 142.)

[338] Michal Czakon and Alexander Mitov. NNLO corrections to top pair production at hadron colliders: the quark-gluon reaction. *JHEP*, 01:080, 2013. (Cited on page 142.)

[339] Michał Czakon, Paul Fiedler, and Alexander Mitov. Total Top-Quark Pair-Production Cross Section at Hadron Colliders Through $O(\frac{4}{S})$. *Phys. Rev. Lett.*, 110:252004, 2013. (Cited on page 142.)

[340] Johannes Bellm et al. Herwig 7.0/Herwig++ 3.0 release note. *Eur. Phys. J.*, C76(4):196, 2016. (Cited on page 142.)

[341] Georges Aad et al. Performance of Missing Transverse Momentum Reconstruction in Proton-Proton Collisions at 7 TeV with ATLAS. *Eur. Phys. J.*, C72:1844, 2012. (Cited on page 143.)

[342] Electron identification measurements in ATLAS using $\sqrt{s} = 13$ TeV data with 50 ns bunch spacing. Technical Report ATL-PHYS-PUB-2015-041, CERN, Geneva, Sep 2015. (Cited on page 143.)

[343] Georges Aad et al. Muon reconstruction performance of the ATLAS detector in proton–proton collision data at $\sqrt{s} =$ 13 TeV. *Eur. Phys. J.*, C76(5):292, 2016. (Cited on page 143.)

[344] M. Wobisch and T. Wengler. Hadronization corrections to jet cross-sections in deep inelastic scattering. In *Monte Carlo generators for HERA physics. Proceedings, Workshop, Hamburg, Germany, 1998-1999*, pages 270–279, 1998. (Cited on page 143.)

[345] Keith Rehermann and Brock Tweedie. Efficient Identification of Boosted Semileptonic Top Quarks at the LHC. *JHEP*, 03:059, 2011. (Cited on page 143.)

[346] Tilman Plehn, Michael Spannowsky, and Michihisa Takeuchi. Boosted Semileptonic Tops in Stop Decays. *JHEP*, 05:135, 2011. (Cited on page 143.)

[347] Tilman Plehn, Gavin P. Salam, and Michael Spannowsky. Fat Jets for a Light Higgs. *Phys. Rev. Lett.*, 104:111801, 2010. (Cited on page 143.)

[348] Gregor Kasieczka, Tilman Plehn, Torben Schell, Thomas Strebler, and Gavin P. Salam. Resonance Searches with an Updated Top Tagger. *JHEP*, 06:203, 2015. (Cited on page 143.)

[349] Georges Aad et al. Performance of b-Jet Identification in the ATLAS Experiment. *JINST*, 11(04):P04008, 2016. (Cited on page 143.)

[350] Search for heavy particles decaying to pairs of highly-boosted top quarks using lepton-plus-jets events in proton–proton collisions at $\sqrt{s} = 13$ TeV with the ATLAS detector. Technical Report ATLAS-CONF-2016-014, CERN, Geneva, Mar 2016. (Cited on page 144.)

[351] David Krohn, Jessie Shelton, and Lian-Tao Wang. Measuring the Polarization of Boosted Hadronic Tops. *JHEP*, 07:041, 2010. (Cited on page 145.)

[352] Lars Sonnenschein. Algebraic approach to solve $t\bar{t}$ dilepton equations. *Phys. Rev.*, D72:095020, 2005. (Cited on page 146.)

[353] Lars Sonnenschein. Analytical solution of ttbar dilepton equations. *Phys. Rev.*, D73:054015, 2006. [Erratum: Phys. Rev.D78,079902(2008)]. (Cited on page 146.)

[354] K. Kondo. Dynamical Likelihood Method for Reconstruction of Events With Missing Momentum. 1: Method and Toy Models. *J. Phys. Soc. Jap.*, 57:4126–4140, 1988. (Cited on page 146.)

[355] B. Abbott et al. Measurement of the top quark mass using dilepton events. *Phys. Rev. Lett.*, 80:2063–2068, 1998. (Cited on page 146.)

[356] Morad Aaboud et al. Measurements of top-quark pair differential cross-sections in the $e\mu$ channel in pp collisions at $\sqrt{s} = 13$ TeV using the ATLAS detector. 2016. (Cited on page 146.)

[357] C. G. Lester and D. J. Summers. Measuring masses of semiinvisibly decaying particles pair produced at hadron colliders. *Phys. Lett.*, B463:99–103, 1999. (Cited on page 146.)

[358] Won Sang Cho, Kiwoon Choi, Yeong Gyun Kim, and Chan Beom Park. M(T2)-assisted on-shell reconstruction of missing momenta and its application to spin measurement at the LHC. *Phys. Rev.*, D79:031701, 2009. (Cited on pages 146 and 150.)

[359] Won Sang Cho, Kiwoon Choi, Yeong Gyun Kim, and Chan Beom Park. Mass and Spin Measurement with M(T2) and MAOS Momentum. *Nucl. Phys. Proc. Suppl.*, 200-202:103–112, 2010. (Cited on page 146.)

[360] Hsin-Chia Cheng and Zhenyu Han. Minimal Kinematic Constraints and m(T2). *JHEP*, 12:063, 2008. (Cited on pages 147 and 148.)

[361] Alan J. Barr, Ben Gripaios, and Christopher G. Lester. Transverse masses and kinematic constraints: from the boundary to the crease. *JHEP*, 11:096, 2009. (Cited on page 147.)

[362] Chrisopher G. Lester and Benjamin Nachman. Bisection-based asymmetric M_{T2} computation: a higher precision calculator than existing symmetric methods. *JHEP*, 03:100, 2015. (Cited on pages 147 and 149.)

[363] Fernando Etayo, Laureano Gonzalez-Vega, and Natalia del Rio. A new approach to characterizing the relative position of two ellipses depending on one parameter. *Computer Aided Geometric Design*, 23(4):324 – 350, 2006. (Cited on pages 147 and 149.)

[364] L. Gonzalez, H. Lombardi, T. Recio, and M.-F. Roy. Sturm-habicht sequence. In *Proceedings of the ACM-SIGSAM 1989 International Symposium on Symbolic and Algebraic Computation*, ISSAC '89, pages 136–146, New York, NY, USA, 1989. ACM. (Cited on page 149.)

[365] Alan J. Barr, Ben Gripaios, and Christopher Gorham Lester. Measuring the Higgs boson mass in dileptonic W-boson decays at hadron colliders. *JHEP*, 07:072, 2009. (Cited on page 150.)

[366] Daniel R. Tovey. Transverse mass and invariant mass observables for measuring the mass of a semi-invisibly decaying heavy particle. *JHEP*, 11:148, 2010. (Cited on page 150.)

[367] Kiwoon Choi, Diego Guadagnoli, and Chan Beom Park. Reducing combinatorial uncertainties: A new technique based on MT2 variables. *JHEP*, 11:117, 2011. (Cited on page 150.)

[368] Chan Beom Park. Reconstructing the heavy resonance at hadron colliders. *Phys. Rev.*, D84:096001, 2011. (Cited on page 150.)

[369] Diego Guadagnoli and Chan Beom Park. M_{T2}-reconstructed invisible momenta as spin analizers, and an application to top polarization. *JHEP*, 01:030, 2014. (Cited on page 150.)